Abstract

The analyses of spray, combustion and emission characteristics for two types of biodiesel fuels, namely coconut methyl ester (CME) and soybean methyl ester (SME) are reported in this thesis. In order to produce high fidelity numerical spray and combustion representation for CME and SME, accurately developed thermo-physical properties and chemical kinetics were integrated with open-source computational fluid dynamics codes. First, the thermo-physical properties of CME and SME which include liquid and vapour properties were calculated using temperature-dependent correlations that were found in the literature. These calculated thermo-physical properties were then incorporated into Open Field Operation and Manipulation (OpenFOAM) to determine the sensitivities of the fuel properties on the spray development. Based on the sensitivity analyses, 5 of 12 thermo-physical properties, including latent heat of vaporisation, liquid density, liquid heat capacity, liquid surface tension and vapour pressure, gave the largest fluctuation to the spray development. Besides, coupled effects among the thermo-physical properties were discovered. The effects of thermo-physical properties were also varied according to the addition of unsaturation levels and combustion chemistries.

Next, a generic reduced chemical kinetic mechanism, with components of methyl decanoate, methyl-9-decenoate and n-heptane was developed to represent the biodiesel fuels. The reduced mechanism with 92 species and 360 elementary reactions was validated under 72 shock tube conditions against experimental measurements in the literature and detailed mechanism predictions, for each zero-dimensional auto-ignition and extinction process using CHEMKIN-PRO. Maximum percentage errors of less than 40.0% were recorded when the ignition delay (ID) period predictions of the reduced mechanism were compared to those of detailed mechanism. Satisfactory agreement was attained when the predictions of the reduced mechanism were validated against the measured species profiles of rapeseed methyl ester oxidation in jet stirred reactor, which were obtained from the literature.

Besides, the ID periods and lift-off lengths (LOL) predicted for the reacting spray at initial temperatures of 900 K and 1000 K achieved a maximum deviation of 29.8% and 43.4%, respectively, as compared to those of the experimental measurements in the literature.

CME and SME were then numerically analysed under both the conditions of constant volume bomb and diesel engine, using the validated thermo-physical properties and reduced mechanism. The ambient oxygen level of the constant volume bomb was raised from 15.0 to 21.0% to emulate the intake air composition in the diesel engine. As such, the spray development was changed from radial to forward propagation, where LOL was reduced by 24.3%. Higher levels of carbon monoxide (CO), carbon dioxide (CO_2) and soot mass concentrations were also obtained. When the unsaturation level was increased from 20.0% (CME) to 80.0% (SME), retarded spray and combustion developments were found in both the constant volume bomb and diesel engine. Besides, the CO, soot and nitric oxide (NO) emissions, including the tailpipe predictions were maximally increased by 32.0%. In overall, CME performs better than SME does because of the improved air-fuel mixing and decreased tailpipe NO, CO and CO_2 emissions. Based on these, it is sufficient to deduce that the phenomena predicted in the constant volume bomb are adequate to replicate those in the diesel engine.

List of Publications

Journals/Technical Paper

1. Cheng X., Ng H. K., Gan S., Ho J. H. and Pang K. M., "Development of a generic reduced biodiesel chemical kinetic mechanism for CFD spray combustion modelling", Combustion and Flame 162, 2354-2370, 2015.

2. Cheng X., Ng H. K., Gan S. and Ho J. H., "Development of biodiesel skeletal mechanisms for kinetic combustion modelling", SAE Technical Paper 2013-01-2633, 2013.

3. Cheng X., Ng H. K., Gan S. and Ho J. H., "Advances in CFD modelling of in-cylinder biodiesel combustion", Energy and Fuels 27, 8, 4489-4506, 2013.

4. Cheng X., Mohamed Ismail H., Ng H. K., Gan S. and Lucchini T., "Effects of fuel thermo-physical properties on spray characteristics of biodiesel fuels", Lecture Notes in Electrical Engineering: Volume 3: Future Automotive Powertrains (I), 191, 117-126, 2013.

5. Cheng X., Ng H. K., Gan S., Ho J. H. and Pang K. M., "Sensitivity analyses of biodiesel thermo-physical properties under diesel engine conditions", Submitted to Energy, 2015.

6. Mohamed Ismail H., Cheng X., Ng H. K., Gan S., Lucchini T. and D'Errico G., "Investigation of biodiesel-diesel fuel blends on combustion characteristics in a light-duty diesel engine using OpenFOAM", Energy and Fuels 27 (1), 208-219, 2013.

7. Mohamed Ismail H., Cheng X., Ng H. K., Gan S., Lucchini T. and D'Errico G., "Development of thermophysical and transport properties for the CFD simulations of in-cylinder biodiesel spray combustion", Energy and Fuels 26 (8), 4857-4870, 2012.

Conferences

1. Cheng X., Mohamed Ismail H., Ng H. K., Gan S. and Lucchini T., "Effects of fuel thermo-physical properties on spray characteristics of biodiesel fuels", In Proceedings of the FISITA 2012 World Automotive Congress, Beijing, China, November 27 – 30, 2012.

Acknowledgement

I would like to express my special appreciation to everyone who has supported me throughout my research period in the University of Nottingham Malaysia Campus. My supervisor, Prof. Ng Hoon Kiat, is especially thanked for his invaluable guidance and advice. I would also like to thank my co-supervisors, Prof. Gan Suyin and Dr. Ho Jee Hou for their practical suggestions and support.

Also in need of acknowledgement are my research group mates, Dr. Pang Kar Mun, Dr. Harun Ismail, Ms. Poon Hiew Mun and Mr. Ong Jiun Cai, for the assistance and laughter they gave. Dr Jean-Guillaume Nerva and Dr Lyle Pickett are also thanked for providing experimental data for model validation.

This research was conducted under the generous financial support from the University of Nottingham Malaysia Campus, by providing the Dean's Scholarship.

Lastly, I would like to express a special thanks to my parents and sisters, for supporting me with continuous love, patience and encouragement during my ups and downs.

Table of Contents

Abbreviations

0D	Zero-dimensional
2D	Two-dimensional
3D	Three-dimensional
ATDC	After top dead centre
B50	50.0% biodiesel and 50.0% diesel
CA50	Crank angle where 50% accumulated heat was released
C_2H_2	Acetylene
C_2H_4	Ethylene
C_7H_{16}	n-heptane
CCM	Chemistry coordinate mapping
CFD	Computational fluid dynamics
CME	Coconut methyl ester
CN	Cetane number
CO	Carbon monoxide
CO_2	Carbon dioxide
DRG	Directed relation graph
DRGASA	Directed relation graph aided sensitivity analysis
DRGEP	Directed relation graph with error propagation
DRGEPSA	Directed relation graph with error propagation and sensitivity analysis
ERC	Engine Research Centre
EVO	Exhaust valve opening
FAME	Fatty acid methyl ester
H_2O_2	Hydrogen peroxide
HCCI	Homogenous charge compression ignition
HO_2	Hydroperoxyl
HRR	Heat release rate
ID	Ignition delay
ISAT	*in-situ* adaptive tabulation
IVC	Intake valve closure
JSR	Jet-stirred reactor

KHRT	Kelvin-Helmholtz and Rayleigh-Taylor
LLNL	Lawrence Livermore National Laboratory
LOL	Lift-off length
LPL	Liquid penetration length
MB	Methyl butanoate
MB2D	Methyl (E)-2-butenoate
MBBio	Methyl butanoate + methyl (E)-2-butenoate
MD	Methyl decanoate
MD5D	Methyl-5-decenoate
MD9D	Methyl-9-decenoate
MDBio	Methyl decanoate + methyl-9-decenoate + n-heptane
MHex	Methyl hexanoate
MHep	Methyl heptanoate
MOct	Methyl octanoate
N_2	Nitrogen
N_2O	Nitrous oxide
NO	Nitric oxide
NO_2	Nitrogen dioxide
NO_x	Nitrogen oxides
NTC	Negative temperature coefficient
O_2	Oxygen
ODE	Ordinary differential equation
OH	Hydroxyl
OpenFOAM	Open Field Operation and Manipulation
OPPDIF	Opposed-flow diffusion flame
PFA	Path flux analysis
PM	Particulate matter
PME	Palm methyl ester
PSR	Perfectly-stirred reactor
RANS	Reynolds-averaged Navier Stokes
RME	Rapeseed methyl ester
RNG	Renormalisation group theory
ROC	Rate of consumption

ROP	Rate of production
RPD	Relative percentage difference
SIBS	Semi-implicit Bulirsch-Stoer
SME	Soybean methyl ester
SOI	Start of injection
SVF	Soot volume fraction
TDAC	Tabulation of dynamic adaptive chemistry
VPL	Vapour penetration length

Nomenclature

Latin symbols

a	Polynomial constant (-); Rate expression for gas phase reactions ($mol\ cm^{-3}\ s^{-1}$); Group contribution parameter (-)
A	Pre-exponential factor (mol cm s K); Surface area (cm^2); Constant (-); Parameter obtained from the regression of the experimental data (-)
b	Temperature exponent (-); Group contribution parameter (-)
B	Second virial coefficient ($m^3\ kg^{-1}$); Constant (-); Parameters obtained from the regression of the experimental data (-)
c	Group contribution parameter (-)
C	Consumption rate (-); Breakup time constant (-); Turbulent model constant (-); Soot model constant (s^{-1}, $kg\ m^{0.5}\ kmol^{-1}\ s^{-1}$); Constant (-); Parameter obtained from the regression of the experimental data (-)
C_p	Specific heat capacity ($cal\ mol^{-1}$); Heat capacity ($J\ mol^{-1}\ K^{-1}$, $cal\ g^{-1}\ mol^{-1}\ K^{-1}$); Molal heat capacity for liquid ($cal\ g^{-1}\ mol^{-1}\ K^{-1}$); Ideal gas heat capacity at constant volume ($cal\ mol^{-1}\ K^{-1}$)
d	Particle diameter (m); Group contribution parameter (-)
D	Binary vapour diffusivity ($cm^2\ s^{-1}$); Constant (-); Parameters obtained from the regression of the experimental data (-)
E	Constant (-)
E_a	Activation energy ($cal\ mol^{-1}$)
f	Optimised constant (-)
F	Residual vector (-); Constant (-);
G	Generation of turbulence kinetic energy ($kg\ m^{-1}\ s^{-3}$); Interaction parameter (-); Constant (-);
H	Enthalpy ($cal\ mol^{-1}$); Constant (-)
ΔH_v	Latent heat of vaporisation ($J\ mol^{-1}$)
k	Rate constants ($mol\ cm\ s\ K^2$)
k'	Binary parameter (-)

K	Equilibrium constant (-)
K_g	Total number of gas phase species (-)
$\dot{m}$	Mass flow rate (kg s^{-1})
M	Soot mass concentration (kg m^{-3})
M_p	Mass of incipient soot particle (kg kmol^{-1})
$[M]$	Molar concentration (mol cm^{-3})
n	Number of carbon atoms in the carboxylic acid minus one (-)
N	Total number of species (-); Soot particle number density (particles m^{-3}); Number (-)
N_c	Number of carbon (-)
N_{cs}	Number of carbon in alcohol (-)
N_{PSR}	Total number of reactor modules in the reactor network (-)
p	Inorganic liquid constant (-)
P	Production rate (-); Pressure (Pa, bar)
$[P]$	Parachor constant (-)
q	Rate of progress (mol cm^{-3} s^{-1}); Organic liquid constant (-)
r	Dependence ratio (-)
R	Universal gas constant (cal mol^{-1} K^{-1}); Gas constant (J mol^{-1} K^{-1}); Fraction of outflow (-)
Re	Reynolds number (-)
S	Entropy (cal mol^{-1}); User-defined source terms (-); Vapour viscosity constant (-)
Sc_t	Schmidt number (-)
s	Optimised constant (-)
$\dot{s}$	Molar surface production rate (mol cm^{-2} s^{-1})
T	Temperature (K); Activation temperature (K)
U_r	Relative velocity (m s^{-1})
V	Reactor volume (cm^3); Volume (ml mol^{-1})
w	First order sensitivity coefficient matrix (-); Weighting factor (-)
W	Molecular weight (kg mol^{-1}, g mol^{-1})
We	Weber number (-)

X_{sgs}	Mole fraction of participating surface growth species (-)
y	Droplet distortion constant (-); Mole fraction (-)
Y	Mass fraction (-)
$\dot{Y}_i$	Reaction rate (s^{-1})
Y_M	Contribution of fluctuating dilatation in compressible turbulence to the overall dissipation rate (-)
$Y_i^*(t + \Delta t)$	Mass fraction in each cell calculated by the chemistry solver (-)
Z_{RA}	Compressibility factor (-)

Greek symbols

δ	Existence ratio (-)
ε	User-defined threshold (-); Turbulent dissipation rate (m^2 s^{-3}); Potential energy parameter (m^2 kg s^{-1})
η	Viscosity (mPa s)
η_{coll}	Collision efficiency parameter (-)
φ	Equivalence ratio (-); Vector of temperature (-); Reduced temperature constant (-); Mixture fraction (-)
φ_N	Particle number density (-)
k	Turbulent kinetic energy (m^2 s^{-2}); Boltzmann's constant (m^2 kg s^{-2} K^{-1})
λ	Thermal conductivity (cal cm^{-1} s^{-1} K^{-1})
μ_t	Turbulent viscosity (Pa s)
v	Stoichiometric coefficient (-); Kinematic viscosity (m^2 s^{-1})
ω	Production rate (mol cm^{-3} s^{-1}); Reaction rate (mol cm^{-3} s^{-1}); Acentric factor (-)
Ω	Reduced collision integral which depends upon the intermolecular potential (-)
ρ	Mass density (g cm^{-3}); Liquid density (kg m^{-3}, kg L^{-1}, g mL^{-1}, mol ml^{-1}); Molal liquid density (g mol cm^{-3})
σ	Liquid surface tension (kg s^{-2}, mN m^{-1}); Prandtl number (-); Potential distance parameter (Å)

τ	Characteristic breakup time (s)

Superscripts

$*$	Inlet stream quantities; Dimensionless
j	jth reactor number
r	Reactor
vp	Vapour

Subscripts

α	Nucleation
atm	Atmosphere
A	Atoms; Avogrado number
b	Backward; Boiling point
bag	Bag breakup
β	Coagulation
c	Critical; Carbon
cs	Carbons from alcohol
d	Drag
f	Forward; Fuel
g	Ambient gas
γ	Surface growth
i	ith reaction; ith pure component
j	jth dependent variables; jth pure component
k	kth species; kth groups
L	Liquid
m	mth material, mixture
r	Reduced
R	Reference temperature
$soot$	Soot
$sphere$	Spherical object
$strip$	Stripping breakup
$w1$	Soot oxidation due to OH radicals
$w2$	Soot oxidation due to O_2 radicals

X   *X* species

Y   *Y* species

List of Figures

List of Tables

Chapter 1
Introduction

1.1 Background

The rise of biodiesel as a reliable alternative fuel has stimulated extensive interest and research to further exploit this fuel for power generation in ground transportation sector. Therefore, numerous studies have been conducted either on experimental or numerical fronts to understand the combustion characteristics of biodiesel under engine environment. This is because biodiesel is comparatively less harmful to the environment than diesel as its utilisation in internal combustion engines and burners reduces pollutants formation such as carbon monoxide (CO) [1,2], unburned hydrocarbons [3,4], particulate matter (PM) [5,6] and soot precursors [7]. Besides, biodiesel also has high compatibility with existing diesel infrastructure and availability of production technology, which in turn give rise to lower cost of production [8,9]. However, several drawbacks are also found with biodiesel usage. For example, the lower heating value of biodiesel as compared to that of diesel contributes to the increased fuel consumption [10] and also reduced engine power output [11,12]. Furthermore, higher levels of nitrogen oxides (NO$_x$) emission [3,4,13,14] are also detected when biodiesel replaces diesel. As such, continuing research efforts are focusing on improving the fundamental knowledge and understanding of biodiesel combustion and emissions characteristics in an effort to address the drawbacks associated with the use of biodiesel.

1.1.1   Numerical Modelling of Biodiesel Combustion

In order to study the combustion characteristics of biodiesel in engines, both experimental and computational approaches are adopted. Computational fluid dynamics (CFD) modelling is a powerful tool that is used to simulate biodiesel combustion with high fidelity results generated at a much lower operating cost as compared to an experimental approach. The accuracy of the CFD results lies in the models chosen to optimise the complex calculations involved during the combustion simulation [15]. Together with the CFD models, combustion kinetics are often coupled into CFD solver to further understand the in-cylinder combustion process. For instance, the need of diesel chemical kinetics to study the growth of soot precursors has been highlighted in the work of Pang et al. [16]. In CFD combustion modelling, it is impractical to utilise the exact compositions of biodiesel comprising complex, long-chained fatty acid methyl esters (FAMEs) especially for three-dimensional (3D) engine simulations [17]. For this reason, simple and well-characterised chemical kinetic mechanisms are applied as surrogates to emulate the kinetic behaviour of biodiesel [18]. Biodiesel surrogate mechanisms are carbon chains with oxygenated compounds such as methyl butanoate (MB, $C_5H_{10}O_2$) [19] and methyl decanoate (MD, $C_{11}H_{22}O_2$) [20]. There has been a steady growth of detailed mechanisms development and utilisation as a result of the demand for more accurate combustion simulations, such as the shift from small mechanisms to large mechanisms in order to study the combustion kinetics accurately [21]. Despite the kinetics comprehensiveness offered by these detailed mechanisms, these mechanisms especially those developed based on less than 5-carbonyl chains lack accuracy in the negative temperature coefficient (NTC) region [22,23] and low temperature reactivity [24]. Besides, the detailed mechanisms also induce difficulty and complexity in the numerical modelling, even for zero-dimensional (0D) kinetic modelling [21]. Furthermore, the large sizes of detailed mechanisms have restricted the applications of 3D CFD combustion modelling using chemical kinetic mechanisms for more comprehensive combustion analysis because these become particularly time-consuming in the CFD modelling [25]. Moreover, Lu and Law [21] also reported that the detailed mechanisms are highly

sensitive to changes in operating conditions and reaction rates. Hence, detailed mechanisms are reduced in an effort to allow them for use in 3D CFD combustion modelling with minimal simulation cost and runtime. However, it must be noted here that there are risks in producing over simplified mechanisms such as the inability to emulate the kinetics of the detailed mechanisms as well as generating erroneous modelling results [21].

Rapid technological advancement in computing power and development of tabulation techniques such as tabulation of dynamic adaptive chemistry (TDAC) [26], *in-situ* adaptive tabulation (ISAT) [27], chemistry coordinate mapping (CCM) [28,29] and analytical Jacobian approach [30] have successfully minimised the computational time involved in solving the chemical kinetics. For instance, the analytical Jacobian approach formulated by Perini et al. [30] improved computational time by approximately two times when the approach was applied onto different reduced and detailed mechanisms ranging from 29 species to 2878 species under 0D kinetic modelling. Meanwhile, Jangi and Bai [29] showed that the introduction of their CCM method into multi-dimensional CFD modelling achieved a reduction of 3.0 to 7.0% in computational time by separating the flow field and chemical kinetics into physical and space phases with every cell in the space phase mapped to several cells in the physical phase. Despite the successful demonstrations of these tabulation techniques and analytical approaches, the demands for reduced mechanisms remain as the number of chemical kinetics that can be integrated into CFD modelling software is limited. Therefore, reduced mechanisms which retain the chemical comprehensiveness from the detailed mechanisms are desired. With reduced mechanisms, the complexity and stiffness associated with detailed chemical kinetic mechanism and simulation cost are also further mitigated [31].

Besides the importance of chemical kinetics in CFD modelling, accurate estimations of thermo-physical properties for biodiesel are also vital [32]. This is because the fuel spray development [33], air and fuel mixing and also the subsequent combustion and emissions processes [32,34] are found heavily

affected by the thermo-physical properties. For example, Genzale et al. [35] suggested that the higher liquid density and liquid viscosity of biodiesel contributed to longer liquid penetration length (LPL) than that of diesel. On the other hand, Nerva et al. [36] noticed that the higher mass flow rate for soybean methyl ester (SME) was due to the higher liquid density and liquid viscosity. Moreover, the outcome from an optical study of the spray behaviour of diesel and palm methyl ester (PME) [37] showed that the LPL was closely related to the liquid surface tension, liquid viscosity and liquid density. Besides, the injection pressure of biodiesel was found to be affected by the liquid viscosity and liquid density [38].

Apart from the experimental findings, the significance of thermo-physical properties is also noticeable in numerical modelling. For example, Kuti et al. [39] detected that the extended LPL of PME as compared to that of diesel was resulted by the higher boiling point of biodiesel. Besides, Lee and Huh [40] also pointed out that the larger SMD and slower mixing rate of SME are induced by the higher liquid viscosity and liquid surface tension of biodiesel as compared to those of diesel. Furthermore, Ra et al. [32] identified that liquid density and vapour pressure were important to the single drop vaporisation, retardation in injection timing, ignition delay (ID) period and in-cylinder peak pressure. However, there were no distinct changes in combustion characteristics when the individual thermo-physical property of SME was substituted. Meanwhile, Mohamed Ismail et al. [41] concluded that liquid density, liquid surface tension, vapour diffusivity and vapour pressure gave rise to the highest sensitivities on the spray development of PME. These aforementioned studies thus pinpoint the significance of fuel thermo-physical properties on the spray characteristics of biodiesel.

1.1.2   Emission Characteristics of Biodiesel

Although biodiesel can be directly used in diesel engine, the resulting spray, combustion and emission characteristics of biodiesel are distinguishable from diesel. This is because the majority components contained within diesel are

hydrocarbons, while biodiesel comprises largely alkyl esters. Overall, the use of biodiesel in diesel engine produces remarkable reduction on the exhaust emissions as compared to those of diesel, particularly PM, where reduced levels between 75.0% and 83.0% were found [42]. In addition, lower soot levels, before which PM is turned into, are also obtained when biodiesel is used in diesel engine. For example, the total soot mass measured for SME under the diesel engine combustion condition is reduced by half as compared to that of diesel [43]. Besides, Feng et al. [44] also found that the presence of methyl functional groups with additional oxygen (O_2) atoms reduces the tendency of soot formation as compared to n-alkanes of similar chain length. However, higher soot emission is found when the level of unsaturation in biodiesel increases [24,45]. This is because the double bonds of FAME components contribute to the increased formation of unsaturated species.

Despite the apparent benefit of soot reduction, biodiesel however tends to produce higher levels of NO_x. As summarised by Xue et al. [10], more than 65.0% of the findings in the literature pointed out that the use of pure biodiesel induces increased NO_x levels of up to 44.8%, depending on the feedstocks of biodiesel. Meanwhile, the remaining studies in the literature show that the NO_x production for biodiesel is identical or less than that of diesel [46,47]. The reason that no definite conclusion can be drawn for the NO_x emission of biodiesel is because NO_x is co-produced by the complex combustion and pollutant chemistry in the turbulent non-premixed flame as well as the consumption of vaporised and pre-mixed fuel within the unsteady turbulent flow of the engine cylinder [48]. Nevertheless, higher level of thermal nitric oxide (NO) emission is detected when the unsaturation level increases [49], which is a similar phenomenon to that of soot emission.

Although the aforementioned works have gathered the overall characteristics for biodiesel, comparisons among different biodiesel fuels are not performed since only specific feedstocks are analysed. Thus, it is imperative to conduct a comparison study for different biodiesel fuels such that the behaviours of biodiesel fuels can be well characterised.

1.2   Research Objectives

Accurate models of thermo-physical properties and chemical kinetics for biodiesel are important in order to produce high fidelity numerical results. Although many relevant research works regarding the thermo-physical properties and chemical kinetics for biodiesel can be found in the literature [34,50–55], only specific feedstocks are studied. Therefore, the main objective of this research study is to analyse the characteristics for two biodiesel fuels, coconut methyl ester (CME) and SME, by developing generic yet accurate thermo-physical properties and chemical kinetic mechanism. This thus forms three main phases of work as highlighted in Figure 1.1, which include the formulations of thermo-physical properties and reduced chemical kinetic mechanism, and also the modelling of spray, combustion and emissions for biodiesel. Detailed descriptions and corresponding phases of work are provided in the subsequent sections.
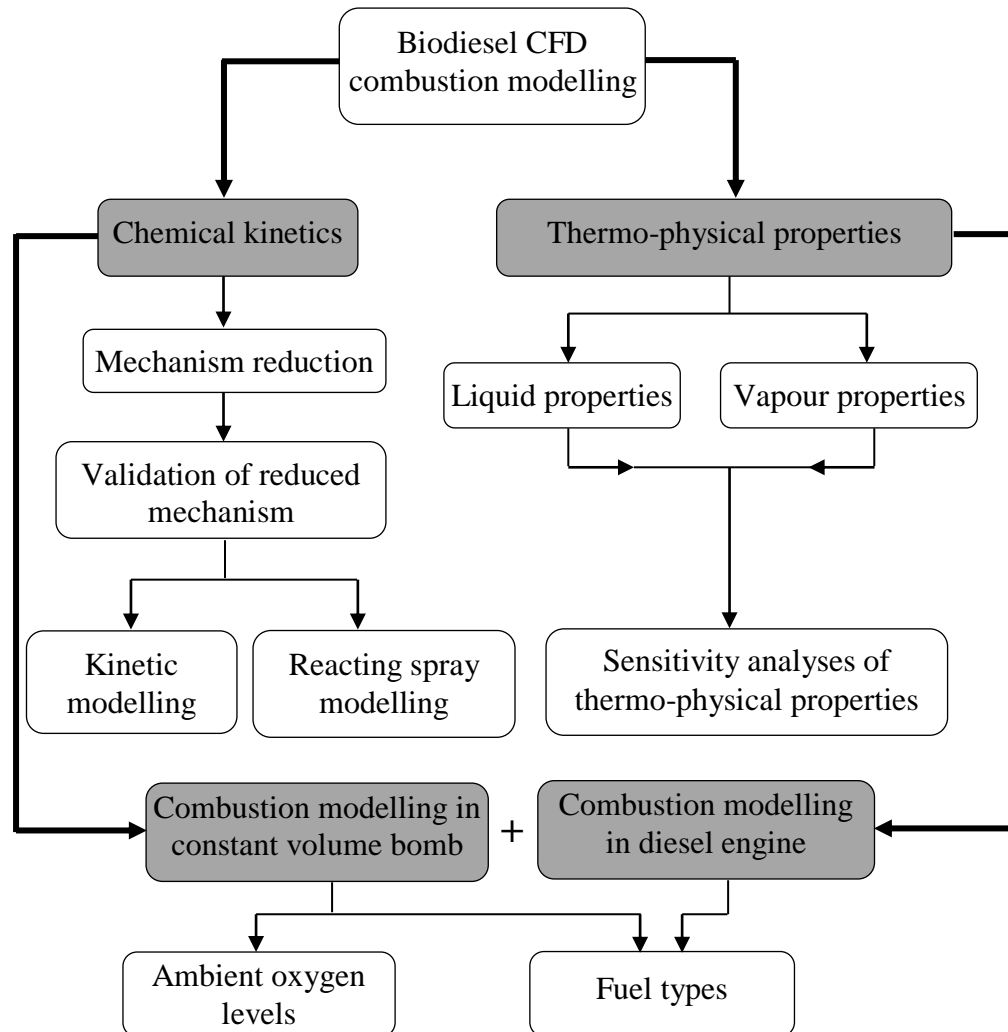
Figure 1.1 Schematic framework of this study (the main phases of work are as highlighted).

1.2.1 To evaluate thermo-physical properties for biodiesel

The thermo-physical properties are important for accurate numerical results, as the development of spray, ignition, combustion and emissions are strongly dependent on the properties [32,37]. Thus, a total of 15 thermo-physical properties including the critical properties, liquid properties and vapour properties are evaluated in this research study. The thermo-physical properties are calculated using correlations found in the literature for CME and SME. Apart from the evaluation of thermo-physical properties, analyses on the sensitivities of thermo-physical properties of CME and SME are also included

in this phase of work such that the significance of the thermo-physical properties can be identified. The thermo-physical properties are examined under the environments of non-reacting and reacting sprays, where the properties are integrated as specific fuel library into Open Field Operation and Manipulation (OpenFOAM). For the sensitivity analyses, the significance of the fuel properties are determined based on the deviations obtained in the predicted spray and soot results during quasi-steady period as compared to a baseline case, when the fuel properties are replaced by those of diesel. Here, the individual and coupled effects among the thermo-physical properties are identified. Besides, the predicted spray and soot results for CME are compared against those of SME such that the significance of unsaturation levels can be identified. Furthermore, the influence of combustion chemistries on the thermo-physical properties is also assessed by comparing the predictions between non-reacting and reacting sprays.

1.2.2   To formulate a generic reduced chemical kinetic mechanism for biodiesel

Developing a reduced surrogate mechanism that is able to provide detailed descriptions of in-cylinder combustion phenomena for biodiesel is important. As such, many works have since been dedicated in developing reduced mechanisms for biodiesel [50–52,55,56]. Nevertheless, these reduced mechanisms found in the literature are only suitable for the applications of their validated operating conditions and fuel compositions.

In line to address this challenge, a generic reduced chemical kinetic mechanism is developed for the applications of various biodiesel fuels and wide range of operating conditions. In this phase of work, a large detailed mechanism with surrogate components similar to those of biodiesel FAMEs is selected. The detailed mechanism which contains large amount of complex chemical kinetics is reduced with various mechanism reduction techniques in order to accommodate current computation power and reduce computational time. The reduced biodiesel mechanism is modelled using the closed

homogeneous reactor and perfectly-stirred reactor (PSR) in CHEMKIN-PRO, under wide range of initial conditions. ID periods and key species profiles computed by the reduced mechanism are validated against the detailed mechanism predictions and also experimental measurements, which are obtained from the literature. Furthermore, the reduced biodiesel mechanism is also validated against experimental data in two-dimensional (2D) reacting spray modelling. A subsequent comparison study is also conducted to elucidate the developed reduced mechanism against two other reduced mechanisms of identical surrogate components found in the literature.

1.2.3 To analyse the effects of unsaturation level on the characteristics of spray, combustion and emissions, under the conditions of constant volume bomb and diesel engine

The main objective of this phase of work is to appraise the effects of unsaturation level on the spray, combustion and emission characteristics for CME and SME. In order to distinguish both the quasi-steady and in-cylinder characteristics, CME and SME are modelled in a constant volume bomb and a light-duty diesel engine. This is because localised predictions can be obtained in the constant volume bomb excluding the effects of in-cylinder flows, while the in-cylinder responses for biodiesel can be emulated through the modelling of diesel engine combustion. As such, CME and SME are first modelled in the constant volume bomb, where the ambient O_2 level is increased from 15.0 to 21.0% in order to replicate the intake air composition of the naturally aspirated diesel engine. Once this is performed, the effects of unsaturation level during quasi-steady state can be identified for both CME and SME. After that, the analysis is furthered to the diesel engine, such that the in-cylinder events for CME and SME can be estimated. By simulating both conditions, the localised and in-cylinder spray, combustion and emissions characteristics for CME and SME can be identified.

1.3   Thesis Outline

In this chapter, the research background and key objectives of this study are discussed. Chapter 2 covers a comprehensive review on the development of biodiesel chemical kinetic mechanisms, mechanism reduction techniques, thermo-physical properties and CFD combustion modelling. The literature review on the development of biodiesel mechanisms includes the historical progress from small to large biodiesel mechanisms. Meanwhile, the reduction techniques that have been applied on large biodiesel mechanisms are reviewed in the following section. The following section of Chapter 2 comprises a compilation of correlations that have been adopted to estimate the thermo-physical properties for biodiesel. In the last section of Chapter 2, a review on the combustion simulations performed using constant volume bomb and diesel engine setups is presented.

Chapter 3 discusses the theoretical backgrounds and governing equations of the numerical models utilised in the modelling of chemical kinetics, spray, turbulence, combustion and soot. The discussed CFD models include discrete phase, turbulence, turbulence-chemistry interaction and soot. Meanwhile, Chapter 4 covers the numerical formulations and experimental validations for the combustion modelling in constant volume bomb and diesel engine. This includes the numerical settings and parametric studies performed for spatial and temporal resolutions as well as CFD models.

The evaluation of thermo-physical properties for CME and SME is discussed in Chapter 5. Besides, the sensitivities of individual thermo-physical property of CME and SME are examined under non-reacting and reacting spray conditions. The effects of the thermo-physical properties on the subsequent spray development are compared with respect to the unsaturation levels and chemical kinetics. Besides, the coupled effects generated by the thermo-physical properties on the spray development are also investigated. The significance of individual thermo-physical property is determined based on parameters such as LPL, ID period, lift-off length (LOL) and soot distribution.

Meanwhile, the developmental work of a generic reduced biodiesel chemical kinetic mechanism is presented in Chapter 6. The formulation of the reduced biodiesel mechanism is thoroughly discussed. Validations of the reduced mechanism predictions against the detailed mechanism predictions and experimental measurements in kinetic modelling are also described. Subsequently, the reduced mechanism is appraised against two other reduced mechanisms available in the literature, under the reacting spray conditions.

Chapter 7 presents the combustion simulations under the conditions of constant volume bomb and diesel engine, with the integration of the evaluated thermo-physical properties in Chapter 5 and validated reduced mechanism in Chapter 6. The development of spray, combustion, soot and emissions predicted in the constant volume bomb and diesel engine are then numerically investigated for CME and SME.

Chapter 8 summarises the important results and key conclusions that are drawn from the entire research study. Finally, areas for future research are addressed.

Chapter 2

Literature Review

2.1   Introduction

For accurate numerical results, both thermo-physical properties and chemical kinetics are equally vital. The thermo-physical properties of biodiesel are found to give significant effects on spray and subsequent combustion development [32]. Meanwhile, the chemical kinetics of biodiesel which contains substantial measured or estimated reaction rates [57] governs important phenomena of ignition, combustion and extinction. In this chapter, the advances and progress achieved in CFD modelling of in-cylinder biodiesel combustion are appraised in terms of three aspects, namely the surrogate chemical kinetic mechanisms, mechanism reduction techniques and thermo-physical properties. The historical development of biodiesel surrogate mechanisms, starting from their use in kinetic modelling is first discussed. Additionally, research efforts in the application of reduced biodiesel mechanisms for CFD combustion modelling are also reviewed. Besides, an evaluation of the strengths and weaknesses of the reduction techniques used, including those based on 0D kinetic modelling and 3D CFD modelling is provided. Furthermore, a detailed review of the evaluation methods for thermo-physical properties that have been used in the CFD modelling of biodiesel combustion is provided. Lastly, the numerical simulations that have characterised biodiesel in constant volume bombs and diesel engines are compiled.

2.2   Biodiesel Chemical Kinetic Mechanism

The flow chart shown in Figure 2.1 depicts how the in-cylinder combustion characteristics of biodiesel are influenced by the chemical kinetics in the

surrogate mechanisms and the thermo-physical properties. Biodiesel chemical kinetic mechanisms typically contain essential species and reactions that describe various combustion characteristics such as ignition, combustion and soot formation. However, it is impractical to utilise the exact compositions of biodiesel comprising complex, long-chained FAMEs in CFD combustion modelling, especially for 3D engine simulations [17]. For this reason, simple and well-characterised chemical kinetic mechanisms are applied as surrogates to emulate the kinetic behaviour of biodiesel [18]. The surrogate mechanism for biodiesel is usually represented by one to two alkyl esters component to minimise the complexity resulted from the chemistries.

Table 2.1 is a bibliographic compilation of the available small and large biodiesel surrogate mechanisms with their respective testing conditions such as the initial pressures, temperatures and equivalence ratios [19,22,24,50,51,53,56–71]. The majority of biodiesel surrogate mechanisms are based on saturated alkyl esters with only a few on unsaturated alkyl esters [72]. The chain length of alkyl esters is also an important criterion as the ignition behaviour is strongly dependent on it [73]. Additionally, the reported literature noted that the O_2 content in biodiesel causes change in ID periods [12] and reactivity level [74] in low temperature combustion region and shift of the NTC region to lower temperatures [75]. Hence, it is important to select a suitable biodiesel surrogate mechanism which contains equivalent amount of O_2 content (approximately 11.0% higher than conventional diesel fuel [76]) and the correct level of unsaturation according to the actual biodiesel composition for accurate modelling results.
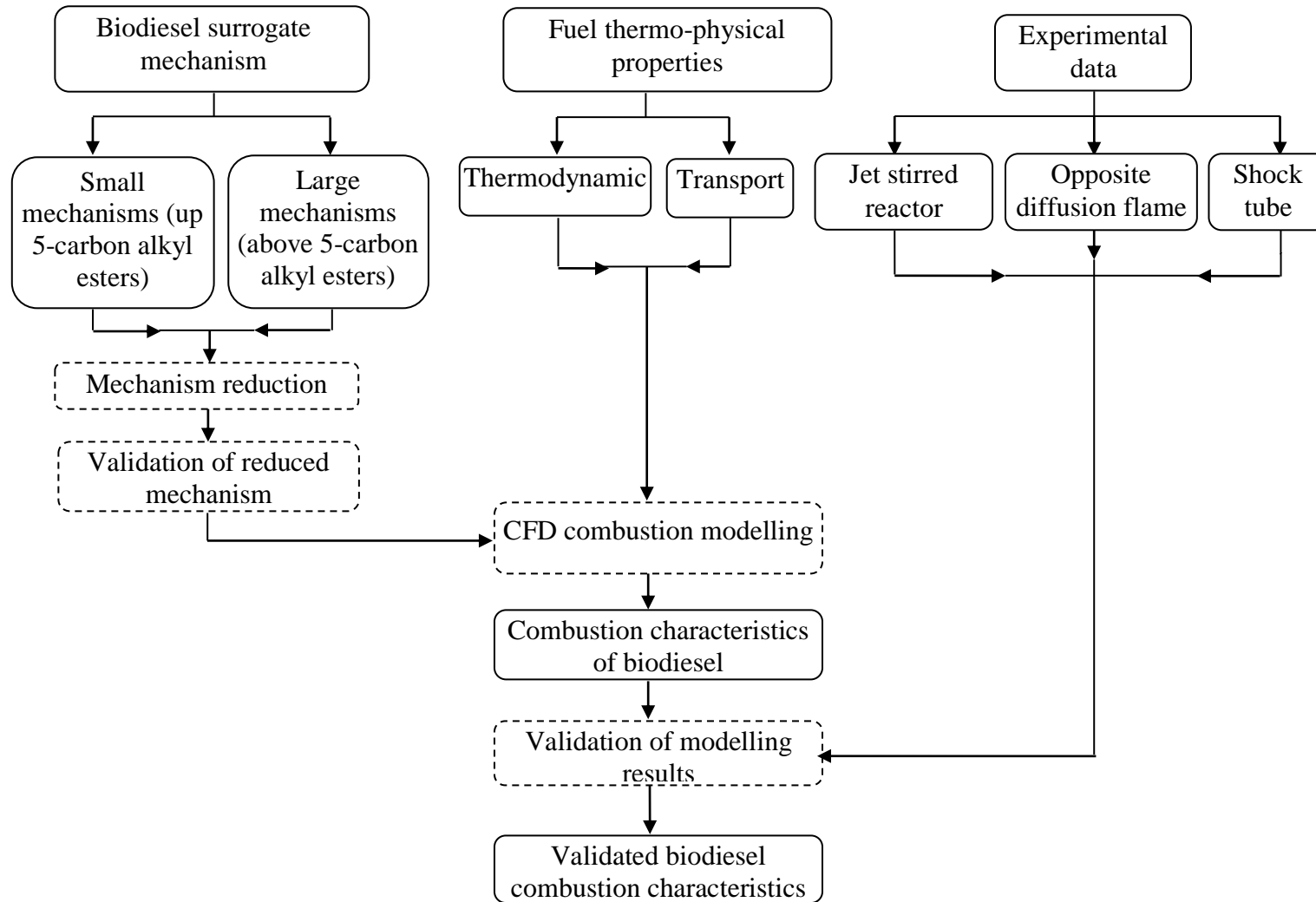
Figure 2.1 Flow chart showing the influence of chemical kinetics in surrogate mechanism and thermo-physical properties on the in-cylinder combustion characteristics of biodiesel.

Table 2.1 Bibliographic compilation of the available small and large biodiesel surrogate mechanisms.

Author	Number of species	Number of reactions	Temperature (K)	Pressure (bar)	Equivalence ratio, φ	Validation conditions	Mechanism structure	Ref.
Small surrogate mechanisms								
MB mechanism								
Fisher et al.	264	1219	541-741	40.5	0.5	Static-reactor[c]	Detailed	[19]
Gail et al.	295	1498	800-1350	1.0	1.13	Jet-stirred reactor (JSR)[d]	Detailed	[22]
			500-900	12.7	0.35-1.5	Variable pressure flow reactor[d]	Detailed	
Brakora et al. (mechanism including n-heptane [77])	41	150	650-1350	40.0, 60.0	0.4-1.5	Auto-ignition[e]	Reduced	[51]
Golovitchev and Yang (mechanism including n-heptane [78] and phenyl methyl ether [78])	88	363	600-1400	10.0-60.0	1.0	Shock tube[e]	Reduced	[58]
MBBio mechanism								
Gail et al.	301	1516	850-1400	1.0	0.375-0.75	JSR[d]	Detailed	[23][24]
Mohamed Ismail et al. (mechanism including n-heptane [79])	113	399	650-1350	13.5, 41.0	0.5-1.5	Shock tube[e]	Reduced	[53]
Ng et al.	80	299	750-1350	40.0,60.0	0.4-1.5	Shock tube[e]	Reduced	[71]
Large surrogate mechanisms								

Methyl hexanoate (MHex, C$_7$H$_{14}$O$_2$) mechanism

Dayma et al.	435	1875	500-1000	10.1	0.5-1.5	JSR[d]	Detailed	[59]
Glaude et al.	401	2440	500-1000	10.1	0.5-1.5	JSR[d]	Detailed	[60]
Methyl heptanoate (MHep, $C_8H_{16}O_2$) mechanism								
Dayma et al.	1087	4592	550-1150	10.1	0.6-2.0	JSR[d]	Detailed	[61]
Glaude et al.	531	3236	550-1150	10.1	0.6-2.0	JSR[d]	Detailed	[60]
Methyl octanoate (MOct, $C_9H_{18}O_2$) mechanism								
Dayma et al.	383	2781	800-1350	1.0	0.6-2.0	JSR[d]	Detailed	[62]
MD mechanism								
Glaude et al.	1251	7171	500-1100	1.1	1.0	JSR[d]	Detailed	[60]
Sarathy et al.	648	2998	900-1800	1.0, 10.0	0.25-2.0	Opposed-flow diffusion flame (OPPDIF)[d]	Reduced	[63]
Seshadri et al.	125	713	900-1300	1.0	0.5-1.5	Auto-ignition[f]	Reduced	[20]
Shi et al.	435	1098	350-390[b]	0.67-1.91[b]	0.71-5.0	Homogenous charge compression ignition (HCCI)[g]	Reduced	[64]
Diévart et al.	2276	7086	653-1336	16.2	0.5-1.5	Shock tube[e]	Detailed	[65]
	530	2396	403	1.0	0.7-1.5	OPPDIF[h]	Reduced	
	238	1244	403	1.0	0.7-1.5	OPPDIF[h]	Reduced	
Herbinet et al.	3012	8820	800-1400	1.0, 10.1	0.25-1.5	JSR[d]	Detailed	[66]
Herbinet et al.	1247	7775	500-1100	1.06	1.0	JSR[i]	Detailed	[67]
Methyl-5-decenoate (MD5D, $C_{11}H_{20}O_2$) mechanism								
Herbinet et al.	2649[a]	9247[a]	800-1400	10.1	0.25-1.5	JSR[d]	Detailed	[68]
Methyl-9-decenoate (MD9D, $C_{11}H_{20}O_2$) mechanism								

16

Herbinet et al.	3298[a]	6904[a]	800-1400	10.1	0.25-1.5	JSR[d]	Detailed	[68]
MDBio mechanism								
Lawrence Livermore National Laboratory (LLNL)	3299	10806	800-1400	10.1	0.5	JSR[d]	Detailed	[69]
Luo et al. (low temperature)	123	394	700-1800 80-1250	1.0-101.3 1.0-101.3	0.5-2.0 0.5-2.0	Auto-ignition[e] JSR[d,j]	Reduced Reduced	[70]
Luo et al. (high temperature)	118	837	1000-1800 700-1100	1.0-101.3 1.0	0.5-2.0 0.5-2.0	Auto-ignition[e] JSR[j]	Reduced Reduced	[56]
Brakora et al.	77	216	700-1300	40.0, 60.0, 80.0	0.5-2.0	Auto-ignition[e]	Reduced	[50]
	69	192	700-1300	40.0, 60.0, 80.0	0.5-2.0	Auto-ignition[e]	Reduced	[80]
An et al.	112	498	700-1800	1.0, 10.0, 100.0	0.5-2.0	Shock tube[c,e]	Reduced	[55]
Other large surrogate mechanisms								
Methyl laurate (C₁₃H₂₆O₂)								
Herbinet et al.	2012	13004	500-1100	1.06	1.0	JSR[i]	Detailed	[67]
Methyl myristate (C₁₅H₃₀O₂)								
Herbinet et al.	3061	20412	500-1100	1.06	1.0	JSR[i]	Detailed	[67]
Methyl palmitate (C₁₇H₃₄O₂)								
Herbinet et al.	4442	30425	500-1100	1.06	1.0	JSR[i,k]	Detailed	[67]
Methyl stearate (C₁₉H₃₈O₂)								
Herbinet et al.	6203	43444	500-1100	1.06	1.0	JSR[i]	Detailed	[67]
Five-component biodiesel mechanism								
Westbrook et al.	4800	20000	550-1100	1.01	1.0	JSR[k,l]	Detailed	[57]

| | 700-1100 | 13.5 | 1.0 | Auto-ignition[m] | Detailed | [57] |

[a] Sizes obtained after processing respective mechanism using CHEMKIN.

[b] Conditions at intake valve closure (IVC).

[c] Validation by comparing ID periods against experimental data.

[d] Validation by comparing species profiles against experimental data.

[e] Validation by comparing ID periods against detailed mechanism for respective engine model.

[f] Validation by comparing residence times against detailed mechanism for respective engine model.

[g] Validation by comparing in-cylinder peak pressures, maximum heat release rate (HRR) and crank angle where 50% accumulated heat was released (CA50) against detailed mechanism.

[h] Validation by comparing flame speed against experimental data.

[i] Validation by comparing species profiles against computed n-hexadecane model.

[j] Validation by comparing species profiles against detailed mechanism.

[k] Validation by comparing species profiles of blends of methyl palmitate and n-decane ($C_{10}H_{22}$) to that of experimental data.

[l] Validation by comparing species profiles of blends of methyl oleate ($C_{19}H_{36}O_2$) and n-decane to that of experimental data.

[m] Validation by comparing ID periods against n-heptane experimental data, computed n-hexadecane, SME and rapeseed methyl ester (RME) models.

As a result of the oxygenated compound, additional O_2 atoms are found in biodiesel as compared to that of fossil diesel. Apart from the oxidation of fuel species especially in the low temperature chain branching phase [81], the O_2 atoms are also responsible for the early formation of CO and CO_2 [68], as well as the oxidation process of soot precursors [44]. It was found that when CO_2 was formed from the consumption of oxygenated compound during the early stage of combustion, the subsequent oxidation of soot precursors did not occur [82]. The oxidation of soot precursors are not only affected by the O_2 content but also by the level of unsaturation in the biodiesel fuel where higher soot species was noted with increasing level of unsaturation [83]. Additionally, extended ID periods are observed as Westbrook et al. [81] found that the reactivity rates at low temperature were restrained by the unsaturated esters and the ID periods was extended as compared to saturated esters.

2.2.1   Small Biodiesel Surrogate Mechanisms

Small biodiesel mechanisms which composed of up to 5-carbon alkyl esters such as MB [19] are a popular option for CFD modelling because of the simple alkyl ester structures and thus easier modelling, as well as the extensive validation data available [84,85]. Nevertheless, there are a few distinct shortcomings of using the MB as surrogate mechanisms, such as the marginal NTC region and insufficient low temperature reactivity. The advantages and disadvantages of small and large detailed chemical kinetic mechanisms are summarised in Table 2.2.

Table 2.2 Advantages and disadvantages of small and large detailed chemical kinetic mechanisms.

Mechanism	Advantages	Disadvantages
Small (up to 5-carbon alkyl esters-)	-Simple structure -Short computational runtime -Wide range of in-cylinder engine validation data	-Lack of low temperature reactivity -Unclear NTC region -Different auto-ignition characteristics from biodiesel
Large (above 5-carbon alkyl esters)	-Similar ester structure to biodiesel -Clear low-temperature reactivity -Obvious NTC region -Similar auto-ignition characteristics to biodiesel	-Complex structure -Rely on smaller sub-mechanisms -Long computational runtime -Limited in-cylinder engine validation data

MB and Its Development

One of the earliest developed biodiesel surrogate mechanisms is the MB mechanism pioneered by Fisher et al. [19], which was able to represent biodiesel with equivalent reactivity level and behaviour. The mechanism was successfully validated against experimental ID periods [86] as seen in Table 2.1. Chain branching and chain propagation processes were determined to be the two dominant processes in MB combustion [19]. Chain branching reactions are addition processes of O_2 and are especially important as they denote the overall reaction rate [19]. Chain propagation meanwhile is contributed by uni-molecular decomposition pathways. Chain propagation is favoured over chain branching at higher temperatures, which leads to a decrease in reactivity level at high temperature regions [19]. These two processes are indicators of the reactivity level of a mechanism such as the NTC region, especially within the combustion temperatures of 900 K to 1500 K. Nonetheless, subsequent adjustments were made to improve the accuracy

of the MB mechanism as its short carbon chain is insufficient to represent the combustion kinetics of biodiesel.

The utilisation of small surrogate mechanism in CFD biodiesel combustion modelling was first initiated by Brakora et al. [51] who managed to build a reduced biodiesel surrogate mechanism with similar structure to that of methyl linoleate ($C_{19}H_{34}O_2$), a FAME component commonly found in biodiesel. The mechanism was composed of 1 mole of MB and 2 moles of n-heptane (C_7H_{16}) [77] sub-mechanisms, in order to obtain similar O_2 content to the actual biodiesel. The reduced mechanism was first validated against the ID periods from detailed mechanism via 0D kinetic modelling in CHEMKIN, where a good level of agreement to within ±25.0% errors was achieved. Then, the reduced mechanism was integrated into KIVA-3V to model the 3D CFD combustion process under diesel engine conditions. The results of in-cylinder peak pressures and HRRs of the reduced MB mechanism were well-matched to those of the test-bed studies using SME. Other validated parameters for this work can be seen in Table 2.3, which summarises all the reduced surrogate mechanisms utilised in CFD biodiesel combustion modelling along with the respective parameters used for benchmarking purposes. The results from CFD were compared against data from other biodiesel or diesel simulation and experimental studies under similar operating conditions for parameters such as peak pressure, HRR and emission profiles. It is evident that applying reduced mechanisms in CFD modelling can provide accurate results on the in-cylinder events.

Table 2.3 Reduced biodiesel surrogate mechanisms for CFD biodiesel combustion modelling.

Mechanism	Reduction techniques	Model	CFD models	Code	Engine	Validation parameters	Ref.
MB (mechanism including n-heptane [77])	Peak concentration analysis,[a] Reaction flux analysis[a]	3D	Kelvin-Helmhotz and Rayleigh Taylor (KHRT), Engine Research Centre (ERC) impingement	KIVA-3V	Diesel	In-cylinder peak pressures,[c] HRR,[c] In-cylinder peak temperatures,[d] Percentage of cylinder gas mass exists at temperature above 2400 K,[d] NO_x mass[d]	[51]
MB (mechanism including n-heptane [78] and phenyl methyl ether [78])	Sensitivity analysis[a]	3D	-	KIVA-3V	Diesel	In-cylinder peak pressures,[e] In-cylinder temperature distributions,[e] HRR,[e] Soot mass,[e] NO_x mass fraction distribution[e]	[58]

MBBio (mechanism including n-heptane [79])	Directed relation graph with error propagation and sensitivity analysis (DRGEPSA) [87], Peak concentration analysis,[a] Reaction flux analysis[a]	3D	Reynolds averaged Navier-Stokes (RANS), Renormalization group theory (RNG) k-ε turbulence, TDAC, Hiroyasu, Nagle-Strickland and Constable, Huh-Gosman, KH-RT, Han-Reitz	OpenFOAM	Diesel	In-cylinder peak pressures,[c] HRR,[c] Normalised soot,[c] NO_x emission index[c]	[53]
MDBio (low temperature)	Improved directed relation graph (DRG) [56], Isomer lumping,[b] Directed relation graph aided sensitivity analysis (DRGASA) [88]	3D	Favre-averaged Navier Stokes, RNG k-ε turbulence	CONVERGE	Reacting spray under diesel engine conditions	Liquid length,[c] Spray penetration,[c] Flame LOL,[c] Soot mole fraction distribution,[c] Hydroxyl (OH) radical mole fraction distribution[c]	[70]
MDBio	Directed relation graph with error propagation (DRGEP) [89], Isomer lumping[b]	3D	Improved KH-RT	KIVA-3V	Diesel	In-cylinder peak pressures,[c] HRR,[c] In-cylinder temperatures,[d] NO_x specific emission[c,d]	[50]

[a] Analysis conducted using CHEMKIN.

[b] Isomers lumped into a single representative species with slight adjustments to rate constants.

[c] Validation by biodiesel experimental combustion measurements.

[d] Validation by biodiesel simulation using different loads.

[e] Validation by diesel simulation under similar combustion conditions.

Apart from Fisher et al. [19] and Brakora et al. [51], another substantial development of small biodiesel surrogate mechanism was carried out by Golovitchev and Yang [58]. The authors built a reduced biodiesel surrogate mechanism using a compilation of MB [19], n-heptane [78] and phenyl methyl ether (C_7H_8O) [78] to represent RME with the chemical formula of methyl oleate. This reduced mechanism of 88 species and 363 reactions was integrated with the surrogate thermo-physical properties of methyl oleate. Reduction with the aid of CHEMKIN was conducted through sensitivity analysis phase, where the low temperature and NTC regions to those of the detailed mechanism were reproduced although large errors between 50.0% and 60.0% were noted. From the in-cylinder peak pressures, HRR and soot emissions results of 3D CFD combustion modelling using KIVA-3V, the reduced mechanism was able to capture similar reactivity behaviour to that of the actual biodiesel.

Nevertheless, the MB mechanism still lacks the necessary accuracy in terms of weak low temperature reactivity [24] and unclear NTC region [19,22,90] due to its short carbon chain structure. In an effort to improve the current MB mechanism, Metcalfe et al. [90] updated the reaction rates and bond strengths. Brakora et al. [51] suggested that a wider range of combustion engine applications such as HCCI be carried out to evaluate the applicability of the reduced MB mechanism. Golovitchev and Yang [58] also stated that further validation of the reduced RME surrogate mechanism against experimental results was required.

Biodiesel not only contains saturated esters but also unsaturated ones. Recognising the contribution of unsaturated FAME to the biodiesel

composition, a combined mechanism, MBBio comprising the saturated MB and the unsaturated MB2D was developed by Gail et al. [24] Compared to the H-atom abstraction pathways in the MB mechanism, decomposition in the MB2D mechanism occurs through the uni-molecular decomposition of CH_3 from the methoxy group in addition to the H-atom abstraction pathways with methyl crotonate radicals [24]. Apart from that, there was an increase in unsaturated species and soot precursors formation due to the additional double bond in the MB2D mechanism as obtained through 0D kinetic modelling using CHEMKIN [24]. This observation is similar to that of Sarathy et al. [91]. The difference in molecular structures of the alkyl esters is important in determining ignition properties as well as the formation of soot precursors [92]. The limited development in unsaturated alkyl ester mechanisms has restricted the progress of developing a complete combined biodiesel mechanism comprising saturated and unsaturated components.

As a result of limited unsaturated surrogate mechanisms that are able to describe the combustion chemistries for biodiesel, Mohamed Ismail et al. [53] have developed a reduced MBBio mechanism by combining the MBBio mechanism proposed by Gail et al. [24] with a reduced n-heptane by Tao et al. [79]. TDAC [26,93], a tabulation method for CFD combustion modelling that combines the advantages of both ISAT [27] and DAC [94] was also coupled to solve the complex chemistries and subsequently, reduce the computational runtime. This reduced mechanism was developed to be generic in nature, thus the mechanism is applicable to CME, PME and SME by varying the chemical compositions according to each fuel. Despite no significant NTC region in 0D kinetic modelling was observed for both the detailed and reduced mechanisms, errors of less than ±30.0% were recorded when the ID periods were compared. The reduced MBBio mechanism was then integrated into 3D CFD modelling using OpenFOAM under diesel engine conditions. Combustion characteristics such as in-cylinder peak pressure, HRR and soot level were in close agreement to those of the experimental results for all three biodiesel fuels. However, this does not necessary imply that reduced mechanisms are adequate for CFD simulations. For the work reported by Mohamed Ismail et al. [53], appropriate

calibrations, which were specific to the combustion conditions of the study, were made to the mechanism for the CFD simulation in order to correctly reproduced the ID periods. This was mainly attributed to the shorter carbonyl chain of the MBBio reduced mechanism as compared to the actual biodiesel FAME components such as the methyl oleate. Besides, the lack of allylic site in MB2D prohibited the reactivity of the reduced mechanism under low temperature environment.

Another pertinent reduced mechanism that used MB and MB2D as surrogate components was developed by Ng et al. [71]. The authors combined individually reduced mechanisms of MB, MB2D and n-heptane to formulate their final reduced mechanism of 80 species and 299 reactions. Arrhenius rate constants for overlapped reactions of identical products and reactants were selectively chosen based on the least errors found in the ID periods prediction between the detailed and reduced mechanisms. Besides, additional Arrhenius rate constants adjustment was made to better predict the ID periods in the NTC region. The average error by the reduced mechanism was recorded between 5.7% and 19.6%, when compared to the detailed mechanisms of MB and n-heptane, respectively. The reduced mechanism was then implemented to 3D CFD combustion modelling for further validation. Although low error of 0.64% was obtained in comparisons to the experimental measurement, the reduced mechanism was not further validated for other biodiesel fuels than PME.

Despite the extensive development and use of MB [19,22,51,58] and MBBio [24,53,71] mechanisms, the prospect of these small biodiesel surrogate mechanisms for future CFD studies is not promising. One possible reason is that the longest carbonyl chain, C_5 and C_7 in these reduced mechanisms are still considered short and insufficient to represent the actual biodiesel FAMEs, even though several adjustments were made. This consequently causes the reduced mechanisms to exhibit low reactivity level [24], marginal NTC region [19,22,53,71,90] and also insufficient oxidation of fuel species as compared to the FAME components of actual biodiesel fuels. Therefore, there is an

increasing demand for larger biodiesel mechanisms with longer carbonyl chains in order to address the identified weaknesses of the small biodiesel surrogate mechanisms for 3D CFD combustion modelling.

2.2.2 Large Biodiesel Surrogate Mechanisms (Greater Than 5-Carbon Alkyl Esters)

Large biodiesel surrogate mechanisms are defined as mechanisms with more than 5-carbon alkyl esters. MHex [59,60,85] and MD [20,65–67] are often chosen as biodiesel surrogate mechanisms due to the similar and succinct reactivity levels to actual biodiesel. Nevertheless, these large mechanisms are impractical for CFD modelling due to the large number of species and reactions involved in the combustion chemistries. Thus, the majority of the large biodiesel surrogate mechanisms are predominantly used in the 0D kinetic modelling only.

MHex, MHep and MOct

Dayma et al. [59] first developed the detailed chemical kinetic mechanism of MHex using JSR experiments and modelling. The work aimed at identifying the main reactions involved in the oxidation of MHex. Subsequently, Dayma et al. [61] performed experimental and modelling studies to evaluate the chemical kinetic mechanism of MHep under PSR code using CHEMKIN. Both the MHex and MHep mechanisms were built upon the comprehensive detailed MB mechanism [19] with additional species and reactions, and adjusted reaction rates for the experimental JSR conditions. Referring to Table 2.1, the MHep mechanism has a larger size compared to the MHex mechanism due to the longer alkyl chain of MHep. Cool flame and high temperature oxidation region including the NTC region predictions from the modelling of these two mechanisms agreed well with experimental data. It was suggested by Dayma et al. [61] that the feasibility of both mechanisms be improved by extending the validation work.

The detailed MHex and MHep mechanisms were also separately built by Glaude et al. [60] using EXGAS, a software for building combustion kinetics. The MHex mechanism contains 401 species and 2440 reactions, whilst the MHep mechanism is made up of 531 species and 3236 reactions. Both mechamisms were validated against the experimental measurements by Dayma et al. [59,61]. The MHex and MHep mechanisms were proved satisfactory, as close agreement was only found at temperatures higher than 850 K compared to the experimental values [59,61] due to rapid fuel consumption under low temperature predicted in EXGAS. Glaude et al. [60] concluded that both the MHex and MHep mechanisms are of equivalent reactivity under similar conditions as the modelling results showed that the increase in alkyl chain length has no significant effect on the reactivity of the respective mechanisms.

Apart from the MHex [59] and MHep [61] mechanisms, Dayma et al. [62] further developed a new mechanism based on MOct. The experimental and kinetic modelling works for the oxidation of MOct were investigated under JSR and OPPDIF conditions. Only high temperature chemistries were included in the kinetic modelling using the MOct mechanism because the cool flame and NTC behaviours were not measured in the JSR experiments due to the diluted fuel mixture input. Species concentrations from the modelling of MOct under JSR and OPPDIF conditions were in good agreement as the predicted maximum mole fraction was within a factor of 1.5 to the measured value, although the species concentration of formaldehyde (CH_2O) was over-predicted. Nevertheless, further validation data for the MOct mechanism under different in-cylinder conditions such as shock tube conditions was required.

The development of these surrogate mechanisms marked an important step in biodiesel combustion modelling in which a wider selection of detailed large mechanisms was made available. However, the experimental validation data needs to be expanded in order to enhance the credibility and applications of these surrogate mechanisms.

MD and Its Development

The MD mechanism was first developed by Glaude et al. [60] using EXGAS. Several reactions and rate constants to represent the behaviour of the alky esters were integrated in the MD mechanism. Firstly, a comprehensive primary mechanism which includes initial organic compounds and O_2 was implemented. For instance, uni-molecular initiations involved in the breaking of a carbon-carbon bond and decompositions through the breaking of carbon-hydrogen bonds in ester alkyl radicals were taken into account in the primary mechanism. Then, the C_0-C_2 reaction base, including all reactions for radicals and molecules with less than three carbon atoms, was continuously updated. A lumped secondary mechanism was added in the last stage of building the MD mechanism. The MD mechanism was validated against the experimental measurements of species profiles under JSR conditions obtained from the same study [60].

Seshadri et al. [20] then investigated the extinction and ignition events utilising a reduced MD mechanism developed in-house by the original authors in laminar non-premixed flows using both experimental and kinetic modelling approaches. The authors concluded that the MD reduced mechanism was able to reproduce measured auto-ignition temperatures from the experiments conducted though with errors of 20.0%. Sarathy et al. [63] first developed a reduced MD mechanism and then extended the application of the reduced mechanism using OPPDIF code in kinetic modelling based on their one-dimensional opposed-flow diffusion flame experiment. In the reduced MD mechanism, the reactions were found to react similarly to a straight-chain alkane and the species profiles were well predicted. However, the modelling results indicated that unsaturated FAME species were formed even though these were not measured from the experiments.

To broaden the range of applications of the MD mechanism, Shi et al. [64] successfully reduced the detailed MD mechanism to be used for HCCI combustion modelling. The reduced MD mechanism agreed well with its detailed mechanism, with validations of the in-cylinder peak pressures,

maximum HRR and CA50. Shi et al. [64] also commented on the need to perform experimental comparisons for the reduced MD mechanism and its incorporation into multi-dimensional CFD combustion modelling.

The primary interest in Diévart et al.'s work [65] was to construct a biodiesel surrogate mechanism and to reduce the constructed mechanism. The mechanism was built based on the chemical kinetics involved in low and high temperature regions. Additionally, the oxidation of smaller methyl esters that may be produced from the parent fuel decomposition was included. The reaction pathways of MD decomposition were clearly shown and described by Diévart et al. [65] The detailed MD mechanism was validated against experimental data by Wang et al. [74] under 0D shock tube conditions using CHEMKIN. The trends of ID periods from the detailed MD mechanism were similar to that of the experimental data, and the NTC region was reproduced clearly. This detailed mechanism was then reduced into two different reduced mechanisms, one with 530 species and 2396 reactions and the other with 238 species and 1244 reactions. A good agreement was obtained with approximately 15.0% deviation between the measured flame speeds [74] and the flame speeds of the two reduced mechanisms.

Based on the detailed MD mechanism from LLNL [69], Herbinet et al. [68] built two large unsaturated alkyl esters mechanisms, MD5D and MD9D to account for the distinct compositions of unsaturated FAME in biodiesel. These two unsaturated mechanisms were built based on the MD mechanism [66] and completed with additional specific chemistry for unsaturated species as well as reaction classes for the location of double bond and ester functional group [95]. The computed ID periods showed that MD5D was the least reactive mechanism followed by MD9D, whereas the MD was the most reactive mechanism. These results demonstrated clearly that the presence of double bond in an alkyl chain has a significant influence on the reactivity level of a mechanism. Besides, Herbinet et al. [68] also performed 0D combustion modelling using blends of MD and n-heptane under JSR conditions within the temperature range of 550 K to 1100 K to investigate the effects of saturated

and unsaturated FAME on the combustion behaviour of RME. The blend model was able to reproduce the species profiles as captured from the experimental runs. The authors reported that a higher level of soot precursors was detected due to the presence of double bond which contributed to the unsaturation level in the biodiesel, a phenomenon in close agreement to the observation by Gail et al. [24] for the MB2D mechanism.

Meanwhile, Luo et al. [56] managed to reduce the detailed MDBio mechanism from LLNL [69] with components of MD, MD9D and n-heptane. Here, a maximum deviation of 40.0% was recorded in the last stage of reduction when compared to the results of the detailed mechanism under auto-ignition and PSR conditions, and experimental JSR results with RME as fuel. The reduced MDBio mechanism was also examined with different biodiesel blends, where small deviations against experimental ID periods were achieved. Nevertheless, the reduced MDBio mechanism is only suitable for high temperature applications.

In order to accommodate the chemical kinetics at low temperature, Luo et al. [70] also reduced the detailed MDBio mechanism and used it under auto-ignition, PSR and JSR conditions. The ID periods and extinction temperature of detailed mechanism in PSR, as well as the species profiles of RME in JSR were well reproduced by the reduced MDBio mechanism. A significant advancement was made when the reduced MDBio mechanism was integrated into CFD combustion modelling to study the spray structure using CONVERGE software [70]. Reasonable errors within ±25.0% were reported for the simulated LOL using the reduced mechanism in comparison to that of the detailed mechanism.

On the other hand, Brakora et al. [50] has successfully reduced the MDBio mechanism from LLNL [69] to a minimum size of 77 species and 209 reactions. In order to achieve such small mechanism size, the reduced mechanism was developed based on the fuel composition of SME. Therefore, the MDBio reduced mechanism produced a deviation of only 15.0% from the

detailed mechanism when the ID periods generated from CHEMKIN were compared. Subsequently, the reduced MDBio mechanism was coupled with KIVA-3V to perform 3D CFD combustion modelling for a test diesel engine. The trends of in-cylinder peak pressures and temperatures, HRR and NO_x were well captured.

Although Luo et al. [56,70] have separately developed the individual mechanisms for low-temperature and high-temperature chemistries, they [52] still further produced a complete reduced MDBIO mechanism that encompasses low and high temperature chemistries. This is because the individual low-temperature and high-temperature mechanisms lack the auto-ignition features in NTC region (850 K to 1050 K). The newly reduced mechanism with 115 species and 460 reactions had better representation of the biodiesel auto-ignition features at the temperature range of 700 K to 1800 K, as maximum under-predictions of 10.0% and 15.0% are achieved for the predicted ID period and LOL, respectively. Nevertheless, the reduced mechanism [52] was only validated for a single fuel blend composition of 50.0% n-heptane, 25.0% MD and 25.0% MD9D.

A recently reduced mechanism of 112 species and 498 reactions which inclusive of soot and NO_x sub-mechanisms was generated by An et al. [55], where the authors additionally integrated the soot and NO_x sub-mechanisms from the 65-species n-heptane mechanism by Tao et al. [79]. Despite the optimisation of Arrhenius rate constants performed by the authors, the largest error in ID predictions was recorded at 52.0% for biodiesel and 27.1% for n-heptane. Although good results of in-cylinder pressure and HRR were obtained when the reduced mechanism was implemented into 3D CFD combustion modelling, the emission trends such as soot and NO_x predicted by the reduced mechanism were not validated. This work, together with the reduced mechanism from Luo et al. [52] marked the most recent developments within the field of CFD biodiesel combustion modelling.

Other Large Biodiesel Surrogate Mechanisms

Since long-chained alkyl esters are commonly found in biodiesel as shown in Figure 2.2, Herbinet et al. [67] constructed large chemical kinetic mechanisms ranging from MD to methyl stearate using the EXGAS software for low temperature region. These detailed mechanisms were created from a comprehensive primary mechanism, a C_0-C_2 reaction base and a lumped secondary mechanism to account for the presence of the ester group. However, only the developed methyl palmitate mechanism was validated against experimental data by Hakka et al. [96], with composition of 26.0% of methyl palmitate and 74.0% of n-decane. This combined mechanism was then modelled under 0D PSR code using CHEMKIN. The combined mechanism built was sufficiently accurate as the trends of species profiles were well captured. Meanwhile, a detailed mechanism comprising methyl oleate, methyl stearate, methyl palmitate, methyl linoleate and methyl linolenate ($C_{19}H_{32}O_2$), such as the FAME components commonly found in SME and RME was developed by Westbrook et al. [57] The five-component mechanism was built partly based on small sub-mechanisms, such as H_2 and CO with 16 low temperature classes [95] and n-alkane kinetic mechanisms with methyl stearate and methyl palmitate mechanisms included. The computed ID periods under 0D shock tube conditions using the five-component mechanism were compared with experimental results of n-heptane and air and simulation results of SME and RME, at an intermediate temperature range of 700 K to 1100 K and pressure of 13.5 bar. The measured ID periods of n-heptane and air [97] were used to benchmark the ID periods predicted for the five-component mechanism over the entire temperature range. Clear NTC region was reproduced by the five-component mechanism as compared to the NTC region obtained from the simulation of SME and RME. Methyl linoleate with two double bonds and methyl linolenate with three double bonds had significantly lower reactivity than methyl stearate and methyl palmitate and methyl oleate.
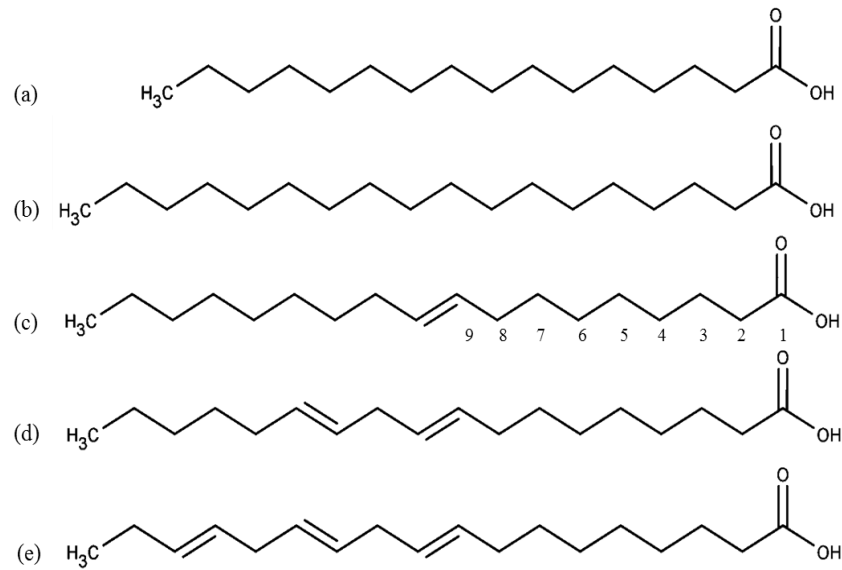
Figure 2.2 Chemical structures of FAMEs in biodiesel: (a) methyl palmitate, (b) methyl stearate, (c) methyl oleate, (d) methyl linoleate and (e) methyl linolenate.

Large mechanisms with long-chained alkyl esters such as methyl stearate and methyl oleate [57,67] can potentially be utilised in CFD combustion modelling since the reactivity and mole fractions of species formed were well predicted [67]. However, it would be necessary to reduce these mechanisms as in the case of the MDBio mechanisms [50,70] before they can be applied for CFD combustion modelling as the computational runtime required for CFD modelling with large detailed mechanisms is simply unrealistic.

From the review covering small to very large biodiesel surrogate mechanisms as discussed in sections 2.2.1 and 2.2.2, it can be concluded that the reduced MDBio mechanism from LLNL [69] is the most widely used mechanism for application of in-cylinder CFD combustion modelling. Adopting detailed mechanisms or large biodiesel surrogate mechanisms in CFD solvers is currently impractical due to the excessive computational time required. One way of addressing this is to formulate a reduced version of these mechanisms so that the number of species and reactions are at a level accessible by the CFD solvers. For example, the use of reduced MD and MDBio mechanisms [20,50,52,55,56,63–65,70,98] have been successful in elucidating the

combustion event of biodiesel fuels as shown in various studies. This demonstrates that the development of biodiesel surrogate mechanisms must proceed in parallel with the development of reduction techniques in order to allow these mechanisms to be integrated with CFD models.

2.3   Mechanism Reduction Techniques

Mechanism reduction techniques are mathematical models that developed to reduce the chemistry sizes of surrogate mechanisms by calculating the dependency among species. The mechanism reduction techniques also function to retain the original chemistry comprehensiveness of detailed mechanisms in the reduced mechanisms. Therefore, the role of mechanism reduction techniques is particularly important to minimise the computational time consumed when chemical kinetics is integrated in numerical modelling.

The mechanism reduction techniques discussed here are in line to the reduced mechanisms reviewed in Section 2.2, namely DRG, DRGEP, DRGASA, DRGEPSA and path flux analysis (PFA). The majority of these mechanism reduction techniques are originally utilised to reduce the chemistry size of n-heptane, the surrogate mechanism for diesel fuel. For instance, the reduced n-heptane mechanism using DRG was able to reproduce the features of the base mechanism with half the original size [99]. Nevertheless, these reduction techniques have been applied successfully as first-step reduction on the detailed biodiesel mechanisms.

2.3.1   DRG

The DRG technique developed by Lu and Law [100] is one of the earliest reduction techniques, which eliminates unimportant species and reactions by calculating the rate of production (ROP) for every species. The theory of DRG [100] is based on the assumption that each species in a mechanism can be distinctively represented by a node. As illustrated in Figure 2.3, species *X* and

Y are each represented by a node while the relationship between both species is connected by a vertex. For instance, if the elimination of species *Y* induces significant error to the ROP of species *X* then species *Y* needs to be retained. This is further supported by the calculation of the vertex between species *X* and *Y* based on a dependence ratio, r_{XY} (Equations 2-1 and 2-2), which is a function of stoichiometric coefficient, $v_{X,i}$, production rate, ω_i and existence ratio, δ_{Yi}. If r_{XY} is more than a user-defined threshold value, ε then species *Y* is retained.
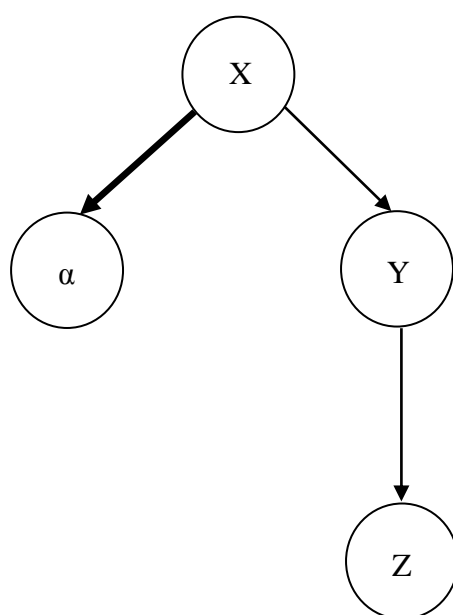
Figure 2.3 Relationship between species based on the theories of DRG [100] and DRGEP [89].

$$r_{XY} \equiv \frac{\sum_{i=1,l}|v_{X,i}\omega_i\delta_{Y,i}|}{|v_{X,i}\omega_i|} \tag{2-1}$$

$$\delta_{Y,i} = \begin{cases} 1 & \text{if the } i\text{th reaction involves species } Y, \\ 0 & \text{otherwise} \end{cases} \tag{2-2}$$

The accuracy of the resulting reduced mechanism depends on minimal user interaction, where only the threshold value defined as the error induced during the reduction process is required. However, Nagy and Turanyi [101] argued that the threshold value is not directly related to the error induced as the threshold value does not always provide the smallest reduced mechanism even at a required simulation error. As can be seen in Table 2.4, the DRG method is

not applicable for fast-slow separation processes [102] and interrelation of species from non-chemical couplings and third bodies' effects. Moreover, every selected species in DRG is assumed to be equally important and unimportant species that are strongly coupled to the selected species may be selected [101]. The capability of the DRG method has been proven in several reduction studies for biodiesel surrogate mechanisms. Using automated DRG method, Sarathy's [63] and Seshadri's [20] MD mechanisms were reduced from the detailed mechanisms of 3012 species and 8820 reactions, and 3026 species and 8555 reactions, respectively to the sizes tabulated in Table 2.1.

Table 2.4 Advantages and disadvantages of mechanism reduction techniques.

Reduction techniques	Advantages	Disadvantages	Ref.
DRG	-Overall-linear reduction time -Controllable error -Minimal user interaction in the reduction process	-Assumes every selected species is equally important -Not applicable to fast-slow separation processes -Unable to handle interrelation of species from non-chemical couplings and third bodies' effects	[99,100, 102]
DRGEP	-Based on the error induced upon species removal along with graph searching path -Smaller reduced mechanism produced than DRG	-Fails to identify the relation between species when both fast ROP and ROC occur at the same time -Weak reaction path selection for indirect relation -Limited to fast processes	[89]
DRGASA	-Effectively eliminates limbo species	-Shielding effect -Computationally expensive	[88]

DRGEPSA	-Produces the smallest size of reduced mechanism -Combined advantages of DRGASA and DRGEP	-Reduction process is time-consuming	[87]
PFA	-Enhanced reduction efficiency -Conservative direct interaction coefficient	-Increase in computational runtime -Target species that have weak chemical couplings to the pre-selected species may not be captured	[103]

2.3.2 DRGEP

In order to improve the discrepancy encountered in DRG, where the ROP and rate of consumption (ROC) for species are assumed to be equal, Pepiot-Desjardins and Pitsch [89] has integrated the mathematical equations of DRG (Equations 2-1 to 2-3) with error propagation. Changes have been made to the dependency ratio of species X and Y, r_{XY} as seen in Equations 2-3 to 2-5, where the ROP, P_X and ROC, C_X of species X are taken into account. Based on Figure 2.3, the removal of species Z, the furthest from species X induces the lowest damped error to species X even though species α has a larger dependence ratio based on the intensity of lines. This is because species Y not only affects the ROP of species X but also the ROC of species Z, as compared to species α. As such, this is known as geometric damping and thus forms the basis of DRGEP.

$$r_{XY} \equiv \frac{\left|\sum_{i=1,n_R} v_{X,i}\omega_i\delta_{Y,i}\right|}{max(P_X,C_X)} \tag{2-3}$$

$$P_X = \sum_{i=1,n_R} max(0,\ v_{X,i}\omega_i) \tag{2-4}$$

$$C_X = \sum_{i=1,n_R} max(0,\ -v_{X,i}\omega_i) \tag{2-5}$$

An application example of the DRGEP method was the incorporation of DRGEP into automated reduction to reduce the detailed MD mechanism in

Shi et al.'s work [64]. The error propagation advantage in DRGEP was able to efficiently remove redundant species and reactions in the detailed MD mechanism. Despite this, several drawbacks were found in this technique. Firstly, only the strongest reaction path which cannot identify the species flux physically is chosen when the intermediate species are more than one in parallel for indirect relations. Secondly, the definition of the interaction coefficient fails to identify the relations between species that have both fast ROP and ROC occurring at the same time. DRGEP is preferably applied to fast processes because the error induced for a species may directly affect other species through couplings due to the inconclusive geometric error damping assumption in the technique [102].

2.3.3 DRGASA

Another improvement to the DRG method is carried out by Zheng et al. [88], where the authors developed a brute-force sensitivity analysis that can be coupled with DRG to perform further reduction for detailed chemical kinetic mechanisms. The effects of species and its reactions removal are evaluated by computing the error induced to the ID periods at all desired operating conditions. If the induced error based on ID periods is larger than the user-defined threshold, ε, then the particular species is retained in the mechanism. This in turn causes the iterative process to be more time-consuming than the DRG and DRGEP methods.

Nevertheless, Niemeyer et al. [87] showed that the DRGASA could not identify all the unimportant species due to species shielding. A larger error than the allowable error might be obtained when many low error removal species are removed in the sensitivity analysis stage [101]. The DRGASA approach was employed by Luo et al. [56,70] to reduce the detailed MDBio mechanism at low and high temperature regions. However, the MDBio mechanism was first reduced using a revised DRG technique to avoid unsafe removal of important isomers. Then, the reduced mechanism with 472 species and 2337 reactions was further reduced by DRGASA to a size of 118 species

and 837 reactions such that pre-selected target species were still retained in an even smaller reduced mechanism. The reason behind the DRGASA application after DRG was that all the retained species in DRG were treated as equivalent importance and the time consumed in the SA process during DRGASA reduction was decreased. Direct DRGASA reduction on biodiesel surrogate mechanisms has yet to be explored to date.

2.3.4 DRGEPSA

Although both the DRGEP and DRGASA methods have proven to perform better than the original DRG method, the time-consuming weakness of both the improved methods have prohibited these two methods to be applied as first-step reduction. By taking the strengths of error propagation in DRGEP and of sensitivity analysis in DRGASA, Niemeyer et al. [87] developed a new mechanism reduction technique known as DRGEPSA. Enhanced reduction efficiency is obtained with DRGEP [89] which efficiently removes unimportant species in the first phase, and with DRGASA [88] that utilises sensitivity analysis to further eliminate unimportant species missed out in the error propagation phase despite the time-consuming species elimination process involved in the sensitivity analysis phase. Table 2.5 compares the number of species and reactions as well as the relative errors induced by the DRG, DRGEP, DRGASA and DRGEPSA techniques when applied to the n-heptane mechanism. The DRGEPSA produced the least number of species and reactions with a large error of 27.0% but within the allowable error margin of 30.0%. Its performance was considered to be equivalent to the other reduction techniques even with its smaller mechanism. Such a comparative study has not been carried out for biodiesel surrogate mechanisms, hence the differences in these reduction techniques as applied to biodiesel surrogate mechanisms remain poorly understood.

Table 2.5 Comparison of reduced mechanism sizes for n-heptane using DRG, DRGASA, DRGEP and DRGEPSA techniques from Niemeyer et al. [87].

Reduction techniques	Number of species	Number of reactions	Maximum error (%)
DRG	211	1044	21.0
DRGASA	153	691	24.0
DRGEP	173	868	28.0
DREPSA	108	406	27.0

Nevertheless, the feasibility of the DRGEPSA technique in reducing biodiesel surrogate mechanisms is demonstrated in a recent study. Mohamed Ismail et al. [53] utilised the DRGEPSA technique to formulate their reduced biodiesel surrogate mechanism, MBBio from a detailed mechanism of 301 species and 1516 reactions to 113 species and 399 reactions. The reduced mechanism was validated against its corresponding detailed mechanism under 48 shock tube conditions ranging from lean to rich fuel conditions and low to high temperature regions, with the aid of CHEMKIN. However, the DRGEPSA technique can be computationally expensive and ineffective as a large number of species is considered in the sensitivity analysis phase [87].

2.3.5 PFA

Apart from the DRG based reduction techniques, reduction techniques that based on the identification of important reaction pathways and related species are also available. One of these reduction techniques is PFA [103], which utilises the analysis of multi-generation fluxes including the formation and consumption fluxes, to eliminate unimportant species and reactions. Besides, the extension and improvements of the DRG theories are also included in the PFA technique to improve its reduction efficiency. The feasibility of the PFA technique is highlighted recently in the case of the MD mechanism in which 2276 species and 7086 reactions were reduced to two separate reduced mechanisms of 530 species and 2396 reactions, as well as 238 species and

1244 reactions [65]. The reduced MD mechanism modelled under the OPPDIF code produced satisfactory results when validated against laminar flame speeds of the detailed mechanism computed using the Premix [104] and Cantera [105] software. An aspect requiring improvement is that the computational runtime during reduction increases following an increase in the number of generation of pre-selected species. Furthermore, the PFA technique might also fail to capture target species that have weak chemical couplings to the pre-selected species.

Despite various weaknesses that are found for the aforementioned reduction techniques, these reduction techniques have proven that a reduced mechanism with minimum chemistry size can be generated without compromising the chemistry comprehensiveness from the detailed mechanism. As such, savings in computational time and reduced complexity in numerical modelling can also be attained.

2.4   Thermo-Physical Properties Models

The importance of fuel thermo-physical properties in CFD biodiesel combustion modelling for accurate predictions has been highlighted by Ra et al. [32] as they play a vital responsibility in determining the combustion characteristics. This is because fuel spray development, air and fuel mixing, combustion and emissions processes are largely affected by the fuel properties [32,34]. In this section, the correlations of thermo-physical properties reviewed are critical properties, liquid density, liquid viscosity, liquid surface tension, liquid heat capacity, liquid thermal conductivity, vapour pressure, latent heat of vaporisation, vapour viscosity, vapour thermal conductivity, vapour diffusivity and second virial coefficients.

The correlations and methods discussed in this section are developed based on extensive experimental data measured for various hydrocarbon components. Depending on the assumptions involved in deriving the correlations and the

range of applicability, these correlations and methods can also be used to determine the thermo-physical properties for biodiesel. With regards to the fuel properties estimation, two handbooks on properties of gases and liquid by Reid et al. [106,107] and Poling et al. [108] serve as useful references. This is because of their comprehensive compilations of various group contributions and experimentally derived correlations for hydrocarbon groups. Additionally, several software are available to estimate the thermo-physical properties of hydrocarbons, namely Knovel critical tables [109], DIPPR [110] and BDProp [111,112]. Mixing rules [113,114] are also reviewed here as these rules are needed when calculating the thermo-physical properties of biodiesel fuels which are dependent on the thermo-physical properties of the FAME components.

The properties software [109–112] functions as an alternative to conventional correlations, where a broad range of temperature dependent correlations is compiled within the software and thus offers easier accessibility. For example, Yaws' developed correlations [115] for the thermo-physical properties of FAME components available in Knovel critical tables [109] are accessed with automatic properties calculation at the desired temperature. Nonetheless, a major drawback to the properties software is that the compiled correlations within these properties software are limited to specific hydrocarbon components. One such example is the lack of thermo-physical properties for methyl linoleate and methyl linolenate in the Knovel critical tables [109]. In addition, only certain correlations are compiled within the properties software and the accessibility to most of these properties software is also restricted by paid subscription. Therefore, conventional correlations are still a preferred option due to the unrestricted accessibility, low cost and availability of a wide range of correlations.

2.4.1   Critical Properties

Critical properties which include critical temperature, critical pressure and critical volume are vital as the evaluation of all other thermo-physical

properties depend on these properties. Moreover, any thermo-physical properties beyond the critical properties are considered invalid. Table 2.6 is a bibliographic compilation of thermo-physical properties models applied in CFD combustion modelling studies of biodiesel.

Among the methods reviewed for critical properties, the Joback's modification of Lydersen's method [116,117] is the most accurate as this method covers all the correlations for critical temperature, critical pressure and critical volume. Furthermore, the Joback's modification of Lydersen's method [116,117] is suitable for various hydrocarbon components unlike the Constantinou and Gani [118], the Wilson and Jasperson [119] and the Marrero and Pardillo methods [120]. Minimal errors have been reported with the use of this method [108] despite the propagation of error contributed by the required boiling point in the correlation for critical temperature. Therefore, the Joback's modification of Lydersen's method [116,117] is widely utilised, as seen in the CFD biodiesel combustion modelling studies [32,34,41,112]. Meanwhile, Brakora et al. [50] preferred the use of the DIPPR [110] software and the correlation by Huber et al. [121] to calculate the critical temperatures for methyl palmitate, methyl stearate, methyl oleate, methyl linoleate and methyl linolenate.

2.4.2   Liquid Properties

The Rackett equation [122] is able to relate the specific volume to liquid density of a compound using the acentric factor and critical temperature of the compound. Several versions of the Rackett equation exist; first is the original equation [122], second is the one modified by Spencer and Danner [123] and third is the Elbro method [124]. Referring to Table 2.6, the modified equation [123] which is also available in one of the properties handbook [107], has been utilised [32,34,41,112] as Poling et al. [108] proved that the Spencer and Danner's version [123] is more accurate than the first and third. Brakora et al. [50] on the other hand utilised Knovel critical tables [109] for this purpose.

Table 2.6 Bibliographic compilation of thermo-physical properties models applied in CFD combustion modelling studies of biodiesel.

Thermo-physical properties	Methods of evaluation					
	Ra et al. [32]	Golovitchev and Yang [58]	Brakora et al. [50]	Chakravarthy et al. [34]	Yuan et al. [112]	Mohamed Ismail et al. [41]
Critical properties	-Correlation based on 400 fuels [107] -Group contribution [112]	-	-DIPPR[a,b] [110] -Huber et al.[a,c] [121]	-Correlation based on 400 fuels [107] -Group contribution [112]	-Joback modification of Lydersen's method [107] -Ambrose method [107]	-Joback modification of Lydersen's method [116,117]
Liquid density	-Orrick & Erbar group contribution [107] -Modified Rackett equation [107]	-	-Knovel critical tables [109]	-Orrick & Erbar group contribution [107] -Modified Rackett equation [107]	-Modified Rackett equation [123]	-Modified Rackett equation [123]
Liquid viscosity	-Group contribution method [112] -Empirical correlations [125] -Logarithmic equation [126] -Weighted average of individual components [127]	-VanVelzen's method [128]	-DIPPR[b] [110] -BDProp[c] [111,112]	-Group contribution method [112] -Empirical correlations [125] -Logarithmic equation [126] -Weighted average of individual components [127]	-Orrick and Erbar method [107] -Letsou and Stiel method [129]	-Orrick and Erbar method [107] -Letsou and Stiel method [129]

Liquid surface tension	-Weighted average of individual liquid surface tension [112]	-Sugden's method [128]	-DIPPR[b] [110] -BDProp[c] [111,112]	-Weighted average of individual liquid surface tension [112]	-Correlation proposed by Allen et al. [130]	-Correlation proposed by Allen et al. [130]
Liquid heat capacity	-Group contribution [19] -Interpolation of Lagrange [131]	-	-DIPPR[b] [110] -BDProp[c] [111,112]	-van Bommel correlation [132]	-	-van Bommel correlation [132]
Liquid thermal conductivity	-GC TCD experimental analysis [133] -Logarithmic equation [134] -Weighted average of individual components [135]	-Baroncini's method [136]	-DIPPR [110]	-	-	-Robbin and Kingsrea [106]
Vapour pressure	-Pitzer method [107] -Araújo and Meireles [137]	-Riedel's method [128]	-DIPPR[b] [110] -BDProp[c] [111,112]	-Pitzer method [107]	-Pitzer method [107]	-Modified Antoine equation [138]
Latent heat of vaporisation	-Araújo and Meireles [137] -Pitzer acentric factor correlation [139]	-Clapeyron's method [128]	-DIPPR[b] [110] -BDProp[c] [111,112]	-Pitzer acentric factor correlation [139]	-Pitzer acentric factor correlation [139]	-Pitzer acentric factor correlation [139]
Vapour viscosity	-Chung et al. method [140,141]	-	-	-Chung et al. method [140,141]	-	-Chung et al. method [140,141]
Vapour thermal conductivity	-Chung et al. method [140,141]	-	-DIPPR [110]	-Chung et al. method [140,141]	-	-Chung et al. method [140,141]

Vapour heat capacity	-GC TCD experimental analysis [133] -Logarithmic equation [134] -Weighted average of individual components [135]	-	-	-GC TCD experimental analysis [133] -Logarithmic equation [134] -Weighted average of individual components [135]	-	-Rihani and Doraiswamy method [142]
Vapour diffusivity	-Chapman-Enskog kinetic theory [143]	-	-DIPPR [110]	Chapman-Enskog kinetic theory [143]	-	-Wilke and Lee method [144]
Second virial coefficients	-	-	-	-	-	-Tsonopoulos method [145]
Mixing rules	-Lee-Kesler equation [107] -Lumped parameter continuous thermodynamic [146]	-	-	-Lee-Kesler equation [107] -Lumped parameter continuous thermodynamic [146]	-Lee-Kesler equation [107]	-Lee-Kesler equation [113] -Kay's rule [114] -Nissan and Grunberg method [147]

[a] Only critical temperature was evaluated.

[b] Properties for methyl palmitate, methyl stearate and methyl oleate.

[c] Properties for methyl linoleate and methyl linolenate.

Liquid viscosity models for FAME components are categorised into low temperature ($T_r < 0.7$) and high temperature ($T_r > 0.7$) regions. The Orrick and Erbar method [106–108] is comparatively more accurate than the Sastri-Rao [148] and the Przezdziecki and Sridhar [149] methods as a result of reduced error propagtion due to decreased input of predicted properties [108]. Specific mixing rules are necessary in order to estimate the liquid viscosity of biodiesel following the Nissan and Grunberg method [147], the UNIFAC-VISCO method [150,151] and the Teja and Rice method [152,153]. The UNIFAC-VISCO method [150,151] is specifically suitable for mixtures with varying sizes components. For that reason, it is advisable that the Nissan and Grunberg [147] and the Teja and Rice [152,153] methods are used for the estimation of liquid viscosity as the FAME components in biodiesel are mainly of similar sizes. As for the estimation of liquid viscosity at high temperature, the correlation proposed by Sastri [108] and Letsou and Stiel [129] can be utilised as both approaches are reasonably accurate due to the addition of corresponding state information. In the literature on the thermo-physical properties of biodiesel, the Orrick and Erbar method [106–108], the Letsou and Stiel method [129] and the Nissan and Grunberg method [147] have been utilised by Yuan et al. [112] and Mohamed Ismail et al. [41]. Meanwhile, Ra et al. [32] and Chakravarthy et al. [34] employed several correlations [112,125–127] to estimate the liquid viscosities of Envirodiesel®. Meanwhile, Golovitchev and Yang [58] used the VanVelzen's method [128] to estimate the liquid viscosity of RME while the DIPPR [110] and BDProp [111,112] software were used by Brakora et al. [50].

The Macleod-Sugden correlation [154,155] is one of the earliest correlations that relates the liquid surface tension to densities of liquid and vapour phases based on the corresponding states of boiling temperature and the temperature of interest. Since the Macleod-Sugden correlation [154,155] only predicts the individual liquid surface tension for a FAME component, Macleod and Sugden [154,155] proposed a mixing rule to be imposed to the liquid surface tension correlation. This correlation is not accurate especially for fuel components based on the Parachor value utilised, which is a quantitative

measurement. Subsequent improvement to the correlation was made when Allen et al. [130] proposed an empirical mixing rule specifically for mixture liquid surface tension with low errors incurred. As errors of less than 10.0% were produced when using the correlations proposed by Macleod and Sugden [154,155] and Allen et al. [130] as reported by Poling et al. [108], these were used by Ra et al. [32], Chakravarthy et al. [34], Yuan et al. [112] and Mohamed Ismail et al. [41] to calculate the liquid surface tensions of biodiesel. The Sugden's method [128] was instead favoured by Golovitchev and Yang [58], whereas Brakora et al. [50] depended on the DIPPR [110] and BDProp [111,112] software.

The liquid heat capacity of hydrocarbon components can be estimated using group contributions methods such as the Rùzicka and Domalski method [156] and the correlation developed from extrapolation of experimental data by van Bommel [132]. Both methods are valid within a small range of temperatures, thus extrapolation is required to estimate the liquid heat capacity beyond the respective temperature ranges. Chakravarthy et al. [34] and Mohamed Ismail et al. [41] applied the van Bommel's correlation [132] to various biodiesel feedstocks over an extended temperature range. In contrast, Ra et al. [32] used a variety of experimental and group contributions methods [19,131] to predict the liquid heat capacity for SME. Similar to the liquid properties evaluation, Brakora et al. [50] employed the DIPPR [110] and BDProp [111,112] software for liquid heat capacity estimation.

For the estimation of the liquid thermal conductivity of biodiesel fuels, the Robbins Kingrea method [106] which is a function of critical temperature, liquid heat capacity, liquid density and latent heat of vaporisation at normal boiling point was utilised by Mohamed Ismail and co-authors [41]. Separately, the Baroncini's method [136] was used in the work reported by Golovitchev and Yang's [58]. Ra et al. [32] meanwhile used similar methods of experimental and group contributions methods [133–135] to estimate the liquid thermal conductivity of SME. The DIPPR [110] software has also been used successfully for this purpose [50].

2.4.3 Vapour Properties

The Antoine equation [157] was developed based on the extrapolation of vapour pressure data. Ceriani et al. [138] improved the original Antoine equation as the extrapolation of the original Antoine equation [157] beyond the stated minimum and maximum temperatures of a compound was not feasible. Thus, the modified Antoine equation [138] was used by Mohamed Ismail et al. [41] for the vapour pressure calculations. In Golovitchev and Yang's work [58], the Riedel method [128] was employed to estimate the vapour pressure of RME because this method is suitable for the prediction of vapour pressure at low temperatures since it was built on the corresponding states of a compound. The Pitzer method [107] is also widely used as reported in the literature [32,34,112]. Additionally, the DIPPR [110] and BDProp [111,112] software are employed [50].

To calculate the latent heat of vaporisation, the Riedel-Factor correlation [158], the Lydersen, Greenkorn and Hougen correlation [159] and the Pitzer acentric factor correlation [139] which were all developed based on the law of corresponding states can be utilised. Nonetheless, the Pitzer acentric factor correlation [139] is favoured in the determination of the latent heat of vaporisation of biodiesel [32,34,41,112] as it is more accurate and convenient than the Riedel-Factor correlation [158]. The Lydersen, Greenkorn and Hougen correlation [159] is the most inaccurate method amongst these correlations as reviewed by Reid et al. [106] Another model for the latent heat of vaporisation includes the Clapeyron's method [128] used by Golovitchev and Yang [58], while Brakora et al. [50] used the DIPPR [110] and BDProp [111,112] software to determine the latent heat of vaporisation.

The Chapman-Enskog kinetic theory [160] can be employed to determine the vapour viscosity of multi-component mixtures such as biodiesel. Based on this, several methods are available such as the Reichenberg method [161−166], the Wilke method [167] and the Chung et al. method [140,141]. The Reichenberg method [161−166] involves intensive calculations as the polarity of a component is taken into account. The Wilke method [167], meanwhile,

considers the theory of binary system as well. To date, only the method by Chung et al. [140,141] has been reportedly used for the estimation of the vapour viscosity for various biodiesel fuels [32,34,41].

Likewise to the vapour viscosity, the Chung et al. method [140,141] is the only reported method utilised by both Ra et al. [32], Chakravarthy et al. [34] and Mohamed Ismail et al. [41]. The Chung et al. method [140,141] which was built upon the theories of the Eucken factor, accurately predicts the vapour thermal conductivity trends, whereby the conductivity reduces with increasing temperature for non-polarised compounds [108]. In Brakora et al.'s work [50], the DIPPR [110] software was utilised to determine the vapour viscosity.

To determine the vapour heat capacity of fuels, the method of Thinh, Duran and Ramalho [106] and method of Rihani and Doraiswamy [142] are available. Both are group additive methods which are also temperature dependent. Comparisons of these have been made by Reid et al. [106], who suggested that the Rihani and Doraiswamy method [142] is applicable to various compounds although it is less accurate at lower temperatures. Thus, this method was used to predict the vapour heat capacity required for the subsequent calculations of vapour viscosity and vapour thermal conductivity [41]. A number of different approaches [133–135] were also used by Ra et al. [32] and Chakravarthy et al. [34] in order to ensure accurate estimation of the vapour heat capacity of SME.

The vapour diffusivity of biodiesel is regarded as the interaction between the fuel species and the oxidiser such as O_2. The correlations which can be employed to determine the vapour diffusivity are the Wilke and Lee method [144] and the Fuller et al. method [168–170]. Similar to vapour viscosity, the basis of these two methods is the Chapman-Enskog kinetic theory [160]. Both methods are reasonably accurate since low deviations were found compared to experimental measurements [108]. Ra et al. [32] and Chakravarthy et al. [34] utilised the Chapman-Enskog kinetic theory adopted from Skelland et al. [143], whereas Mohamed Ismail et al. [41] utilised the Wilke and Lee method [144]

51

to estimate the vapour diffusivities of biodiesel fuels. Separately, the DIPPR [110] software was favoured over correlations in another study [50].

The Tsonopoulos method [145] has been regarded as the most accurate method relating second virial coefficients and gas expansion related coefficients to reduced temperature (T_r) pressure and critical temperature. Many researchers [171–174] have tried to improve the original Tsonopoulos method [145] such that the modified method can be used for wider range of compounds. Nonetheless, these modifications are limited as fitted parameters are required, of which parts of the parameters are often unavailable.

Based on the discussion above, it can be concluded that both conventional correlations and properties software are able to calculate the thermo-physical properties for biodiesel from various feedstock options. Conventional correlations have a wider range of coverage for different structural components (such as esters and hydrocarbons) and at different conditions which are dependent on pressure or temperature, as well as the lower operating cost. On the other hand, only limited correlations are found in the properties software and the availability of the software is mostly through paid subscription. Therefore, the use of conventional correlations is preferred despite the apparent ease of use of the properties software on the part of the user.

2.5   CFD Combustion Modelling of Biodiesel

Substantial effort has been carried out to analyse the spray, combustion and emission characteristics for biodiesel. Diesel engine combustion is often modelled in order to identify the corresponding combustion and emission characteristics for biodiesel, despite the complexity induced by turbulence-chemistry interaction, heat transfer and combustion chemistry of fuel oxidation and emission formation [175]. This is because the turbulence effects caused by the motions of intake and exhaust valves, piston and swirling in the

diesel engine are pertinent to the development from spray to pollutants oxidation [176]. However, qualitative validation against the experimental measurement cannot be performed as localised measurements such as the soot concentrations are difficult to be obtained due to the high operating cost of optically accessible diesel engines. Thus, most of the diesel engine combustion simulations concentrate on the quantitative agreement achieved against the experimental measurements, such as ID period, in-cylinder pressures and tailpipe emissions. In general, biodiesel exhibits shorter ID period and lower combustion temperature when compared to those of diesel [177–180]. Besides, the use of biodiesel in diesel engine generates lower soot emissions, regardless of the biodiesel feedstocks [49,177,180–182]. Nevertheless, the absolute soot concentrations are dependent on the unsaturated FAMEs contained in biodiesel [177]. Meanwhile, increased NO levels are found as a result of the trade-off between the soot and NO [182,183].

Apart from the diesel engine combustion, the characteristics of biodiesel can also be analysed in a constant volume bomb. This is because the development in the constant volume bomb also involves identical key processes to those of the diesel engine combustion such as the fuel droplet breakup, air-fuel mixing, ignition, combustion as well as formation and oxidation of pollutants of soot and CO [176]. In addition, the combustion process in the constant volume bomb is less complex to be modelled as compared to that of the diesel engine, due to the constant volume environment. Besides, the engine-like conditions with well-characterised initial and boundary conditions used in the constant volume bomb are more effective for model development and validation [175]. As such, localised predictions such as the spray growth and soot formation during the quasi-steady period can be produced. Therefore, various research works have been conducted using the constant volume bomb setup in order to analyse the effects and structures of biodiesel. This is because accurate modelling of the interaction of spray flows is important to the simulations of entire engine flow and combustion process [184]. Overall, biodiesel demonstrates longer LPL, shorter ID period and LOL when compared to those of diesel [185–187]. In addition, it is also found that the spray interaction for

biodiesel is greater than that of diesel [185,188]. In terms of emissions, reduced soot concentrations are predicted for biodiesel as compared to those of diesel [186,188], which is a similar observation to that of the diesel engine combustion. Besides, the phenomenological soot development for biodiesel is also studied under the constant volume bomb conditions. Cui et al. [186] found that only the rates of soot formation from nucleation and surface growth are affected when diesel is replaced by methyl oleate, which is a common FAME component found in biodiesel. On the other hand, the rates of soot oxidation by OH and O_2 radicals are not affected. These studies have thus proven that the characteristics of different biodiesel fuels can be sufficiently distinguished in constant volume bomb.

Although the aforementioned combustion studies in constant volume bombs and diesel engines have successfully characterised different biodiesel fuels, these studies are not performed under both the environments of constant volume bomb and diesel engine. This is because the combustion structures predicted for different fuels in the constant volume bomb are insufficient to provide the in-cylinder characteristics of the biodiesel fuels [41,185–188]. Meanwhile, the simulations of diesel engine combustion cannot produce the quasi-steady state behaviours for biodiesel [49,177–183].

2.6   Concluding Remarks

Based on the conducted literature review, large sized surrogate mechanisms for biodiesel are preferable over small sized mechanisms. This is because more comprehensive chemistries information is contained within the large surrogate mechanisms to reproduce the unique combustion characteristics of biodiesel. However, longer computational runtime is required to solve the complex chemistries [94,99] due to the large amount of species and reactions involved. For this reason, large detailed mechanisms such as MD are difficult to be integrated into CFD without any further reduction.

The demonstration of reduction techniques such as DRG, DRGEP, which have been used to reduce different biodiesel detailed mechanisms, have proven that equivalent combustion chemistries to those of the detailed mechanisms can be retained in the reduced mechanisms, with smaller chemistry size. This henceforth eases the resulting chemistries complexity when the reduced mechanisms are implemented with CFD codes.

On the other hand, accurate representation of the thermo-physical properties is as important as the chemical kinetics in the surrogate mechanisms in order to produce numerical predictions which can elucidate the in-cylinder combustion processes for biodiesel. Although a number of software for the calculation of thermo-physical properties is found, conventional correlations are preferable because these correlations are built upon extensive empirical data.

It has been proven that the characteristics of biodiesel can be separately understood using the constant volume bomb and diesel engine setups. However, the combustion of biodiesel should be modelled under both the constant volume bomb and diesel engine conditions to identify the localised and in-cylinder behaviours for biodiesel.

Chapter 3
Governing Equations

3.1 Introduction

In this chapter, the governing equations of chemical kinetics and CFD models employed in both the kinetic modelling and combustion modelling are reported. For the kinetic modelling, CHEMKIN-PRO is utilised to solve the chemical kinetics from the detailed and reduced mechanisms. The relevant governing equations used in the modelling of chemical kinetics are discussed in Section 3.2. Meanwhile, OpenFOAM is employed to simulate the processes of spray, in-cylinder turbulent flows and combustion. Detailed descriptions of the CFD models and their respective governing equations are presented in Section 3.3.

3.2 Chemical Kinetics

CHEMKIN-PRO is one of the kinetic modelling software available that solves species of gas-phase, bulk and surface efficiently in various 0D reactor models, such as closed homogeneous reactor, plasma reactor and multi-zone engine simulator. Here, two 0D homogenous reactor models, namely the closed homogenous reactor and PSR are selected to model the auto-ignition and extinction processes for the detailed and reduced mechanisms. Apart from this, the temperature sensitivity analysis tool is also utilised to provide quantitative understanding of the reactions dependency on temperature change.

3.2.1 Gas Phase Chemistry

In CHEMKIN-PRO, both gas-phase chemistry and thermodynamic data are required to perform calculations, as illustrated in Figure 3.1. Gas-phase chemistry contains elements, species and reactions, with corresponding Arrhenius rate parameters that describe the chemistry interactions among the gas-phase species. Meanwhile, thermodynamic data is a compilation of temperature coefficients in polynomial fits to calculate the species specific heat capacity (C_p), enthalpy (H) and entropy (S), using Equations 3-1 to 3-3, respectively. With the integration of gas-phase chemistry and thermodynamic data in CHEMKIN-PRO, the equilibrium constants and reverse-rate coefficients of a reaction can thus be calculated.
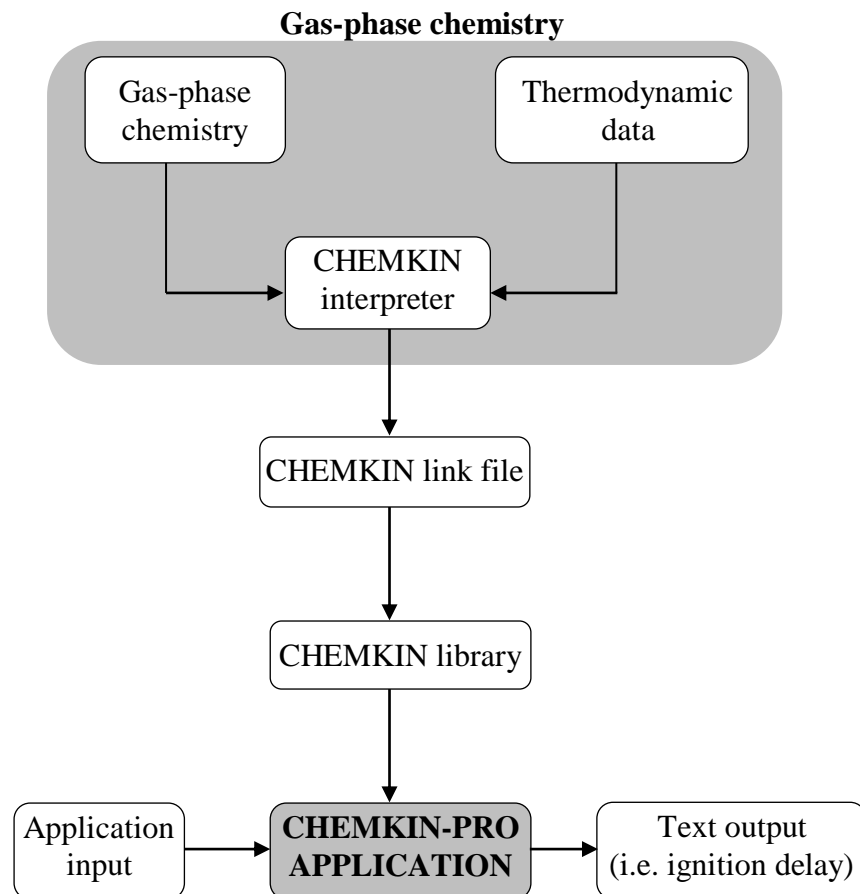
Figure 3.1 Schematic diagram of CHEMKIN-PRO application structure.

$$\frac{C_p}{R} = a_1 + a_2 T + a_3 T^2 + a_4 T^3 + a_5 T^4 \tag{3-1}$$

$$\frac{H}{R} = a_1 + \frac{a_2}{2}T + \frac{a_3}{3}T^2 + \frac{a_4}{4}T^3 + a_5T^4 + \frac{a_6}{T} \tag{3-2}$$

$$\frac{S}{R} = a_1 \ln T + a_2 T + \frac{a_3}{2}T^2 + \frac{a_4}{3}T^3 + \frac{a_5}{4}T^4 + a_7 \tag{3-3}$$

The calculations performed in CHEMKIN-PRO are based on the equation of state for gas as shown in Equation 3-4, where P and T_k are the pressure and temperature respectively. The molar concentration of kth species is denoted by M_k, while N is the total number of species.

$$P = \sum_{k=1}^{N}[M_k]\,RT_k \tag{3-4}$$

The production rate of kth species, ω_k which sums the rate-of-progress variables for ith reactions involving the kth species, q_i is shown in Equation 3-5. Meanwhile, the stoichiometric coefficient of kth species in ith reactions, $v_{i,k}$ is defined in Equation 3-6.

$$\omega_k = \sum_{i=1}^{I} v_{i,k}q_i \tag{3-5}$$

$$v_{i,k} = v''_{i,k} - v'_{i,k} \tag{3-6}$$

Meanwhile, the rate of progress for ith reactions q_i is defined by the difference of forward and backward rates, as displayed in the following

$$q_i = k_{i,f}\prod_{k=1}^{K}[M_k]^{v'_{i,k}} - k_{i,b}\prod_{k=1}^{K}[M_k]^{v''_{i,k}} \tag{3-7}$$

The forward and backward rate constants of ith reactions, $k_{i,f}$ and $k_{i,b}$ are defined in Equations 3-8 and 3-9, where A_i is the pre-exponential factor, b_i is the temperature exponent and $E_{a,i}$ is the activation energy.

$$k_{i,f} = A_i T^{b_i}\exp\left(\frac{-E_{a,i}}{RT}\right) \tag{3-8}$$

$$k_{i,b} = \frac{k_{i,f}}{K_{i,c}} \tag{3-9}$$

The equilibrium constants, $K_{i,c}$ is defined as

$$K_{i,c} = K_{i,p} \left(\frac{P_{atm}}{RT} \right)^{\sum_{k=1}^{K} v_{i,k}} \tag{3-10}$$

where P_{atm} is the atmospheric pressure, and $K_{i,p}$ is expressed in Equation 3-11.

$$K_{i,p} = \exp \left(\frac{\Delta S°_i}{R} - \frac{\Delta H°_i}{RT} \right) \tag{3-11}$$

ΔS_i and ΔH_i defined in Equations 3-12 and 3-13 are the entropy and enthalpy changes, respectively.

$$\Delta S_i = \sum_{k=1}^{K} v_{i,k} \frac{S_k}{RT} \tag{3-12}$$

$$\Delta H_i = \sum_{k=1}^{K} v_{i,k} \frac{H_k}{RT} \tag{3-13}$$

When a third body is required in a reaction, the rate of progress, q_i is modified to Equation 3-14.

$$q_i = \left(\sum_{k=1}^{K} (a_{i,k}) [M_k] \right) \left(k_{i,f} \prod_{k=1}^{K} [M_k]^{v'_{i,k}} - k_{i,b} \prod_{k=1}^{K} [M_k]^{v''_{i,k}} \right) \tag{3-14}$$

Where $a_{i,k}$ is unity for all kth species and the first factor is equivalent to the total concentration of the mixture, $[M]$ as expressed in Equation 3-15, when all species are contributed to third bodies.

$$[M] = \sum_{k=1}^{K} [M_k] \tag{3-15}$$

3.2.2 Homogenous Reactor Models

Two homogenous reactor models, which are the closed homogenous reactor and PSR models are employed here to simulate the auto-ignition and extinction processes, respectively. For the closed homogeneous reactor and PSR models, the rate of conversion of reactants to products is controlled by

the chemical reaction rates since mixture is assumed to be well-mixed due to high diffusion rates or turbulent mixing. These two reactor models are henceforth considered to be limited by changes of chemical kinetics. The closed homogenous reactor model defined in CHEMKIN-PRO is an enclosed volume without any inlet or outlet duct, where initial pressure and temperature are the only varying parameters. Therefore, this reactor model is particularly suitable to simulate the auto-ignition process. On the other hand, PSR is selected to simulate the extinction process because this reactor model contains a combustion chamber with inlet and outlet ducts, which are equally similar to the intake and exhaust valves of diesel engine.

The homogenous system in CHEMKIN-PRO solves chemical kinetics by using the conservation of mass, energy and species. As illustrated in Figure 3.2, the solution for homogenous reactor system includes the consumption and production of chemical species within the reactor volume and the net loss of species and mass to surfaces in the reactor.
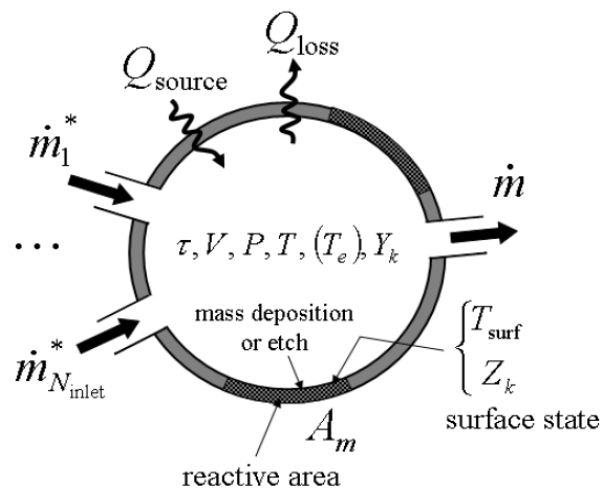
Figure 3.2 Conceptual representation of a homogenous reactor model in CHEMKIN-PRO.

The global mass and species conservations displayed in Equations 3-16 and 3-17 are solved transiently in the homogenous systems, even for steady state problems since the computational algorithm requires partial solution of the

related transient problems. For example, a user-defined residence time (τ), which is shown in Equation 3-18 is required as characteristic parameter in the homogenous reactors in order to solve the chemical kinetics for both the auto-ignition and extinction processes.

$$\frac{d}{dt}(\rho V)^{(j)} = \sum_{i=1}^{N_{inlet}(j)} \dot{m}_i^{*(j)} + \sum_{r=1}^{N_{PSR}} \dot{m}_i^{(r)} R_{rj} - \dot{m}_i^{(j)} + \sum_{m=1}^{M} A_m^{(j)} \sum_{k=1}^{K_g} \dot{s}_{k,m}^{(j)} W_k$$

(3-16)

Where j is the reactor number, ρ is the mass density, V is the reactor volume, $\dot{m}^*$ and $\dot{m}$ are the inlet and outlet mass flow rate, respectively. $N_{inlet}(j)$ is the number of inlets for reactor j, while N_{PSR} is the total number of reactor modules in the reactor network. R_{rj} is the fraction of outflow of reactor r that is recycled into reactor j. The last term on the right-hand side is used when the outlet mass flow is different from the sum of the inlet and recycled mass flow due to the deposition of materials. A_m is the surface area of the mth material defined within the reactor, $\dot{s}_{k,m}$ is the molar surface production rate of kth species on the mth material per unit surface area. There are K_g gas-phase species and m materials.

$$(p_k V)^{(j)} \frac{dY_k^{(j)}}{dt} = \sum_{i=1}^{N_{inlet}(j)} \dot{m}_i^{*(j)} \left(Y_{k,i}^* - Y_k \right) + \sum_{r=1}^{N_{PSR}} \dot{m}_i^{(r)} R_{rj} \left(Y_k^{(r)} - \right.$$
$$\left. Y_k^{(j)} \right) - Y_k^{(j)} \sum_{m=1}^{M} A_m^{(j)} \sum_{k=1}^{K_g} \dot{s}_{k,m}^{(j)} W_k + (\dot{\omega}_k V)^{(j)} M_k + \sum_{m=1}^{M} A_m^{(j)} \dot{s}_{k,m}^{(j)} W_k$$

(3-17)

Y_k is the mass fraction of the kth species, W_k is the molecular weight of kth species, and $\dot{\omega}_k$ is the molar ROP of the kth species by gas-phase chemical reactor per unit volume. The superscript * indicates inlet stream quantities.

$$\tau = \frac{\rho V}{\left[\sum_{i=1}^{N_{inlet}(j)} \dot{m}_i^{*(j)} + \sum_{r=1}^{N_{PSR}} \dot{m}_i^{(r)} R_{rj} \right]}$$

(3-18)

The mass density (ρ) is related to the pressure and gas temperature through the multi-fluid ideal gas equation of state expressed in Equation 3-4.

3.2.3 Temperature Sensitivity Analysis for Reactions

The temperature sensitivity analysis for reactions is transiently solved by the implicit methods for time integration. This is because the system of ordinary differential equations (ODEs) is typically stiff, where the species in the reactor system evolves inconsistently with time. Therefore, CHEMKIN-PRO employs a software package called DASPK to solve the time integration using backward differentiation and first order sensitivity analysis. The system of ODE that describes the physical problem is arranged in a general form of Equation 3-19.

$$\frac{d\phi}{dt} = F(\boldsymbol{\varphi}, t; a) \tag{3-19}$$

Where F is the residual vector, $\boldsymbol{\varphi}$ is the vector of temperature, a is the rate expression for gas-phase reactions. The first order sensitivity coefficient is defined as

$$w_{j,i} = \frac{\partial \boldsymbol{\varphi}}{\partial a_i} \tag{3-20}$$

where $w_{j,i}$ is the first order sensitivity coefficient matrix, with indices j and i as the dependent variables and reactions. After differentiating with respective to a_i, Equation 3-20 becomes

$$\frac{dw_{j,i}}{dt} = \frac{\partial F}{\partial \boldsymbol{\varphi}} \cdot w_{j,i} + \frac{\partial F_j}{\partial a_i} \tag{3-21}$$

Although backward differentiation method is utilised for time integration in the sensitivity analysis, the linearity in Equation 3-21 is deemed sufficient to solve the non-linear chemical kinetics. This is because the Jacobian matrix, $\frac{\partial F}{\partial \boldsymbol{\varphi}}$

corresponds to the backward differentiation method in solving the original model problem. Hence, the solution conforms accordingly, for which each column corresponds to the sensitivities with respect to one of the reaction pre-exponential constants. The corresponding sensitivities of elementary reactions to temperature changes can be then approximated using the normalised sensitivity coefficient in logarithmic derivatives, as displayed in Equation 3-22.

$$\frac{\partial lnY_k}{\partial lna_i}\bigg|_F = \frac{a_i}{Y_k}\frac{\partial Y_k}{\partial a_i}\bigg|_F \tag{3-22}$$

3.3 CFD Models

OpenFOAM provides a wide range of solvers for different fluid flows of laminar, turbulent and reacting. The Finite Volume Method in Eulerian approach is adopted in OpenFOAM to solve the governing equations of mass, energy and momentum for gas phase. Meanwhile, the development spray is solved in the Lagrangian approach.

This section presents the CFD models utilised to predict the phenomena of spray, combustion and soot, as illustrated in Figure 3.3. In the first section, the spray model employed to estimate primary and secondary breakup is described. Subsequently, the theoretical background of standard drag model in OpenFOAM is discussed. This is followed by the explanation of turbulence models and turbulent-chemistry interactions. For turbulence estimation, the standard k-ε turbulence model is specified for the combustion modelling in constant volume bomb, while the diesel engine combustion is simulated with RNG k-ε turbulence model. Besides, the turbulence-chemistry interaction is also discussed. The calculation for soot formation is described in the last section, where the Leung and Lindstedt soot model [189] is employed.
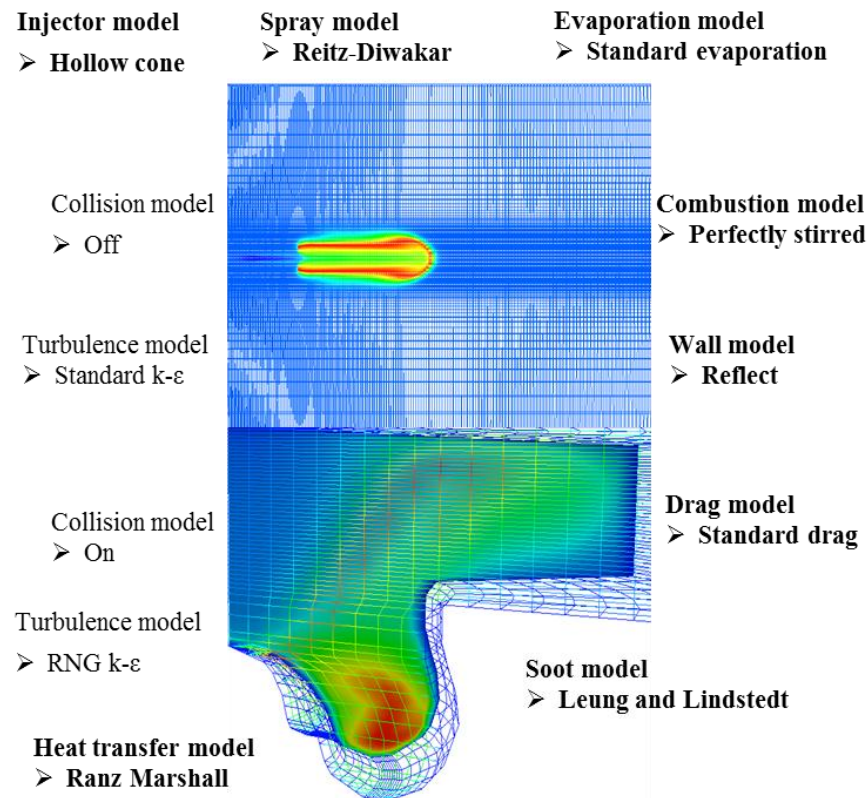
Figure 3.3 Illustration of the CFD models utilised for the combustion modelling in constant volume bomb and diesel engine. The CFD models highlighted in bold are identically specified for the simulations of constant volume bomb and diesel engine combustion.

3.3.1 Discrete Phase Models

As a result of unstable physical forces in the combustion chamber, the injected fuel is broken up into a large number of spray droplets. Two distinct physical processes are observed, first is the primary breakup and then followed by secondary breakup. In the primary breakup regime, which is also known as the liquid core atomisation, droplets are immediately disintegrated from the liquid fuel surface due to injection pressure. Meanwhile, the secondary breakup involves the dispersion of droplets in the continuous phase, where the breakup can be estimated based on the droplet Weber number [190]. Since the primary breakup occurs at a fraction of time due to the high injection pressure, only the secondary breakup is simulated here with the aid of CFD model. Apart from

the spray breakup model, a drag model is also integrated into the simulations because the droplets are subjected to various drag forces. Details of the discrete phase sub-models are discussed here.

Reitz-Diwakar Spray Breakup Model

The spray breakup process is an important multi-phase flow process to the applications of liquid atomisation, dispersed multi-phase flow and combustion instability of sprays [191]. The breakup of a liquid jet into droplets is typically resulted by a combination of aerodynamic forces, turbulence within the liquid jet and cavitation in the nozzle [192]. The Reitz-Diwakar model [193], which assumes spray breakup is caused by aerodynamic forces, is selected here to estimate the secondary spray breakup of the intact liquid core. This is because of the spray is largely disintegrated by aerodynamic forces, due to the high injection pressure. As illustrated in Figure 3.4, the Reitz-Diwakar model distinguishes the breakup of liquid spray as two different regimes, namely bag breakup and stripping breakup.

Bag breakup   Stripping breakup
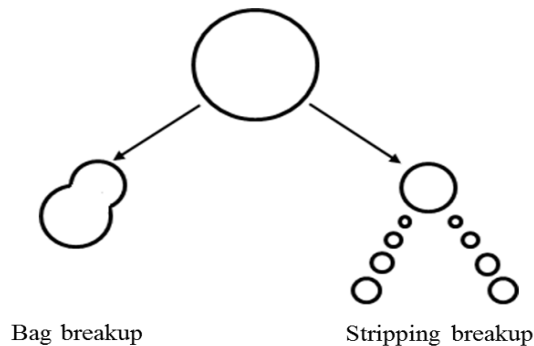
Figure 3.4 Estimation of droplet breakup in Reitz-Diwakar spray model.

In the bag breakup regime, the fuel droplets are expanded in the low-pressure wake region due to the non-uniform pressure field [194]. Then, the breakup of fuel droplet occurs when the surface tension forces are overcome. The calculation for bag breakup, with governing equations shown in Equation 3-23, takes place when the Weber number, We exceeds the value of critical Weber number, We_c of 6.0 [195].

$$\tau_{bag} = C_b d \sqrt{\frac{\rho_f d_p}{\sigma}} \tag{3-23}$$

$$d_{bag} = \frac{2C_{bag}\sigma}{\rho_g U_r^2} \tag{3-24}$$

Where τ_{bag} is the characteristic breakup time for bag (s) and d_{bag} is the new droplet diameter (m). The breakup time constant for bag, C_b is valued at 0.785, respectively. d_p is the droplet diameter prior to breakup (m), σ is the liquid surface tension of fuel (kg s^{-2}), ρ_f and ρ_g are the densities of fuel and ambient gas (kg m^{-3}), and U_r is the relative velocity (m s^{-1}). The Weber number as displayed in Equation 3-25 is defined as the ratio of fluid's inertia to surface tension.

$$We = \frac{\rho_f U_r^2 d_p}{\sigma} \tag{3-25}$$

In the stripping breakup, the liquid core is assumed to be sheared or stripped from droplet surface. Calculation for stripping breakup executes when $We/\sqrt{Re}$ exceeds C_{strip} of 0.5 [195], as shown in the following

$$\tau_{strip} = \frac{C_s d_p}{U_r} \sqrt{\frac{\rho_f}{\rho_g}} \tag{3-26}$$

$$d_{strip} = \frac{4C_{strip}^2 \sigma^2}{\rho_g U_r^3 v_g} \tag{3-27}$$

Where τ_{strip} is the characteristic breakup time for strip (s), d_{strip} is the new particle diameter (m), v_g is the kinematic viscosity of ambient gas (m^2 s^{-1}). The breakup time constant for stripping, C_s is varied between 1.5 and 15, depending on the fuel types.

For both the bag and stripping breakup regimes, the rate change of particles diameter is estimated using Equation 3-28.

$$\frac{dd_p}{dt} = \frac{-(d_p - d_{p,stable})}{\tau} \tag{3-28}$$

Where $d_{p,stable}$ is the new diameter for stable droplet (m) and τ is the characteristic breakup time from either bag or stripping regime (s).

Standard Drag Model

The calculation of drag coefficient is particularly important as it determines the momentum exchange between liquid and gas phases [196]. Hence, the assumption that fuel droplets remain spherical throughout the domain is insufficient since the fuel droplets are subjected to aerodynamic force, velocity and heat transfer to other fuel droplets. The interactions among fuel droplets, particularly for flows with large Weber number, cause an increase in drag that distorts the fuel droplets to disk-like droplets in extreme case. The standard drag model in OpenFOAM thus linearly varies the drag coefficient calculations between a sphere and a disk, as presented in Equations 3-29 and 3-30 to enhance the drag calculation for fuel droplets.

$$C_{d,sphere} = \begin{cases} \dfrac{24(1+\frac{1}{6}Re^{2/3})}{Re} & Re < 1000 \\ 0.44 & Re \geq 1000 \end{cases} \qquad (3\text{-}29)$$

$$C_d = C_{d,sphere}(1 + 2.632y) \qquad (3\text{-}30)$$

$C_{d,sphere}$ is the drag coefficient for spherical object and C_d is the drag coefficient. y is the droplet distortion constant, where sphere has a minimum value of 0, while disk has a maximum value of 1.0 as illustrated in Figure 3.5.

y=0   **y=1**
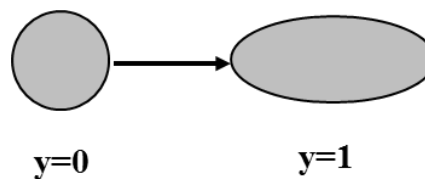
Figure 3.5 Droplet deformation due to aerodynamic drag.

3.3.2   Turbulence Models

Turbulence of a flow, particularly mixing and turbulent dispersion [197], substantially modifies the mean characteristics of that particular flow. This is because the flow fields are largely changed due to the mixing of transport properties such as mass, momentum and species. Therefore, turbulence models are developed to enhance the estimation of flow characteristics by accounting the effects of compressibility and also to improve the calculations of mass and heat transfer [192].

Standard k-ε Turbulence Model

The standard k-ε turbulence model solves turbulence in an ensemble-averaged approach by calculating the turbulent viscosity (μ_t), kinetic energy (k) and dissipation rate (ε) displayed in Equations 3-31 and 3-32. This model is implemented for the simulations of constant volume bomb to estimate the highly turbulent flow.

$$\frac{\partial}{\partial t}(\rho k) + \frac{\partial}{\partial x_i}(\rho k u_i) = \frac{\partial}{\partial x_j}\left[\left(\mu + \frac{\mu_t}{\sigma_k}\right)\frac{\partial k}{\partial x_j}\right] + G_k + G_b - \rho\varepsilon - Y_M + S_k \quad (3\text{-}31)$$

$$\frac{\partial}{\partial t}(\rho\varepsilon) + \frac{\partial}{\partial x_i}(\rho\varepsilon u_i) = \frac{\partial}{\partial x_j}\left[\left(\mu + \frac{\mu_t}{\sigma_\varepsilon}\right)\frac{\partial\varepsilon}{\partial x_j}\right] + C_{1\varepsilon}\frac{\varepsilon}{k}(G_k + C_{3\varepsilon}G_b) - C_{2\varepsilon}\rho\frac{\varepsilon^2}{k} + S_\varepsilon$$

$$(3\text{-}32)$$

The turbulent viscosity, μ_t (Pa s) is calculated using Equation 3-33.

$$\mu_t = \rho C_\mu \frac{k^2}{\varepsilon} \qquad\qquad (3\text{-}33)$$

G_k denotes the generation of turbulence kinetic energy due to the mean velocity gradients, G_b is the generation of turbulence kinetic energy due to buoyancy. Y_M is the contribution of fluctuating dilatation in compressible turbulence to the overall dissipation rate. σ_k and σ_ε are the inverse effective Prandtl numbers for k and ε, respectively. $C_{1\varepsilon}$, $C_{2\varepsilon}$ and $C_{3\varepsilon}$ are the model

constants. S_k and S_ε are the user-defined source terms. The initial values of k and ε are 0.735 m^{2}s^{-2} and of 3.835 m^2 s^{-3}, respectively.

RNG k-ε Turbulence Model

The RNG k-ε turbulence model which derived from the instantaneous Navier-Stokes equations utilises the RNG mathematical technique to compute the k and ε, as displayed in Equations 3-34 and 3-35. This model is relatively better than the standard k-ε turbulence model in accounting the swirling effects, turbulent viscosity and near-wall treatment. Therefore, the RNG k-ε turbulence model is integrated to the simulations of diesel engine combustion.

$$\frac{\partial}{\partial t}(\rho k) + \frac{\partial}{\partial x_i}(\rho k u_i) = \frac{\partial}{\partial x_j}\left[\alpha_k \mu_{eff}\frac{\partial k}{\partial x_j}\right] + G_k + G_b - \rho\varepsilon - Y_M + S_k \qquad (3\text{-}34)$$

$$\frac{\partial}{\partial t}(\rho\varepsilon) + \frac{\partial}{\partial x_i}(\rho\varepsilon u_i) = \frac{\partial}{\partial x_j}\left[\alpha_\varepsilon \mu_{eff}\frac{\partial\varepsilon}{\partial x_j}\right] + C_{1\varepsilon}\frac{\varepsilon}{k}(G_k + C_{3\varepsilon}G_b)$$

$$-C_{2\varepsilon}\rho\frac{\varepsilon^2}{k} - R_\varepsilon + S_\varepsilon \qquad (3\text{-}35)$$

R_ε is the strain rate term for turbulent dissipation rate equation. G_k denotes the generation of turbulence kinetic energy due to the mean velocity gradients, G_b is the generation of turbulence kinetic energy due to buoyancy. Y_M is the contribution of fluctuating dilatation in compressible turbulence to the overall dissipation rate. α_k and α_ε are the inverse effective Prandtl numbers for k and ε, respectively. S_k and S_ε are the user-defined source terms.

3.3.3   Chemistry Model

In order to take account of the in-cylinder turbulence and chemistry interactions, a well-stirred model is employed. This model assumes that fuel mixture is homogeneous in each computational cell and neglects any sub-grid scale turbulent-chemistry interaction [93]. As such, the reactive mixture within each computational cell is treated as a closed system. In this study, a multi-

step ODE stiff solver, Semi-Implicit Bulirsch-Stoer (SIBS) solver [198] is employed to solve the equations for reacting flow, using species and energy equations. The chemical equation is first integrated by extracting the initial thermodynamic conditions of temperature, pressure and mass fraction at each computational cell. After that, the reaction rate ($\dot{Y}_i$) is calculated using Equations 3-36 and 3-37.

$$\dot{Y}_i = \frac{Y_i^*(t+\Delta t) - Y_i(t)}{\Delta t} \tag{3-36}$$

$$Y_i^*(t + \Delta t) = Y_i(t) + \int_t^{t+\Delta t} \dot{\omega}_i \frac{W_i}{\rho} dt \tag{3-37}$$

Where subscript i denotes the number of species, $Y_i^*(t + \Delta t)$ is the mass fraction in each cell calculated by the chemistry solver, $\dot{\omega}_i$ is the reaction rate (mol cm^{-3} s^{-1}), W_i is the molecular weight (kg mol^{-1}) and ρ is the density (kg m^{-3}).

3.3.4   Soot Model

Soot formation is predicted using the Leung and Lindstedt two-step soot model [189], where acetylene (C_2H_2) is set as the soot precursor. In order to precisely calculate the soot formation, processes of inception, coagulation, surface growth and oxidation due to O_2 and OH radicals are accounted. The soot oxidation by OH radical is estimated based on the model proposed by Fenimore and Jones [199], while the oxidation of soot by O_2 radical is computed using the formulation by Lee et al. [200]. The Leung and Lindstedt soot model [189] solves two transport equations of particle number density, φ_N and soot mass fraction, Y_{soot} as displayed in Equations 3-38 and 3-39.

$$\frac{\partial}{\partial t}(\rho \varphi_N) + \nabla \cdot (\rho \vec{v} \varphi_N) = \nabla \cdot \left(\frac{\mu_t}{Sc_t} \nabla \varphi_N\right) + \frac{1}{N_A} \frac{dN}{dt} \tag{3-38}$$

$$\frac{\partial}{\partial t}(\rho Y_{soot}) + \nabla \cdot (\rho \vec{v} Y_{soot}) = \nabla \cdot \left(\frac{\mu_t}{Sc_t} \nabla Y_{soot}\right) + \frac{dM}{dt} \tag{3-39}$$

Where ρ, $\vec{v}$, μ_t, Sc_t are the fluid density (kg m^{-3}), velocity (m s^{-1}), turbulent viscosity (Pa s), turbulent Schmidt number, respectively. N_A is the Avogrado number, valued at 6.022045 x 10^{26} kmol^{-1}, N is the soot particle number density (particles m^{-3}) and M is the soot mass concentration (kg m^{-3}).

The last term, $\frac{dN}{dt}$ in Equation 3-38 which is a source term denotes the instantaneous production rate of soot particles that is subjected to nucleation from the gas phase and coagulation in the free molecular regime, as seen in Equation 3-40.

$$\frac{dN}{dt} = C_\alpha \cdot N_A \left(\frac{X_{prec}P}{RT}\right) \exp\left(-\frac{21000}{T}\right) - C_\beta \left(\frac{24RT}{\rho_{soot}N_A}\right)^{1/2} \left(\frac{6M}{\pi\rho_{soot}}\right)^{1/6} N^{11/6}$$

$$(3\text{-}40)$$

Whilst, $\frac{dM}{dt}$, the last term in Equation 3-39 is a source term for soot mass concentration that considers the processes of nucleation, surface growth and oxidation. The equation for soot mass concentration is given in Equation 3-41, where C_α, C_γ, C_{w1} and C_{w2} are additional model constants.

$$\frac{dM}{dt} =$$

$$C_\alpha M_p \left(\frac{X_{prec}P}{RT}\right) \exp\left(-\frac{T_\alpha}{T}\right) + C_\gamma \left(\frac{X_{sgs}P}{RT}\right) \exp\left(-\frac{T_\gamma}{T}\right)\left[(\pi N)^{1/3} \left(\frac{6M}{\rho_{soot}}\right)^{2/3}\right]^{1/2}$$

$$-C_{w2} \left(\frac{X_{OH}P}{RT}\right) \exp\left(-\frac{T_{w2}}{T}\right) \sqrt{T}(\pi N)^{1/3} \left(\frac{6M}{\rho_{soot}}\right)^{2/3}$$

$$(3\text{-}41)$$

The mass of incipient soot particle, M_p, which is set at 1200 kg kmol^{-1}, is assumed to consist of 100 carbon atoms. Since soot particles have been found to grow primarily by the addition of gaseous species at their surface, especially C_2H_2, the mole fraction of participating surface growth species, X_{sgs} is therefore substituted by the mole fraction of C_2H_2.

3.4　Concluding Remarks

The theoretical backgrounds and governing equations of the chemical kinetics and CFD models employed in the simulations of chemical kinetics and combustion are discussed in this chapter. CHEMKIN-PRO is utilised to calculate and solve the species thermodynamic properties, transport properties and reaction equilibrium constants for the detailed and reduced chemical kinetic mechanisms. Meanwhile, OpenFOAM provides a robust solution to estimate the processes of spray, combustion and soot by using the CFD models selected particularly for spray dynamics, turbulence flow and soot formation.

Chapter 4

Numerical Formulation and

Experimental Validation

4.1   Introduction

This chapter discusses the evaluation of CFD models for the combustion modelling in constant volume bomb and diesel engine. Section 4.2 presents the experimental setup and numerical formulation for the combustion modelling under the constant volume bomb conditions, while Section 4.3 is dedicated to the experimental and computational settings for the diesel engine combustion. The numerical formulation includes parametric studies of spatial and temporal resolutions for computational cell sizes and time-step, respectively. Besides, calibrations to the CFD model constants of spray breakup, turbulence and soot are also discussed.

4.2   Combustion Modelling in Constant Volume Bomb

4.2.1   Experimental Setup and Conditions

The simulations of non-reacting spray and reacting spray under constant volume bomb conditions are modelled based on the experiment conducted by Nerva et al. [36], using the Spray A configurations from Sandia National Laboratory. The constant volume combustion chamber illustrated in Figure 4.1 has equivalent characteristic dimension of 108.0 mm. The experiment is conducted at initial temperatures of 900 K and 1000 K, while the initial density is maintained at 22.8 kg m^{-3}.
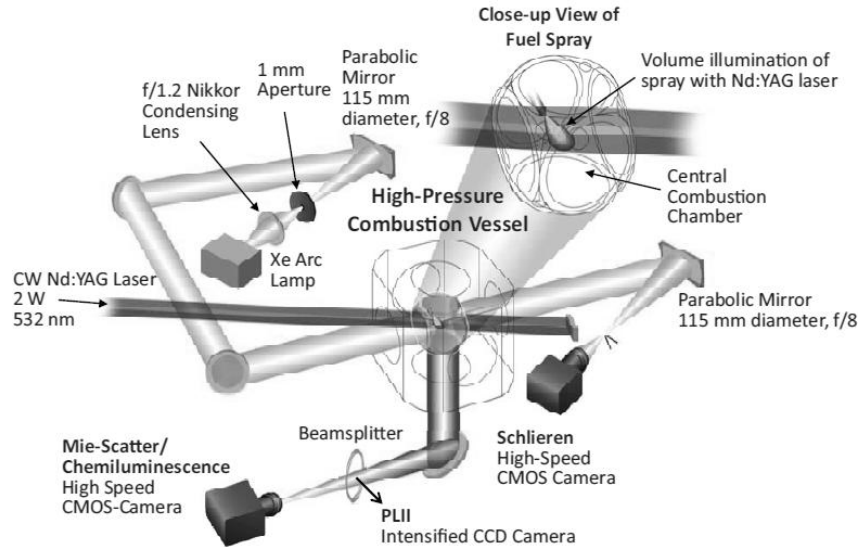
Figure 4.1 Experimental setup of the constant volume bomb with optical imaging for liquid, vapour and combustion luminosity, adapted from Nerva et al. [36].

SME fuel is initially injected at a constant pressure of 1500 bar for injection duration of 7.5 ms. Fuel injection is operated using a single hole common rail injector with nominal diameter of 90.0 μm. Due to higher density and viscosity of SME prior to injection, SME is injected at a higher flow rate with initial injected mass of 22.7 mg [36]. Further operating conditions of the experiment are tabulated in Table 4.1.

Table 4.1 Operating conditions of the constant volume bomb experiment.

Initial conditions			
Temperature (K)	900, 1000		
Pressure (bar)	60.0, 67.0		
Density (kg m^{-3})	22.8		
Injector settings			
Type	Bosch common rail, single hole		
Injection duration (ms)	7.5		
Injection pressure (bar)	1500		
Nominal nozzle diameter (μm)	90.0		
Fuel	SME		
Fuel temperature (K)	363		
Discharge coefficient	0.94		
Conditions	Non-reacting	Reacting	
Mole fractions of air composition			
N_2	0.8971	0.7515	0.7900

O_2	-	0.1500	0.2100
H_2O	0.0377	0.0362	-
CO_2	0.0652	0.0623	-

4.2.2 Numerical Case Settings

Spatial Resolution

The combustion modelled here employs an axi-symmetric wedge mesh to minimise the computational time involved in solving the chemical kinetics. The use of wedge mesh is achievable, for which the total volume of the wedge mesh has to be equivalent to that of experimental combustion chamber [30]. Thus, the axial length of the computational mesh seen in Figure 4.2, which is a 4° sector of a cylindrical mesh, is adjusted to 138.0 mm to match the measured volume. Meanwhile, the radial length of the computational mesh is maintained at 54.0 mm.
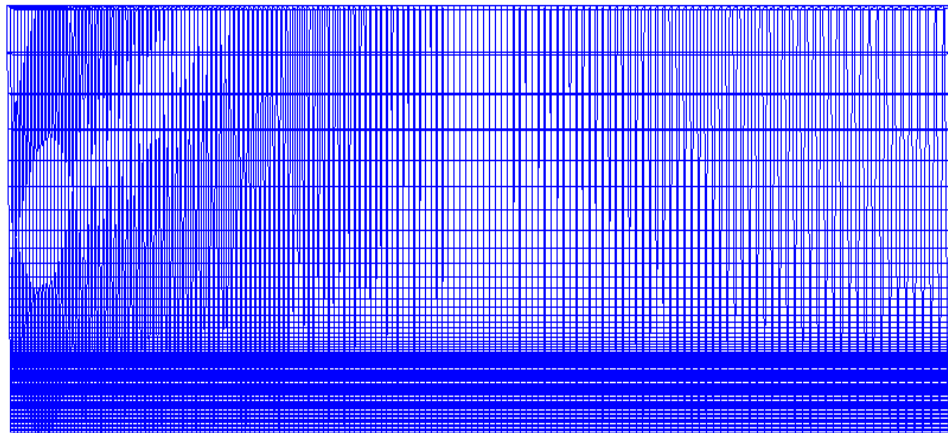
Figure 4.2 The 4° axi-symmetric wedge computational mesh of the constant volume combustion chamber.

Mesh independent studies are performed for the cell sizes in the axial and radial directions using the non-reacting spray conditions. The predicted LPL and vapour penetration length (VPL) for the non-reacting spray at an initial temperature of 900 K are validated against the experimental measurements. Here, the predicted LPL is defined as the furthest axial position with 99.0% of

the injected mass entrained, while VPL is denoted as the distance where 0.1% of fuel mass is detected. For the numerical case settings at initial temperature of 1000 K, equivalent specifications to those of the initial temperature of 900 K are defined.

Three different cell sizes of 0.25 mm, 0.50 mm and 1.00 mm in the axial direction are examined. Each of these cell sizes represents the mesh resolution of fine, intermediate and coarse, respectively. Although the LPL generated by 1.00 mm shows that grid independency has been achieved, the distribution of VPL is relatively unstable as compared to those of 0.25 mm and 0.50 mm, as seen in Figure 4.3(b). Therefore, 0.50 mm is defined as the minimum cell size in the axial direction since the computational time is reduced by 43.0% when compared to that of 0.25 mm, seen in Table 4.2.

Figure 4.4(a) and (b) illustrate the predicted LPL and VPL using radial cell sizes of 0.25 mm, 0.50 mm and 1.00 mm. For the cell sizes of 0.50 mm, large under-prediction up to 1.50 ms is observed in the LPL. Meanwhile, the LPL of 1.00 mm cell size is also under-predicted and becomes unstable at time-step beyond 2.0 ms. The subsequent VPLs for 1.00 mm and 0.50 mm are also unable to replicate the experimental measurements. As such, 0.25 mm is concluded to reach grid independency since the LPL and VPL are accurately reproduced though the computational time is increased by almost 31.0%, as shown in Table 4.2. With the cell sizes of 0.50 mm and 0.25 mm defined in the axial and radial directions, a wedge mesh of 10816 computational cells is formed as seen in Figure 4.2.
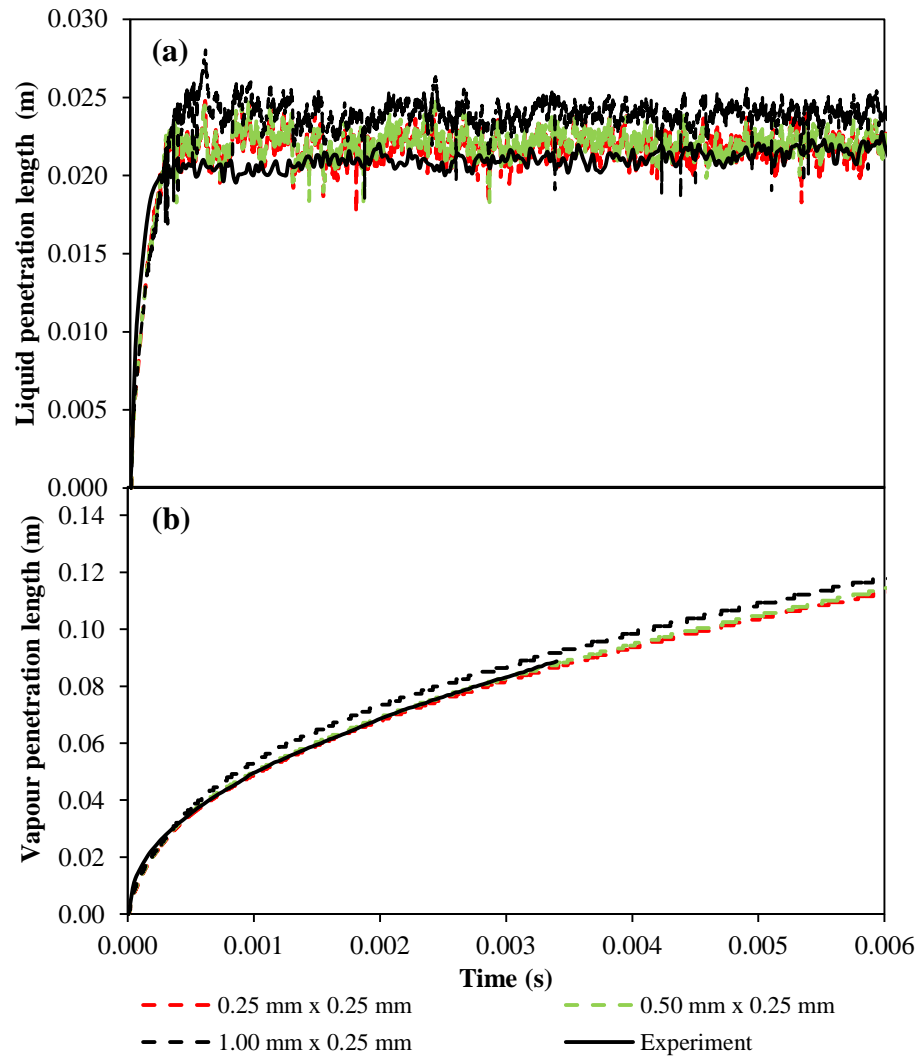
Figure 4.3 Predictions of (a) LPL and (b) VPL against the experimental measurements [36] using cell sizes of 0.25 mm, 0.50 mm and 1.00 mm in the axial direction, at initial temperature of 900 K, non-reacting spray condition.

Table 4.2 Computational times recorded for the axial and radial cell sizes of 0.25 mm, 0.50 mm and 1.00 mm, at initial temperature of 900 K, non-reacting spray condition.

Cell size (mm)	0.25	0.50	1.00
Mesh resolution	Fine	Intermediate	Coarse
Axial			
Computational time (minutes)	45.50	25.80	24.70
Radial			
Computational time (minutes)	25.80	23.00	19.70
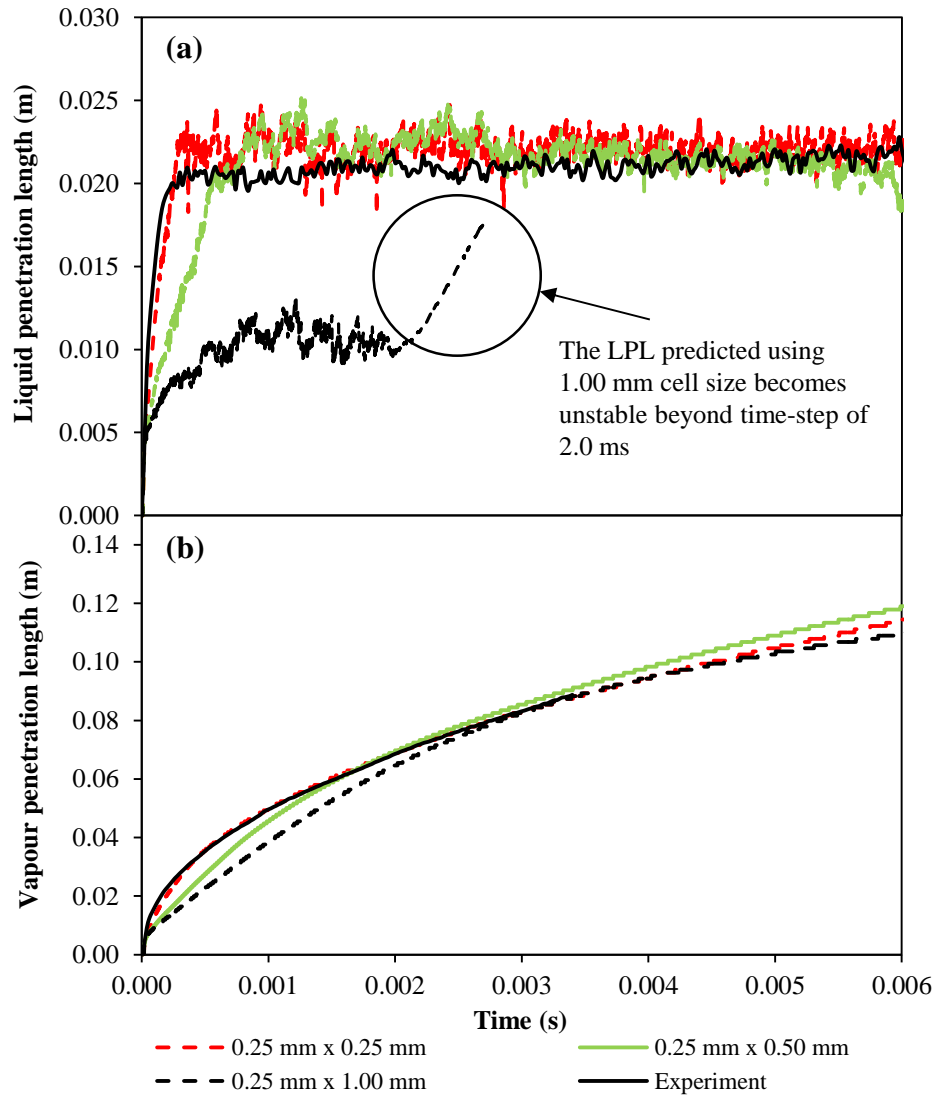
Figure 4.4 Predictions of (a) LPL and (b) VPL against experimental measurements [36] using cell sizes of 0.25 mm, 0.50 mm and 1.0 mm in the radial direction, at initial temperature of 900 K, non-reacting spray condition.

Temporal Resolution

For the temporal resolution, time-step sizes of 1.0 μs, 0.5 μs and 0.1 μs are evaluated. Since the spray in OpenFOAM is solved in the Lagrangian approach, time-step independency is rather difficult to be achieved as depicted in Figure 4.5(a) and (b). Nevertheless, a suitable time-step size needs to be selected in order to produce accurate results. Based on Figure 4.5(a) and (b), the LPL is over-predicted while the VPL is under-predicted from the

beginning of the simulation up to 1.0 ms, when the time-step size is specified to 1.0 µs. On the other hand, improved LPL predictions but with larger fluctuations are found for the time-step size of 0.1 µs, when compared to those of 1.0 µs and 0.5 µs. Nevertheless, the VPL prediction is deteriorated when 0.1 µs is defined, where under-prediction is noticed after 2.0 ms. As such, 0.5 µs is chosen to calculate the simulations since steady results are produced and reasonable computational time is achieved as shown in Table 4.3.
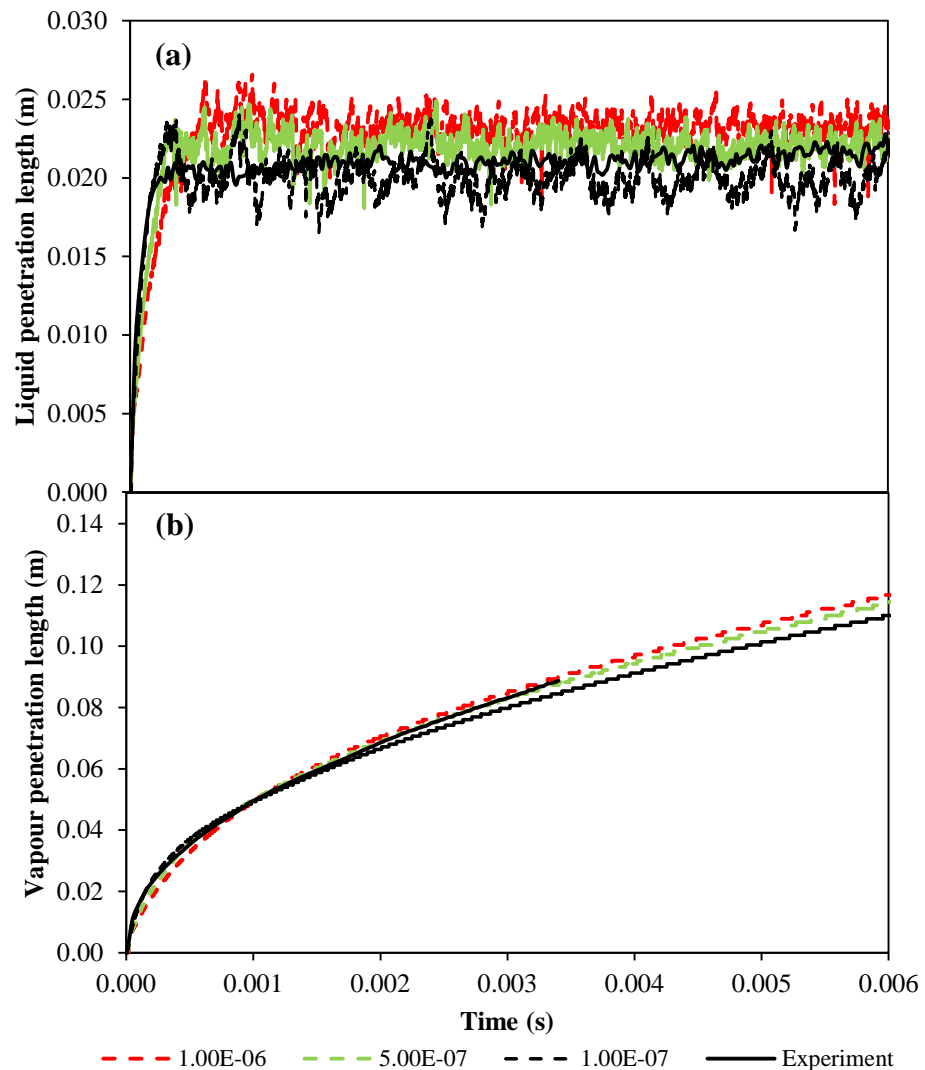
Figure 4.5 Predictions of (a) LPL and (b) VPL against experimental measurements [36] using time-step sizes of 1.0 µs, 0.5 µs and 0.1 µs, at initial temperature of 900 K, non-reacting spray condition.

Table 4.3 Computational times recorded using time-steps of 1.0 μs, 0.5 μs and 0.1 μs, at initial temperature of 900 K, non-reacting spray condition.

Time step (μs)	1.0	0.5	0.1
Computational time (minutes)	14.4	25.8	130.7

Reitz-Diwakar Spray Breakup Model

Secondary spray breakup plays an essential role not only to the spray droplets distribution and fuel consumption, but also to other subsequent processes such as air-fuel mixing, combustion and emissions formation. Therefore, the constants of Reitz-Diwakar spray breakup model are carefully calibrated in order to optimise the secondary breakup of fuel spray.

Since the spray flow is highly turbulent due to the large injection pressures, it is therefore deemed appropriate to calibrate the time model constant (C_s), which is the stripping breakup time factor for flows of large Weber number. Here, LPL is used as the benchmarking parameter as over-prediction in LPL results in spray wall impingement while under-prediction causes under-utilisation of the ambient air [188]. Fuel is injected at a solid angle of 20° with injected parcels of 70,000.

Figure 4.6 shows the LPLs predicted with C_s calibrated to values of 10 and 15. It is clear that optimum LPL prediction under the condition of non-reacting spray is achieved when C_s is adjusted to 10, as compared to the experimental measurements. Despite this, C_s of 15 is selected in order to match the LPL of reacting spray as shown in Figure 4.6(b). Further numerical settings of the non-reacting and reacting sprays are compiled in Table 4.4.
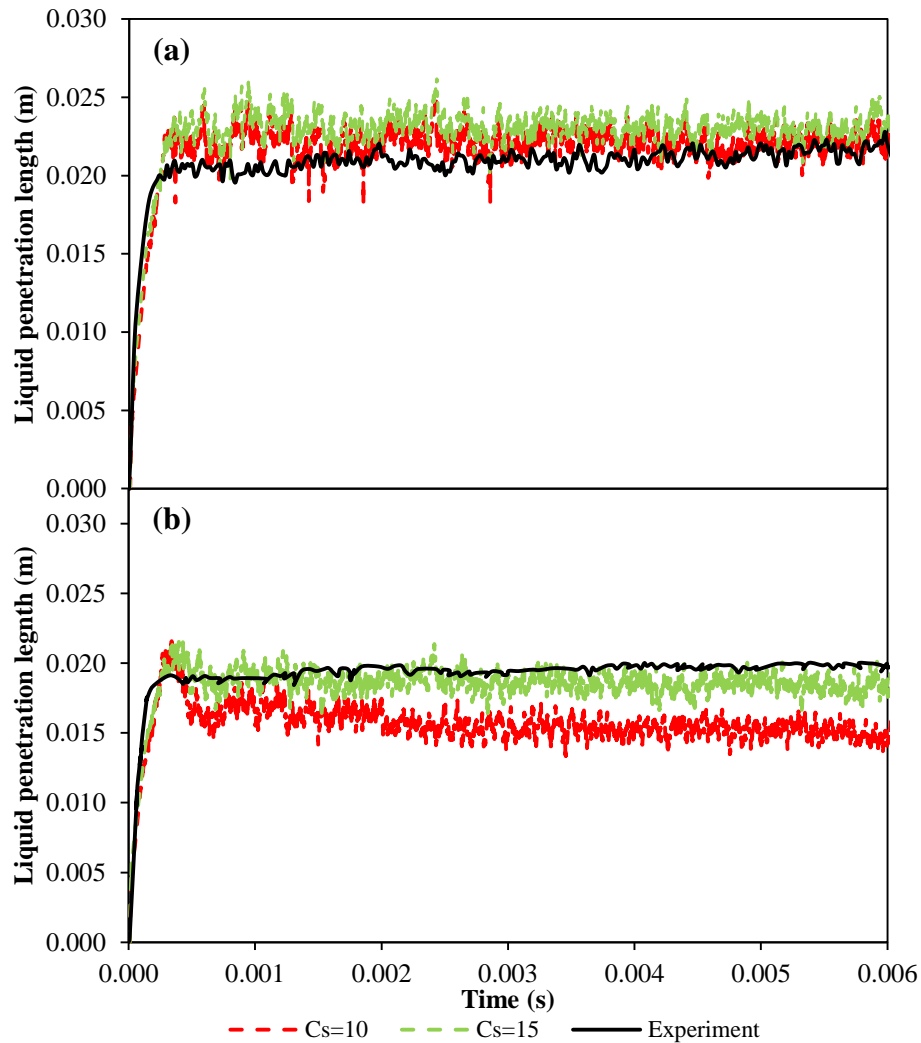
Figure 4.6 Predictions of LPL against experimental measurements [36] under (a) non-reacting spray and (b) reacting spray conditions, with the value of C_s adjusted to 10 and 15, at initial temperature of 900 K.

Table 4.4 Numerical settings of the non-reacting and reacting sprays.

Models	Name
Injector	Hollow cone injector
Breakup	Reitz-Diwakar
Drag	Standard drag
Evaporation	Frossling
Heat transfer	Ranz Marshall
Turbulence	Standard k-ε
Wall	Reflect
Oscillation	Off
Smallest cell size in axial direction (mm)	0.50
Smallest cell size in radial direction (mm)	0.25
Time step (µs)	0.50

Time discretisation	PISO
Model constants	Model coefficients
Reitz-Diwakar spray breakup model	
σ_ε (-)	1.30
C_b (-)	0.785
C_{bag} (-)	6.0
C_{strip} (-)	0.5
C_s (-)	15.0
Standard k-ε turbulence model	
C_μ (-)	0.09
$C_{1\varepsilon}$ (-)	1.58
$C_{2\varepsilon}$ (-)	1.92
$C_{3\varepsilon}$ (-)	-0.33
σ_ε (-)	1.30
k (m^2 s^{-2})	0.735
ε (m^2 s^{-3})	3.835
Leung and Linstedt soot model	
C_α (s^{-1})	10000
T_α (K)	21000
C_β (-)	3.0
C_γ (kg m$^{0.5}$ kmol^{-1} s^{-1})	500 at 900 K
	4000 at 1000 K
T_γ (K)	12100
C_{w1} (kg m$^{0.5}$ kmol^{-1} s^{-1})	8.8177
η_{coll} (-)	0.04
C_{w2} (kg m$^{0.5}$ kmol^{-1} s^{-1})	10000
T_{w2} (K)	19800

Turbulence Model

Two turbulence models, namely, the standard k-ε turbulence model and RNG k-ε turbulence model are evaluated here. Based on the predictions of VPL displayed in Figure 4.7, the model constant ($C_{\varepsilon1}$) in both the standard k-ε and RNG k-ε turbulence models are adjusted to 1.58 and 1.55, respectively, in order to replicate measured VPL. It is noticeable from Figure 4.7 that the standard k-ε turbulence model replicates identical VPL to that of the experiment. Whilst, the under-predicted VPL beyond 2.0 ms simulation time proves that the RNG k-ε turbulence model is unsuitable to account for the turbulence effects. Therefore, the standard k-ε turbulence model is selected for the simulations of non-reacting and reacting sprays.
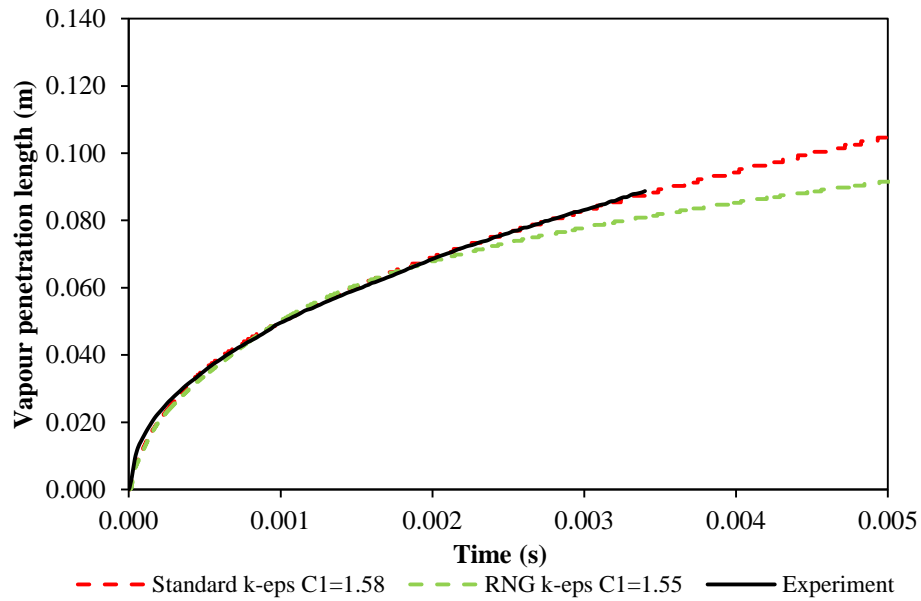
Figure 4.7 Predictions of VPL using the standard *k-ε* model and RNG *k-ε* model against experimental measurements [36], at initial temperature of 900 K, non-reacting spray condition.

Soot Model

The model constants of Leung and Lindstedt soot model are calibrated in order to match the predicted peak soot volume fraction (SVF) with the experimental measurements. As such, the soot model constants that are involved in the soot formation from the processes of nucleation (C_α) and surface growth (C_γ) are adjusted carefully for the reacting spray. Figure 4.8(a) and (b) display the rates of soot formation from the nucleation and surface growth processes at an initial temperature of 900 K, where C_α and C_γ are calibrated from their original values of 10000 and 6000, respectively to a value of 500. Although both the rates of soot formation from nucleation and surface growth are affected by the adjusted model constants, the influence of the C_γ on the absolute SVF is greater than that of the C_α, as seen in Figure 4.9. This clearly shows that the soot formation is prone to the change of C_γ than C_α. Thus, C_γ is chosen to calibrate the peak SVF. For the reacting spray modelling at the initial temperatures of 900 K and 1000 K, C_γ is adjusted to the values of 500

and 4000, respectively. The coefficients of the Leung and Lindstedt soot model constants are listed in Table 4.4.
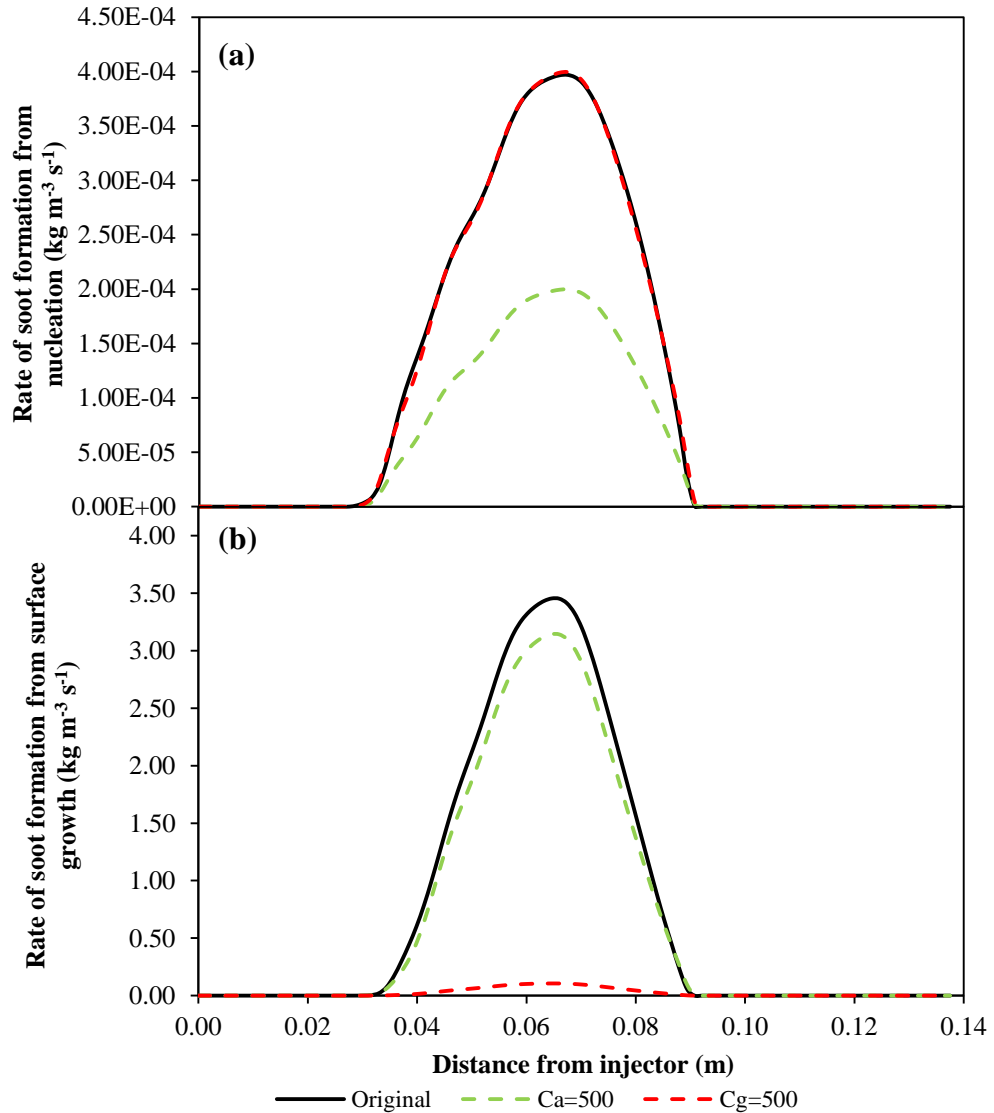
Figure 4.8 Predicted rates of soot formation from nucleation and surface growth using the original and adjusted Leung and Lindstedt model constants, at initial temperature of 900 K, reacting-spray condition.
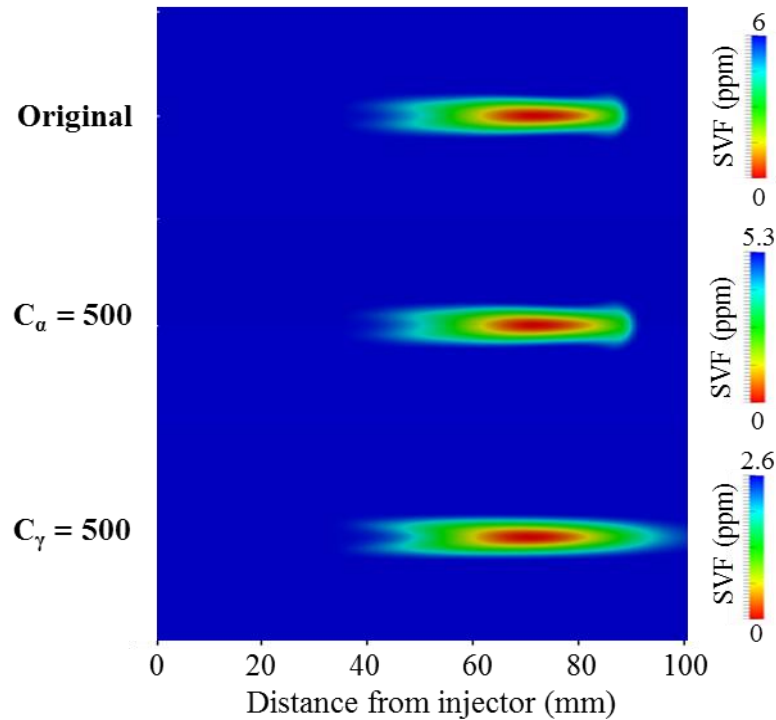
Figure 4.9 Predicted SVFs using the original and adjusted Leung and Lindstedt model constants, at initial temperature of 900 K, reacting spray condition.

4.3   Combustion Modelling in Diesel Engine

4.3.1   Experimental Setup and Conditions

Table 4.5 tabulates the experimental setup of the Nottingham test engine [3]. The test engine, which is a light-duty diesel engine with a bowl-in-piston, has a bore of 80.0 mm, stroke of 69.0 mm and connecting rod length of 114.5 mm. The test engine of 0.347 L volume is operated between rotational speeds of 1500 rpm to 3500 rpm with varying loads of 0.5 kW to 2.5 kW.

Table 4.5 Experimental setup of Nottingham test engine.

Engine type	Light-duty diesel engine
Piston type	Bowl-in-piston
Cylinder head type	Flat cylinder head
Number of injector holes	4
Nozzle diameter (mm)	0.128

Nozzle nap angle (°)	152
Intake valve closure (° ATDC)	-140
Exhaust valve open (° ATDC)	+140
Displacement volume (L)	0.347
Piston bowl volume (L)	0.0116
Bore (mm)	80.0
Stroke (mm)	69.0
Connecting rod length (mm)	114.5
Compression ratio	19.1:1
Initial temperature (K)	320
Initial pressure (bar)	1.13
Fuel temperature (K)	312
Operating speed (rpm)	1500-3500
Operating power (kW)	0.5-2.5

4.3.2   Numerical Case Settings

For the diesel engine combustion simulations, an engine condition of 1.5 kW load and 2344 rpm rotational speed is selected. This condition, which is the intermediate condition (denoted by 3) of the European Stationary Cycle as presented in Figure 4.10, depicts the medium range of typical light-duty diesel engine.
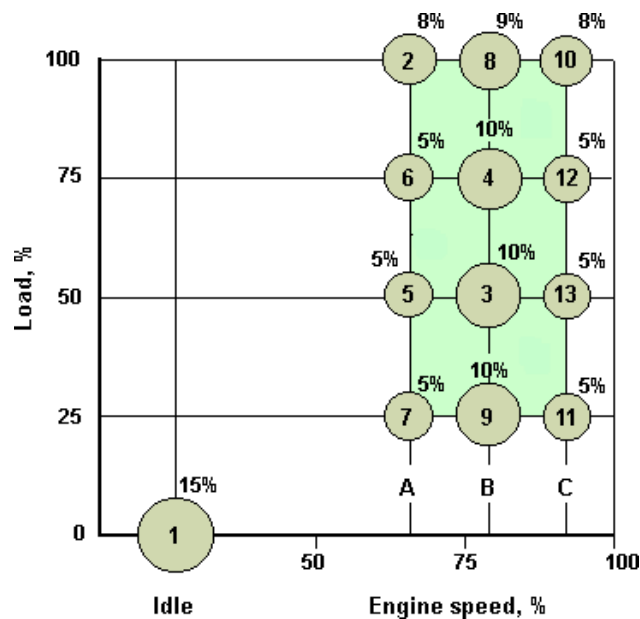
Figure 4.10 Load and speed mapping of European Stationary Cycle [201].

The simulation performed here concentrates only on the closing part of the diesel engine cycle, which is between the IVC at -140° after top dead centre (ATDC) and exhaust valve opening (EVO) at +140° ATDC. The initial temperature and pressure at IVC are defined at 1.13 bar and 320 K, respectively. Figure 4.11 displays a 90° sector computational mesh of the light-duty diesel engine. This is done by taking the advantage of the four equally-spaced injectors such that the computational time can be expedited. The boundary conditions for the diesel engine mesh are defined in Table 4.6.
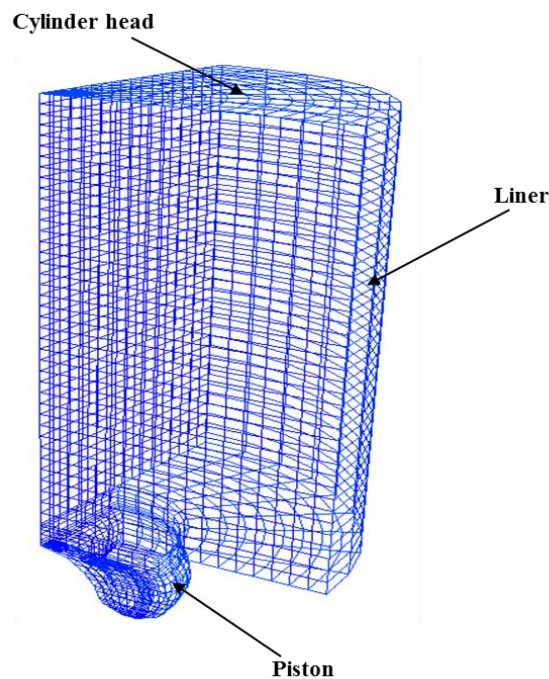
Figure 4.11 The computational mesh of the light-duty diesel engine.

Table 4.6 Initial and boundary conditions defined for the diesel engine combustion simulations.

Initial temperature (K)	Initial pressure (bar)		
320	1.13		
Boundary	Cylinder head	Liner	Piston
Temperature (K)	450	410	450

Two types of biodiesel fuels namely, CME and SME are specified for the diesel engine combustion simulations. The fuel injection system is controlled

at an injection pressure of 200.0 bar and discharge coefficient of 0.75. The duration of fuel injection is calculated based on the measured fuel consumption rate [3]. Table 4.7 compiles the details of injection setup in diesel engine for CME and SME. For the diesel engine combustion simulations, a single processor with processing speed of 3.4 GHz is utilised since the parallel processing routine is unavailable in OpenFOAM version 2.0.x.

Table 4.7 Injection specifications for CME and SME in the diesel engine.

Fuel types	Start of injection (° ATDC)	End of injection (° ATDC)	Total fuel consumption (kg hr^{-1})	Total fuel injection quantity (mg cycle^{-1})	Fuel injection quantity per injector hole (mg cycle^{-1})
CME					
C100	-15.50	0.12	0.554	7.873	1.968
SME					
S100	-15.50	-0.76	0.523	7.428	1.857

Spatial Resolution

Three different mesh configurations for the light-duty diesel engine are evaluated. These include cell sizes of 1.0 mm, 1.5 mm and 2.5 mm, which represent fine, medium and coarse mesh, respectively. Here, the predicted in-cylinder pressures are validated against the experimental measurements. Figure 4.12 shows the predicted profiles of in-cylinder pressure using cell sizes of 1.0 mm, 1.5 mm and 2.5 mm. It is clearly observed that mesh independency is achieved with 1.5 mm cell size, where the predicted peak pressure deviates approximately 1.5% from the measured data. Furthermore, a reasonable computational time with savings of 17.2% are attained for 1.5 mm cell size, when compared to that of 1.0 mm, as shown in Table 4.8.
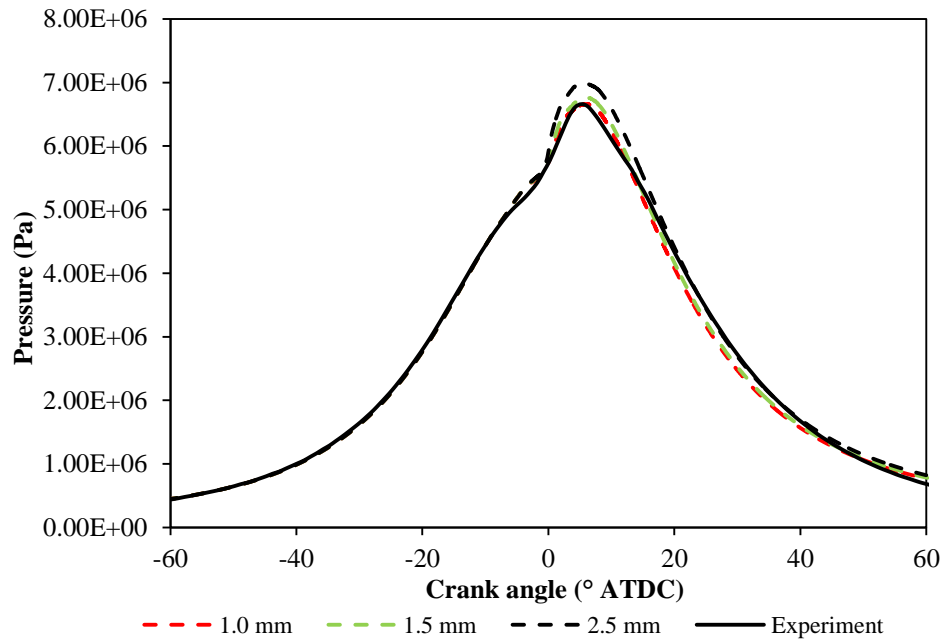
Figure 4.12 Predicted in-cylinder pressures for CME against experimental measurements [3], using cell sizes of 1.0 mm, 1.5 mm and 2.5 mm.

Table 4.8 Computational times recorded for the diesel engine combustion simulations from -140 to +60° ATDC, using cell sizes of 1.0 mm, 1.5 mm and 2.5 mm.

Cell sizes (mm)	1.0	1.5	2.5
Computational time (hrs)	70.3	60.0	53.7

Temporal Resolution

A study of the time-step sizes is conducted here in order to replicate the combustion process accurately. The time-step sizes are varied between 0.01° and 0.005° because further reducing the time-step size results in unrealistic computational time. These two time-step sizes are equivalent to 1.07 μs and 0.53 μs, respectively, after converting to time in seconds by using Equation 4-1.

$$t\ (s) = \frac{Crank\ angle\ degree\ defined}{4\ x\ Engine\ Speed\ (rpm)} \tag{4-1}$$

As seen in Figure 4.13, the profiles of in-cylinder pressures are reproduced when the time-step size of 0.01° is defined. Besides, the time-step size of 0.01° also achieves a reduction of 23.7% in computational runtime, when compared to that of 0.005° time-step size as recorded in Table 4.9. Therefore, the time-step size of 0.01° is selected.
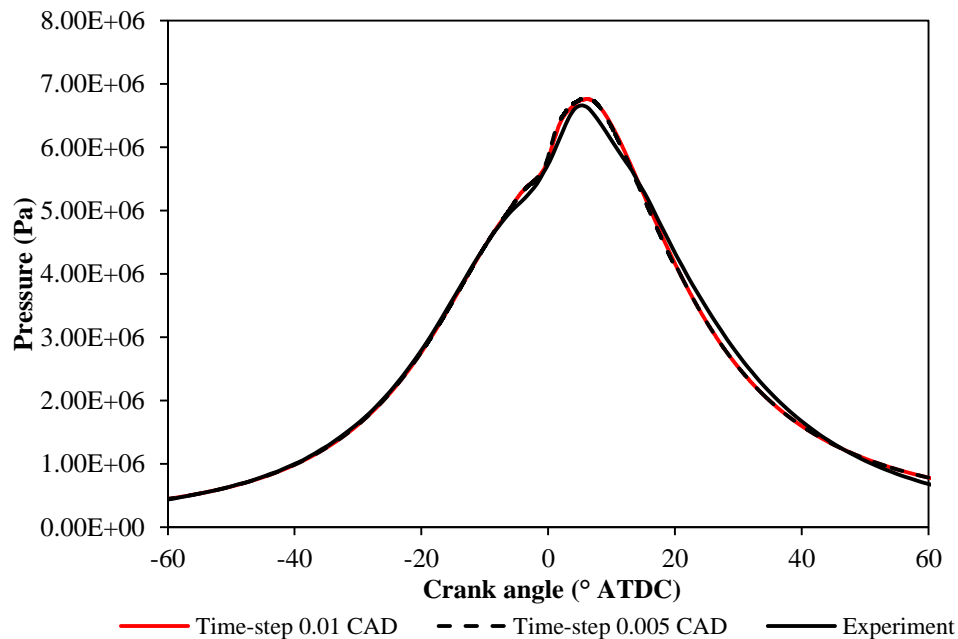
Figure 4.13 Predicted in-cylinder pressures for CME against experimental measurements [3], using time-step sizes of 0.01° and 0.005°.

Table 4.9 Computational times recorded for the diesel engine combustion simulations from -140 to +60° ATDC, using time-step sizes of 0.01° and 0.005°.

Time-step size (°)	0.01	0.005
Computational time (hours)	59.4	77.9

Reitz-Diwakar Spray Breakup Model

The spray breakup process in the diesel engine is important as it affects the subsequent processes of ignition, combustion and emission formation. Here, the fuel spray is modelled at a solid angle of 25° using hollow cone injector model, whilst the number of parcels is maintained at 70,000.

The time model constant (C_s) from the Reitz-Diwakar spray breakup model is calibrated to adjust the spray penetration length for the diesel engine combustion. Here, the predicted in-cylinder pressures are validated against the experimental measurements, such that appropriate C_s values can be selected, as seen in Figure 4.14. Table 4.10 compiles the numerical case settings for the diesel engine combustion.
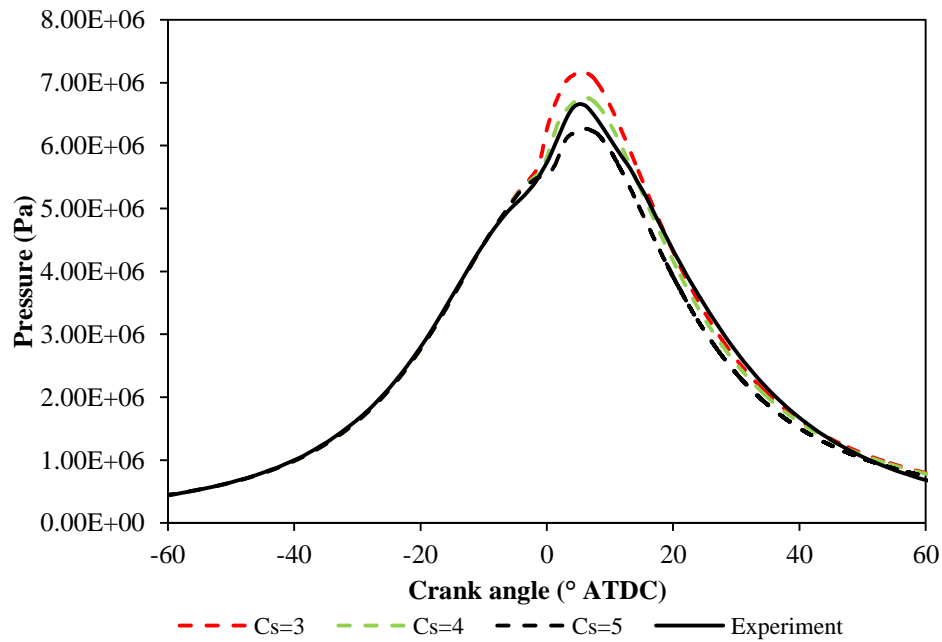
Figure 4.14 Predicted in-cylinder pressures for CME against the experimental measurements [3], with the value of C_s adjusted to 3, 4 and 5.

Table 4.10 Numerical settings of the diesel engine combustion.

Models	Name
Injector	Hollow cone injector
Breakup	Reitz-Diwakar
Drag	Standard drag
Evaporation	Frossling
Heat transfer	Ranz Marshall
Turbulence	RNG k-ε
Wall	Reflect
Oscillation	On
Cell size (mm)	1.50
Time step (°)	0.01
Time discretisation	PISO
Model constants	Model coefficients

Reitz-Diwakar spray breakup model

σ_ε (-)	1.30
C_b (-)	0.785
C_{bag} (-)	6.0
C_{strip} (-)	0.5
C_s (-)	4.0 for CME
	5.0 for SME
RNG k-ε turbulence model	
C_μ (-)	0.0845
$C_{1\varepsilon}$ (-)	1.42
$C_{2\varepsilon}$ (-)	1.68
$C_{3\varepsilon}$ (-)	-0.333
σ_k (-)	0.71942
σ_ε (-)	0.71942
Mean piston speed (m s^{-1})	5.391
k (m^2 s^{-2})	29.060
ε (m^2 s^{-3})	3211.421
Leung and Linstedt soot model	
C_α (s^{-1})	10000
T_α (K)	21000
C_β (-)	3
C_γ (kg m$^{0.5}$ kmol^{-1} s^{-1})	500
T_γ (K)	12100
C_{w1} (kg m$^{0.5}$ kmol^{-1} s^{-1})	8.8177
η_{coll} (-)	0.04
C_{w2} (kg m$^{0.5}$ kmol^{-1} s^{-1})	10000
T_{w2} (K)	19800

Turbulence Model

The initial values of k and ε for the diesel engine combustion simulations are estimated using Equations 4-2 to 4-4. The calculated initial values are tabulated in Table 4.10.

$$k = (mean\ piston\ speed)^2 \tag{4-2}$$

$$l = \frac{k^{3/2}}{\varepsilon} \tag{4-3}$$

$$\varepsilon = \frac{1.64 k^{3/2}}{Bore} \tag{4-4}$$

Comparisons have been made between the standard k-ε and RNG k-ε turbulence models for the simulations of diesel engine combustion. Figure 4.15 shows the in-cylinder pressure predicted using the standard k-ε and RNG

k-ε turbulence models. As anticipated, better predictions are achieved with the RNG k-ε turbulence model since this model includes turbulence calculations from swirling effects, turbulent viscosity and near-wall treatment, as aforementioned in Chapter 3. Meanwhile, over-prediction in the in-cylinder pressure is obtained for the standard k-ε turbulence model. Besides, the calibration of the standard k-ε turbulence model does not improve the in-cylinder pressure predictions. Because of these reasons, the RNG k-ε turbulence model is favoured over the standard k-ε turbulence model to estimate the turbulent flows in the diesel engine. The coefficients of RNG k-ε turbulence model constants are compiled in Table 4.10.
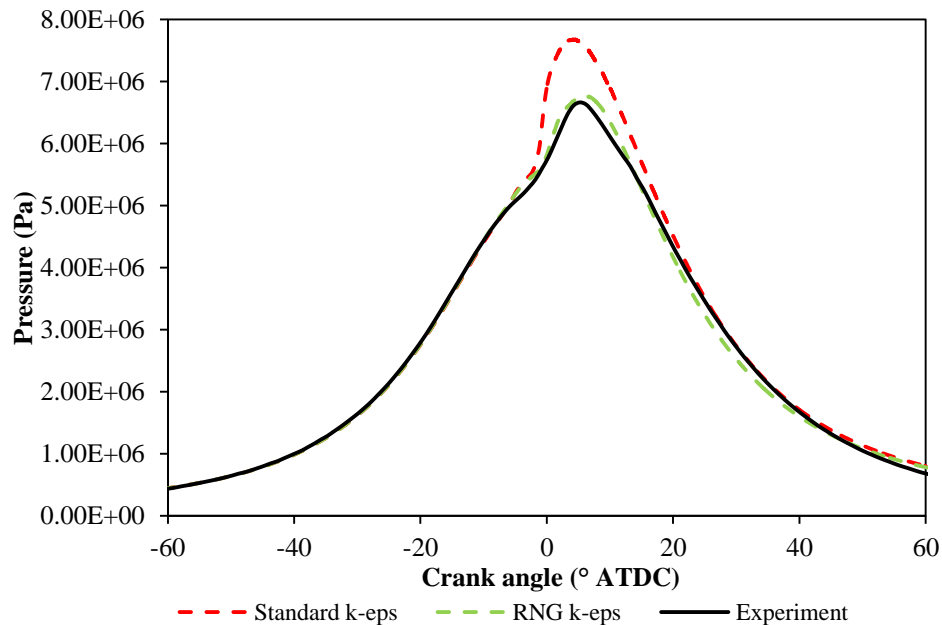
Figure 4.15 Predicted in-cylinder pressures for CME against experimental measurements [3], using the standard k-ε and RNG k-ε turbulence models.

Soot Model

For the soot calculation in the diesel engine, identical calibration to that of the reacting spray at the initial temperature of 900 K is specified, where C_γ is set to 500. This approach is adopted in order to relate the comparison study

performed between the simulations of constant volume bomb and diesel engine combustion for CME and SME in Chapter 7.

4.4　Concluding Remarks

This chapter summarises the numerical case settings that are employed to formulate high fidelity simulation results. For the simulations under the constant volume bomb conditions, a mesh configuration of 0.50 mm x 0.25 mm is employed, while a time-step of 0.50 μs is defined. For the spray and turbulence calculations, the model constants of the Reitz-Diwakar spray breakup model and standard k-ε turbulence model are appropriately adjusted to replicate the experimental measurements. Besides, C_γ of the Leung and Lindstedt soot model is calibrated to match the peak SVFs measured at initial temperatures of 900 K and 1000 K.

On the other hand, the simulation of diesel engine combustion utilises a computational mesh of 1.5 mm cell size, with a fixed time-step size of 0.01°. In terms of the calculation for spray development, C_s of the Reitz-Diwakar spray breakup model is adjusted accordingly for each CME and SME. In order to accurately reproduce the turbulence effects in the diesel engine, the RNG k-ε turbulence model is selected over the standard k-ε turbulence model. Meanwhile, equivalent calibration to that of reacting spray at the initial temperature of 900 K is adopted for the soot calculation in the diesel engine.

The computational cell sizes, time-step sizes, CFD models and adjusted models constants are retained for the simulations of non-reacting spray, reacting spray and diesel engine combustion performed in the following Chapters of 5, 6 and 7.

Chapter 5

Development of Thermo-Physical Properties for Biodiesel

5.1   Introduction

This chapter discusses the development and sensitivity analyses of thermo-physical properties for biodiesel. Since biodiesel contains substantial levels of unsaturation, it is therefore important to estimate the thermo-physical properties accurately. This is because the mixture preparation, spray development and subsequent combustion performance are found to be affected by the thermo-physical properties [32]. Section 5.2.1 presents the evaluation of thermo-physical properties for CME and SME. A total of 15 thermo-physical properties including the critical properties, liquid properties and vapour properties are evaluated. The evaluated thermo-physical properties are then integrated into the fuel library of OpenFOAM, as explained in Section 5.2.2. Meanwhile, Section 5.3 describes the simulations performed for the thermo-physical properties under the conditions of non-reacting and reacting sprays. In Section 5.4, the individual and coupled effects among the thermo-physical properties are discussed. Besides, the significance of the thermo-physical properties with respect to the change of unsaturation levels and combustion kinetics is also appraised.

5.2   Development of Thermo-Physical Properties

5.2.1   Evaluation of Thermo-Physical Properties

In this section, the thermo-physical properties of CME and SME are evaluated using the methods of evaluation compiled in Table 5.1, which are identical to

those employed by Mohamed Ismail et al. [41]. The compositions of CME and SME are listed in Table 5.2. Improvement is made to the evaluation of vapour diffusivity by taking into account of the binary interaction between fuel and air as proposed in the Lennard-Jones potential [107], instead of the binary interactions among FAME components considered by Mohamed Ismail et al. [41].

The methods of evaluation selected here, which are developed based on experimental measurements, are functions of temperature and hydrocarbon group contributions. Thus, these methods are particularly suitable to calculate the thermo-physical properties for biodiesel, which are composed of different types of methyl esters. Besides, the temperature-dependent correlations also ease the function coding written for OpenFOAM. Here, only the evaluations for critical properties and liquid properties are presented. Meanwhile, the remaining calculations for vapour properties are presented in Appendix A.

Meanwhile, the thermo-physical properties for diesel are calculated using the correlations of n-tetradecane ($C_{14}H_{30}$) obtained from the fuel properties library of OpenFOAM. n-tetradecane is selected here to represent diesel among the fuel range of cyclohexane (C_6H_{12}) to heneicosane ($C_{21}H_{44}$) as examined by Lin and Tavlarides [202] because the thermo-physical properties of this component were tested to be 92.0% similar to those of diesel [202]. Here, the calculated thermo-physical properties for CME, PME, RME and SME are benchmarked against those of the diesel, which is an approach adopted according to those of Chakravarthy et al. [34] and Ra et al. [32]. This is because the measurements of thermo-physical properties for different biodiesel fuels and wide range of temperatures, specifically those fuel types and temperatures included in this research study, are unavailable in the literature.

Table 5.1 Methods of evaluation for the thermo-physical properties.

Thermo-physical properties	Methods of evaluation	Ref.
Boiling point	Measured from experiment	-
Critical temperature	Joback modification of Lydersen's method	[107]
Critical pressure	Joback modification of Lydersen's method	[107]
Critical volume	Joback modification of Lydersen's method	[107]
Latent heat of vaporisation	Pitzer acentric factor correlation	[106]
Liquid density	Modified Rackett equation	[107]
Liquid heat capacity	van Bommel correlation	[132]
Liquid surface tension	Correlation proposed by Allen et al.	[130]
Liquid thermal conductivity	Robbin and Kingsrea method	[107]
Liquid viscosity	Orrick and Erbar method, Letsou and Stiel method	[107]
Second virial coefficient	Tsonopoulos method	[107]
Vapour diffusivity	Lennard-Jones potential, Wilke and Lee method	[107], [108]
Vapour heat capacity	Rihani and Doraiswamy method	[107]
Vapour pressure	Modified Antoine equation	[203]
Vapour thermal conductivity	Correlation by Chung et al.	[140,141]
Vapour viscosity	Correlation by Chung et al.	[140,141]

Table 5.2 Compositions for CME, PME, RME and SME as calculated based on the percentages of saturation and unsaturation in each biodiesel fuel.

FAMEs	Fuel types			
	CME	PME	RME	SME
	(%)[a]	(%)[a]	(%)[b]	(%)[a]
Saturated				
Methyl laurate ($C_{13}H_{26}O_2$)	47.0	-	-	-
Methyl myristate ($C_{15}H_{30}O_2$)	19.0	1.0	-	-
Methyl palmitate ($C_{17}H_{34}O_2$)	10.0	42.0	4.3	10.0
Methyl stearate ($C_{19}H_{38}O_2$)	3.0	5.0	1.3	4.0
Unsaturated				
Methyl oleate ($C_{19}H_{36}O_2$)		41.0	59.9	28.0
Methyl linoleate ($C_{19}H_{34}O_2$)	2.0	10.0	21.1	55.0
Methyl linolenate ($C_{19}H_{32}O_2$)	-	-	13.2	4.0
Percentage of saturation (%)	~80.0	~50.0	~10.0	~20.0
Percentage of unsaturation (%)	~20.0	~50.0	~90.0	~80.0

[a] adapted from Mohamed Ismail et al. [41].

[b] averaged from Golovitchev and Yang [58].

Critical Properties

The critical properties of biodiesel are important, as these properties are used to calculate other thermo-physical properties such as, liquid density, surface tension, vapour pressure, latent heat of vaporisation, liquid thermal conductivity, vapour diffusivity and second virial coefficient. Joback modification of Lydersen's method [107] is used to estimate the critical temperature, critical pressure and critical volume for individual FAME component, as shown in Equations 5.1 to 5.3. Then, Lee-Kesler Equation, which is a mixing equation as shown in Equations 5.4 to 5.13, is applied to calculate the critical properties for biodiesel mixtures. Table 5.3 compiles the predicted critical properties for FAME components, CME and SME.

$$T_{i,c} = T_b[0.584 + 0.965 \sum \Delta_T - (\sum \Delta_T)^2] \tag{5-1}$$

$$P_{i,c} = (0.13 + 0.0032n_A - \sum \Delta_P)^{-2} \tag{5-2}$$

$$V_{i,c} = 17.5 + \sum \Delta_V \tag{5-3}$$

$$T_{m,c} = \frac{1}{V_{m,c}^{1/4}} \sum_i \sum_j y_i y_j V_{ij,c}^{1/4} T_{ij,c} \tag{5-4}$$

$$V_{m,c} = \sum_i \sum_j y_i y_j V_{ij,c} \tag{5-5}$$

$$V_{ij,c} = 0.125 \left[(V_i)^{1/3} + (V_j)^{1/3} \right]^3 \tag{5-6}$$

$$T_{ij,c} = (T_{i,c} T_{j,c})^{1/2} k'_{ij} \tag{5-7}$$

$$P_{m,c} = (0.2905 - 0.085\omega_m)RT_{m,c}/V_{m,c} \tag{5-8}$$

$$\omega_m = \sum_i y_i \omega_i \tag{5-9}$$

$$\omega_i = \frac{\alpha}{\beta} \tag{5-10}$$

$$\alpha = -\ln P_{i,c} - 5.97214 + 6.09648\,\theta^{-1} + 1.28862\ln\theta - 0.169347\theta^6 \tag{5-11}$$

$$\beta = 15.2518 - 15.6875\,\theta^{-1} - 13.472\ln\theta - 0.43577\theta^6 \tag{5-12}$$

$$\theta = \frac{T_{i,b}}{T_{i,c}} \tag{5-13}$$

Where subscript m refers to mixture, subscripts i and j refer to pure components, P_c is the critical pressure (bar), T_b is the normal boiling point (K) and T_c is critical temperature (K) and V_c is the critical volume (ml mol^{-1}). n_A is the number of atoms in the molecule, k'_{ij} is the binary parameters, which are simplified to be unity since no published data are available. y_i, y_j are the mole fractions of pure components i or j and ω is the acentric factor of pure component i.

Table 5.3 Calculated critical properties for FAME components, CME and SME.

FAMEs	Critical properties		
	Temperature (K)	Pressure (bar)	Volume (ml mol^{-1})
Saturated			
Methyl laurate ($C_{13}H_{26}O_2$)	695.3	14.2	789.5

Methyl myristate ($C_{15}H_{30}O_2$)	724.1	14.2	901.5
Methyl palmitate ($C_{17}H_{34}O_2$)	767.1	14.2	1013.5
Methyl stearate ($C_{19}H_{38}O_2$)	775.6	14.2	1125.5
Unsaturated			
Methyl oleate ($C_{19}H_{36}O_2$)	774.4	14.1	1105.5
Methyl linoleate ($C_{19}H_{34}O_2$)	798.5	14.0	1085.5
Methyl linolenate ($C_{19}H_{32}O_2$)	801.7	13.8	1065.5
Biodiesel			
CME	721.2	15.3	885.0
SME	789.2	13.0	1084.0

Latent Heat of Vaporisation

The Pitzer acentric factor correlation [106] displayed in Equation 5-14, which relates latent heat of vaporisation to temperature and acentric factor, is employed to predict the latent heat of vaporisation for biodiesel mixtures. This correlation is particularly accurate between T_r of 0.6 and 1.0. The calculated latent heat of vaporisations for CME and SME are presented in Figure 5.1(a). To calculate the latent heat of vaporisation at boiling point, the correlation displayed in Equations 5-15 and 5-16 as suggested by Fish and Lielmezs [106] is utilised.

$$\Delta H_v = RT_{m,c}[7.08(1 - T_r)^{0.354} + 10.75\omega_m(1 - T_r)^{0.456}] \tag{5-14}$$

$$\Delta H_v = \Delta H_{v,b}\frac{T_r}{T_{r,b}}\frac{\chi + \chi^q}{1 + \chi^p} \tag{5-15}$$

$$\chi = \frac{T_{r,b}}{T_r}\frac{1 - T_r}{1 - T_{r,b}} \tag{5-16}$$

Where ΔH_v is defined as the latent heat of vaporisation (J mol^{-1}) and R is the gas constant (J mol^{-1}K^{-1}), the latent heat of vaporisation at the normal boiling point is denoted by $\Delta H_{v,b}$ (J mol^{-1}), while the reduced temperature at normal boiling point is given by $T_{r,b}$. p and q are the inorganic and organic liquid constants, with values of 0.35298 and 0.13856, respectively [106].

Liquid Density

The liquid densities for CME and SME shown in Figure 5.1(b) are computed using the Rackett equation modified by Spencer and Danner [107]. The modified equations by Spencer and Danner, which are originally used to estimate specific volumes, are converted to liquid densities as suggested by Tat and van Gerpen [204]. Equations 5-17 to 5-19 show the expressions for liquid density.

$$\rho = \frac{\rho_R}{Z_{RA}{}^{\phi}} \qquad (5\text{-}17)$$

$$\phi = \left(1 - \frac{T}{T_c}\right)^{2/7} - \left(1 - \frac{273.15}{T_c}\right)^{2/7} \qquad (5\text{-}18)$$

$$Z_{RA} = 0.29056 - 0.08775\omega_m \qquad (5\text{-}19)$$

Where ρ is the liquid density (kg L^{-1}), ρ_R is the experimental density value at reference temperature T_R (kg L^{-1}), Z_{RA} is the compressibility factor and φ is the reduced temperature constant.

Liquid Heat Capacity

The correlation for liquid heat capacity suggested by van Bommel and co-workers [132] is employed to evaluate the liquid heat capacities for the biodiesel fuels. The liquid heat capacity for each FAME component is first calculated using Equation 5-20 and then the simple mixing rule given in Equation 5-21 is applied to obtain the liquid heat capacities for the biodiesel fuels. Figure 5.1(c) shows the liquid heat capacities estimated for CME and SME.

$$C_{p,L,i} = 103.16 + 16.273n + 0.047355nT \qquad (5\text{-}20)$$

$$C_{p,L,m} = \sum_i y_i C_{p,L,i} \qquad (5\text{-}21)$$

Where subscripts i and m represent pure component and mixture, respectively, $C_{p,L}$ is defined as the liquid heat capacity (J mol^{-1} K^{-1}), n is the number of

carbon atoms in the carboxylic acid minus one, T is the fuel temperature (K) and y_i is the mole fraction.
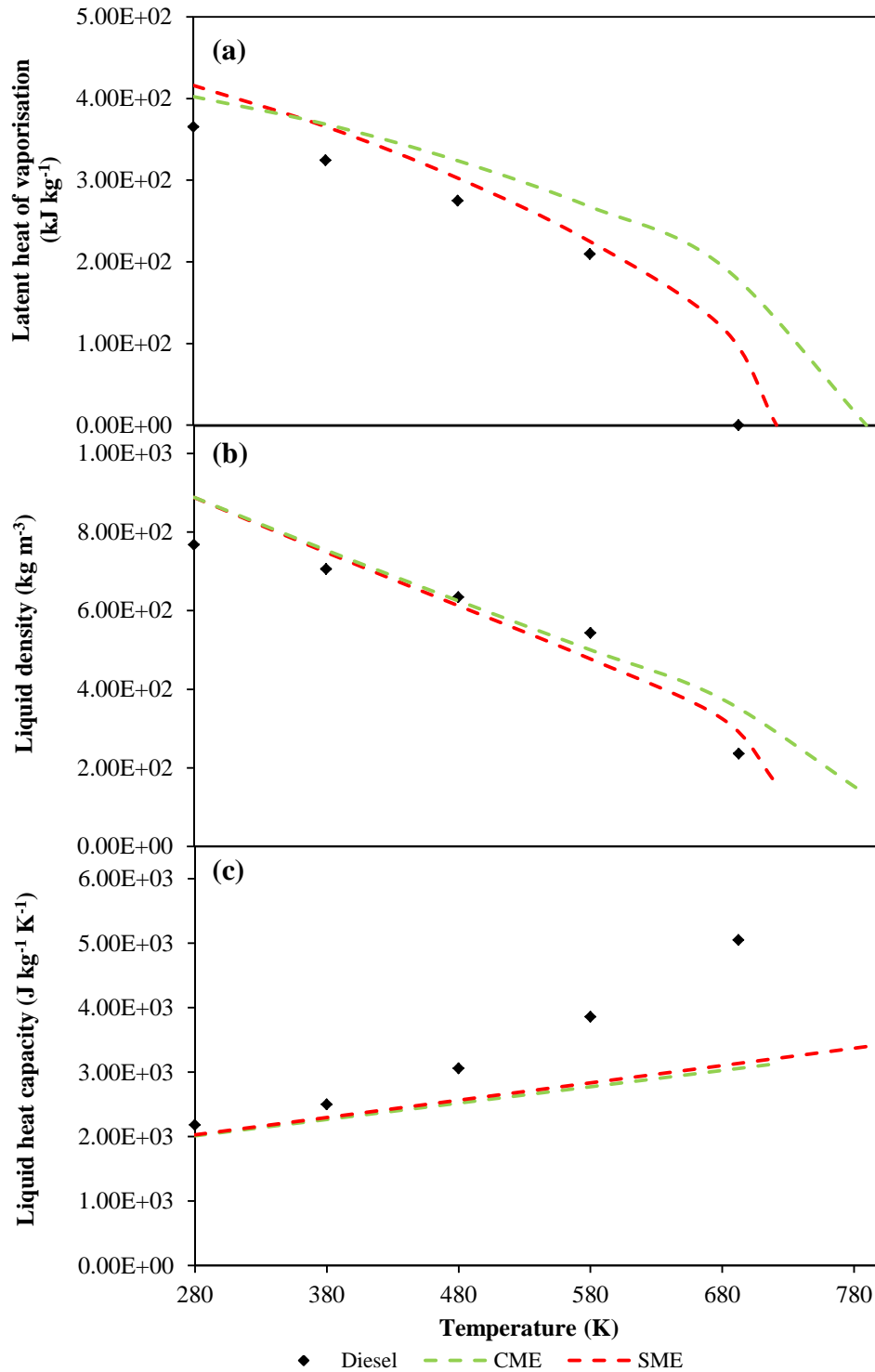
Figure 5.1 Evaluated thermo-physical properties of CME, SME and diesel over temperatures of 280 K to critical temperatures of each fuel: (a) latent heat of vaporisations, (b) liquid densities and (c) liquid heat capacities.

Liquid Surface Tension

The liquid surface tensions for FAME components, as expressed in Equation 5-22 are first calculated using the equation proposed by Macleod and Sudgen [107]. Since the FAME components with higher liquid surface tension induce higher intensity of attraction to each other in a mixture, components with lower liquid surface tension thus give less influence on the surface. Therefore, a linear weight function [130] is utilised to estimate the liquid surface tensions for biodiesel mixtures. For the minimum and maximum liquid surface tensions evaluated among the FAME components, weight factors of 0.93 and 1.0 are applied, respectively. Meanwhile, the linear weight function, w_i as shown in Equation 5-23 is calculated for the remaining FAME components. Consequently, the liquid surface tensions for CME and SME, displayed in Figure 5.2(a) are evaluated using Equation 5-24 [130].

$$\sigma_i = \left([P]\rho_{L,b}\right)^4 \left(\frac{1-T_r}{1-T_{r,b}}\right)^{4n} \tag{5-22}$$

$$w_i = m\sigma_i + c \tag{5-23}$$

$$\sigma_m = \sum_i^n w_i \sigma_i Y_i \tag{5-24}$$

Where subscript i refers to pure component and subscript m refers to mixture. σ is the liquid surface tension (mN m^{-1}), $[P]$ is the Parachor constant given by Allen et al. [130], $\rho_{L,b}$ is the liquid density of fuel at normal boiling point (mol ml^{-1}), $4n$ has a value of 1.1, Y_i is the mass fraction of pure component i and w_i is the weighting factor given of pure component i. m and c are determined by applying a weight factor of 1.0 to the maximum liquid surface tension and a factor of 0.93 to the minimum liquid surface tension.

Liquid Thermal Conductivity

The correlations developed by Robbin and Kingrea [107], as shown in Equations 5-25 and 5-26 are adopted to estimate liquid thermal conductivity for the FAME components. The Li's equations [107] expressed in Equations

5-27 to 5-59 are then applied to calculate the liquid thermal conductivities for CME and SME, as shown in Figure 5.2(b).

$$\lambda_{L,i} = \frac{(88.0 - 4.94H)(10^{-3})}{\Delta S^*} \left(\frac{0.55}{T_r}\right)^N C_p \rho^{4/3} \tag{5-25}$$

$$\Delta S^* = \Delta H_{v,b}/T_b + R(\ln 273/T_b) \tag{5-26}$$

$$\lambda_{L,m} = \sum_i \sum_j \phi_i \phi_j \lambda_{ij} \tag{5-27}$$

$$\lambda_{ij} = 2\left(\lambda_i^{-1} + \lambda_j^{-1}\right)^{-1} \tag{5-28}$$

$$\varphi_i = \frac{Y_i V_i}{\sum_j x_j V_j} \tag{5-29}$$

Where subscript m refers to mixture, while subscripts i and j refer to pure components. λ_L is the liquid thermal conductivity (cal cm^{-1} s^{-1} K^{-1}), T_r is the reduced temperature, C_p is the molal heat capacity for liquid (cal g^{-1}mol^{-1}K^{-1}) and ρ is the molal liquid density (g mol cm^{-3}). ΔS^* is the entropy constant, $\Delta H_{v,b}$ is the molal heat of vaporisation at normal boiling point (cal g^{-1}mol^{-1}), R is the gas constant, T_b is the normal boiling point (K). Y_i and φ_i are the mass fraction and mixture fraction of pure component i, respectively. H and N are the group contributor factors with values of 3.0 and 1.0, respectively.

Liquid Viscosity

The liquid viscosities for FAME components at T_r less than 0.7 are predicted using the correlation suggested by Orrick and Erbar [107], as seen in Equation 5-30. Then, the Grunberg and Nissan method [107], provided in Equation 5-31 are utilised to estimate the liquid viscosities for the biodiesel mixtures.

$$ln\frac{\eta_{L,i}}{\rho_{L,i}W_i} = A + \frac{B}{T} \tag{5-30}$$

$$\ln \eta_{L,m} = \sum_i y_i \ln \eta_{L,i} + \sum_{i \neq j} \sum_j y_i y_j G_{ij} \tag{5-31}$$

Where subscript m refers to mixture, subscripts i and j refer to pure components, η_L denotes the liquid viscosity (mPa s) and $\rho_{L,i}$ is the liquid

density of pure component i at 20°C (g mL^{-1}; each component is assumed to have the same density as the mixture). W_i is the molecular weight of pure component i (g mol^{-1}), y_i is the mole fraction of pure component i and G_{ij} is the interaction parameter, which is a function of components i and j as well as temperature.

In order to calculate liquid viscosities at T_r above 0.7, the Letsou and Stiel approach [107] shown in Equations 5-32 to 5-35 is employed to calculate the liquid viscosities. Figure 5.2(c) illustrates the evaluated liquid viscosities for CME and SME, over temperature range of 280 K to the critical temperature of each fuel.

$$\eta_{L,m}\zeta = (\eta_L\zeta)^{(0)} + \omega_m(\eta_L\zeta)^{(1)} \tag{5-32}$$

$$(\eta_L\zeta)^{(0)} = 10^{-3}(2.648 - 3.725T_r + 1.309T_r{}^2) \tag{5-33}$$

$$(\eta_L\zeta)^{(1)} = 10^{-3}(7.425 - 13.39T_r + 5.933T_r{}^2) \tag{5-34}$$

$$\zeta = 0.176\left(\frac{T_{m,c}}{M^3P_{m,c}{}^4}\right)^{1/6} \tag{5-35}$$

Where $\eta_{L,m}$ is the liquid viscosity of mixture (mPa s) and ω_m is the acentric factor of mixture.
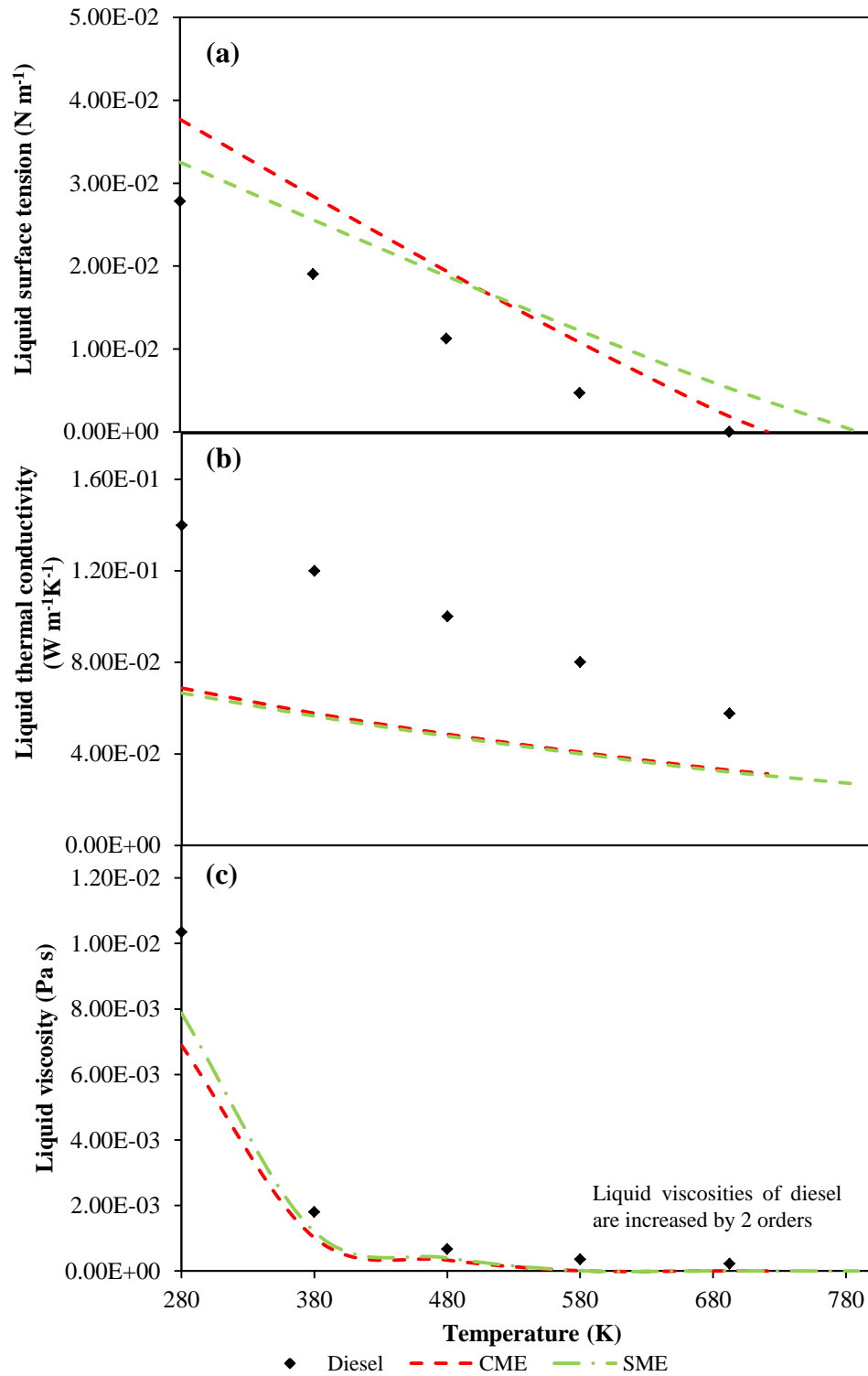
Figure 5.2 Evaluated thermo-physical properties of CME, SME and diesel over temperatures of 280 K to critical temperatures of each fuel: (a) liquid surface tensions, (b) liquid thermal conductivities and (c) liquid viscosities.

5.2.2 Integration of Thermo-Physical Properties into OpenFOAM

In this section, the integration of thermo-physical properties of CME and SME into OpenFOAM is explained. The fuel properties library in OpenFOAM version 2.0.x is illustrated in Figure 5.3. The fuel properties library consists of two main libraries, which are the "thermophysicalFunction" and "liquidProperties". Under the library of "liquidProperties", there is a sub-library named "NSRDSfunctions", which contains all the thermo-physical properties. Here, new function classes for the thermo-physical properties evaluated in Section 5.2.1 are introduced. In the new function classes, each thermo-physical property is assigned to a new function name as tabulated in Table 5.4. The evaluated thermo-physical properties are then written as arrays with respect to a temperature range of 280 K to the critical temperature of each biodiesel fuel. An example of the C++ code programming written for the thermo-physical properties is available in Appendix B. Here, a separate library of thermo-physical fuel properties is built for each CME and SME. Once the compilation of "NSRDSfunctions", "thermophysicalFunctions" and "liquidProperties" for the fuel properties libraries are completed, the solvers of "dieselFoam" and "dieselEngineFoam" are re-compiled such that the newly introduced fuel properties are coupled to the solvers.
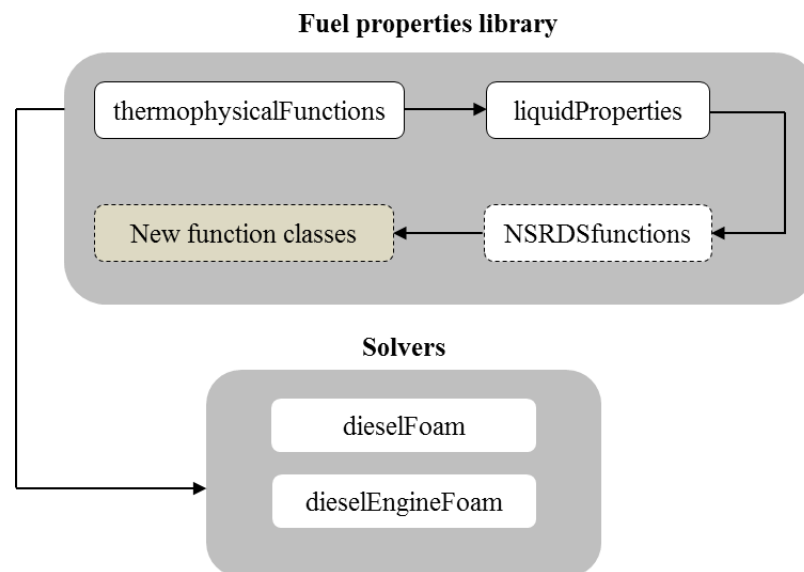
Figure 5.3 Schematic diagram of the fuel properties library and solver in OpenFOAM version 2.0.x.

Table 5.4 Function class names for the thermo-physical properties.

Thermo-physical property	Function class name
Latent heat of vaporisation	NSRDSfuncgHl
Liquid density	NSRDSfuncgRho
Liquid heat capacity	NSRDSfuncgCp
Liquid surface tension	NSRDSfuncgSigma
Liquid thermal conductivity	NSRDSfuncgK
Liquid viscosity	NSRDSfuncgMu
Second virial coefficient	NSRDSfuncgB
Vapour diffusivity	APIdiffCoefFuncgD
Vapour heat capacity	NSRDSfuncgCpg
Vapour pressure	NSRDSfuncgPv
Vapour thermal conductivity	NSRDSfuncgKg
Vapour viscosity	NSRDSfuncgMug

5.3 Sensitivity Analyses of Thermo-Physical Properties

The sensitivity analyses are performed such that the numerical case of SME with the integration of all thermo-physical properties, including the critical properties is defined as the baseline case. Then, the thermo-physical properties of SME are individually replaced by those of diesel. The significance of the fuel properties is determined based on the deviations found in the predicted spray parameters in comparisons to those of the baseline case, under the conditions of non-reacting and reacting sprays. The approach taken here to perform the sensitivity analyses is similar to those carried out by Ra et al. [32] and Mohamed Ismail et al. [41]. Since the experimental data is only available for SME, the simulations for CME are carried out based on the quantitative case settings of SME, except for the thermo-physical properties and fuel compositions.

5.3.1 Non-Reacting Spray

Individual Thermo-Physical Property

This sensitivity analysis is performed to determine the significance of individual thermo-physical property under the non-reacting spray condition. The reason for this is to isolate the combustion chemistries effects, such that the fuel spray development is only influenced by the thermo-physical properties. Here, the deviations found in the predictions of LPL, VPL, SMD, radial mixture fraction and fuel evaporation ratio are used to determine the significance of the individual thermo-physical property. These parameters are chosen because they are indicators for the spray development. For example, LPL and SMD represent the breakup of liquid fuel, while the mixture fraction and evaporation ratio denote the fuel mixing and evaporation, respectively. For the predicted LPL and VPL, additional relative percentage differences (RPDs) for the individual CME and SME thermo-physical property are calculated using Equations 5-36 and 5-37. Meanwhile, the radial mixture fraction is obtained at a position 40.0 mm away from the injector. The fuel evaporation ratio as expressed in Equation 5-38 is defined as the ratio of mass of fuel evaporated to mass of fuel injected [184].

$$RPD \ for \ liquid \ penetration \ (\%) = \frac{Average \ LPL \ of \ individual \ properties}{Average \ LPL \ of \ base}$$

$$(5\text{-}36)$$

$$RPD \ for \ vapour \ penetration \ (\%) = \frac{Maximum \ VPL \ of \ individual \ properties}{Maximum \ VPL \ of \ base}$$

$$(5\text{-}37)$$

$$Fuel \ evaporation \ ratio = \frac{mass \ of \ fuel \ evaporated}{mass \ of \ fuel \ injected} \qquad (5\text{-}38)$$

Based on Figures 5.4 and 5.5, the latent heat of vaporisation gives the greatest increment in the LPL of SME and CME, with a maximum RPD of 34.6% as compared to other fuel properties. This is followed by vapour pressure (-17.6%), liquid heat capacity (7.9%), liquid density (-7.0%) and liquid surface tension (-4.6%).
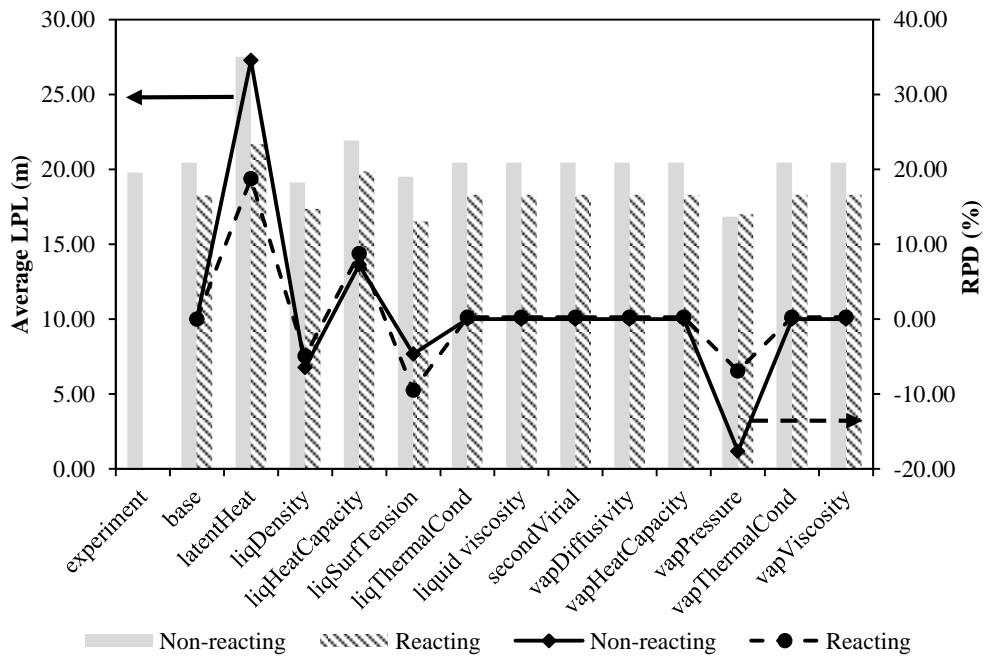
Figure 5.4 Sensitivities of individual thermo-physical property of SME under non-reacting and reacting spray conditions on the predicted LPL (with calculated RPD, plotted as line).
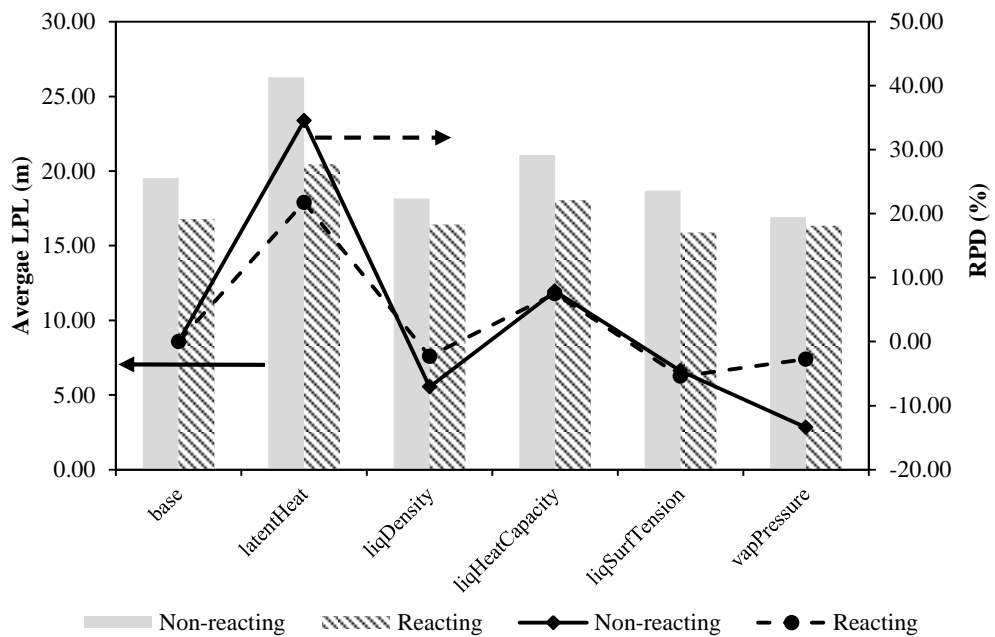
Figure 5.5 Sensitivities of individual thermo-physical property of CME under non-reacting and reacting spray conditions on the predicted LPL (with calculated RPD, plotted as line).

Meanwhile, the effects of the remaining fuel properties which include liquid viscosity, vapour heat capacity, second virial coefficient, liquid thermal

110

conductivity, vapour thermal conductivity, vapour viscosity and vapour diffusivity are marginal because the calculated RPDs of these properties are equivalent to that of the benchmark case. Whilst, the predicted VPLs for the individual fuel property of SME and CME as illustrated in Figure 5.6(a) and (b) exceed by a maximum RPD of 2.5%, when compared to that of baseline case. One possible reason for this is because the penetration of vapour fuel is mainly governed by the fuel-air mixing and turbulence effects.
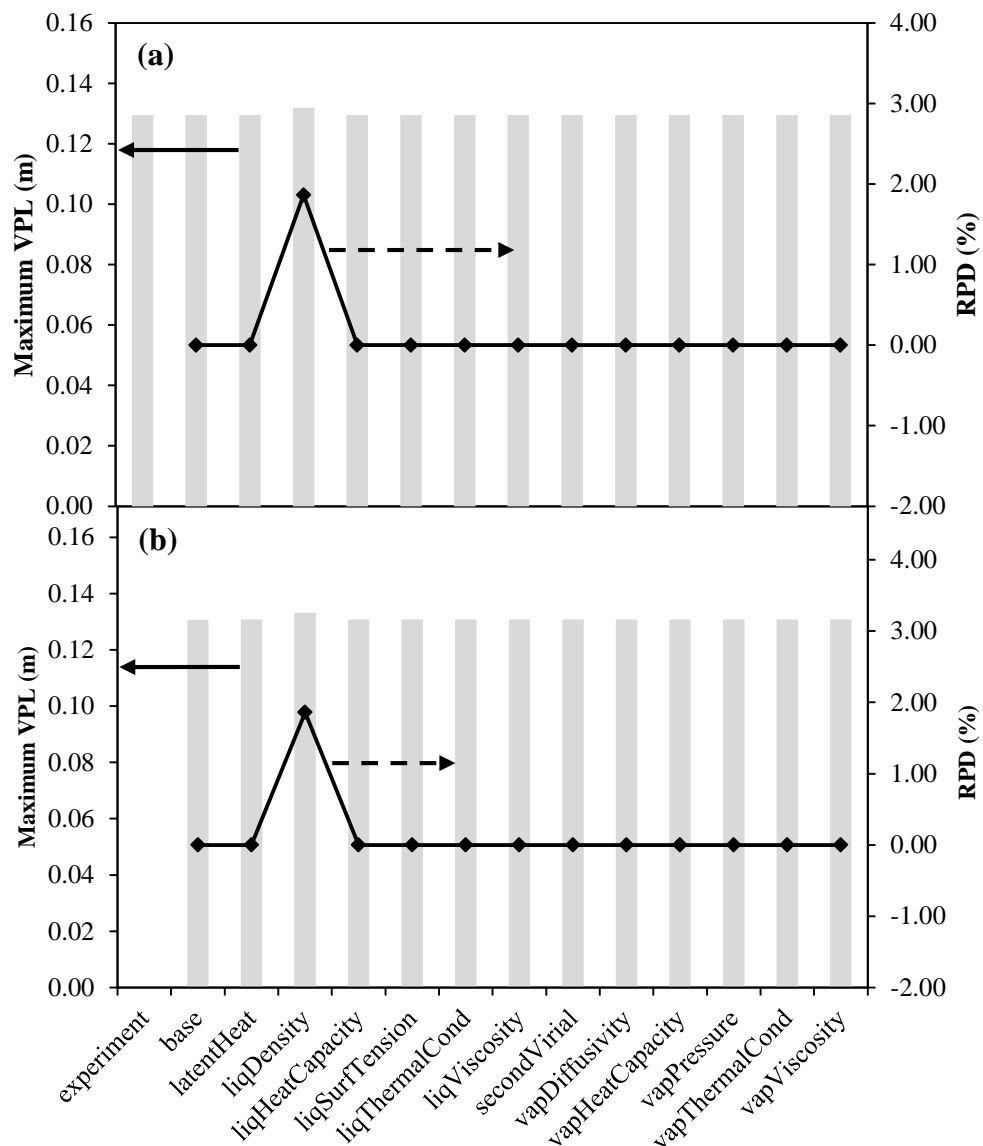
Figure 5.6 Sensitivities of individual thermo-physical property of (a) SME and (b) CME under non-reacting spray condition on the predicted VPL (with calculated RPD, plotted as line).

In terms of the SMD predictions seen in Figure 5.7(a) and (b), the significance of the individual thermo-physical property excluding liquid density is only prominent upon reaching steady-state, where the SMDs are generally under-predicted as compared to those of benchmark case. However, over-predicted SMD is found for vapour pressure, while the SMD for liquid heat capacity remains unchanged. Here, only the SMDs for vapour pressure and latent heat of vaporisation do not correspond to their LPLs. This in turn shows that the SMD prediction does not necessarily affect the subsequent spray penetration.
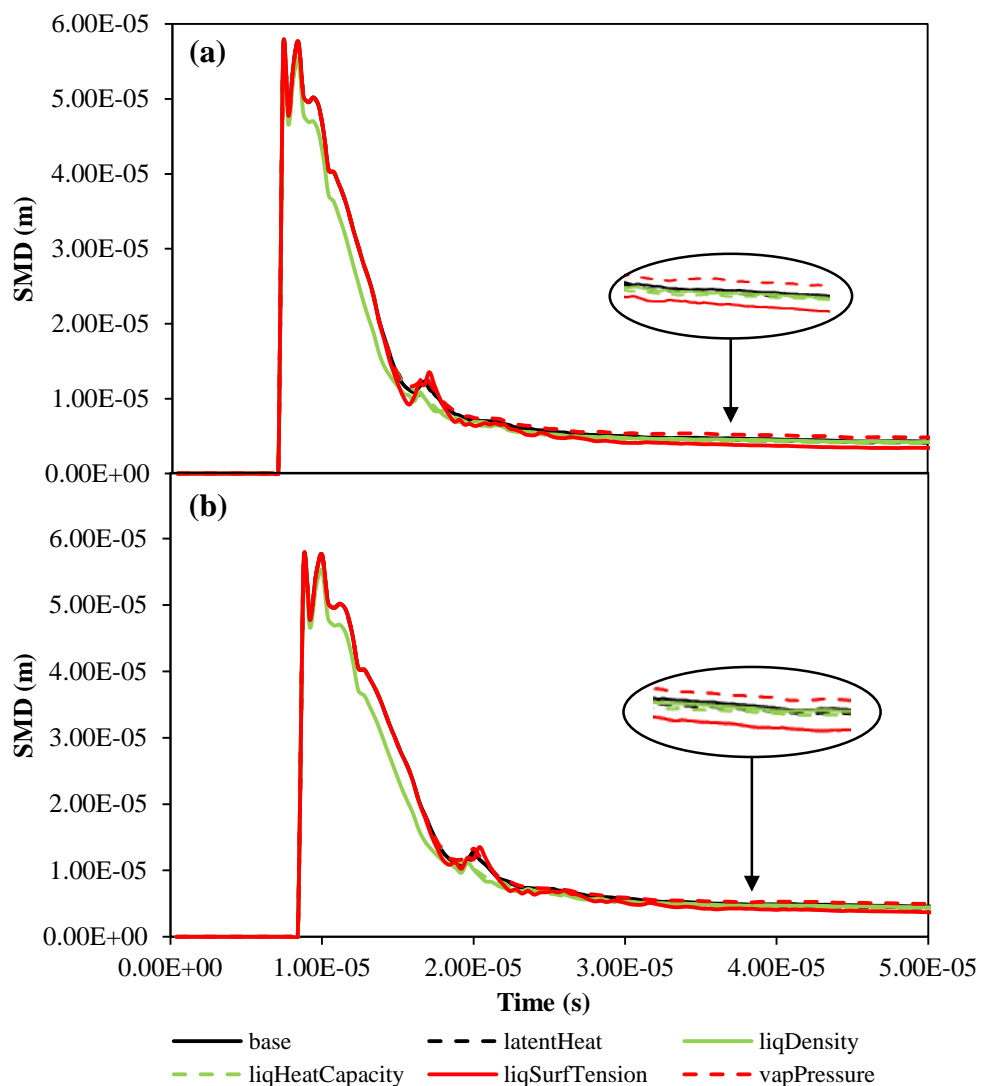
Figure 5.7 Sensitivities of individual thermo-physical property of (a) SME and (b) CME under non-reacting spray condition on the predicted SMD.

For the predicted mixture fractions, the effect of individual fuel property is equivalent to that of LPL, where the latent heat of vaporisations for CME and SME record the highest mixture fraction values of 0.14 and 0.13 than the remaining fuel properties do, as displayed in Figure 5.8(a) and (b). In terms of the calculated fuel evaporation ratios shown in Figure 5.9(a) and (b), latent heat of vaporisation and vapour pressure are clearly the most sensitive fuel properties, for which both properties give the highest and lowest deviations, respectively.
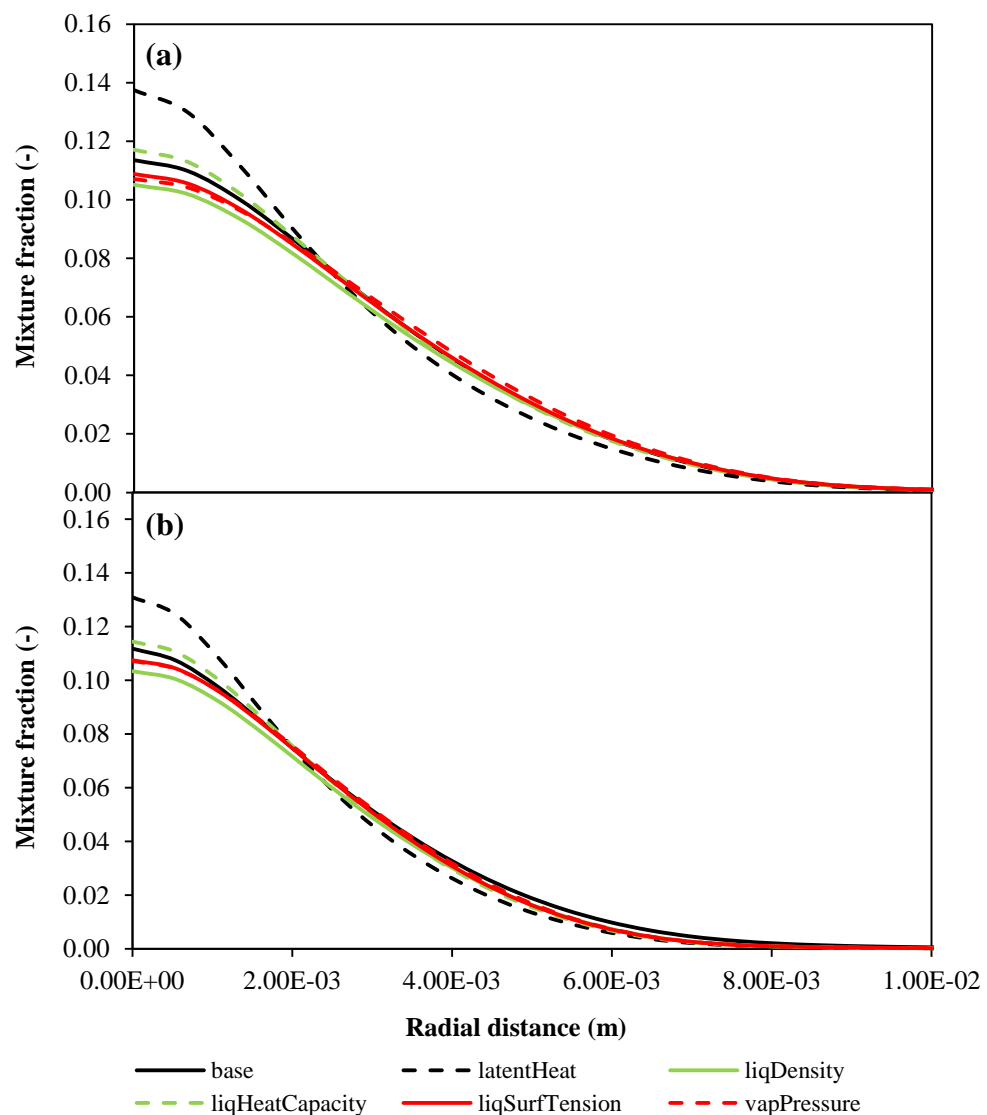
Figure 5.8 Sensitivities of individual thermo-physical property of (a) SME and (b) CME under non-reacting spray condition on the predicted mixture fraction.
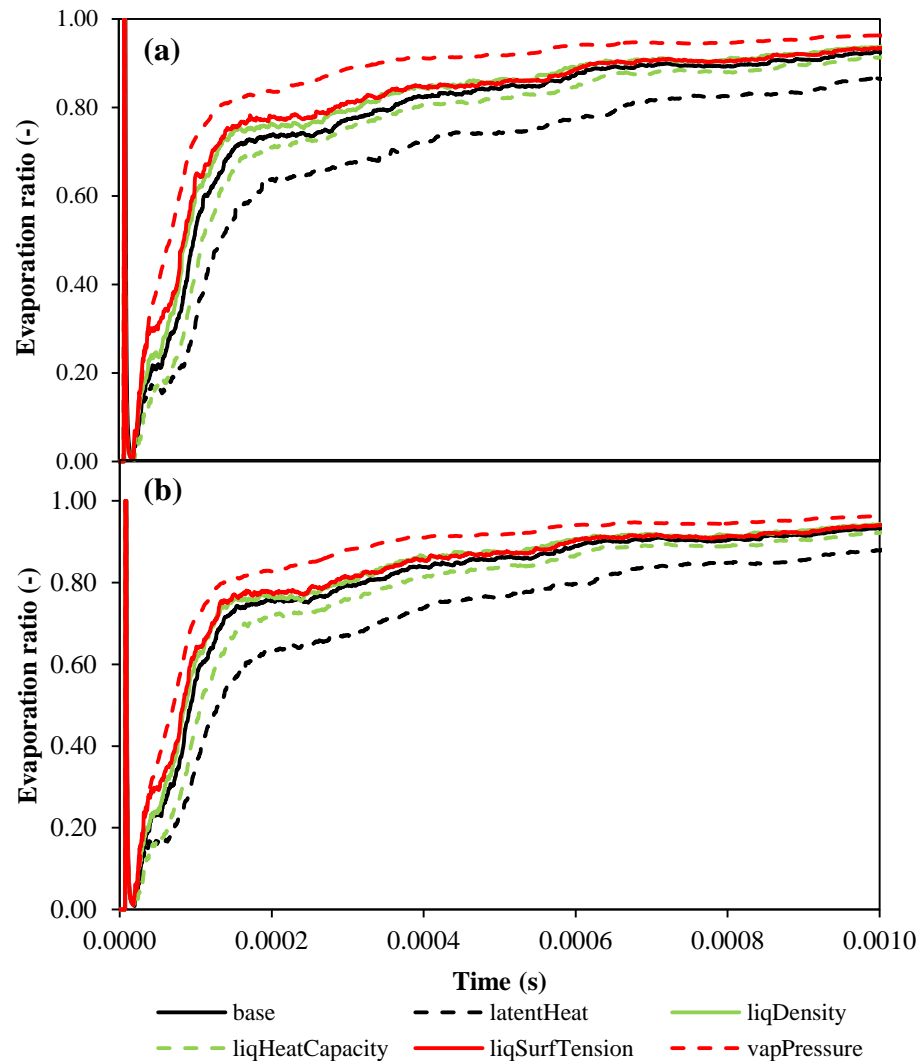
Figure 5.9 Sensitivities of individual thermo-physical property of (a) SME and (b) CME under non-reacting spray condition on the calculated evaporation ratio.

Coupled Thermo-Physical Properties

In order to examine the coupled effects of thermo-physical properties on the spray development, the significant individual thermo-physical property, which are identified from the sensitivity analysis of non-reacting spray, are iteratively combined together. Based on the average LPL predictions shown in Figure 5.10(a), coupled effects among the combined individual fuel properties are found for both CME and SME. For example, the coupling of vapour pressure and latent heat of vaporisation (labelled as 2,3 in Figure 5.10(a) and

(b)) with average LPL values of 16.9 mm and 27.5 mm, respectively gives rise to an average LPL of 21.3 mm. The resulting LPL, which is approximately 4.1% above that of the SME baseline case, indicates that there exists a coupled effect between the two thermo-physical properties. Since similar results are obtained in the remaining analyses of CME and SME, the development of fuel spray is thus deduced to be dependent on the coupled effects among the thermo-physical properties.
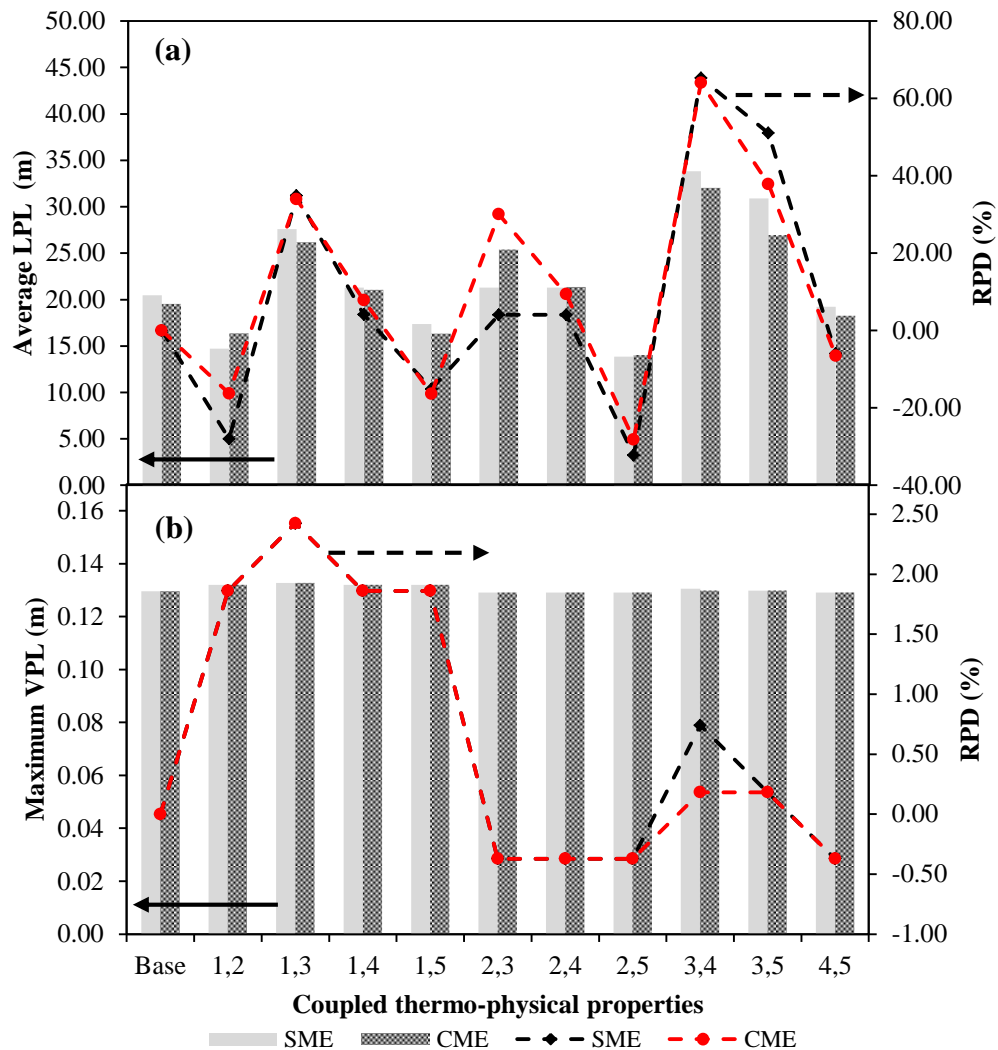
Figure 5.10 Sensitivities of coupled thermo-physical properties of SME and CME under non-reacting spray condition on the predicted (a) LPL (with calculated RPD, plotted as line) and (b) VPL (with calculated RPD, plotted as line). Order of the individual thermo-physical property: 1. Liquid density, 2. Vapour pressure, 3. Latent heat of vaporisation, 4. Liquid heat capacity, 5. Liquid surface tension.

For the vapour spray development, the coupled effects among the thermo-physical properties are also found as seen in Figure 5.10(b). Although this demonstrates the dependency of vapour spray development on the thermo-physical properties, the changes observed in VPL are considered insignificant, where the maximum RPD is calculated to be only at 2.5%. These marginal deviations again prove that the development of vapour fuel is also dependent on the physical processes of mixing and turbulence. Since the coupled effects among the thermo-physical properties are co-produced from the individual effects, only the sensitivity of the individual thermo-physical property is further examined in the reacting spray.

5.3.2   Reacting Spray

Individual Thermo-Physical Property

In this sensitivity analysis, the effect of individual thermo-physical property on spray development is studied for reacting spray, where the combustion chemistries are incorporated. This analysis is performed to further justify the significance of individual thermo-physical property since the development of reacting spray also depends on the combustion chemistries. Here, the compositions of combustion chemistries for CME and SME are retained during the substitution of thermo-physical properties such that the effects of chemical kinetics are maintained throughout the analyses. For example, the fuel composition of SME is retained at 20.0% MD and 80.0% MD9D, when the thermo-physical property of SME is individually substituted by that of the diesel fuel.

Additional benchmarking parameters such as ID period, LOL and SVF are included. Here, VPL is excluded since marginal effects of the fuel properties on VPLs are found, as reported in the non-reacting spray sensitivity analysis. This exclusion is further justified by the observation from Kuti et al.'s work [185], where shorter LPL than flame LOL denoted faster completion of fuel vaporisation before combustion. In their study, the 18.50 mm LPL predicted

for SME is 29.33% shorter than the LOL of 26.18 mm. Since OH chemiluminescence is used to measure LOL in the experiment [36], LOL is measured here as the axial distance from the nozzle to the first position where 2.0% of maximum Favre-averaged OH radical mass fraction is detected. The use of OH chemiluminescence as reported by Higgins and Siebers [205] is a good indicator to locate high temperature, stoichiometric conditions, where flame LOL normally takes place. On the other hand, ID period of the 2D reacting spray is defined as the interval between the start of injection (SOI) to where temperatures of 2000 K is first observed in any computational cell [52].

Based on the LPL predictions for SME as seen in Figure 5.4, only liquid density, liquid heat capacity, liquid surface tension, latent heat of vaporisation and vapour pressure are found to be influential, where a maximum RPD of 18.8% is obtained. On the contrary, the LPL predicted by liquid viscosity, liquid thermal conductivity, vapour thermal conductivity, vapour diffusivity, vapour viscosity and second virial coefficient are equivalent to that of the baseline case. Since the sensitivities of thermo-physical properties for SME found here are identical to those obtained from the non-reacting spray sensitivity analyses, the remaining sensitivity analyses for CME are only performed for the significant fuel properties.

5.4   Effects of Thermo-Physical Properties on the Spray Development

Based on the simulation results estimated from the non-reacting and reacting sprays as illustrated in Figures 5.4 to 5.9, the significant thermo-physical properties identified for CME and SME are latent heat of vaporisation, liquid density, liquid heat capacity, liquid surface tension and vapour pressure. These results predicted for CME and SME generate several key observations. According to the calculated RPD shown in Figures 5.4 and 5.5, the effects exerted by the individual thermo-physical property excluding liquid surface tension are relatively less than those of the non-reacting spray. These

predictions thus prove that the combustion chemistries are involved in the development of reacting spray. Besides, the effects of individual thermo-physical property are also varied in accordance to the unsaturation levels. In the analyses of non-reacting and reacting sprays, the LPL, ID period and LOL predictions for liquid density, liquid heat capacity, liquid surface tension and vapour pressure are extended with the increase of unsaturation levels. On the contrary, reduced RPDs are obtained for latent heat of vaporisation when the unsaturation level increases. Apart from that, the effects of all the thermo-physical properties are also varied with respect to the unsaturation levels. For instance, the predicted ID period of 0.646 ms for CME, which has the lowest unsaturation level is approximately 2.2% shorter than the 0.660 ms of SME, which has the highest level of unsaturation. Similarly, the predicted SVF is also affected by the thermo-physical properties, where CME records a peak SVF of 0.17 ppm, while the highest SVF of SME is predicted at 0.25 ppm. However, an opposite trend is observed in the LOL, where LOL is shortened with the increase of unsaturation level.

Among the significant thermo-physical properties, latent heat of vaporisation and vapour pressure exert the largest influence on the spray development. In general, spray development is retarded when latent heat of vaporisation is substituted, while the substitution of vapour pressure induces advancement. Comparing the effects of latent heat of vaporisations between CME and SME, the retardation in the spray development produced by the latent heat of vaporisation of CME is less than that of the SME. This is because the evaluated values of latent heat of vaporisation for CME are closer to those of the diesel fuel than SME does, particularly at temperatures above 480 K as seen in Figure 5.1(a). For CME and SME, the LPLs predicted in the non-reacting and reacting sprays are extended by maximum deviations of 34.6% and 21.8%, respectively when compared to those of the baseline cases. Despite the 5.0% decreased SMD predicted for latent heat of vaporisation as shown in Figure 5.7(a) and (b), the longer LPL for latent heat of vaporisation is supported by the higher value of mixture fraction, as evident in Figure 5.8(a) and (b). Additionally, the lower fuel evaporation ratio shown in Figure 5.9(a)

and (b) also suggests longer LPL as this parameter denotes longer time is needed for the evaporated fuel mass to be equivalent to the injected fuel mass [184]. These results in turn imply that poor mixing is produced with changes in the latent heat of vaporisation. Apart from this, latent heat of vaporisation also demonstrates the largest retardation effects on the ID period and LOL, with maximum RPDs of 12.1% and 8.6%, respectively, seen in Figures 5.11 and 5.12. Figure 5.13(a) and (b) illustrates the normalised SVF along the axial direction, where the width of the SVF profile represents the area of soot formation. Based on Figure 5.13(a) and (b), the normalised SVF peaks for the latent heat of vaporisations of SME and CME are reduced by RPD of 22.8% and 15.8%, respectively. Here, the reduced SVF peak predicted for latent heat of vaporisation is caused by the extended LOL, where longer LOL leads to a less fuel rich central reaction zone by allowing more air entrainment [206].
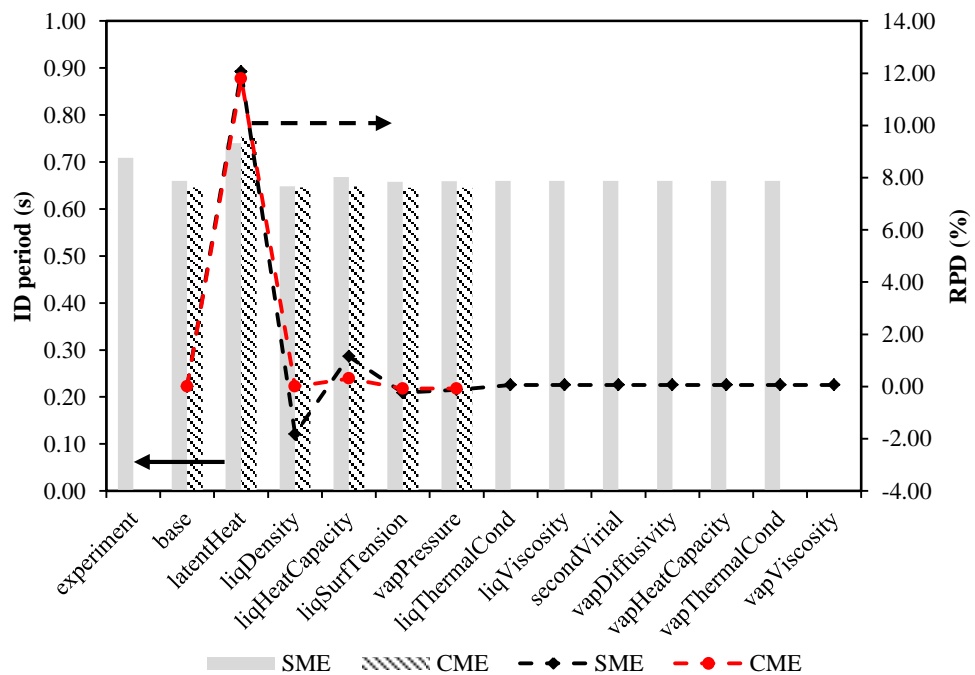

Figure 5.11 Sensitivities of individual thermo-physical property of SME and CME under reacting spray condition on the predicted ID periods (with calculated RPD, plotted as line).
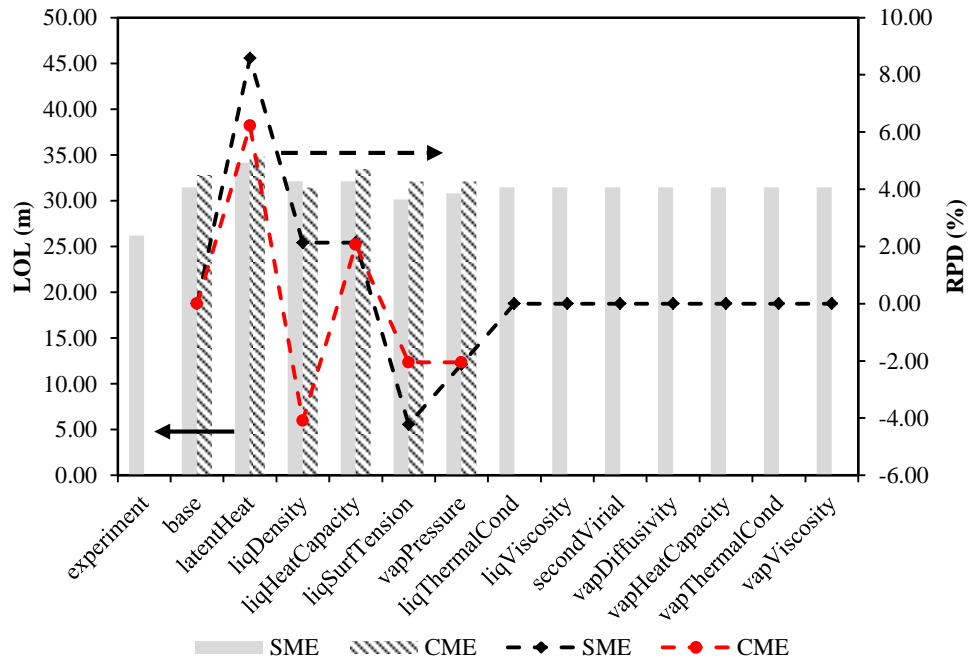
**Figure 5.12 Sensitivities of individual thermo-physical property of SME and CME under reacting condition on the predicted LOL (with calculated RPD, plotted as line).**

Vapour pressure often relates to the volatility [207] and stability [208] of a fuel. Moreover, vapour pressure also denotes the evaporation rate of a fuel [209] since it relates to the tendency of particles to escape from liquid to gaseous phase. For these reasons, reduced LPLs of 17.6% and 6.9% are obtained in the non-reacting and reacting sprays, respectively, as seen in Figures 5.4 and 5.5. Here, it is observed that the effects of vapour pressure on the spray development of CME and SME are similar, where reduced deviations are obtained. For both the fuels, the higher rate of fuel evaporation is evident from the lower mixture fractions and higher fuel evaporation ratios as seen in Figures 5.8 and 5.9, although the SMD predictions are about 10.0% higher than those of the baseline cases. This is because the volatility among the fuel droplets is increased when the lower vapour pressures of CME and SME are replaced by the higher vapour pressures of diesel. As such, the predicted ID period and LOL are shortened by 0.1% and 2.1%, respectively as seen in Figures 5.11 and 5.12.
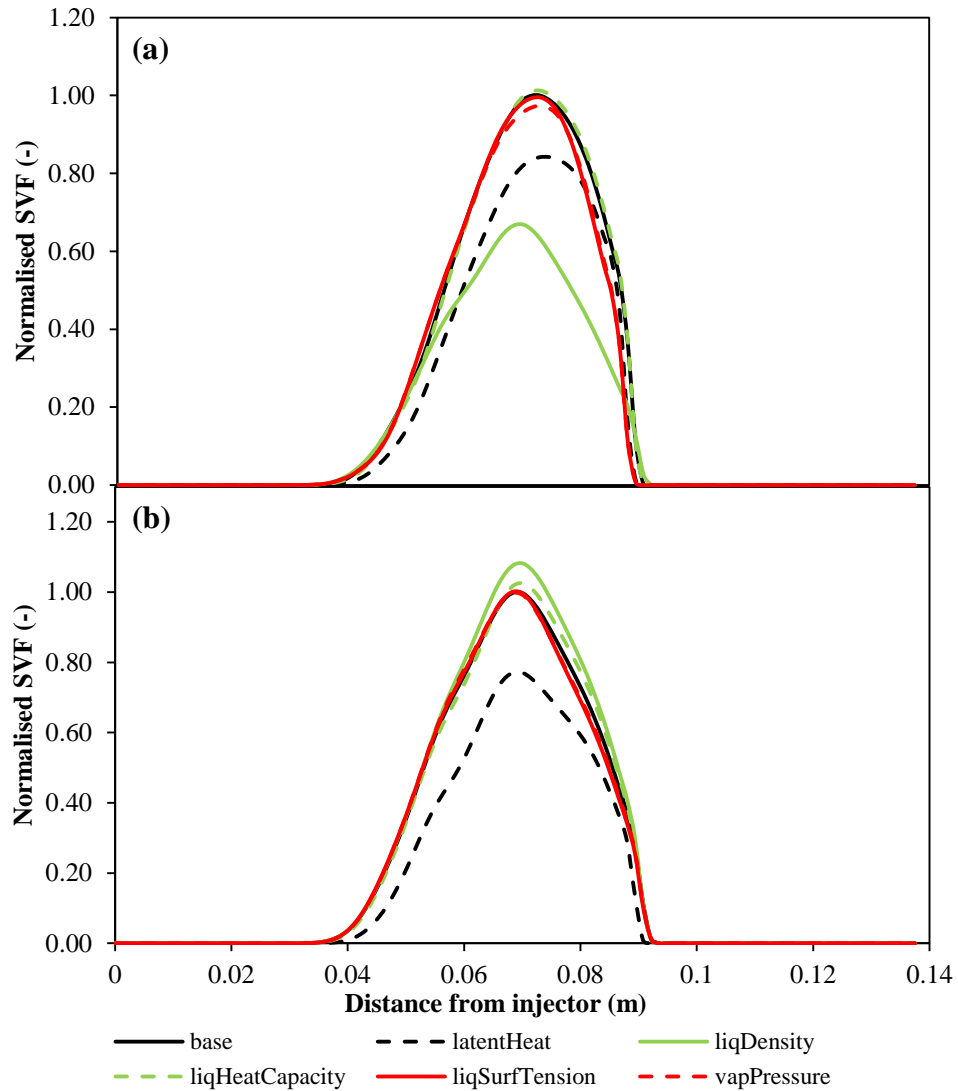
Figure 5.13 Sensitivities of individual thermo-physical property of (a) SME and (b) CME under reacting spray on the predicted normalised SVF.

In terms of the SVF prediction as shown in Figure 5.13(a) and (b), the normalised SVF peaks for the vapour pressures of CME and SME remain unchanged when compared to those of the baseline cases. This could be attributed to the marginal 0.1% advanced ID periods and 2.1% shortened LOLs, which are insufficient to produce any changes to the soot formed from the nucleation and surface growth processes. Meanwhile, greater deviation in the spray prediction is found as the unsaturation level is increased from CME to SME. Based on Figure A.2(a) in Appendix A, the evaluated vapour pressures for SME are about 1 order less than those of the CME. These values

indicate that higher volatility than CME is expected for SME, when the vapour pressures are replaced by those of the diesel fuel. Therefore, larger RPD is obtained when the vapour pressures of SME are replaced, as compared to that of the CME.

Here, the influences of liquid surface tension and liquid viscosity on the development of spray are interrelated, where both properties behave in contrary [210]. As seen in Figure 5.4, the effect of liquid viscosity is relatively marginal as compared to that of the liquid surface tension. The average value of diesel liquid viscosities at 26.7 μPa s, which is approximately 2 orders lower than those of the CME and SME, is particularly small. Thus, the substitution of this fuel property does not produce any effect to the spray development. On the contrary, the impact of liquid surface tension on the spray development is more prominent, where the LPL and SMD are under-predicted by 7.1% and 20.5%, respectively, as seen in Figures 5.4, 5.5 and 5.7. Comparing the predicted results between CME and SME, it is clear that the influence of liquid surface tension rises as the unsaturation level is increased. This is because the predicted values of liquid surface tension for CME are closer to those of the diesel fuel than the liquid surface tensions of SME are, at temperatures beyond 480 K. The lower values of liquid surface tension from diesel thus allow less tension on the droplet surfaces, and hence fuel droplets are easily atomised. For this reason, the fuel evaporation is improved as illustrated in Figures 5.8 and 5.9. In terms of the ID period and LOL, the substitution of liquid surface tension reduces the predictions by 0.2% and 4.2%, respectively as compared to those of the baseline case. However, these predictions cannot influence the soot development, where the normalised SVF peak and soot distribution predicted for liquid surface tension are identical to those of the baseline case as displayed in Figure 5.13(a) and (b).

The replacement of biodiesel liquid heat capacities to those of the diesel fuel gives rise to an increased LPL prediction when compared to that of the baseline case, as seen in Figures 5.4 and 5.5. This is because the liquid heat capacities of diesel are 29.2% higher than those of the biodiesel, where larger

amount of heat is required to break up the fuel droplets. In addition, the unchanged SMDs shown in Figure 5.7(a) and (b) further restrict the atomisation and breakup processes to transform fuel droplets into gaseous particles. This is also evident with the lower fuel evaporation ratio and higher mixture fraction as compared to those of the baseline case, as seen in Figures 5.8 and 5.9. Since the liquid heat capacities predicted for CME and SME are almost identical, the substitution of this fuel property to that of the diesel fuel therefore induces identical RPDs in the predictions of LPL, ID and LOL. Here, the ID periods and LOLs for both fuels are extended with maximum RPD of 1.2% and 2.1%, respectively. Furthermore, the subsequent soot formation is also affected, where marginal increments in the normalised SVF peak of 3.0% and 1.0% are observed for CME and SME, respectively as illustrated in Figure 5.13(a) and (b).

Figure 5.1(b) displays the evaluated liquid densities for diesel and biodiesel, where the liquid densities of diesel are 37.0% lower than those of CME and SME. When the liquid densities of biodiesel are substituted by those of diesel, fuel droplets with smaller SMD are produced, particularly before 0.02 ms as seen in Figure 5.7(a) and (b). The decrease in SMD leads to higher surface to volume ratio and thus the penetration of liquid fuel is lowered. The subsequent fuel evaporation is promoted because of the smaller fuel droplets produced, as evident in Figures 5.8 and 5.9. In the reacting spray analysis, the predicted ID period and LOL with the substitution of liquid density are subjected to an increase of 1.8% and 2.1% for SME. For CME, the ID period remains identical to that of baseline case, while the LOL is in contrast to that of SME as a shortened length of 31.5 mm is obtained. Here, the SVF distributions predicted for the liquid densities of CME and SME are entirely different. The liquid density of CME displays an 8.0% increase in the normalised SVF peak as well as an expanded soot area when compared to those of baseline case, as seen in Figure 5.13(b). On the contrary, lower normalised SVF peak of 33.1% and reduced soot area are obtained when comparing the prediction for SME liquid density to that of the baseline case, as seen in Figure 5.13(a). These

results evidently prove that liquid density is sensitive to the saturation and unsaturation levels.

For the remaining thermo-physical properties which include liquid thermal conductivity, vapour viscosity, vapour thermal conductivity, vapour diffusivity, vapour heat capacity and second virial coefficient, the predicted LPLs in non-reacting and reacting sprays are identical to those of their respective baseline cases, as seen in Figure 5.4. Similarly, the effects of these fuel properties are also marginal based on the predictions of the ID period and LOL as illustrated in Figures 5.11 and 5.12, where a maximum deviation of only 0.06% is recorded for the ID periods, whilst the LOLs are identical to that of the baseline case. These results suggest that the vapour thermo-physical properties are insignificant to the spray development. This is because the vapour properties take place after the fuel droplets are transformed to gaseous particles through the processes of spray breakup and mixing.

5.5   Concluding Remarks

A total of 15 thermo-physical properties which include the critical properties, liquid properties and vapour properties, are evaluated for each CME and SME. The thermo-physical properties have been successfully embedded into the fuel properties library of OpenFOAM. In order to examine the significance of these properties, sensitivity analyses using non-reacting and reacting sprays were performed. Based on the analyses, 5 significant thermo-physical properties including latent heat of vaporisation, liquid density, liquid heat capacity, liquid surface tension and vapour pressure were identified. Among the identified thermo-physical properties for both CME and SME, latent heat of vaporisation gives the largest deviations of 35.0% in LPL, 12.1% in ID period and 8.6% in LOL. The poor mixing predicted for latent heat of vaporisation as indicated by the higher mixture fraction contributes to a 22.8% decreased SVF peak as compared to that of baseline case. Meanwhile, liquid density demonstrates two contrasting effects on the soot concentrations. The SVF peak predicted for

SME is reduced by 33.1%, while the SVF peak for CME is raised by 8.0%. This proves that the effects of thermo-physical properties vary according to unsaturation levels. Despite the varied LPL, ID period and LOL predicted for vapour pressure, liquid heat capacity, liquid surface tension and liquid density, these variations are insufficient to affect the SVF. In the reacting spray analyses, the individual thermo-physical property exhibits identical effects as compared to those of non-reacting spray, although at reduced level of magnitudes. Apart from that, coupled effects among the thermo-physical properties are also discovered, where the effects are combined from the effects of individual thermo-physical property. These results thus show that the individual and coupled effects of the thermo-physical properties are important the development of the fuel spray and soot.

Chapter 6

Development of Reduced Chemical

Kinetic Mechanism for Biodiesel

6.1   Introduction

This chapter reports the development of a generic reduced chemical kinetic mechanism for biodiesel. In the first section, the selection of an appropriate detailed chemical kinetic mechanism for biodiesel is discussed. The following section explains the formulation of reduced chemical kinetic mechanism using 3 reduction techniques, namely DRG, isomer lumping and temperature sensitivity analysis for elementary reactions. Here, the theoretical background of each reduction technique employed is also described. Section 6.4 presents the validations of the formulated reduced mechanism under the conditions of 0D auto-ignition and extinction as well as 2D reacting spray. Besides, this section also includes a comparison study of the developed reduced mechanism against other reduced mechanisms. This is followed by the integration of thermal NO mechanism into the reduced mechanism. In the last section, the main conclusions of this chapter are highlighted.

6.2   Selection of Detailed Chemical Kinetic Mechanism

The detailed chemical kinetic mechanism developed by Herbinet et al. [68] with fuel species of a saturated alkyl ester (MD), an unsaturated alkyl ester (MD9D) and a diesel surrogate component (n-heptane) is selected to describe the combustion kinetics for CME, PME, RME and SME. Here, the carbonyl chain lengths in MD and MD9D are deemed sufficient in emulating the combustion kinetics of biodiesel due to the similar double bond location in MD9D to that of methyl oleate as shown in Figure 2.2(c) in Chapter 2 and also

Figure 6.1(b) [68]. Additionally, MD9D can be used to represent the levels of unsaturation in biodiesel. Here, MD9D is favoured over MD5D although the increased reactivity of MD9D in NTC region contradicted the results reported by Westbrook et al. [81]. This is because the species concentrations predictions of MD9D in JSR are relatively better than those of MD5D, for which the formation of key species such as O_2, CO_2 and C_2H_2 are restricted by the double bond location of MD5D [68]. Besides, the oxidation of MD9D which leads to the formation of MD in the detailed mechanism creates important links between the MD and MD9D species. Meanwhile, the dissociation pathways of MD and MD9D and subsequent species formation such as CO and CO_2 are appropriately retained in the detailed mechanism as these predicted results are validated against the experimental data of RME in a JSR [68]. The kinetic parameters for MD in the detailed mechanism are updated in terms of the activation energy for second H-atom abstraction by OH radicals and reaction kinetic parameters for the addition of radical to O_2 in C=O and activation energy [68]. The reason for these is to further enhance the reactivity level of the detailed mechanism under low temperature [68].
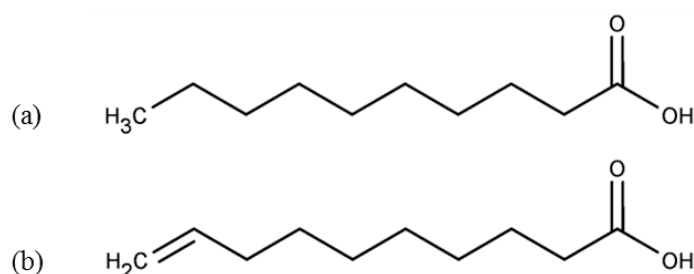
Figure 6.1 Chemical structures of methyl esters in the detailed mechanism of MD, MD9D and n-heptane: (a) MD and (b) MD9D.

Here, the compositions of CME, PME, RME and SME are re-adjusted since the detailed mechanism contained only a saturated ester (MD) and an unsaturated ester (MD9D) each. This is because the carbonyl chain of MD is shorter than those of methyl palmitate and methyl stearate, while MD9D lacks the double bond to represent the unsaturated methyl linoleate and methyl linolenate (with 2 or more double bonds). As such, the saturation and

unsaturation levels of each methyl ester fuel are appropriately represented by the MD and MD9D, respectively. The compositions of CME, PME, RME and SME are grouped into percentages of saturation and unsaturation as tabulated in Table 5.2 of Chapter 5.

6.3 Reduction Methodology of Reduced Biodiesel Chemical Kinetic Mechanism

The reduction process is initiated first with the multi-stage DRG reduction [56] followed by isomer lumping [211], DRG reduction [56] and finally ended with the elimination of unimportant reactions identified using temperature sensitivity analysis. Due to the large number of species and isomers contained in the detailed mechanism, it is therefore essential to commence the reduction process with DRG [56] such that the relations among important species are understood through the species relations calculated by DRG. Besides, Pepiot-Desjardins and Pitsch [212] proved that the order of reduction techniques had only marginal effects on the resulting reduced mechanism although they suggested that isomer lumping should be performed on a pre-reduced mechanism to further limit the mechanism size. This is because Pepiot-Desjardins and Pitsch [212] found that the reduced mechanism developed from multi-stage directed relation graph with error propagation (DRGEP) reduction followed by isomer lumping retained more relevant chemical kinetics of the detailed mechanism, as compared to a reduced mechanism which is first reduced from isomer lumping and then DRGEP.

6.3.1 Reduction Stage I: Revised DRG Calculation

The detailed mechanism of 3299 species and 10806 reactions is first reduced by the revised DRG method [56] with integrated revised depth first search [99], as indicated in Figure 6.2. Species and reactions are removed based on the calculation of importance among species with the mathematical equations shown in Equations 6-1 and 6-2.

$$r_{XY} \equiv \frac{max_i |v_{X,i} \omega_i \delta_{Y,i}|}{max_i |v_{X,i} \omega_i|} \tag{6-1}$$

$$\delta_{Y,i} = \begin{cases} 1 & \text{if the } i\text{th reaction involves species } Y, \\ 0 & \text{otherwise} \end{cases} \tag{6-2}$$

```
┌─────────────────────────────────────┐
│        Detailed Mechanism           │
│  (3299 species and 10806 reactions) │
└─────────────────────────────────────┘
                  │
                  ▼
┌ ─ ─ ─ ─ ─ ─ ─ ─ ─ ─ ─ ─ ─ ─ ─ ─ ─ ─┐
           Revised DRG
└ ─ ─ ─ ─ ─ ─ ─ ─ ─ ─ ─ ─ ─ ─ ─ ─ ─ ─┘
                  │
                  ▼
┌─────────────────────────────────────┐
│        Reduced Mechanism            │
│   (404 species and 1819 reactions)  │
└─────────────────────────────────────┘
                  │
                  ▼
┌ ─ ─ ─ ─ ─ ─ ─ ─ ─ ─ ─ ─ ─ ─ ─ ─ ─ ─┐
           Isomer Lumping
└ ─ ─ ─ ─ ─ ─ ─ ─ ─ ─ ─ ─ ─ ─ ─ ─ ─ ─┘
                  │
                  ▼
┌─────────────────────────────────────┐
│        Reduced Mechanism            │
│   (279 species and 1179 reactions)  │
└─────────────────────────────────────┘
                  │
                  ▼
┌ ─ ─ ─ ─ ─ ─ ─ ─ ─ ─ ─ ─ ─ ─ ─ ─ ─ ─┐
           Revised DRG
└ ─ ─ ─ ─ ─ ─ ─ ─ ─ ─ ─ ─ ─ ─ ─ ─ ─ ─┘
                  │
                  ▼
┌─────────────────────────────────────┐
│        Reduced Mechanism            │
│   (189 species and 844 reactions)   │
└─────────────────────────────────────┘
                  │
                  ▼
┌ ─ ─ ─ ─ ─ ─ ─ ─ ─ ─ ─ ─ ─ ─ ─ ─ ─ ─┐
    Temperature Sensitivity Analysis
└ ─ ─ ─ ─ ─ ─ ─ ─ ─ ─ ─ ─ ─ ─ ─ ─ ─ ─┘
                  │
                  ▼
┌─────────────────────────────────────┐
│    Generic Reduced Mechanism        │
│    (92 species and 360 reactions)   │
└─────────────────────────────────────┘
```
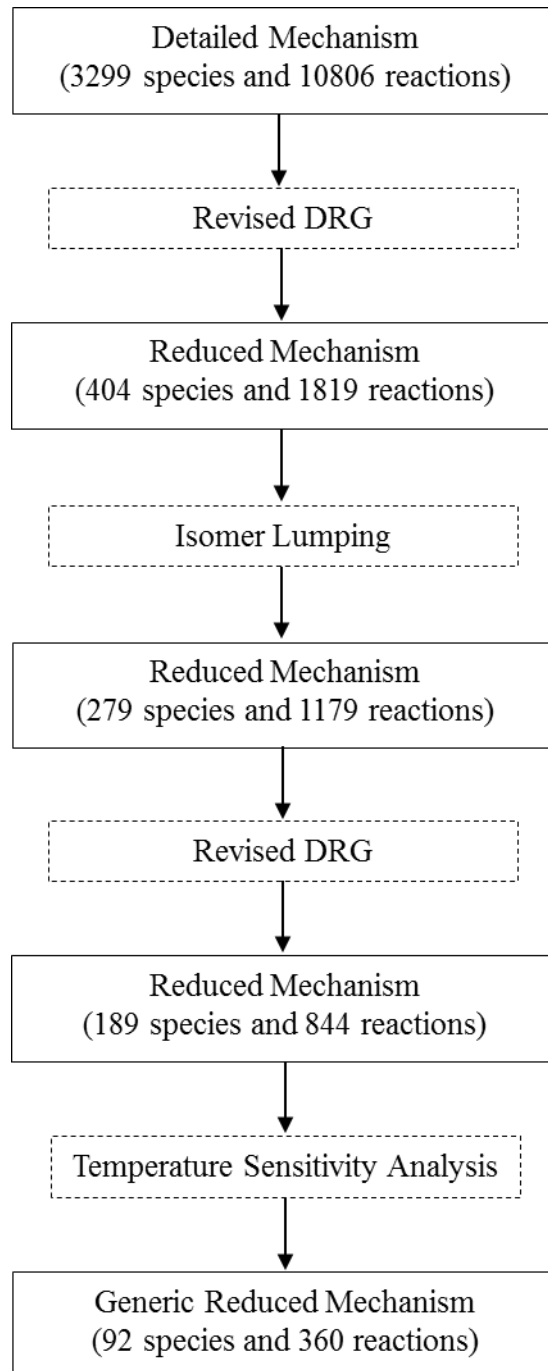
Figure 6.2 Flow chart of the reduction processes and the corresponding reduced mechanism sizes.

The production rates (ω_i) of all validating conditions are included to enhance the accuracy of the DRG calculation. If the dependence ratio (r_{XY}) for a species is more than the user-defined threshold value (ε), this species would need to be retained since large error is induced with its removal, specifically in predicting the auto-ignition process. These calculations are written in MATLAB programming code format as enclosed in Appendix C such that the reduction of the detailed mechanism can be expedited. In order to retain the chemical kinetics comprehensiveness from the original mechanism, key target species including fuel, oxidation and combustion products such as MD, MD9D, C_7H_{16}, nitrogen (N_2), oxygen, hydrogen peroxide (H_2O_2), CO_2 are specified. The reduction process is repeated thrice until no other species could be further removed. This is conducted in line with Lu and Law's [99] suggestion that multi-step DRG reduction is necessary to obtain a further reduced mechanism from a large detailed mechanism. The three-step DRG reduction performed here is also to avoid eliminating important isomers in a single-step process [56]. Besides, large percentage errors are induced in single-step DRG reduction when the mechanism size dropped significantly, as illustrated in Figure 6.3. The selection of ε shown in Figure 6.3 is important as highlighted by Lu and Law [21] to attain optimised accuracy for the reduced mechanism without compromising the mechanism size. Therefore, multi-step reduction using DRG calculation is performed here.
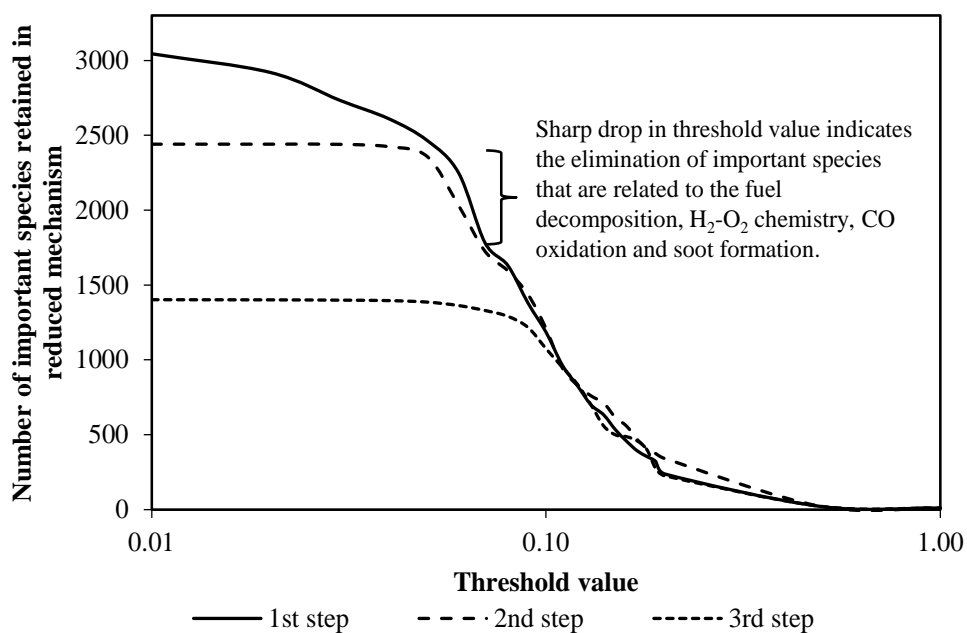
Figure 6.3 Threshold selection values for the three-step DRG reduction.

Maximum allowable percentage errors of 40.0% are specified according to Luo et al. [56] in order to achieve a reduced mechanism with substantially manageable size owing to the large size of the detailed mechanism. The resulting reduced biodiesel mechanism with 404 species and 1819 reactions is validated under the shock tube conditions as presented in Table 6.1, at the initial pressures of 40.0 bar and 60.0 bar.

Table 6.1 Initial conditions for 0D closed homogeneous reactor and PSR.

Parameter	Range
Pressure (bar)	10.1^a, 13.5^b, 15.0^c, 40.0^b, 60.0^b
Equivalence ratio, φ (-)	0.5, 1.0, 1.5
Temperature (K)	650-1350 (increment of 100 K)

[a] JSR conditions defined based on the experiment by Dagaut et al. [18].

[b] Shock tube conditions defined for the predictions of detailed and reduced mechanisms.

[c] Shock tube conditions defined based on the experiment by Wang et al. [74].

6.3.2 Reduction Stage II: Isomer Lumping

To further eliminate the remaining species, isomer lumping is performed. All isomers with common compositions and thermodynamic data [211] are lumped into a single representative isomer. The main reaction pathway as illustrated in Figure 6.4 is analysed using CHEMKIN-PRO. This served as a guide to ensure oxidation pathways between important species are retained. Besides, the selection of representative isomers is also important to maintain the oxidation comprehensiveness from the detailed mechanism. For example, MD9D is first dissociated to 9 different isomers at the point of ignition as depicted in Figure 6.4. However, MD9D6J is the representative isomer amongst other isomers based on the ROP for each isomer enclosed in the parentheses. Subsequently, MD9D6J is substituted into reactions that involved the remaining 8 isomers. Similarly, this process is repeated for the other species and isomers. A total of 125 species and 640 reactions are removed during the process and resulted in a reduced biodiesel mechanism with 279 species and 1179 reactions. The grouped isomers and represented are tabulated in Table D.1, Appendix D.
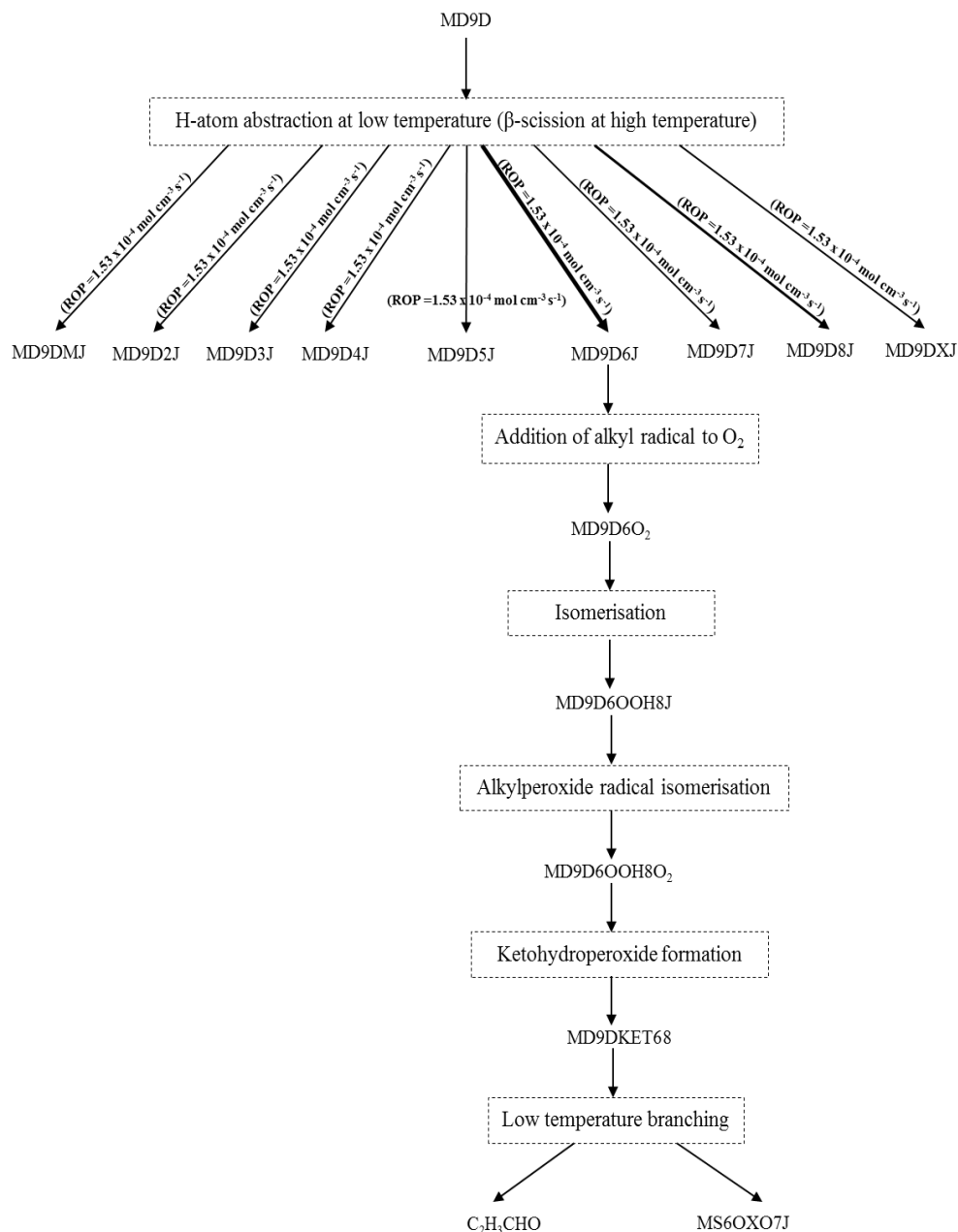
Figure 6.4 Main oxidation pathway of MD9D.

6.3.3   Reduction Stage III: Revised DRG Calculation

Since the original reaction pathways among species are removed when most of the species are lumped in the isomer lumping stage, a two-step DRG reduction is conducted using Equations 6-1 and 6-2 to eliminate newly induced unimportant species. Here, additional target species such as CO, OH, hydroperoxyl (HO_2), C_2H_2, ethylene (C_2H_4) are specified such that the original

fuel oxidation and soot formation pathways are preserved. This is because the relations among the remaining species became stronger due to the removal of unimportant interconnecting species and shortened reaction pathways. Consequently, a reduced mechanism with 189 species and 844 reactions is produced.

6.3.4 Reduction Stage IV: Temperature Sensitivity Analysis for Elementary Reactions

A temperature sensitivity analysis is performed to distinguish insignificant elementary reactions for further elimination. The analysis, aided with CHEMKIN-PRO is taken at the point of ignition for all the initial temperatures from 650 K to 1350 K, in an interval of 100 K. Normalised sensitivity coefficient for each reaction as shown in Equation 6-3 is calculated, where reactions with coefficient values lower than a user-defined threshold (ε) are eliminated. The final reduced chemical kinetic mechanism is made up of 92 species and 360 reactions, with a total reduction of more than 97.0% in species size achieved in comparisons to that of the detailed mechanism.

$$\text{Normalised individual temperature sensitivity coefficient}$$
$$= \frac{\text{Absolute individual temperature sensitivity coefficient}}{\text{Maximum temperature sensitivity coefficient}}$$

$$(6-3)$$

6.3.5 Optimisation of Arrhenius Rate Constants

In the development of the reduced mechanism, the skeletal models are typically optimised such that the influence of eliminated reactions is included in the Arrhenius rate constants of the retained reactions [51,53]. For instance, Brakora et al. [51] and Mohamed Ismail et al. [53] separately adjusted the Arrhenius rate constants in their reduced MB mechanisms in order to replicate

the ID periods obtained from the detailed mechanism predictions and experimental measurements. Here, the optimisation of Arrhenius rate constants is conducted due to the elimination of isomers. Since the biodiesel oxidation pathway varied according to the largest ester composition (MD, MD9D), a sensitivity analysis is performed to determine significant elementary reactions for the optimisation of rate constants. This is to satisfy the auto-ignition and extinction features for all the biodiesel fuels tested here. Based on the analysis, the oxidation reactions for fuel species, MD and MD9D are found to be the most reactive. Thus, the optimisation of Arrhenius rate constants is strictly limited to the oxidation reactions of the fuel species as shown in Table 6.2. Individual and collective effects of the adjusted Arrhenius rate constants on the ID period predictions for both CME and SME (with two contrasting unsaturation levels) are presented in Table 6.2. Although the adjustment of individual rate constant caused deterioration in the predicted ID periods as seen in Figures 6.5, 6.6 and E.1, E.2 in Appendix E, the practice is retained since the collective effect improved the overall ID period predictions. The final reduced mechanism, with the optimisation of Arrhenius rate constants is provided in Table F.1 of Appendix F.

Table 6.2 Optimised Arrhenius rate constants for the MDBio-Nottingham mechanism.

No.	Reactions	Remarks	A (mol cm s K)	b	E_a (cal mol^{-1})	Individual effects on ID periods		Collective effects on ID periods[a]	
						CME	SME	CME	SME
1	md+ho2=md6j+h2o2	Original	5.880E+04	2.50	14860.0	Improvement in all temperature regions	Improvement in NTC region, deterioration in low-temperature and high-temperature regions	-	-
		Adjusted	5.880E+06	2.50	14860.0				
2	md+oh=md6j+h2o	Original	4.670E+07	1.61	-35.0	Improvement in NTC region[b], deterioration in low-temperature and high-temperature regions	Deterioration in low-temperature and NTC regions	Improvement in NTC and high-temperature regions, deterioration in low-temperature region	Improvement in high-temperature region, deterioration in low-temperature and NTC regions
		Adjusted	4.670E+08	1.61	-35.0				
3	md9d+oh=md9d6j+h2o	Original	4.670E+07	1.61	-35.0	Improvement in all the temperature regions	Improvement in NTC and high-temperature regions, deterioration in low-temperature region	Improvement in low-temperature region, deterioration in NTC region	Improvement in all temperature regions
		Adjusted	4.670E+08	1.61	-35.0				

4	md9d6ooh8o2=md9dket68 +oh	Original	1.250E+10	0.00	17850.0	Deterioration in low-temperature and NTC regions	Deterioration in low-temperature and NTC regions	Deterioration in low-temperature region	Improvement in NTC region, deterioration in low-temperature region
		Adjusted	2.250E+09	0.00	17850.0				
5	md9dket68=oh+c2h3cho +ms6oxo7j	Original	1.050E+16	0.00	41600.0	Improvement in low-temperature region	Deterioration in low-temperature region	Improvement in low-temperature region	Improvement in low-temperature region
		Adjusted	5.050E+16	0.00	41600.0				

[a] For the collective effects, the adjustment of rate constants is performed collectively in the sequence of the reactions number stated in the table. For example, the collective effect of reaction no. 1 to 3 denotes the effects of tuning these 3 reactions together in the reduced mechanism.

[b] Low-temperature region: 650 K to 850 K; NTC region: 850 K to 1050 K; high-temperature region: 1050 K to 1350 K.
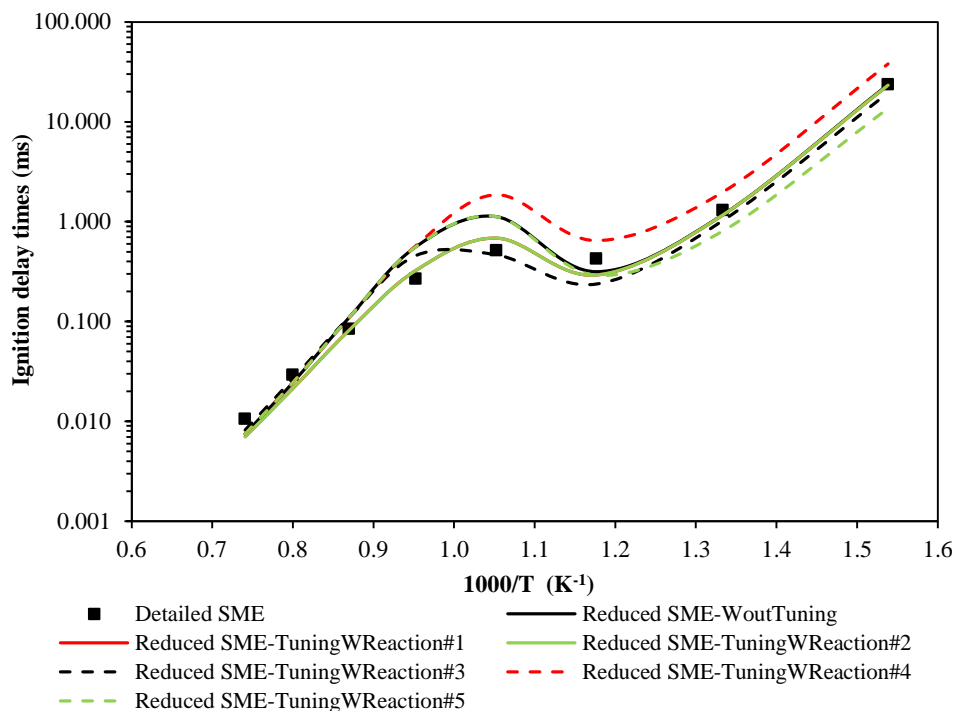
Figure 6.5 Predicted ID periods for the detailed and reduced mechanisms of SME at an initial pressure of 40.0 bar and equivalence ratio of 1.0, with adjustment to individual Arrhenius rate constants.
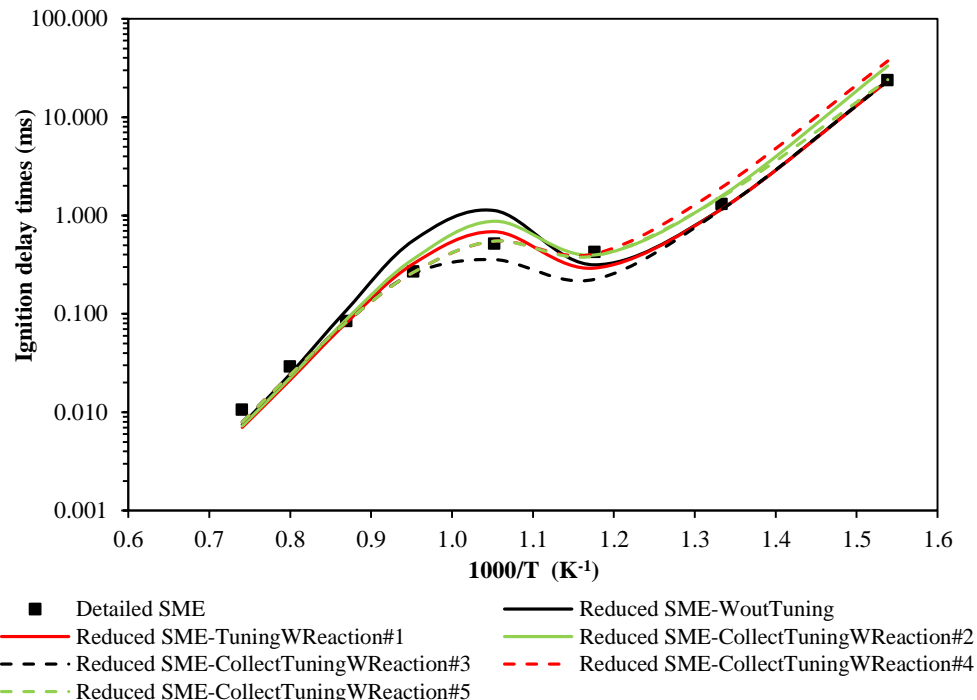
Figure 6.6 Predicted ID periods for the detailed and reduced mechanisms of SME at an initial pressure of 40.0 bar and equivalence ratio of 1.0, with adjustment to collective Arrhenius rate constants.

6.4 Validation of Reduced Biodiesel Chemical Kinetic Mechanism

6.4.1 Kinetic Modelling

Closed Homogenous Reactor

The shock tube initial conditions as tabulated in Table 6.1 are specified since these initial conditions represented the typical in-cylinder diesel engine conditions. Higher initial pressures of 40.0 bar and 60.0 bar are modelled to re-produce the typical initial pressures inside a diesel engine at the start of the main injection. ID periods are defined as the interval for air-fuel mixture to increase its initial temperature by 400 K [51]. The predicted ID periods of SME by the reduced mechanism are validated at each reduction step against those of the detailed mechanism, with the comparison based on the final reduced mechanism as illustrated in Figure 6.7. This is to ensure that the maximum deviations for predicted ID periods of the reduced mechanism are limited to no more than 40.0%. Similar process is performed for CME, PME and RME in order to obtain good level of accuracy in the final predicted ID periods, as presented in Figures E.3 to E.5 in Appendix E. For extended validations, the developed reduced mechanism is examined under 24 additional shock tube conditions at low pressure of 13.5 bar. The initial pressure of 13.5 bar is chosen to emulate the initial in-cylinder pressure when the pilot injection is delivered. The largest percentage errors are 45.0%, as shown in Figures 6.7 and E.3 to E.5 for CME, PME, RME and SME, respectively.
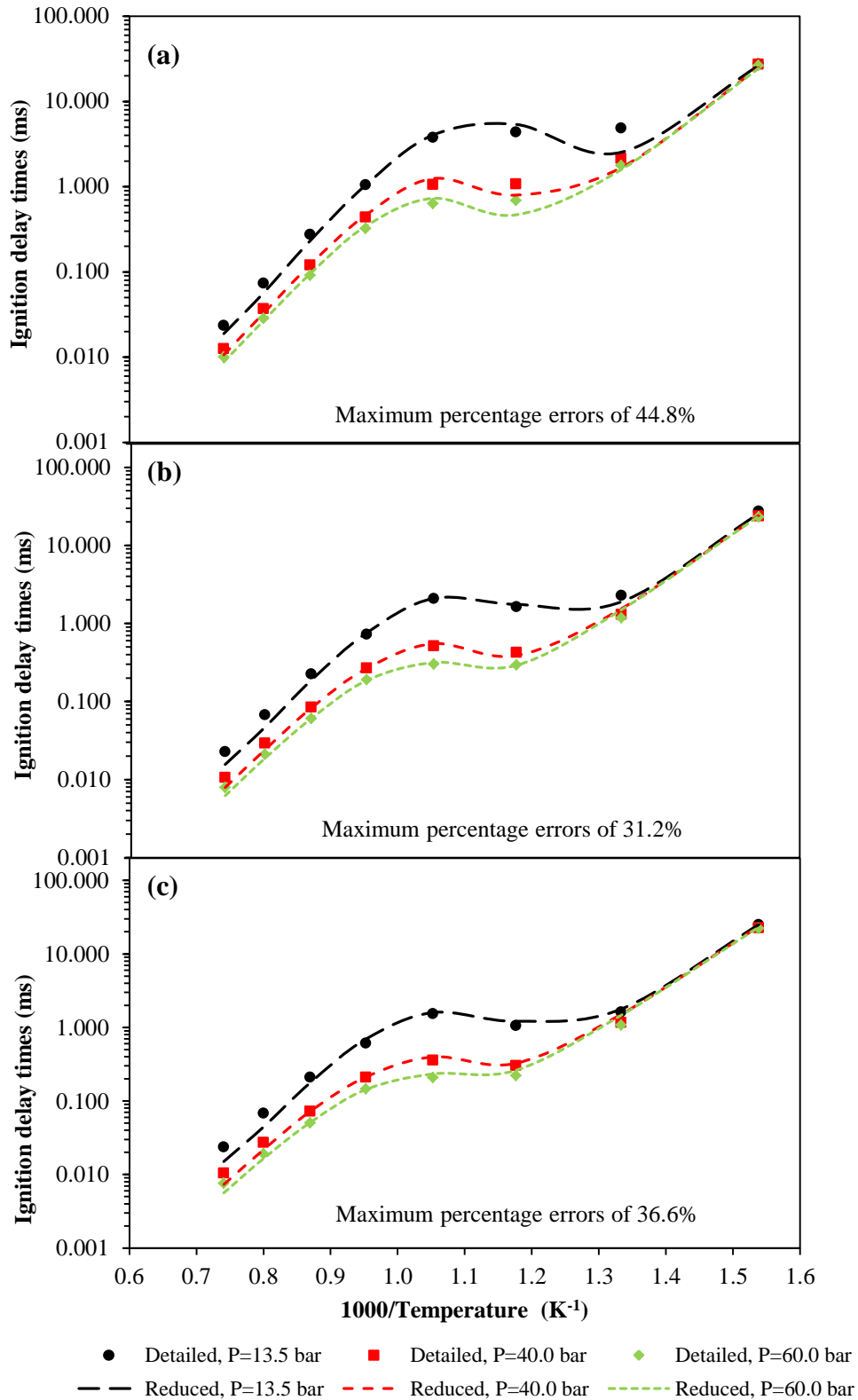
Figure 6.7 Predicted ID periods for the detailed and reduced mechanisms of SME at initial pressures of 13.5 bar, 40.0 bar and 60.0 bar, with equivalence ratios of (a) 0.5, (b) 1.0 and (c) 1.5.

Additionally, the reduced mechanism is further validated against the shock tube auto-ignition measurements of MD [74]. As seen in Figure 6.8, the reduced mechanism is able to reproduce the ID periods at both low-temperature and high-temperature regions although a maximum deviation of 67.0% is recorded in the NTC region. Here, the predicted ID periods for the pressure of 13.5 bar are the longest, followed by those of 15.0 bar, 40.0 bar and 60.0 bar. The increase in initial pressures contributes to faster chain branching and propagations, as well as species oxidation which culminates in advanced ID periods at elevated initial pressures. Additionally, a significant reduction in computational time of approximately 30.0% is also observed. The detailed chemical kinetic mechanism used around 5 hours in serial processing for a complete case with 8 shock tube conditions, while the reduced mechanisms required only 10 minutes.

Apart from the validations for neat biodiesel fuels, the ID periods of biodiesel-diesel blends predicted by the reduced mechanism are also validated against those of the detailed mechanism. The validations for biodiesel-diesel blends are maintained at initial pressures of 40.0 bar and 60.0 bar. The main motivation for extending the validation to include fuel blends is to examine the fidelity and robustness of the reduced mechanism. The highest blend level that can be achieved within the maximum percentage errors of 40.0% is B50 (50.0% biodiesel and 50.0% diesel). These reported results are identical for all the SME, CME, PME and RME, as shown in Figures 6.9 and E.6 to E.8. Based on Table 6.3, the predicted ID periods for biodiesel-diesel blends are delayed by a maximum of 68.8% as compared to those of neat biodiesel fuels, particularly at temperatures above 850 K. This is resulted by the kinetics effects of C_7H_{16} since the cetane number (CN) of diesel is lower than that of the biodiesel fuel [213].
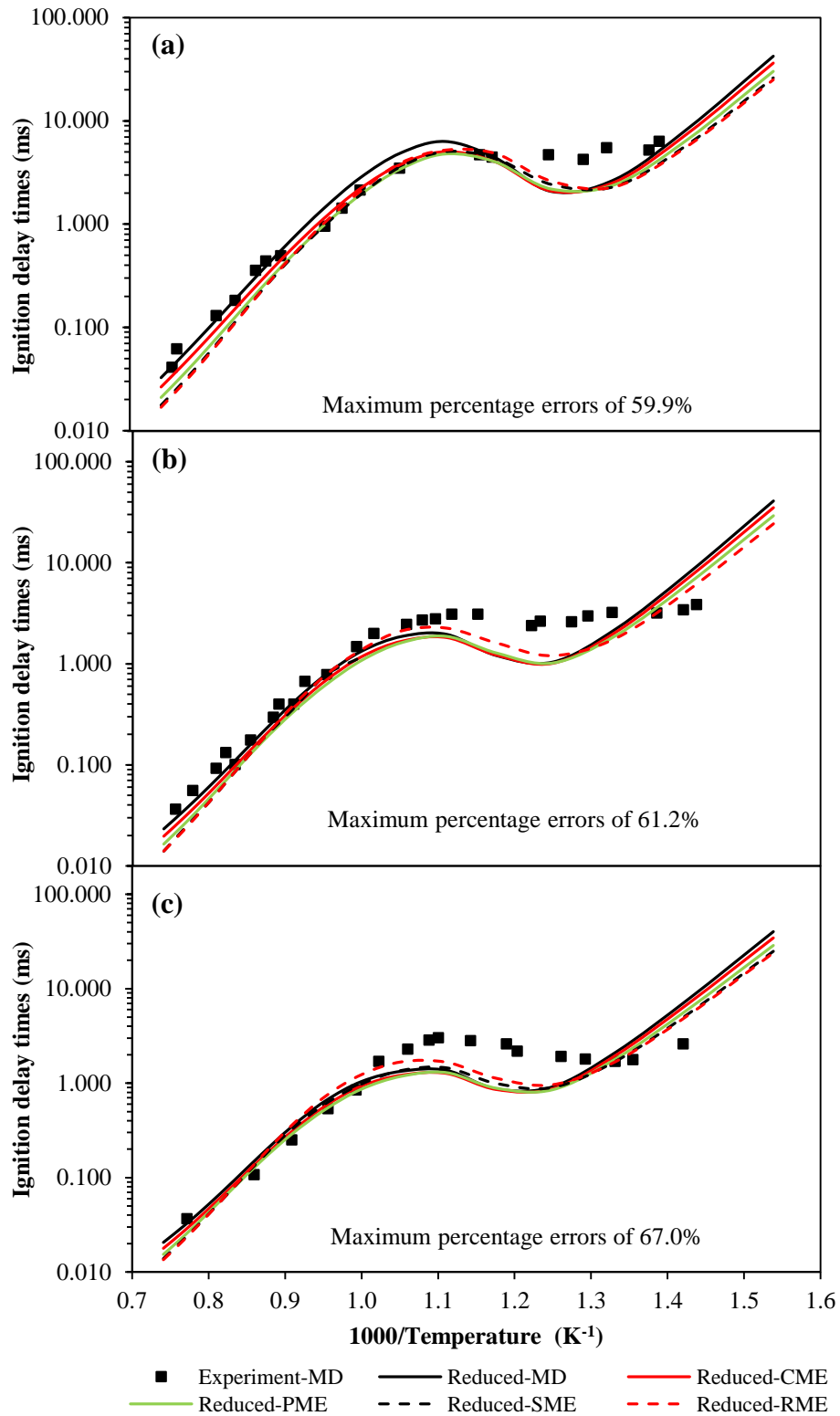
Figure 6.8 Predicted ID periods for the reduced mechanisms of MD, CME, PME, SME and RME against the experimental measurements of MD auto-ignition process under shock tube conditions [74], at an initial pressure of 15.0 bar and with equivalence ratios of (a) 0.5, (b) 1.0 and (c) 1.5.
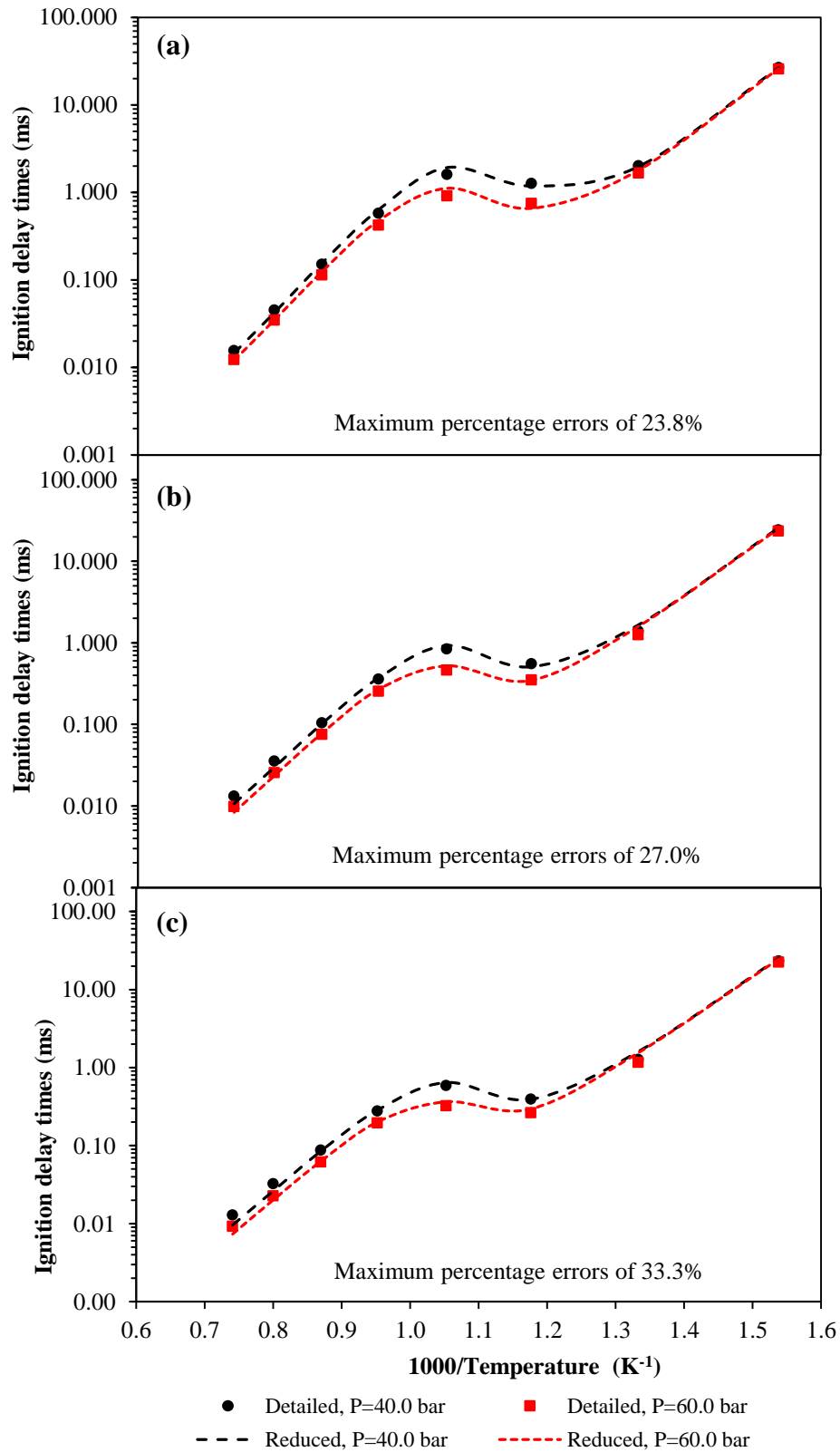
**Figure 6.9 Predicted ID periods for the detailed and reduced mechanisms of B50 SME at initial pressures of 40.0 bar and 60.0 bar, with equivalence ratios of (a) 0.5, (b) 1.0 and (c) 1.5.**

In general, there exist observable changes in the ID periods due to the variations of fuel compositions as shown in Table 6.3. The ID periods decrease when the unsaturation levels are increased, except for temperatures between 950 K and 1150 K. This discrepancy might be caused by the adjustment of rate constants as discussed in Section 6.3.5, where the purpose is to retain the ID periods with percentage errors of less than 40.0%. Based on Table 6.3, the ID periods of RME with the largest unsaturation levels of 90.0% are shown to be the shortest. This is followed by the ID periods of SME, PME and CME. This observation implies that MD9D oxidises faster than MD, the main oxidation fuel species for CME and PME. The higher reactivity level of MD9D is caused by the double bond location since equivalent activation energies for both MD and MD9D are observed in the detailed mechanism. This is because the location of double bond at the end of the MD9D chain promotes higher possibility of chain branching [68]. Therefore, shorter ID periods are produced, which is an observation similar to that reported by Herbinet et al. [68] and Brakora and Reitz [80]. These results indicate that the ID periods for biodiesel chemical kinetic mechanism is considerably affected by the location of double bond.

Table 6.3 Predicted ID periods for the reduced mechanism of B100 and B50 of CME, PME, RME and SME at an initial pressure of 40.0 bar and equivalence ratio of 0.5.

Temperature	Predicted ID periods (ms)							
(K)	CME		PME		RME		SME	
	B100	B50	B100	B50	B100	B50	B100	B50
650.0	34.281	35.633	28.652	30.398	23.936	26.791	24.897	25.848
750.0	1.953	2.261	1.797	2.111	1.637	1.981	1.672	1.942
850.0	0.730	1.216	0.746	1.203	0.841	1.181	0.797	1.175
950.0	1.148	1.554	1.119	1.648	1.340	1.924	1.246	2.103
1050.0	0.487	0.600	0.440	0.586	0.511	0.635	0.463	0.687
1150.0	0.139	0.191	0.122	0.157	0.120	0.156	0.121	0.159
1250.0	0.042	0.053	0.036	0.046	0.032	0.042	0.033	0.042
1350.0	0.015	0.020	0.012	0.017	0.010	0.015	0.011	0.014

PSR

An additional reactor model, PSR is included in the 0D kinetic modelling to simulate the steady-state extinction process of the reduced mechanism in spite of the importance of the local extinction process during the combustion process. This is to ensure the extinction features are retained in the 92-species reduced biodiesel mechanism apart from auto-ignition since the residence time is the only variable parameter in PSR [214]. Equivalent operating conditions to the JSR experiment performed by Dagaut et al. [18] are defined accordingly in PSR as the extinction process in 0D modelling resembles the EVO of diesel engine. In order to model the extinction process, the steady-state extinction region which is the upper region as indicated in Figure 6.10 is selected. According to Shan and Lu [214], this steady-state region is to eliminate the time involved in solving the unsteadiness of flame after the ignition state as shown in Figure 6.10. The importance of residence time is highlighted by Oh et al. [215] before, where shorter residence time denotes that the flame in a reactor is more readily extinguished. The auto-ignition temperature profiles predicted for the detailed and reduced mechanisms, which emulated the regions shown in Figure 6.10, are used to determine the minimum residence time in the PSR model. Here, residence time of 1 s is defined based on Figures 6.11 and E.9 since 1 s is the minimum extinction time for the initial temperatures of 650 K, 950 K and 1350 K to represent low-temperature, NTC and high-temperature regions, respectively.
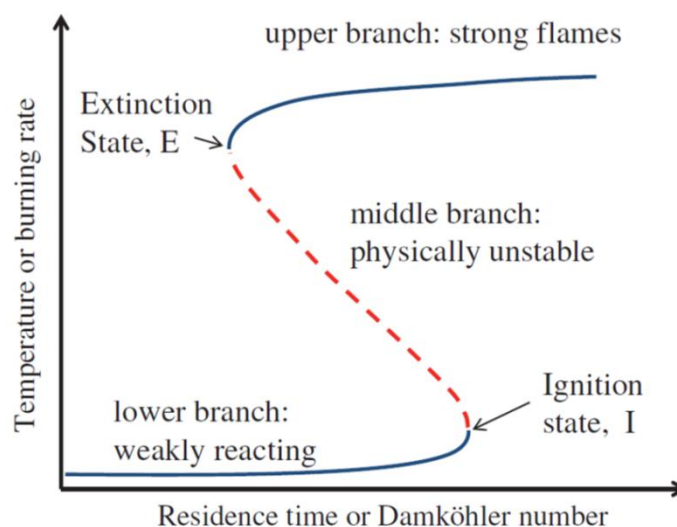
Figure 6.10 Temperature against residence time for complete 0D kinetic combustion modelling (adapted from Shan and Lu [214])**.**
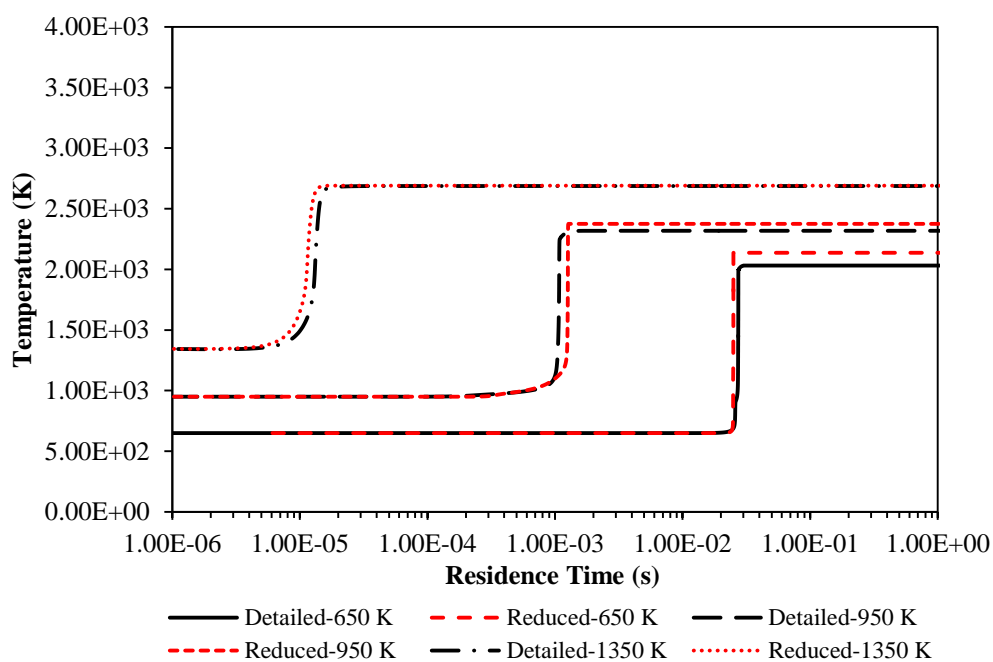
Figure 6.11 Predicted temperatures against residence times for the detailed and reduced mechanisms of SME, with an initial pressure of 40.0 bar, equivalence ratio of 0.5 and initial temperatures of 650 K, 950 K and 1350 K.

The reduced mechanism is validated based on the measured species profiles for RME oxidation under the JSR conditions as shown in Figures 6.12 and 6.13, with identical inlet fuel compositions to those of the experiment and at

146

an initial pressure of 10.1 bar, temperatures of 800 K to 1400 K and equivalence ratio of 1.0 [18]. The predicted profiles of O_2, CO, CO_2 and C_2H_4 by the reduced mechanism are deemed satisfactory despite the under-prediction of 2.5 orders when compared with experimental measurements, as evident in Figures 6.12 and 6.13.
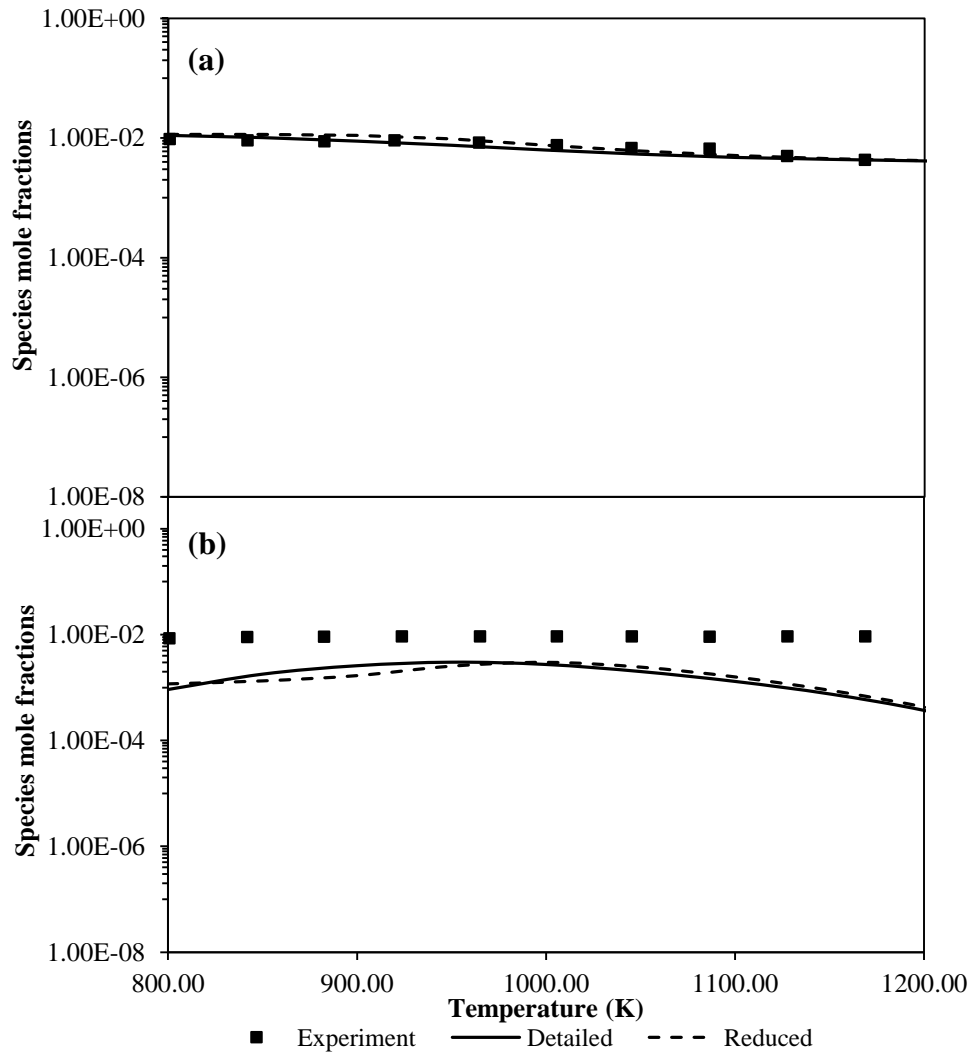
Figure 6.12 Predicted species mole fractions for the detailed and reduced mechanisms of (a) O_2 and (b) CO against experimental measurements [18] under JSR conditions, with an initial pressure of 10.1 bar, equivalence ratio of 1.0 and N_2 dilution of 99.95%.
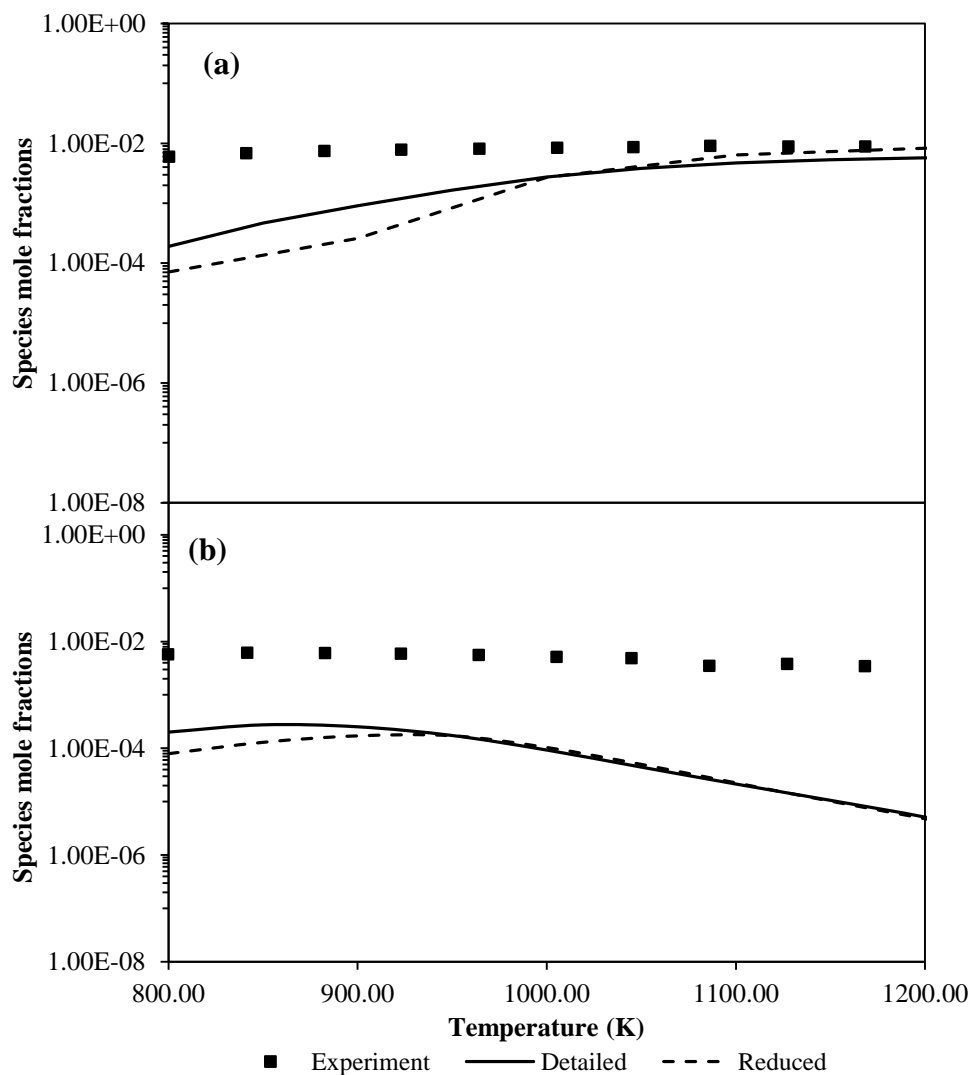
Figure 6.13 Predicted species mole fractions for the detailed and reduced mechanisms of (a) CO_2 and (b) C_2H_4 against experimental measurements [18] under JSR conditions, with an initial pressure of 10.1 bar, equivalence ratio of 1.0 and nitrogen dilution of 99.95%.

For the tested biodiesel fuels, the compositions of MD with 0.05% mole fraction are adjusted according to the saturation and unsaturation levels of each fuel. As shown in Figures 6.14, 6.15, E.10 and E.11, the capability of the generic 92-species reduced mechanism is proven here where important oxidation and soot formation species such as OH, H_2O_2, HO_2, O_2, C_2H_2 and C_2H_4 are predicted satisfactorily, with deviation of less than 1 order. Similarly, MD and MD9D fuel species as well as the formation of CO and CO_2 are also well predicted.
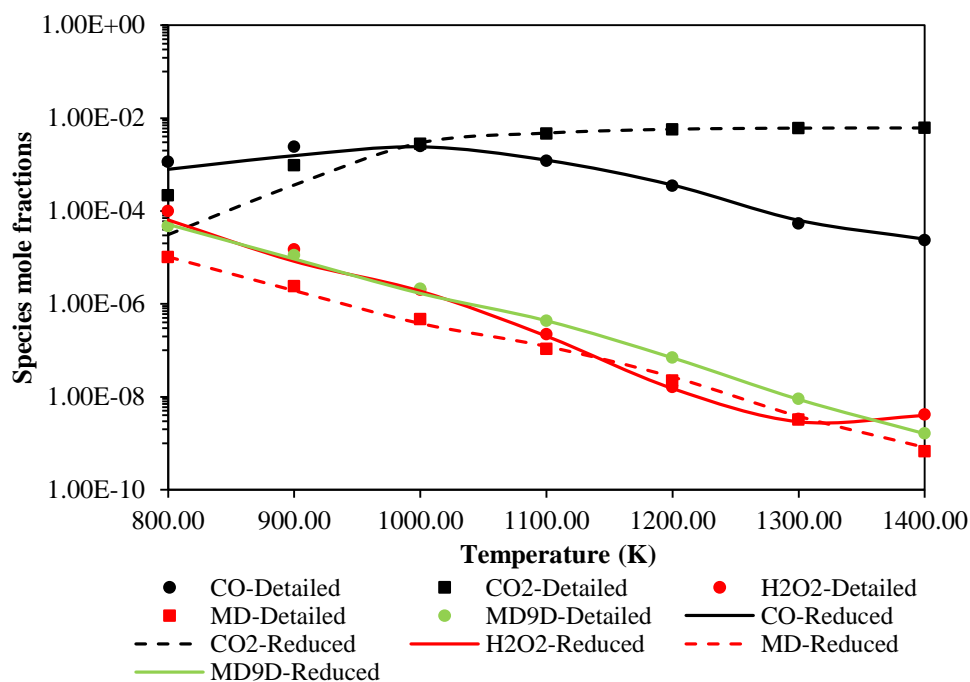
Figure 6.14 Predicted mole fractions of CO, CO$_2$, H$_2$O$_2$, MD and MD9D under JSR conditions for the detailed and reduced mechanisms of SME, with an initial pressure of 10.1 bar, equivalence ratio of 1.0 and nitrogen dilution of 99.95% [18].

Low calculated C$_2$H$_2$ and C$_2$H$_4$ concentrations as observed in Figures 6.15 and E.11, especially at temperatures between 800 K and 1000 K, are in line to the predictions by Luo et al. [52]. Here, the validation of calculated C$_2$H$_2$ and C$_2$H$_4$ mole fractions cannot be solely based on the comparison with those of the detailed mechanism. This is because certain reactions in the detailed mechanism are assumed to decompose into smaller species such as C$_2$H$_2$, CO and methane (CH$_4$) by a single global reaction, as explained by Herbinet et al. [68]. This has a direct impact on the prediction of C$_2$H$_2$ and C$_2$H$_4$ by the detailed mechanism, where over-predictions for C$_2$H$_2$ and C$_2$H$_4$ species at equivalence ratio of 0.5 and temperatures between 800 K and 1100 K are observed by Herbinet et al. [68] when compared to those of the experimental measurements.
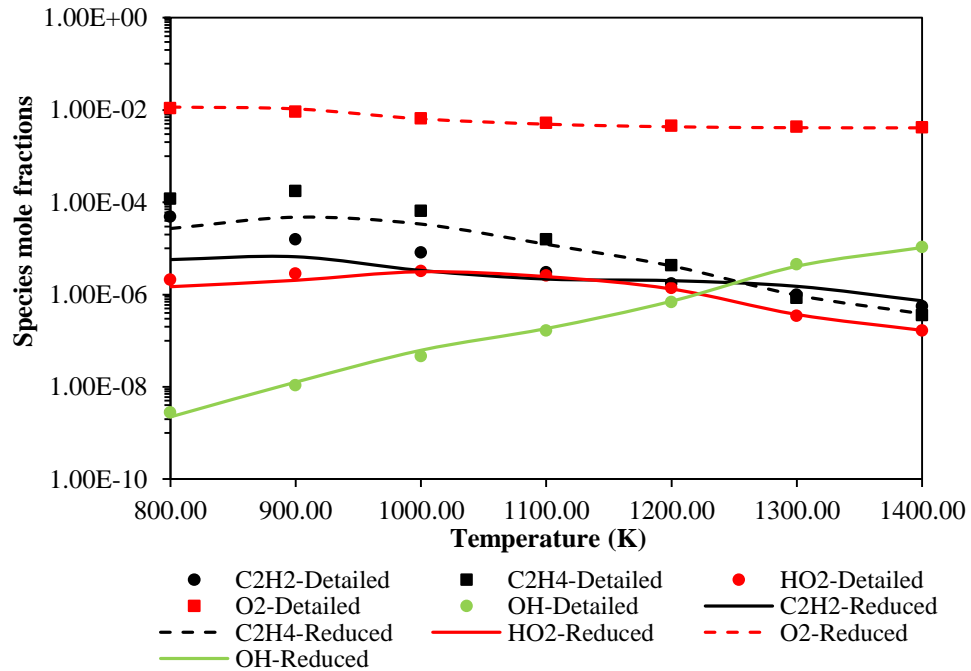
Figure 6.15 Predicted mole fractions of C_2H_2, C_2H_4, HO_2, O_2 and OH under JSR conditions for the detailed and reduced mechanisms of SME, with an initial pressure of 10.1 bar, equivalence ratio of 1.0 and nitrogen dilution of 99.95% [18].

6.4.2 Reacting Spray Modelling

In order to further validate the reduced mechanism (which is hereafter denoted as MDBio-Nottingham), the mechanism is integrated into 2D modelling of reacting spray. The simulations are conducted under diesel engine-like conditions, at initial temperatures of 900 K and 1000 K, with a density value of 22.8 kg m^{-3}. In the first sub-section, the MDBio-Nottingham mechanism is validated against the experimental measurements. The following sub-section reports the comparison study of the MDBio-Nottingham mechanism against other reduced mechanisms available in the literature.

MDBio-Nottingham Mechanism

The predicted LPLs for SME as depicted in Figure 6.16 are vital indicators for combustion efficiency, where over-penetration results in spray wall impingement while under-penetration causes under-utilisation of the ambient air [188]. Although the reduced mechanism is also validated for CME, PME and RME using the quantitative case settings of SME, only numerical results for SME are reported here based on the availability of experimental data.
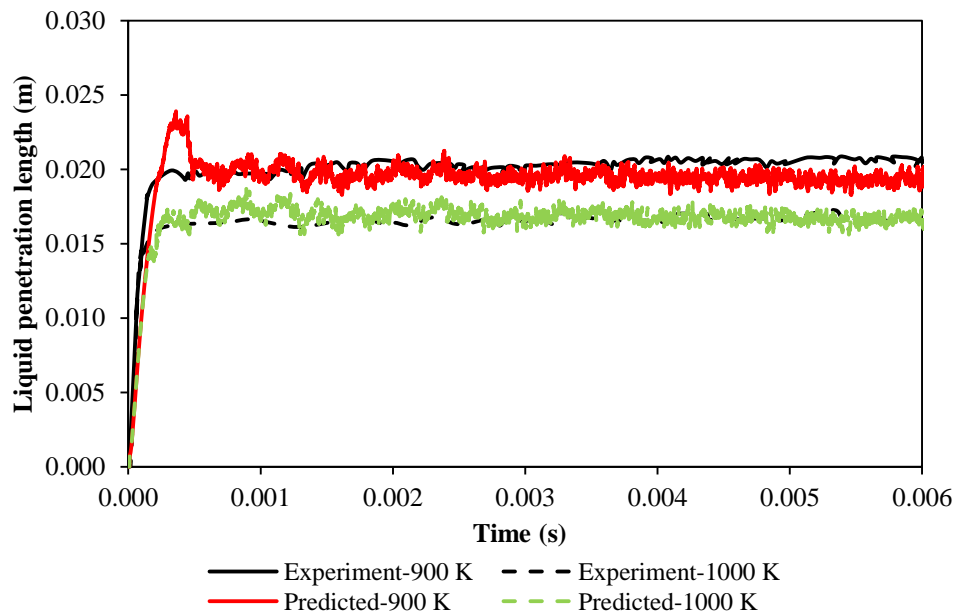
Figure 6.16 Predicted and measured [36] LPLs for SME reacting spray, at initial temperatures of 900 K and 1000 K.

The calculated ID periods and LOLs for SME are validated against the experimental measurements, as shown in Table 6.4 and Figure 6.17. The predicted ID period for SME with a value of 0.658 ms is advanced by 7.2% as compared to that of experimental measurement. Meanwhile, the predicted LOL of 30.78 mm for SME, defined by the vertical dashed line in Figure 6.17 is over-predicted by 17.6%. At an initial temperature of 1000 K, the reduced mechanism over-predicts the ID period by 34.8%, while the LOL is extended by 37.2%. Shorter ID period and LOL at the initial temperature of 1000 K are observed as compared to those at 900 K because of the enhanced spray atomisation and break-up as the initial temperature rises.

Table 6.4 Validations of predicted ID period and LOL against experimental measurements [36] at initial temperatures of 900 K and 1000 K, with a density of 22.8 kg m^{-3}.

Initial temperature (K)	Parameter	Measured	Predictions by reduced mechanisms		
			MDBio-Nottingham	UCONN-Luo	ERC-Brakora
900	ID period (ms)	0.709	0.658	0.586	0.670
	Percentage error (%)	-	-7.2	-17.4	-5.4
	LOL (mm)	26.18	30.78	34.47	29.67
	Percentage error (%)	-	+17.6	+31.7	+13.3
1000	ID period (ms)	0.377	0.508	0.433	0.534
	Percentage error (%)	-	+34.8	+14.8	+41.5
	LOL (mm)	17.27	23.70	24.77	21.15
	Percentage error (%)	-	+37.2	+43.4	+22.5
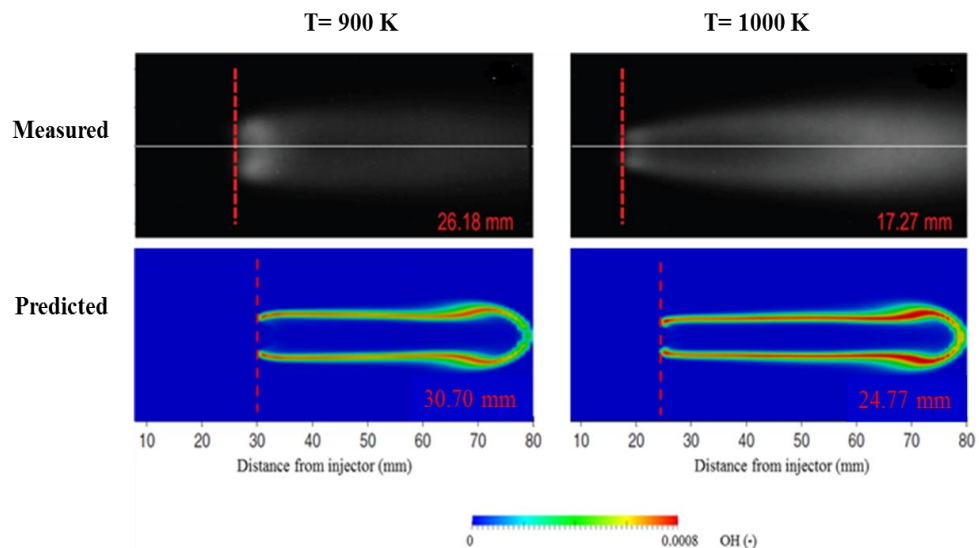
Figure 6.17 Comparisons of measured OH chemiluminescence (adapted from Nerva et al. [36]) and predicted OH mass fractions, at initial temperatures of 900 K and 1000 K. LOL is denoted by vertical dashed line.

Figure 6.18 presents the measured SVFs from experimental measurement and the predicted SVFs based on the soot precursor, C_2H_2. The peak SVFs at both initial temperatures of 900 K and 1000 K are qualitatively and quantitatively predicted by the MDBio-Nottingham mechanism, when compared to the experimental measurements. In addition, the predicted soot formation around the jet periphery agrees well with the conceptual model proposed by Dec [216], for which the central region of the predicted fuel spray is a fuel rich zone where the highest SVF is located. It is evident that soot formation increases when the initial temperature is raised. The fuel rich mixture is formed due to insufficient time for mixing. Moreover, the increase in soot formation corresponds well to the increase in OH mass fractions as shown in Figure 6.17, where the oxidation of soot by OH radicals is reduced due to the increase in initial temperature.
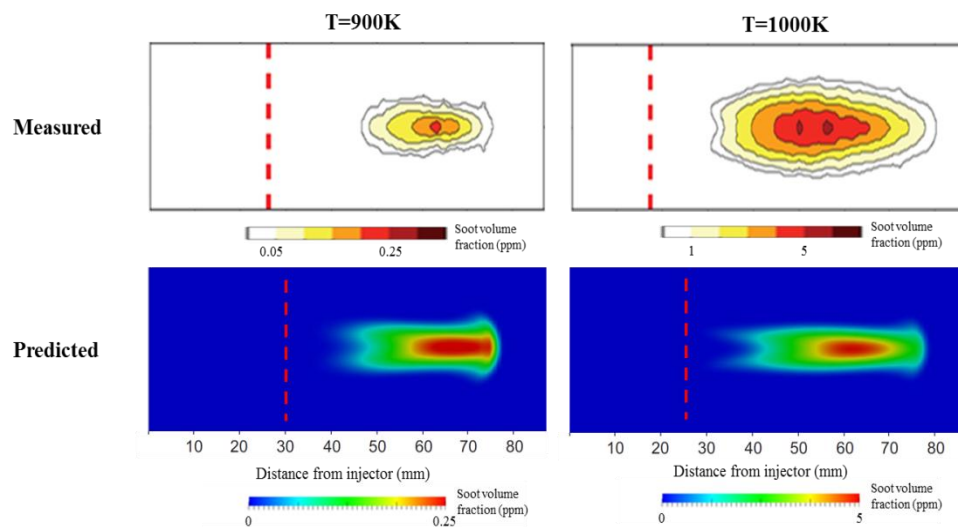
Figure 6.18 Comparisons of measured (adapted from Nerva et al. [36]) and predicted SVFs, at initial temperatures of 900 K and 1000 K. LOL is denoted by vertical dashed line.

Comparison Study of Various Reduced Biodiesel Chemical Kinetic Mechanisms

A comparison study is performed to further investigate the robustness of the MDBio-Nottingham reduced mechanism, where the reduced mechanism is compared against different reduced mechanisms reported in the literature. As tabulated in Table 6.5, the reduced mechanisms for comparisons are inclusive of the MDBio-Nottingham mechanism with 92 species, the reduced mechanism of 69 species by Brakora and Reitz [80] (ERC-Brakora) and the reduced mechanism of 115 species by Luo et al. [52] (UCONN-Luo). For benchmark comparison, only reduced mechanisms with low-temperature and high-temperature chemistries are included. As such, the individual low-temperature and high-temperature mechanisms by Luo et al. [56,70] are excluded. In order to examine the effects of chemical kinetics, identical case settings are applied to all the reduced mechanisms. The predicted ID periods and LOLs are the key parameters for comparisons as these parameters are found to be heavily affected by the chemical kinetics, where changes in LPL due to chemical kinetics are negligible as illustrated in Figure 6.19.

Table 6.5 Reduced mechanisms included in the comparison study for reacting spray modelling.

Reduced mechanism	No. of species	No. of reactions	Ref.
MDBio-Nottingham	92	360	In-house
UCONN-Luo	115	460	[52]
ERC-Brakora	69	192	[80]
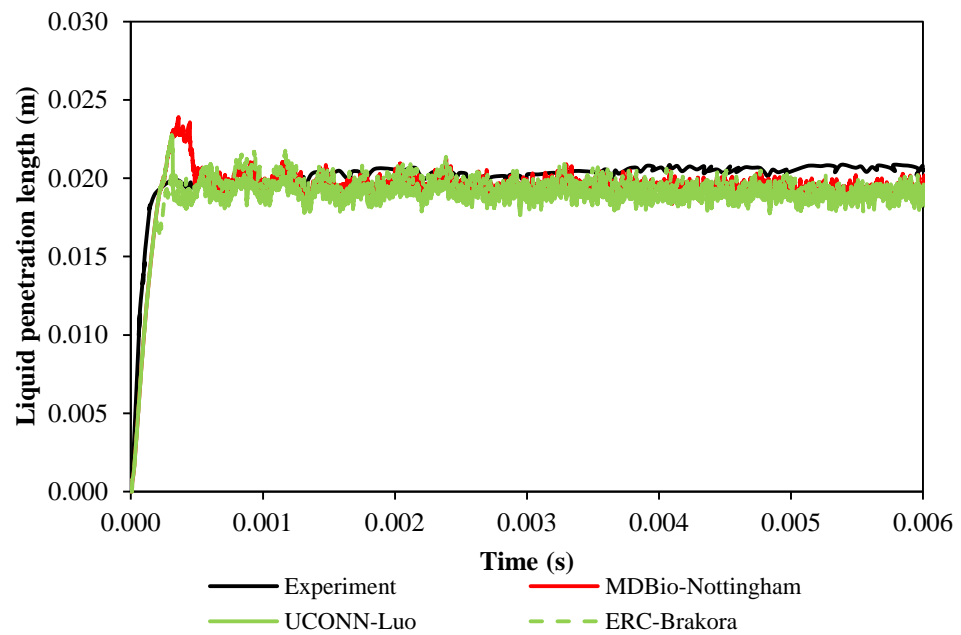
Figure 6.19 Predicted and measured [36] LPLs for SME reacting spray, using various reduced mechanisms, at an initial temperature of 900 K.

Table 6.4 compiles the predicted ID periods and LOLs with the corresponding percentage errors for the respective reduced mechanisms. In terms of the ID period predictions at an initial temperature of 900 K, the MDBio-Nottingham mechanism produces a percentage error of 7.2%, while UCONN-Luo and ERC-Brakora mechanisms under-predict by 17.4% and 5.4%, respectively. Over-predicted LOLs are recorded for all the reduced mechanisms, with the lowest percentage errors of 13.3% produced by the ERC-Brakora mechanism [80] while the highest percentage errors of 31.7% are observed with the UCONN-Luo mechanism [52]. Meanwhile, the MDBio-Nottingham mechanism achieves an over-estimation of approximately 17.6% in the LOL. Based on the computed results at the initial temperature of 1000 K, the ID periods and LOLs are generally over-predicted by all the reduced mechanisms. For LOLs, a maximum extension of 43.4% is observed for the UCONN-Luo [52] mechanism, whilst the MDBio-Nottingham and ERC-Brakora mechanisms [80] extend by 37.2% and 22.5%, respectively. On the other hand, the MDBio-Nottingham mechanism over-predicts ID period by 34.8%. Over-estimations in ID period are also found for the UCONN-Luo [52] and ERC-Brakora [80] mechanisms, with percentage errors of 14.8% and 41.5%,

respectively. The computational time for each reduced mechanism is also monitored throughout the simulations. For the MDBio-Nottingham mechanism, 24 hours is needed to complete 6.0 ms of simulation time with 8 parallel processors. Meanwhile, the UCONN-Luo [52] and ERC-Brakora [80] mechanisms used approximately 33 hours and 12 hours, respectively.

In general, the MDBio-Nottingham mechanism computes reasonable ID periods and LOLs at different initial temperatures despite the large percentage errors of 37.2%. Comparatively, the UCONN-Luo mechanism [52] is considerably less accurate than the MDBio-Nottingham and ERC-Brakora [80] mechanisms based on the ID period and LOL predictions. This is because the UCONN-Luo mechanism [52] is only validated for the composition of 50.0% n-heptane, 25.0% MD, 25.0% MD9D. Meanwhile, the ERC-Brakora mechanism [80] predicts relatively well in terms of ID and LOL at different initial temperatures as compared to the MDBio-Nottingham and UCONN-Luo [52] mechanisms since the mechanism is adjusted based on SME composition. However, large percentage errors of 41.5% are introduced for the ID period prediction at the initial temperature of 1000 K. This in turn implies that the ERC-Brakora mechanism [80] may need further adjustment when fuel composition is varied from SME. With these computed results, the chemical kinetics contained in the MDBio-Nottingham mechanism is hence proven to be sufficient in describing the ignition and combustion behaviours of different biodiesel fuels, without the need for further rate constant adjustment when fuel composition is changed.

6.5   Integration of Thermal NO Mechanism

The formation of NO_x is an important emission event for biodiesel combustion because NO_x levels are found increased by 2.0 to 10.0%, when biodiesel is blended with diesel for heavy-duty highway engines [217]. Therefore, the thermal NO mechanism [218] is integrated into the MDBIO-Nottingham reduced mechanism. Here, only thermal NO formation is considered because

the nitrogen dioxide (NO_2) species is directly dissociated from the NO species. This means that the NO species is the precursor for the following NO_2 formation. Besides, Ban-Weiss et al. [49] also found out the contribution of NO_2 to the NO_x emissions from the nitrous oxide (N_2O) mechanism is less than 1.0%. Additionally, Ren and Li [183] also stated that a major fraction of NO_x emission in diesel engine is contributed by the thermal NO. The three-step thermal NO is given in Table F.2 in Appendix F.

6.6   Concluding Remarks

With the aid of revised DRG, isomer lumping and sensitivity analysis reduction techniques, a generic reduced biodiesel chemical kinetic mechanism with 92 species and 360 reactions is formulated. The reduced biodiesel mechanism encompassing low-temperature and high-temperature chemistries is applicable to a wide range of biodiesel fuels such as CME, PME, RME and SME. The MDBio-Nottingham mechanism is thoroughly examined under 0D kinetic modelling and 2D reacting spray modelling. The percentage errors found for the ID periods predicted by the reduced mechanism when compared to those of detailed mechanism predictions and experimental data are up to 40.0% and 67.0%, respectively. Predicted key species profiles of the MDBio-Nottingham mechanism under the JSR conditions are also in reasonable agreement to those of the detailed mechanism predictions and experimental measurements. The fidelity of the MDBio-Nottingham mechanism is further demonstrated in the 2D reacting spray modelling. The ID periods and LOLs are accurately replicated by the reduced mechanism, with maximum percentage errors of 34.8% and 37.2%, respectively. The ID period and LOL predictions are relatively good even when the MDBio-Nottingham mechanism is appraised against other reduced mechanisms of identical species components in the comparison study.

Chapter 7

Spray, Combustion and Emission Characteristics of Biodiesel

7.1   Introduction

In this chapter, the thermo-physical properties evaluated in Chapter 5 and reduced mechanism developed in Chapter 6 are integrated with CFD models in an effort to numerically analyse the formations of spray, combustion and emissions for CME and SME, under the conditions of diesel engine. However, quasi-steady state which favours for combustion and formation analysis cannot be produced in the diesel engine because of the in-cylinder flows induced by piston motion during compression and expansion, spray impingement and also swirling flow. Thus, both CME and SME are firstly analysed for reacting spray, using the constant volume bomb setup. As such, the effects of the unsaturation level on the spray, combustion and emissions formation can be clearly examined without the disturbance of the in-cylinder flows. After identifying the effects of the unsaturation level, the numerical analyses are then extended to the light-duty diesel engine to study the in-cylinder phenomena for CME and SME.

The initial condition of the constant volume bomb simulations is designed to imitate that at SOI in the diesel engine combustion simulations, such that the events of the constant volume bomb can be related to those of the diesel engine. Here, the case setup of constant volume bomb with the initial temperature of 900 K, which is used for validation purpose as presented in Chapter 4, is favoured over 1000 K because the former temperature is closer to the predicted ambient temperature at SOI in the diesel engine. Meanwhile, the

initial pressure is fixed at 60.0 bar. Subsequently, the ambient O_2 level is increased from 15.0 to 21.0% to emulate the intake air composition of the naturally aspirated diesel engine, as shown in Figure 7.1. As such, the predictions of spray, combustion and emissions for CME and SME with respect to the variation of unsaturation levels can then be discussed under both the conditions of constant volume bomb and diesel engine, as presented in Sections 7.2 and 7.3, respectively.

Simulations of constant volume bomb at 15.0% ambient O_2 level

Simulations of constant volume bomb at 21.0% ambient O_2 level

Simulations of diesel engine combustion at 21.0% ambient O_2 level
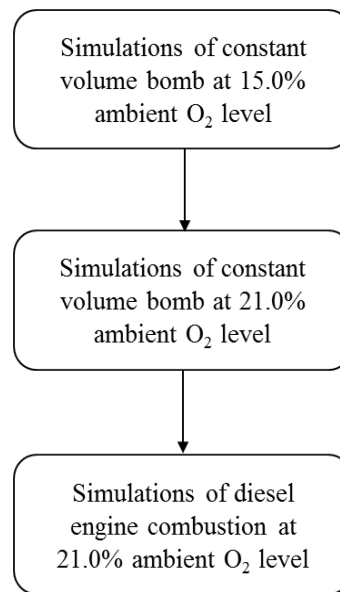
Figure 7.1 Flowchart of the simulations performed for both CME and SME, under the conditions of constant volume bomb and diesel engine.

7.2   Combustion Modelling in Constant Volume Bomb

7.2.1   Effects of Ambient O_2 Level

In this section, the spray, combustion and emissions characteristics of CME and SME are compared for ambient O_2 levels of 15.0% and 21.0%. Figure 7.2(a) and (b) shows the temporal plots of LPL predicted for CME and SME, at ambient O_2 levels of 15.0% and 21.0%. When the ambient O_2 level is increased to 21.0%, shorter LPLs are observed for CME and SME, where reductions of 5.9% and 4.9% are obtained, respectively. Since identical spray trends are observed for CME and SME, the following explanation for SME

thus applies to CME. The results predicted for CME are attached in Appendix G. For the ease of comparisons, the cases with ambient O_2 levels of 15.0% and 21.0% are hereafter referred as Case I and Case II, respectively. The longer LPL observed in Case I, implies less fuel is evaporated as compared to that of Case II. This shows that the spray in Case II concentrates on the mixing with air due to higher ambient O_2 concentration, which in turn results in shorter LPL and higher fuel evaporation rate [43]. Table 7.1 compiles the effects of ambient O_2 level and unsaturation level on the spray, combustion and emissions characteristics of CME and SME, under the conditions of constant volume bomb and diesel engine.
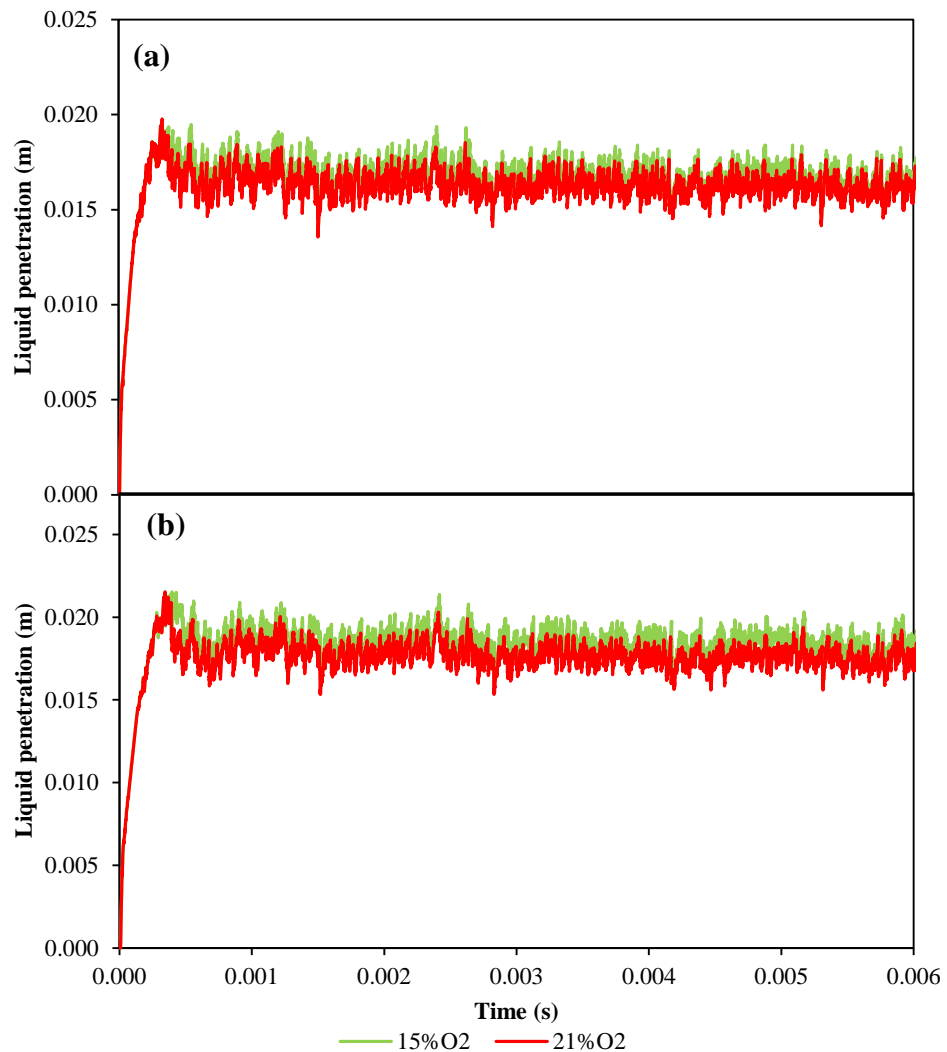
Figure 7.2 Predicted temporal LPLs for (a) CME and (b) SME, at 15.0% and 21.0% ambient O_2 levels.

Table 7.1 Effects of ambient O_2 level and unsaturation level on the spray, combustion and emissions characteristics.

Varying parameters	Results									
	LPL	ID period	LOL	Local flame temperature	In-cylinder peak pressure	In-cylinder peak temperature	Soot mass concentrations	CO	CO_2	NO
Increase of ambient O_2 level	*Constant volume bomb*									
	↓	↓	↓	↑	-	-	↑	↑	↑	-
Increase of unsaturation level	*Constant volume bomb*									
	↑	↑	↑	↑	-	-	↑	↑	=	-
	Diesel engine									
	-	↑	-	↑	↑	↑	↑	↑	=	↑

Legend: ↑ Increased/ delayed; ↓ Decreased/advanced; = Not affected; - Not investigated

161

Because of the increased ambient O_2 levels, the subsequent flame development for Case II from auto-ignition to steady-state is also affected. The ignition sites for Cases I and II are different based on the temperature plots at the start of ignition, seen in Figures 7.3 and G.1 in Appendix G, respectively. For Case I, the first site of ignition is located at the furthest radial distance away from the spray core. On the other hand, the first ignition site for Case II is located further upstream with an enlarged ignition region and a higher ignition temperature of 400 K than that of Case I is also observed. At 1.2 ms, the diffusion flames in Cases I and II start to develop around the stoichiometric mixture. This denotes that the combustion process still remains in the pre-mixing state as suggested by Jangi et al. [219]. As the flames reach steady-state at 3.0 ms, the flame predicted in Case I demonstrates a larger growth in the radial direction, while the flame of Case II shows a forward propagation. As such, it can be deduced that the diffusion flame grows axially as the ambient O_2 concentration is increased.
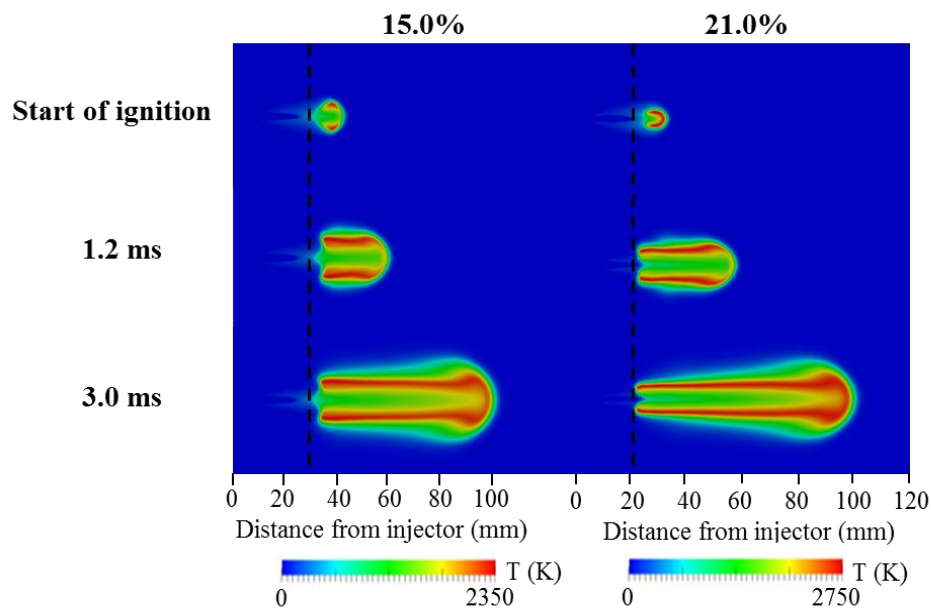
Figure 7.3 Predicted flame distributions for SME, at 15.0% and 21.0% ambient O_2 levels, constant volume bomb condition. LOL is denoted by vertical dashed line.

Table 7.2 tabulates the predicted ID periods and LOLs. Comparing the ID period of Case II against to that of Case I, identical observation to that of LPL is found here, where the ID period predicted for Case II is shortened by 24.0%. As the ID period is advanced due to the increase of ambient O_2 level, the flame LOL is shortened. This is because the ignition site is closer to the injector nozzle when the fuel ignites earlier. Therefore, the estimated LOL for Case II is reduced from 30.78 mm of Case I is reduced to 23.70 mm. Although Pickett et al. [220] mentioned that the relationship between ID period and LOL is not necessarily one-to-one, the trend of shortened LOL predictions as observed here corresponds well to that of advanced ID periods for Cases I and II.

Table 7.2 Predicted ID periods and LOL for CME and SME, at 15.0% and 21.0% ambient O_2 levels, constant volume bomb condition.

Fuel types	Ambient O_2 level (%)	ID period (ms)	LOL (mm)
CME	15.0	0.646	32.12
	21.0	0.497	24.33
SME	15.0	0.658	30.78
	21.0	0.500	23.70

As a result of the increased ambient O_2 levels, the soot mass concentrations predicted for Case II as displayed in Figures 7.4 and G.2 in Appendix G are raised by twice as compared to that of Case I. Since the formation of soot is strongly dependent on the local flame temperatures, the higher soot mass concentrations produced in Case II are thus induced by the higher local flame temperature of 400 K than that of Case I. As C_2H_2 is defined as the species for soot precursor, the soot mass concentrations for Case II are also affected by the twice increased C_2H_2 mass fractions, as shown in Figures 7.4 and G.2. Besides, the increased soot mass concentrations observed for Case II are further justified by the rates of soot formation and oxidation, as illustrated in Figures 7.5, 7.6, G.3 and G.4. Although increased soot oxidation rates due to O_2 and OH radicals are observed for Case II as compared to that of Case I,

these rates are insufficient to overcome the soot formation rates, which are nearly 7.2 times higher. Meanwhile, the rates of soot formation for Case I are only 6.1 times above the rates of soot oxidation. As such, more soot is formed in Case II.

It is interesting to note that the increase of ambient O_2 levels also influences the soot oxidants for both Cases I and II. Under the condition of Case I, equivalent soot oxidation rates due to the O_2 and OH radicals are generated for SME, while CME produces higher rate of soot oxidation due to OH radicals than O_2 radicals. When Case II is applied, the rates of soot oxidation due to O_2 radicals are enhanced for both CME and SME. Despite the variation obtained for Case I, it is clearly depicted that the increase of ambient O_2 levels leads to higher rate of soot oxidation by O_2 radicals.
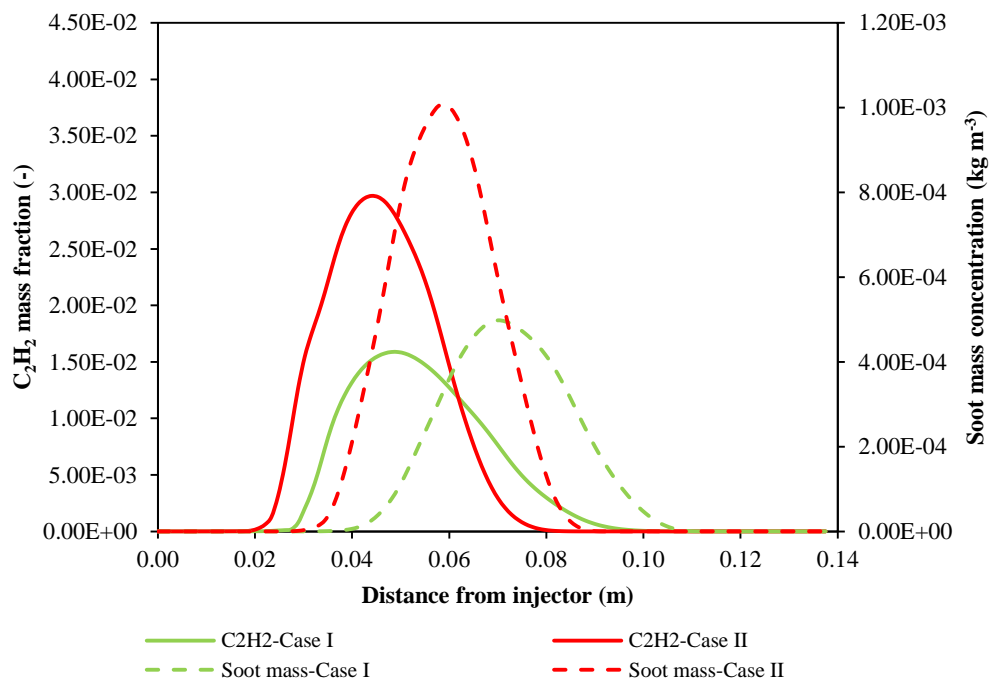
Figure 7.4 Predicted spatial C_2H_2 mass fractions and soot mass concentrations for SME, at 15.0% and 21.0% ambient O_2 levels, constant volume bomb condition.
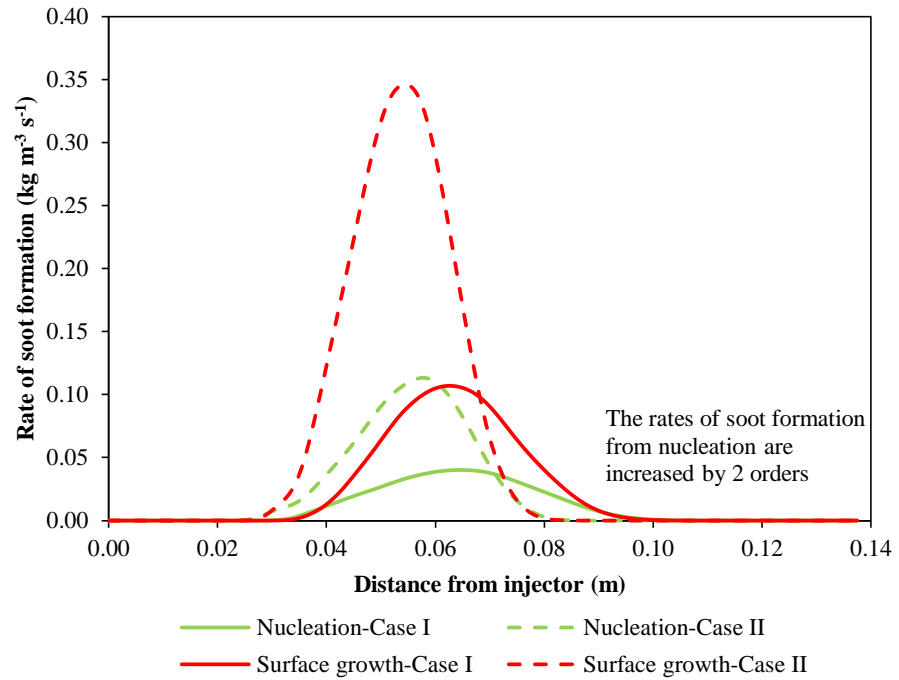
Figure 7.5 Predicted spatial rates of soot formation from nucleation and surface growth for SME, at 15.0% and 21.0% ambient O$_2$ levels, constant volume bomb condition.
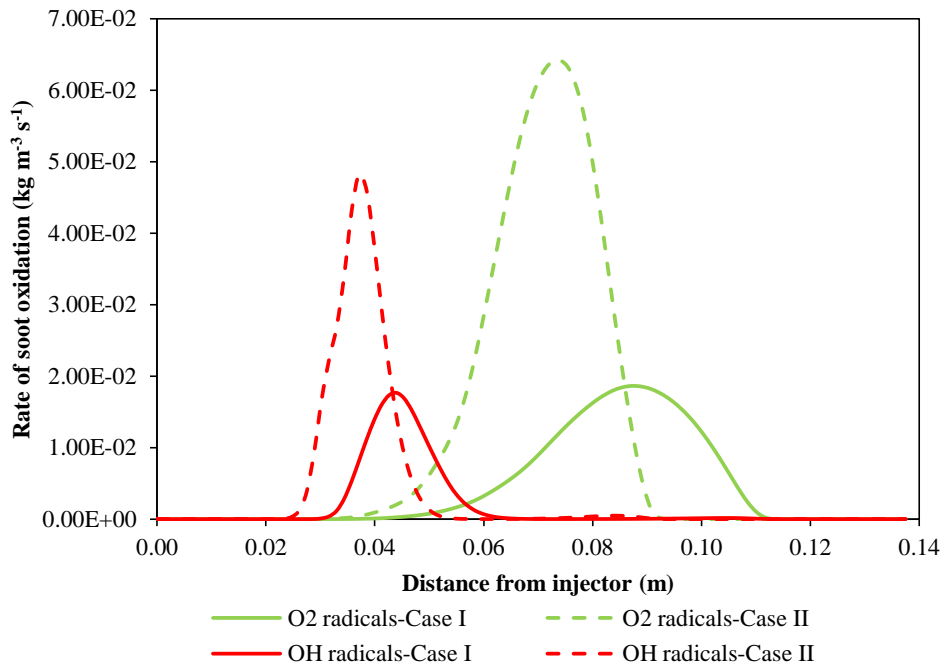
Figure 7.6 Predicted spatial rates of soot oxidation by O$_2$ and OH radicals for SME, at 15.0% and 21.0% ambient O$_2$ levels, constant volume bomb condition.

Due to the increase of ambient O_2 level, a more complete combustion is obtained for Case II. Therefore, the productions of CO and CO_2 for Case II are higher than those of Case I, as presented in Figures 7.7 and G.5. Comparing the mass fractions of CO and CO_2 for Case II against those of Case I, increments of 1.6 and 1.2 times are obtained, respectively. Besides, enlarged areas of CO and CO_2 are obtained for Case II, when comparing the CO and CO_2 distributions between Cases I and II. Here, the formation of CO is also closely related to C_2H_2, based on the reactions $C_2H_2+OH<=>CH_3+CO$ and $C_2H_2+O<=>CH_2+CO$ found in the reduced chemical kinetic mechanism. As seen in Figures 7.4 and G.2, the maximum mass fraction of C_2H_2 for Case II is 1.9 times to that of Case I. Subsequently, this increases the mass fractions of CO in Case II. Since the CO production is enhanced, the mass fractions of CO_2 are also increased. This is because CO_2 is directly dissociated from CO, based on the $CO + O (+M) <=> CO_2 (+M)$ found in the surrogate mechanism.
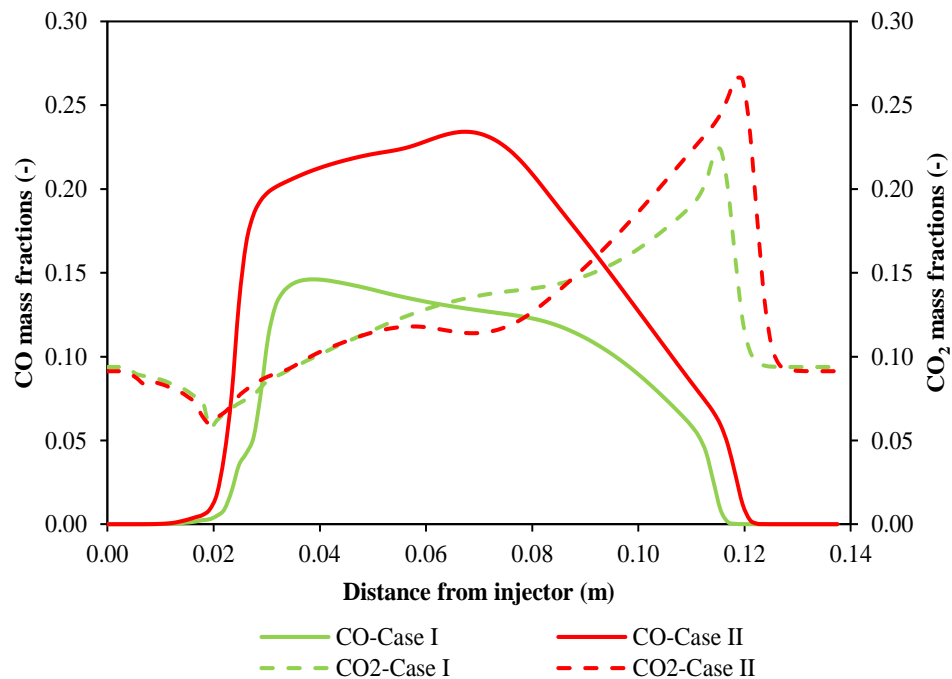
Figure 7.7 Predicted spatial CO and CO_2 mass fractions for SME, at 15.0% and 21.0% ambient O_2 levels constant volume bomb condition.

7.2.2 Effects of Unsaturation Level

In this section, the predictions of spray, combustion and emissions at 21.0% ambient O_2 level for CME are compared against to those of SME such that the effects of unsaturation level are addressed. The change of fuel compositions plays a vital role in the development of spray especially the spray penetration, ID period, LOL and emissions formation. Due to the high saturation content in CME, higher rate of fuel evaporation is produced as compared to that of SME. This is evident with the predicted LPLs for CME and SME, as seen in Figure 7.8. The LPL predicted for CME level is 9.9% shorter than that of SME. Besides, the better fuel evaporation predicted for CME is also observable from the 0.6% advanced ID period and 2.7% elongated LOL as compared to those of SME. Despite the marginal advancement, the ID period predictions for CME and SME are consistent with the CNs of the fuels. CME with a CN of 65 has a shorter ID of 0.497 ms, whilst SME with a CN of 52 has a longer ID of 0.5 ms. Owing to the shorter ID period, the subsequent spray development for SME is slightly retarded as compared to that of CME, seen in Figure 7.9. Besides, the flame temperatures are also increased marginally as the unsaturation level increases, as displayed in Figure 7.10.
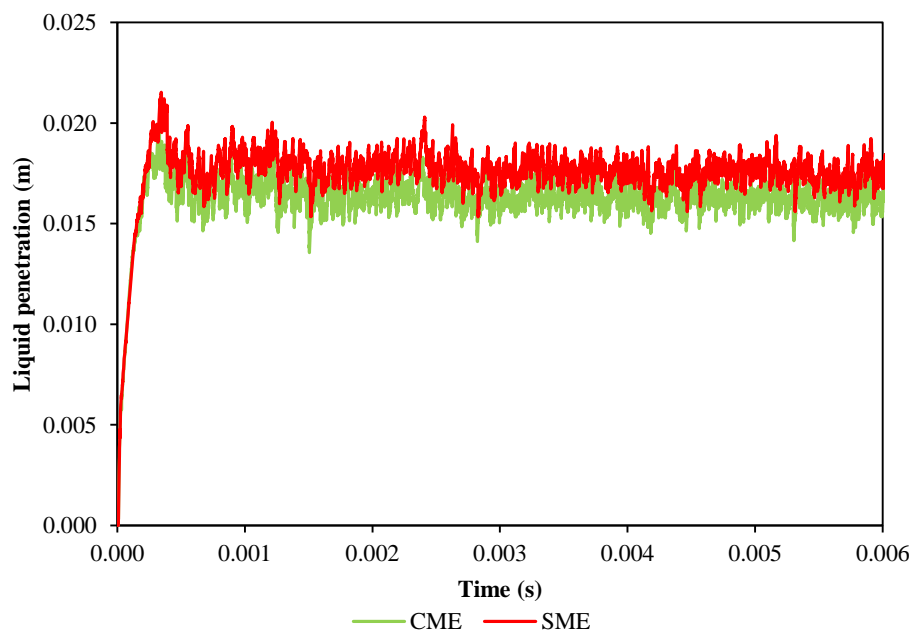
Figure 7.8 Predicted temporal LPL for CME and SME, at 21.0% ambient O_2 level, constant volume bomb condition.

Here, contrasting trends of LOL with respect to the change of ID periods is observed as compared to that of found in Section 7.2.1, where an extension in LOL is observed for CME as the ID period advances. Such behaviour is expected since Pickett et al. [220] has proven that the trends of LOL do not correspond directly to the trends of ID period. Nonetheless, the LOL is found in agreement with the unsaturation level, where the fuel with lower level of unsaturation extends the location of lift-off. For instance, CME predicts a longer LOL of 24.33 mm as compared to that of SME at 23.70 mm. Furthermore, the LOL predictions also correspond to the CN, where fuel with greater CN produces shorter LOL [221].
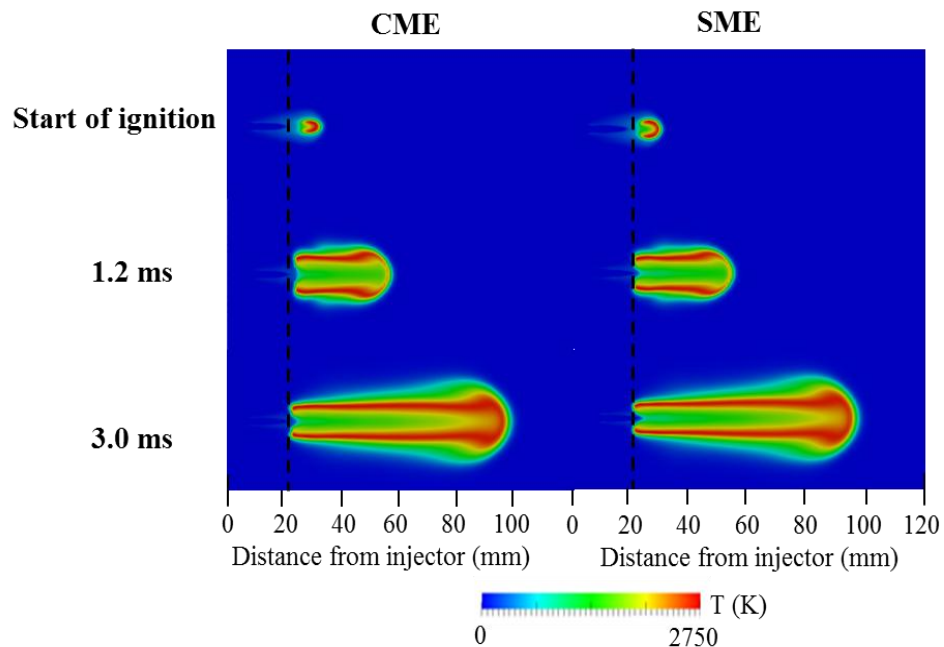
Figure 7.9 Flame distributions for CME and SME, at 21.0% ambient O_2 level, constant volume bomb condition. LOL is denoted by vertical dashed line.

168
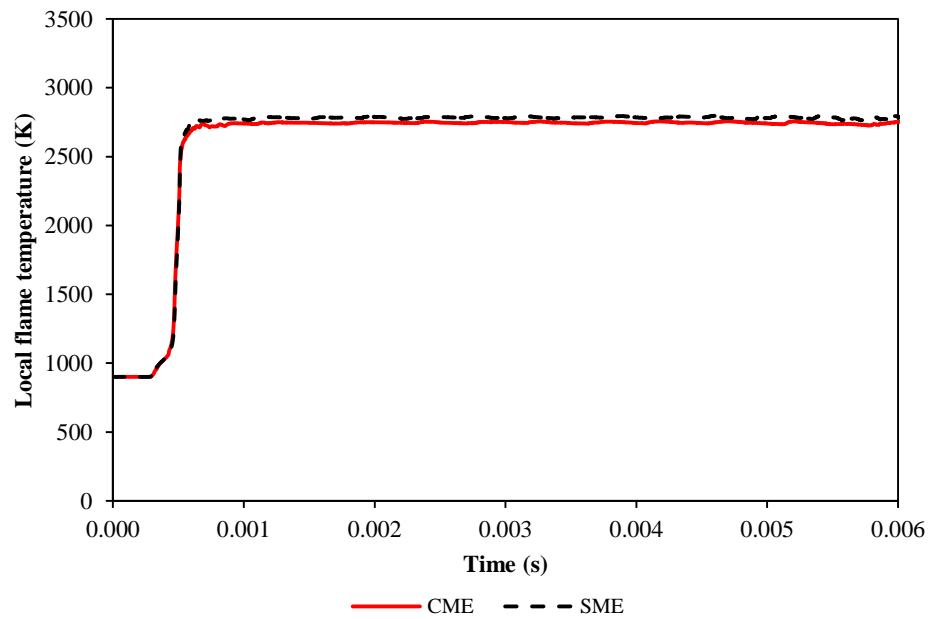
Figure 7.10 Predicted temporal local flame temperatures for CME and SME, at 21.0% ambient O_2 level, constant volume bomb condition.

The increase of unsaturation level also leads to higher soot mass concentrations, as shown in Figure 7.11. The peak soot mass concentration predicted for SME is increased by 20.0% compared to that of CME. Besides, the soot distribution for SME is also enlarged. The lower soot mass concentration predicted for CME is justified by the reduced C_2H_2 mass fractions as illustrated in Figure 7.11. This phenomenon is expected since the species profiles predicted by the MDBio-Nottingham mechanism under the JSR conditions shows that CME produces less unsaturated soot species, as found in Figure E.11(a). In addition, the soot formation is also affected by the LOL, for which longer LOL tends to form less soot. This is in agreement with that of Siebers and Higgins [206]. The extended LOL of CME, which is approximately 2.7% longer than that of SME, allows more air entrainment. The subsequent pre-mixing of air and fuel at the upstream of the LOL is enhanced [206] and as a result a less fuel rich central reaction zone is formed.
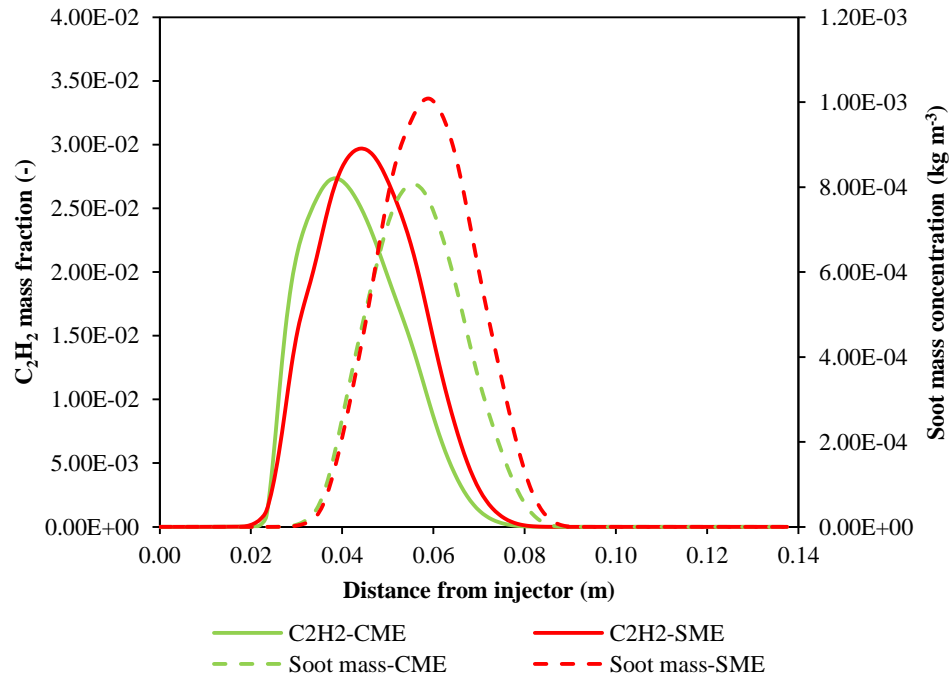
Figure 7.11 Predicted spatial C_2H_2 mass fractions and soot mass concentrations for CME and SME, at 21.0% ambient O_2 level, constant volume bomb condition.

Based on Figures 7.12 and 7.13, it is evident that the rates of soot formation and oxidation are influenced by the unsaturation levels. The higher soot mass concentrations predicted for SME as compared to that of CME can also be explained with the soot formation and oxidation rates. Here, increased rates of soot formation from the processes of nucleation and surface growth are obtained when the unsaturation level increases. As an example, the soot formation rate from surface growth process for SME is 17.5% higher than that of CME. In addition, the ratio of total rates of soot formation against the total rates of soot oxidation for SME is 6.4% higher than that of CME. As such, the soot mass concentrations predicted for SME are raised.
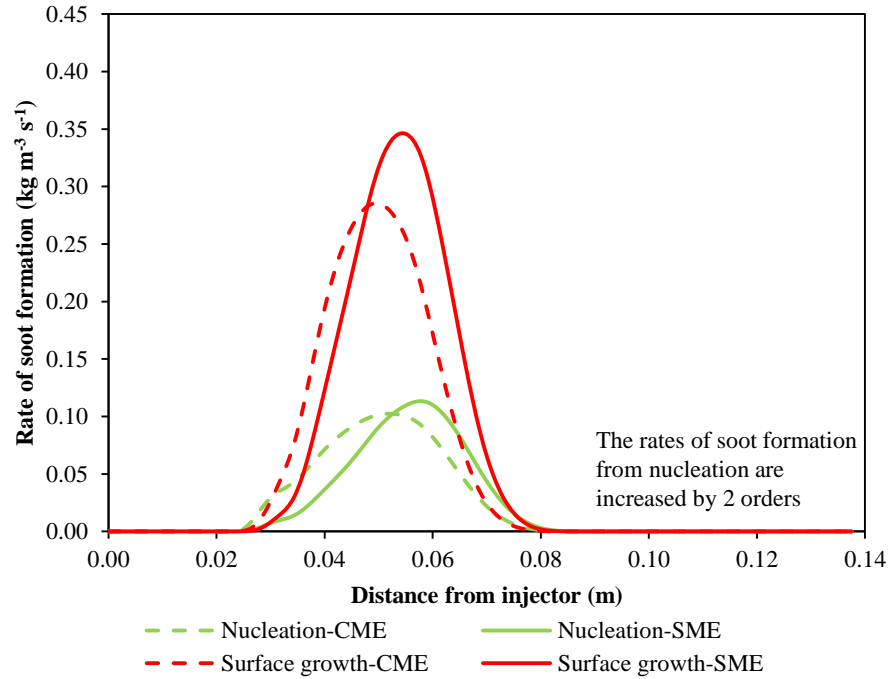
Figure 7.12 Predicted spatial rates of soot formation from nucleation and surface growth for CME and SME, at 21.0% ambient O$_2$ level, constant volume bomb condition.
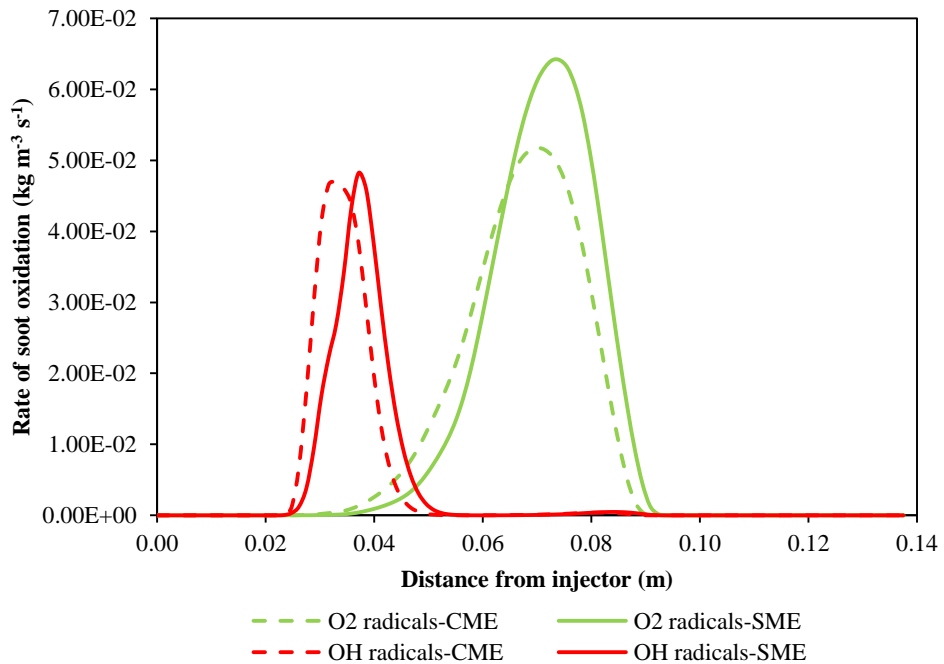

Figure 7.13 Predicted spatial rates of soot oxidation by O$_2$ and OH radicals for CME and SME, at 21.0% ambient O$_2$ level, constant volume bomb condition.

171

The increase of unsaturation level is also significant to the formation of CO, as seen in Figure 7.14. Despite the identical CO distributions predicted for CME and SME, the peak mass fractions of CO for SME are increased by 6.1% as compared to those of CME. The higher CO mass fractions for SME is resulted by the 7.7% increased C_2H_2 mass fractions since the mass fractions of CO are influenced by the C_2H_2 mass fractions as aforementioned in Section 7.2.1. Due to the rather equivalent CO mass fractions, the mass fractions of CO_2 predicted for CME and SME are thus identical.
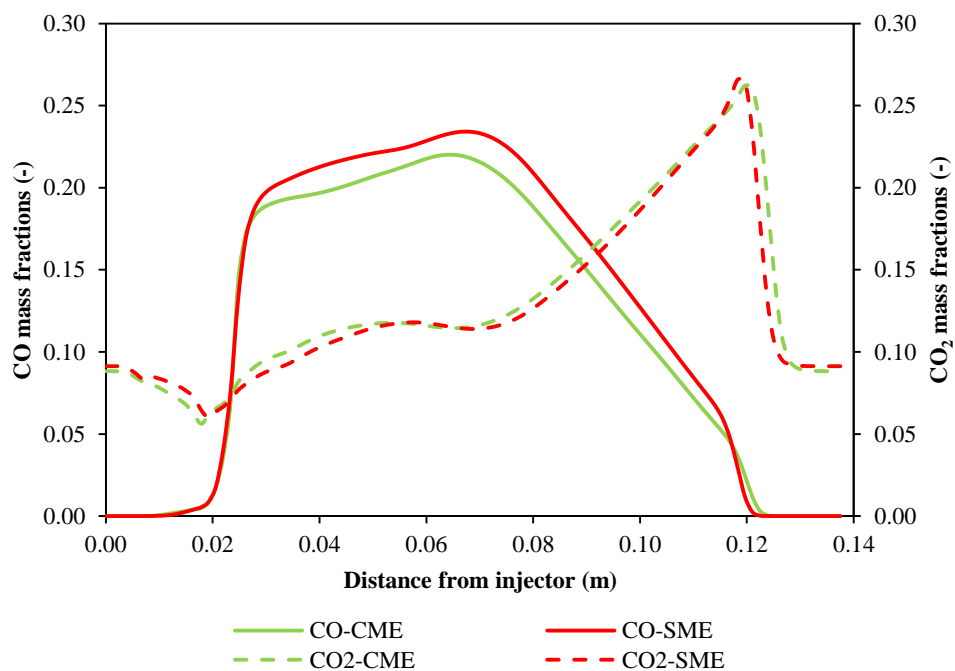
Figure 7.14 Predicted spatial CO and CO_2 mass fractions for CME and SME, at 21.0% ambient O_2 level, constant volume bomb condition.

7.3   Combustion Modelling in Diesel Engine

7.3.1   Effects of Unsaturation Level

The increase of unsaturation level in the diesel engine also exhibits identical effects to those of the constant volume bomb. Here, the predicted ID period, which is defined as the timing from the SOI to the start of combustion [222], is also increased when the unsaturation level increases. CME, which contains

approximately 60.0% lower unsaturation level than that of SME, records a 4.0% shorter ID period, as demonstrated in Table 7.3. Although the ID periods for CME and SME are under-predicted by deviations of 15.6% and 16.4%, respectively, the predictions are consistent with the experimental measurements. Besides, these ID period predictions are in agreement with the CNs of CME and SME, which is an observation similar to that of the constant volume bomb simulations. The in-cylinder pressures and temperatures are also subsequently affected by the unsaturation level as seen in Figure 7.15, where the peak pressure and temperatures for SME are higher than those of CME. The reason for this is that SME demonstrates a shorter similar flame front than CME does, as displayed in Figure 7.9.

Table 7.3 Predicted ID periods under the diesel engine condition for CME and SME.

Fuel types	Predicted ID period (°)	Measured ID period (°)	Deviation (%)
CME	11.75	10.16	-15.65
SME	12.25	10.52	-16.44
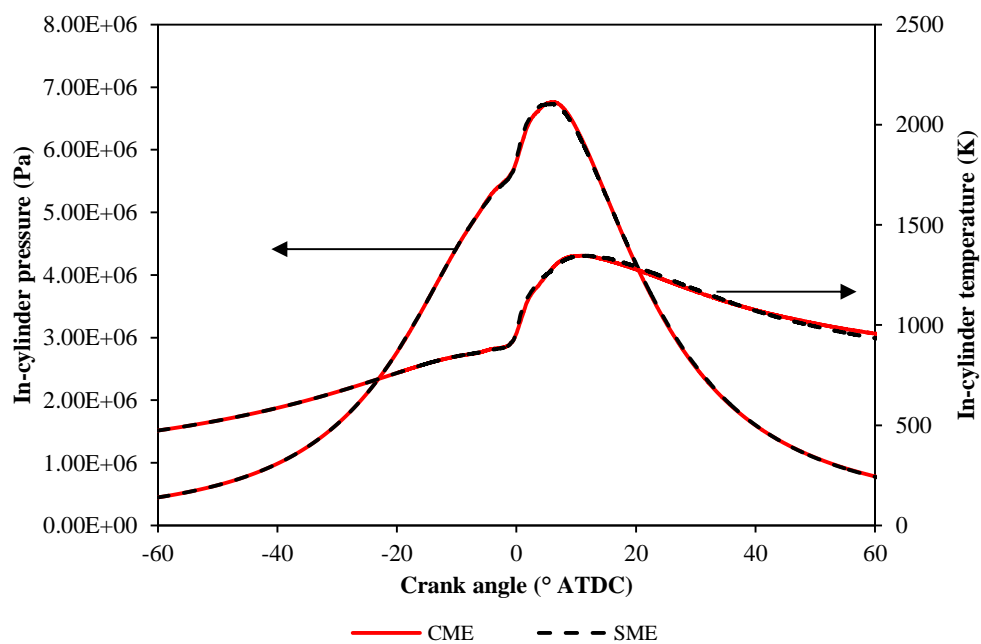
Figure 7.15 Predicted temporal in-cylinder pressures and temperatures for CME and SME, under the diesel engine condition.

Based on these numerical results, it is sufficient to deduce that the spray and combustion characteristics of biodiesel are influenced by the unsaturation level. The delayed ID periods for SME predicted in both the constant volume bomb and diesel engine are because of the longer time required to break the double bond of unsaturated species in SME. Although it is mentioned in Chapter 6 that the ID periods predicted by the MDBio-Nottingham mechanism for highly unsaturated fuel are shorter than those of saturated fuel, a contrasting observation is obtained here. However, these predictions are in agreement with the findings in the literature [81,223]. Therefore, it is believed that these predictions are produced collectively by the chemical kinetics and the thermo-physical properties.

Since the rates of soot formation and soot oxidation in the constant volume bomb are elevated due to the increase of unsaturation level, similar predictions are also found here for the diesel engine combustion. Under the diesel engine condition, the rates of soot formation from surface growth and the rates of oxidation due to O_2 and OH radicals are increased in response to the increase of unsaturation level, as presented in Figures 7.16 and 7.17, respectively. Meanwhile, the rates of soot formation from nucleation predicted for both CME and SME are unchanged due to the equivalent mass fractions of C_2H_2 as seen in Figure 7.18. Nevertheless, the formation of soot is dominant by the surface growth process, which is identical to that of the constant volume bomb. In terms of the soot oxidation, it is noticeable that the maximum soot oxidation by OH radicals occurs earlier for both CME and SME, approximately at $+7°$ ATDC. Meanwhile, the peak soot oxidation due to O_2 radicals is located at $+9°$ ATDC. Such observation corresponds to that of the constant volume bomb, where the soot in the spray cores of CME and SME is oxidised by O_2 radicals than the OH radicals, found in Figure 7.13.
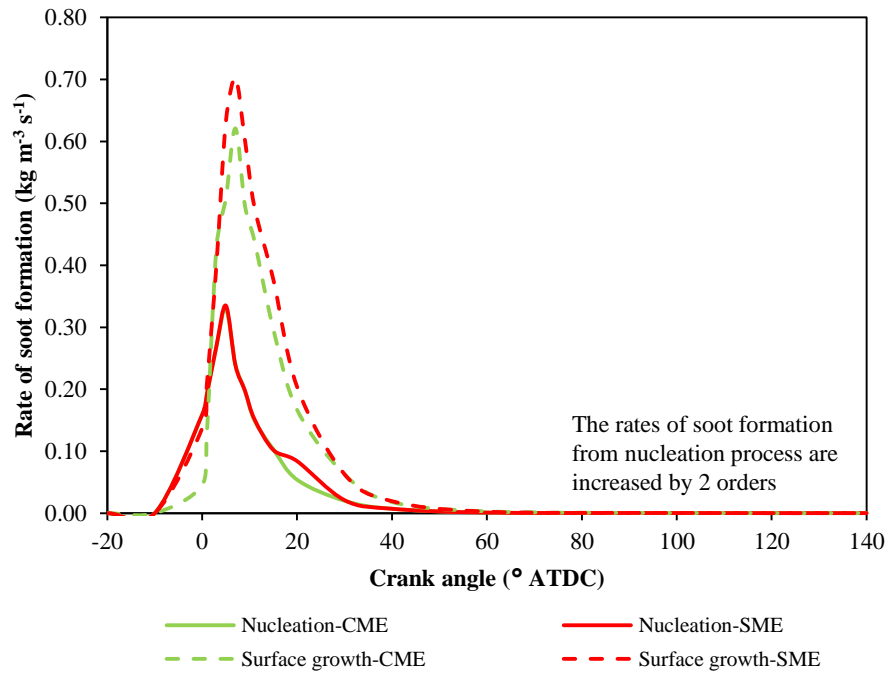
Figure 7.16 Predicted temporal rates of soot formation from nucleation and surface growth for CME and SME, under the diesel engine condition.
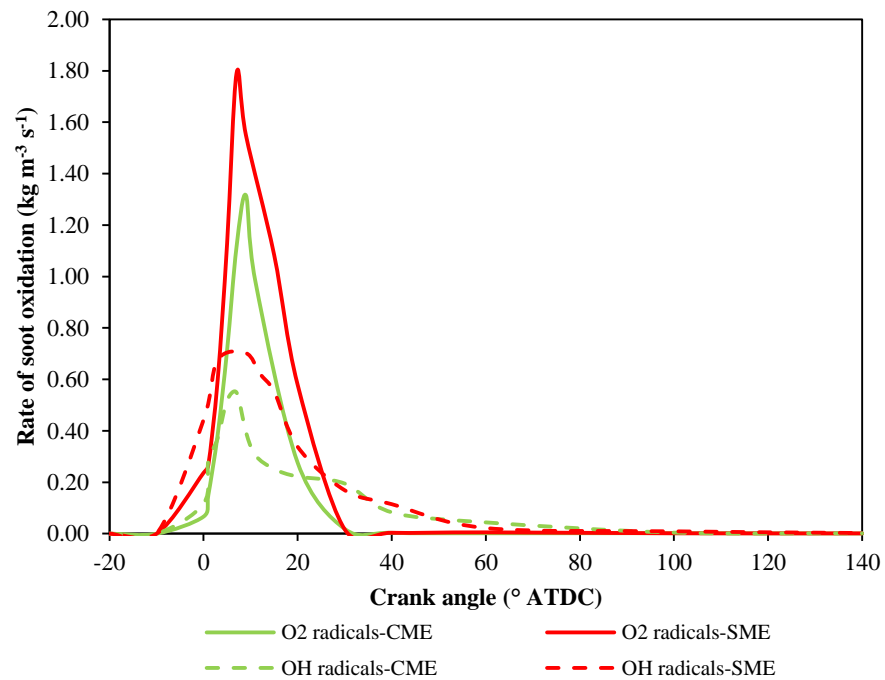
Figure 7.17 Predicted temporal rates of soot oxidation by OH and O_2 radicals for CME and SME, under the diesel engine condition.
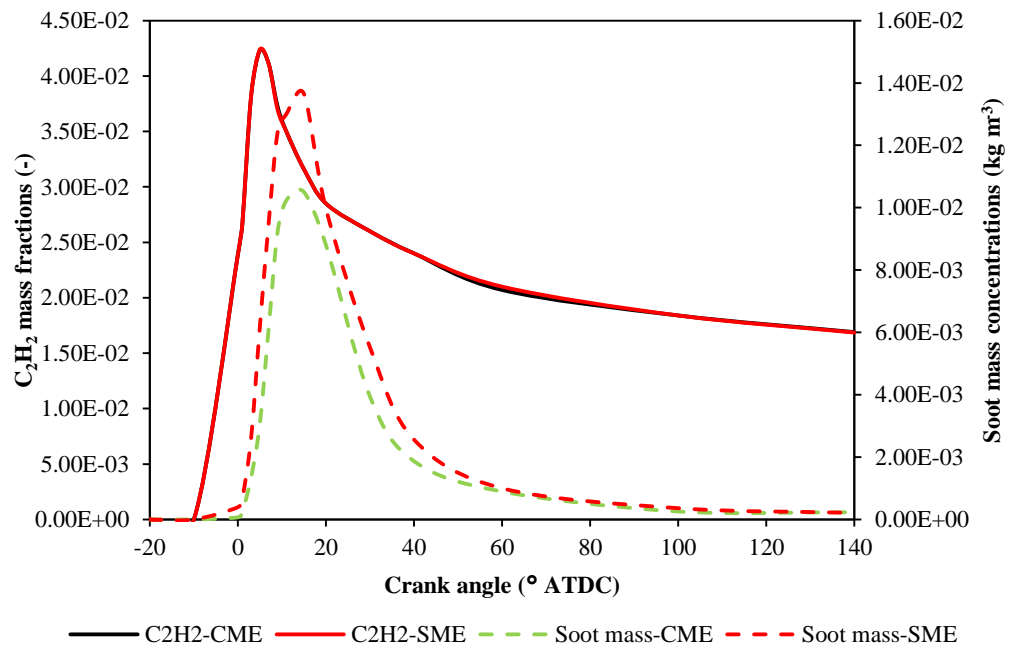
Figure 7.18 Predicted temporal soot mass concentrations and C_2H_2 mass fractions for CME and SME, under the diesel engine condition.

Despite the increase of soot oxidation rates, soot formation is favoured because the raised soot formation rates coincides with the highest local flame temperatures, at the period between +6° ATDC and +10° ATDC. Since SME contains higher unsaturation level, the number of double bonds is also increased. As such, the subsequent ignition for SME requires longer time than CME does, which is evident with the predicted ID periods shown in Tables 7.2 and 7.3. Additionally, higher local flame temperatures are yielded for SME in the constant volume bomb and diesel engine, as shown in Figures 7.10 and 7.19. Besides, the shorter LOL of CME draws lesser air into the spray flame for soot reduction than the shorter LOL of SME does. As such, higher concentration of soot mass by 23.1% is produced when the unsaturation level increases, as illustrated in Figure 7.18. The subsequent tailpipe soot emission, which is represented by the prediction obtained at EVO, is also enhanced by 32.0%. This result is in agreement with the finding of Schonborn et al. [45]. Despite the difference in absolute soot mass concentrations, the soot for both CME and SME identically resides on the engine bowl, as presented in Figure 7.20.
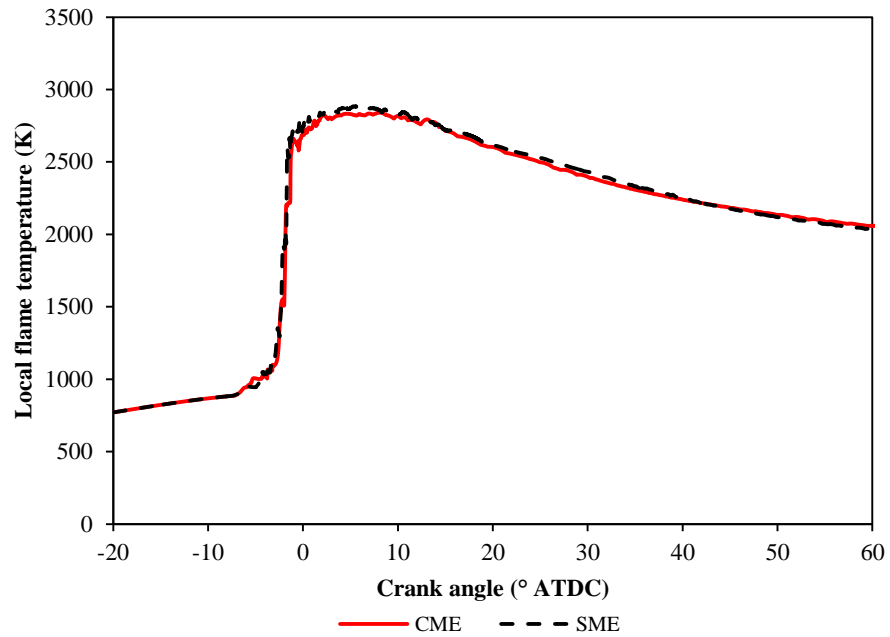
Figure 7.19 Predicted temporal local flame temperatures for CME and SME, under the diesel engine condition.
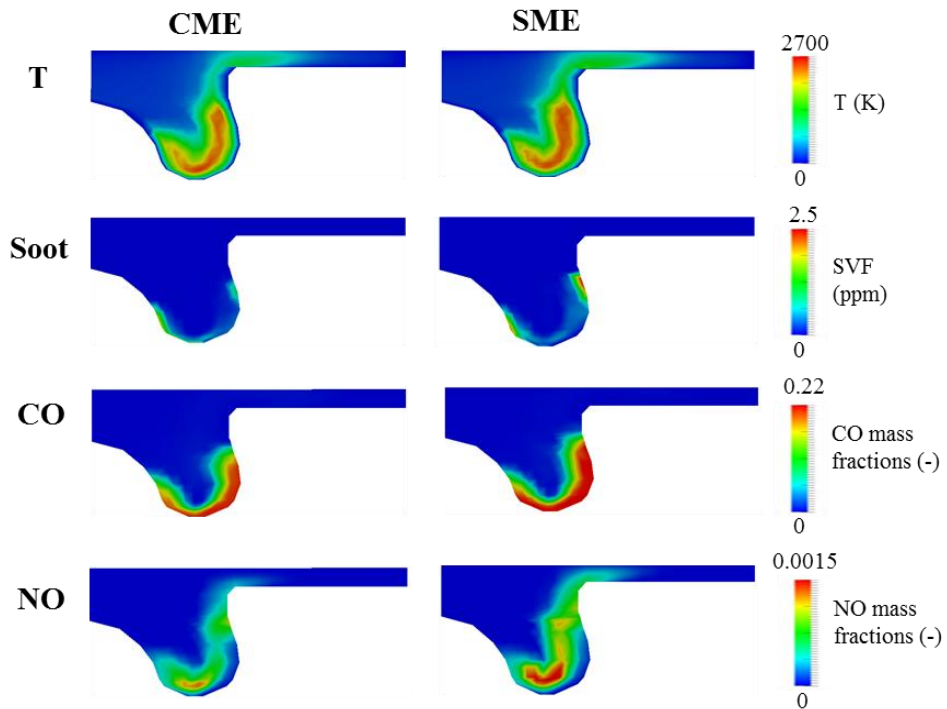
Figure 7.20 Predicted local temperature, soot, CO and NO for CME and SME, at +10° ATDC.

The longer spray penetration of SME has resulted in a poorer fuel evaporation rate as compared to that of CME. This is supported by the higher mixture fraction and lower fuel evaporation rate for SME, as shown in Figures 5.8 and 5.9 of Chapter 5. In addition, the retarded ID of SME gives rise to 1.5% higher local flame temperatures than those of CME. Besides, the shorter LOL of SME than CME also reduces the air drawn into the spray flame. These predictions in turn contribute to poor combustion as the unsaturation level increases, where higher levels of CO and NO are formed, seen in Figure 7.21. The peak mass fractions of CO and NO predicted for SME are 4.4% and 14.2% higher than those of CME, respectively. These results are identical to those of Ban-Weiss et al. [49]. However, the mass fractions of CO_2 are unaffected by the unsaturation levels, which are similar to the predictions in the constant volume bomb. The trends of these emissions are retained until EVO, as shown in Figure 7.22. Despite the difference in the absolute mass fractions, both CME and SME exhibit similar CO and NO distributions, as highlighted in Figure 7.20. The peak CO concentrations for CME and SME are located at the edge of the bowl. Meanwhile, the peak NO concentrations for CME and SME reside above of the peak CO concentrations, where the highest flame temperatures are found. This shows that the formations of NO are dependent on the local flame temperatures since the thermal NO formation favours at temperature above 2000 K [224,225]. In response to the decrease of local flame temperatures, the mass fractions of NO for CME and SME are decreased from +20° ATDC onwards and became saturated at +40° ATDC.
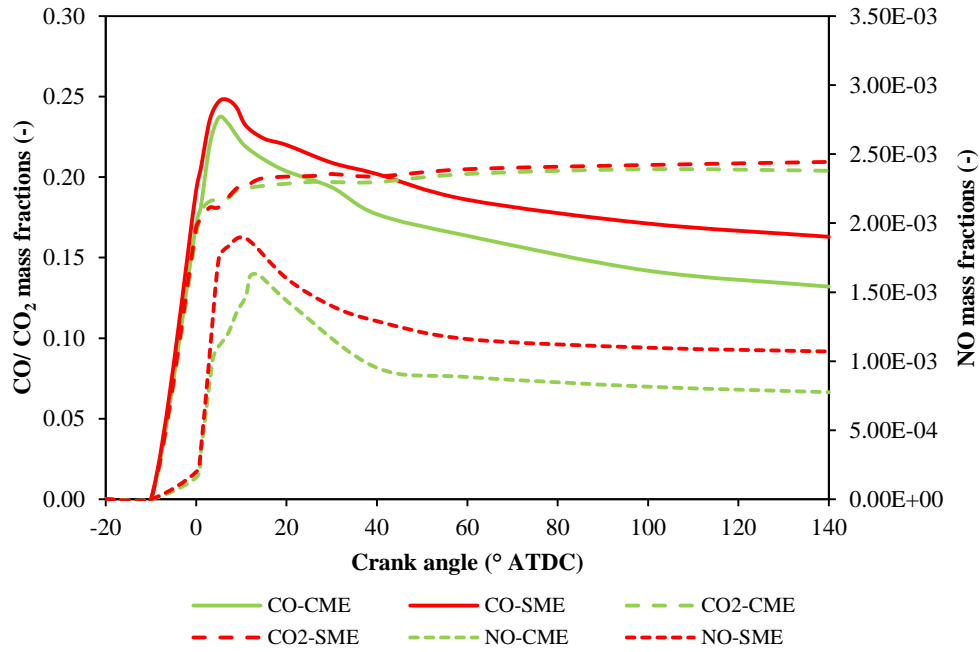
Figure 7.21 Predicted temporal CO, CO$_2$ and NO mass fractions for CME and SME, under the diesel engine condition.
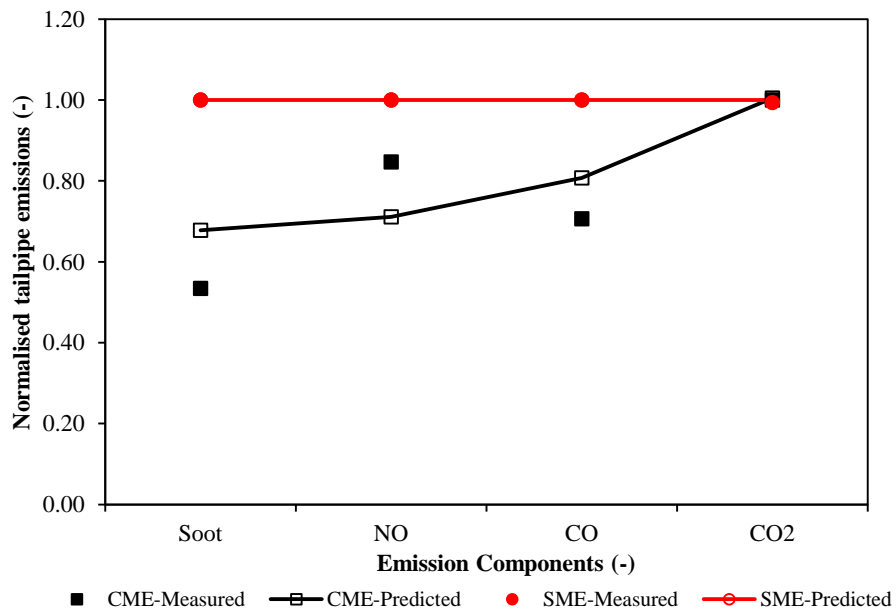
Figure 7.22 Comparisons of measured and predicted tailpipe soot, NO CO and CO$_2$ emissions for CME and SME, under the diesel engine condition.

7.4   Concluding Remarks

The characteristics of CME and SME are examined with respect to the variations of ambient O_2 level and unsaturation level, under the conditions of constant volume bomb and diesel engine. It is found that spray developments for CME and SME are highly sensitive to the increase of ambient O_2 level, where forward propagation is predicted when the ambient O_2 level is increased. Besides, the ID period and LOL are also shortened by the raised ambient O_2 level. Nevertheless, the soot mass predicted at 21.0% ambient O_2 level is twice higher than that of 15.0% ambient O_2 level. Furthermore, the mass fractions of CO and CO_2 are increased by 1.6 and 1.2 times, respectively. The species responsible for soot oxidation also changes in accordance to the increase of ambient O_2 levels, where soot is dominantly oxidised by O_2 than OH radicals when the ambient O_2 level is raised to 21.0%.

The results predicted for CME and SME at 21.0% ambient O_2 level in the constant volume bomb demonstrate good agreement to the predictions obtained in the diesel engine. For both the simulations of constant volume bomb and diesel engine combustion, the increase of unsaturation level displays prolonging effects on the spray and combustion development, where maximum retardations of 4.0% in the ID period and LOL are observed. Besides, the LPL is also extended by 9.9% due to the increase of unsaturation level. This in turn contributes to lower fuel evaporation rate for SME. As such, the concentrations of soot mass, NO and CO are promoted for SME. Apart from that, the rates of soot formation and oxidation are also raised. Nevertheless, the CO_2 emissions are unaffected by the change of unsaturation level in both the constant volume bomb and diesel engine. Comparing the predicted results between CME and SME, better combustion performance is achieved with CME. This is because the shorter ID period of CME, which is related to higher CN, denotes that CME is more stable than SME does. Additionally, the tailpipe emissions generated for CME particularly soot, CO and NO are lower than those of SME, by a maximum deviation of 32.0%. From here, it can be concluded that the spray events captured in the constant volume bomb are sufficient to emulate to those took place in the diesel engine.

Chapter 8

Conclusions and Future Work

8.1   Conclusions

The investigations reported in this thesis deal with the model developments of thermo-physical properties and reduced chemical kinetics for the modelling of biodiesel combustion. The conclusion first summarises the significance of thermo-physical properties on the developments of quasi-steady reacting spray and soot for both CME and SME. The subsequent section presents the formulation and validation of the generic reduced mechanism for biodiesel. In the last section, the spray, combustion and emission characteristics elucidated with respect to the variations of ambient O_2 level and unsaturation level in the constant volume bomb and diesel engine are highlighted. Future works are suggested in Section 8.2 to improve the accuracy of current numerical results.

8.1.1   Thermo-Physical Properties of Biodiesel

- Based on the sensitivity analyses of non-reacting and reacting sprays performed for CME and SME, 5 significant thermo-physical properties are identified. These properties include latent heat of vaporisation, liquid density, liquid heat capacity, liquid surface tension and vapour pressure.

- Meanwhile, liquid thermal conductivity, liquid viscosity, second virial coefficient, vapour diffusivity, vapour thermal conductivity and vapour viscosity contribute insignificant effect to the spray development of CME and SME.

- The development of vapour spray is unaffected by the replacement of thermo-physical properties since a marginal RPD of 2.5% is obtained for the VPL predictions.

- Among the identified thermo-physical properties for both CME and SME, latent heat of vaporisation gives the largest deviations of 35.0% in LPL, 12.1% in ID period and 8.6% in LOL.

- However, the poor mixing predicted for latent heat of vaporisation as indicated by the higher mixture fraction contributes to a 22.8% decreased SVF peak as compared to that of baseline case.

- On the other hand, liquid density demonstrates two contrasting effects on the soot concentration. The SVF peak predicted for SME is reduced by 33.1%, while the SVF peak for CME is raised by 8.0%. This proves that the effects of thermo-physical properties vary according to the unsaturation levels.

- Despite the varied LPL, ID period and LOL predicted for vapour pressure, liquid heat capacity, liquid surface tension and liquid density, these variations are insufficient to affect the SVF.

- In the reacting spray analyses, the individual thermo-physical property exhibits identical effects as compared to those of non-reacting spray, although at reduced level of magnitudes.

- Apart from that, coupled effects among the thermo-physical properties are also discovered, where the effects are combined from the effects of individual thermo-physical property.

- These results thus show that the individual and coupled effects of the thermo-physical properties are important to the development of the fuel spray and soot.

8.1.2 Reduced Chemical Kinetic Mechanism for Biodiesel

- A generic reduced chemical kinetic mechanism with 92 species and 360 reactions is formulated.

- The reduction methodology applied is important to retain the important species and reactions that are related to the events of ignition, combustion and emissions formation.

- The reduced mechanism successfully reproduced the ID periods under 72 shock tube conditions, where maximum deviations of 40.0% and 67.0% are attained, respectively as compared to the detailed mechanism predictions and experimental data.

- Besides, species profiles such as CO, C_2H_4, MD and MD9D under the JSR conditions are also satisfactorily replicated by the reduced mechanism, when compared to the experimental measurements and detailed mechanism predictions.

- Furthermore, the ID periods and LOL predicted by the reduced mechanism for the reacting spray, at initial temperatures of 900 K and 1000 K achieve maximum deviations of 29.8% and 43.4%, respectively. These predictions are comparatively better than those of the reduced mechanisms included in the comparison study.

- Meanwhile, the predicted SVFs in terms of qualitative and quantitative distributions also show good agreement with the experimental measurements.

8.1.3   Spray, Combustion and Emission Characteristics of Biodiesel

Effects of Ambient O_2 Level

- When the ambient O_2 level is increased from 15.0 to 21.0% in the constant volume bomb, the LPL is shortened by a maximum deviation of 5.9%. Besides, the ID period and LOL are also shortened by maximum deviations of 24.0% and 24.3%, respectively.

- The flame development is also changed from radial growth to forward propagation, where the flame temperature for Case II is increased by 400 K. This shows that enhanced combustion efficiency is obtained for Case II since shorter LPL denotes better air-fuel mixing and higher fuel evaporation rate.

- For the soot mass concentration, increment by twice is predicted for Case II as compared to that of Case I. This is resulted by the enhanced C_2H_2 mass fractions and soot formation rates.

- In terms of emissions, the mass fractions of CO and CO_2 for Case II are increased by 1.6 and 1.2 times, respectively when compared to those of Case I.

Effects of Unsaturation Level

- The change of fuel composition from low unsaturation level (represented by CME) to high unsaturation level (represented by SME) demonstrates retardations under both the conditions of constant volume bomb and diesel engine.

- In the constant volume bomb, the ID period calculated for SME is elongated by 0.6% whereas the LOL is shortened by 2.7%. Similarly, the predicted ID period in the diesel engine for SME is delayed by 0.36° when compared to that of CME.

- As such, shorter spray development and higher in-cylinder pressures and temperatures are obtained for SME.

- The longer ID periods recorded in the constant volume bomb and diesel engine are resulted by the greater number of double bonds contained in SME. As such, the flame temperatures of SME in both constant volume bomb and diesel engine are higher than those of CME.

- Additionally, higher rates of soot formation are observed for SME. Thus, the peak soot mass concentrations for SME in the constant volume bomb and diesel engine are also significantly enhanced by 20.0% and 23.1%, respectively.

- In terms of emissions, the simulation results in both the constant volume bomb and diesel engine combustion display identical trends. Increased levels of CO and NO are predicted for SME, where a maximum deviation of 14.2% is achieved when the predictions are compared to those of CME. Meanwhile, the productions of CO_2 under both the constant volume bomb and diesel engine conditions are unaffected by the increase of unsaturation level.

- CME generally offers better combustion efficiency than SME does. This is because the shorter ID period of CME, which corresponds to greater CN, indicates that the fuel is more stable and less prone to engine knock. Besides, decreased emissions of soot, CO and NO are also achieved with CME as compared to those of SME.

- Based on these results, the predictions generated in the constant volume bomb adequately represent the development of spray, combustion and emission took place in the diesel engine.

8.2   Future Work

For future work, the thermo-physical properties evaluated for CME, PME, RME and SME can be validated against experimental measurements. Meanwhile, the numerical simulations with integrated reduced chemical kinetic mechanism, using the constant volume bomb setup can be extended to different initial temperatures in order to emulate the temperature at SOI in the diesel engine. This will improve the understanding of quasi-steady spray characteristics for biodiesel, where comparisons against the results predicted at initial temperature of 900 K can be performed.

The simulations of diesel engine combustion can be further performed under different engine speed and load conditions, such that the combustion characteristics for biodiesel can be further elucidated. Besides, different fuel injection strategies can also be adopted to reduce the NO emissions for biodiesel.

References

1.   Ng H. K. and Gan S., "Combustion performance and exhaust emissions from the non-pressurised combustion of palm oil biodiesel blends", Applied Thermal Engineering 30, 2476-2484, 2010.

2.   Ghorbani A., Bazooyar B., Shariati A., Mohammad S., Ajami H. and Naderi A., "A comparative study of combustion performance and emission of biodiesel blends and diesel in an experimental boiler", Applied Energy 88, 4725-4732, 2011.

3.   Ng J. H., Ng H. K. and Gan S., "Engine-out characterisation using speed-load mapping and reduced test cycle for a light-duty diesel engine fuelled with biodiesel blends", Fuel 90, 2700-2709, 2011.

4.   Ng J. H., Ng H. K. and Gan S., "Characterisation of engine-out responses from a light-duty diesel engine fuelled with palm methyl ester (PME)", Applied Energy 90, 58-67, 2012.

5.   Balat M. and Balat H., "Progress in biodiesel processing", Applied Energy 87, 1815-1835, 2010.

6.   Rounce P., Tsolakis A. and York A. P. E., "Speciation of particulate matter and hydrocarbon emissions from biodiesel combustion and its reduction by aftertreatment", Fuel 96, 90-99, 2012.

7.   Westbrook C. K., Pitz W. J. and Curran H. J., "Chemical kinetic modeling study of the effects of oxygenated hydrocarbons on soot emissions from diesel engines", Journal of Physical Chemistry A 110(21), 6912-6922, 2006.

8.   Ng J. H., Ng H. K. and Gan S., "Advances in biodiesel fuel for application in compression ignition engines", Clean Technologies and Environmental Policy 12, 459-493, 2010.

9.   Ng J. H., Ng H. K. and Gan S., "Recent trends in policies, socioeconomy and future directions of the biodiesel industry", Clean Technologies and Environmental Policy 12, 213-238, 2010.

10.   Xue J., Grift T. E. and Hansen A. C., "Effect of biodiesel on engine performances and emissions", Renewable and Sustainable Energy Review 15(2), 1098-1116, 2011.

11.	Murillo S., Míguez J. L., Porteiro J., Granada E. and Morán J. C., "Performance and exhaust emissions in the use of biodiesel in outboard diesel engines", Fuel 86, 1765-1771, 2007.

12.	Zhang S., Broadbelt L. J., Androulakis I. P. and Ierapetritou M. G., "Comparison of biodiesel performance based on HCCI engine simulation using detailed mechanism with on-the-fly reduction", Energy and Fuels 26, 976-983, 2012.

13.	Lapuerta M., Armas O. and Rodríguez-Fernández J., "Effect of biodiesel fuels on diesel engine emissions", Progress in Energy and Combustion Science 34, 198-223, 2008.

14.	Fontaras G., Karavalakis G., Kousoulidou M., Tzamkiozis T., Pistikopoulos P., Ntziachristos L., Bakeas E., Stournas S. and Samaras Z., "Effects of biodiesel on passenger car fuel consumption, regulated and non-regulated pollutant emissions over legislated and real-world driving cycles", Fuel 88, 1608-1617, 2009.

15.	Mohamed Ismail H., Ng H. K. and Gan S., "Evaluation of non-premixed combustion and fuel spray models for in-cylinder diesel engine simulation", Applied Energy 90, 271-279, 2012.

16.	Pang K. M., Ng H. K. and Gan S., "Development of an integrated reduced fuel oxidation and soot precursor formation mechanism for CFD simulations of diesel combustion", Fuel 90, 2902-2914, 2011.

17.	Um S. and Park S.W., "Modeling effect of the biodiesel mixing ratio on combustion and emission characteristics using a reduced mechanism of methyl butanoate", Fuel 89, 1415-1421, 2010.

18.	Dagaut P., Gaïl S. and Sahasrabudhe M., "Rapeseed oil methyl ester oxidation over extended ranges of pressure, temperature, and equivalence ratio: Experimental and modeling kinetic study", Proceedings of the Combustion Institute 31(2), 2955-2961, 2007.

19.	Fisher E. M., Pitz W. J., Curran H. J. and Westbrook C. K. "Detailed chemical kinetic mechanisms for combustion of oxygenated fuels", Proceedings of the Combustion Institute 28(2), 1579-1586, 2000.

20.	Seshadri K., Lu T., Herbinet O., Humer S., Niemann U., Pitz W. J., Seiser R. and Law C. K., "Experimental and kinetic modeling study of

extinction and ignition of methyl decanoate in laminar non-premixed flows", Proceedings of the Combustion Institute 32(1), 1067-1074, 2009.

21.   Lu T. and Law C. K., "Toward accommodating realistic fuel chemistry in large-scale computations", Progress in Energy and Combustion Science 35, 192-215, 2009.

22.   Gail S., Thomson M. J., Sarathy S. M., Syed S. A., Dagaut P., Diévart P., Marchese A. J. and Fryer F. L., "A wide-ranging kinetic modeling study of methyl butanoate combustion", Proceedings of the Combustion Institute 31, 305-311, 2007.

23.   Dooley S., Curran H. J. and Simmie J. M., "Autoignition measurements and a validated kinetic model for the biodiesel surrogate, methyl butanoate", Combustion and Flame 153, 2-32, 2008.

24.   Gaïl S., Sarathy S. M., Thomson M. J., Diévart P. and Dagaut P., "Experimental and chemical kinetic modeling study of small methyl esters oxidation: Methyl (E)-2-butenoate and methyl butanoate", Combustion and Flame 155, 635-650, 2008.

25.   He K., Androulakis I. P. and Ierapetritou M. G., "On-the-fly reduction of kinetic mechanisms using element flux analysis", Chemical Engineering Science 65, 1173-1184, 2010.

26.   Contino F., Jeanmart H., Lucchini T. and D'Errico G., "Coupling of in situ adaptive tabulation and dynamic adaptive chemistry: An effective method for solving combustion in engine simulations", Proceedings of the Combustion Institute 33, 3057-3064, 2011.

27.   Pope S. B., "Computationally efficient implementation of combustion chemistry using in situ adaptive tabulation", Combustion Theory Modelling 1, 41-63, 1997.

28.   Jangi M., Yu R. and Bai X. S., "A multi-zone chemistry mapping approach for direct numerical simulation of auto-ignition and flame propagation in a constant volume enclosure", Combustion Theory Modelling 16(2), 221-249, 2012.

29.   Jangi M. and Bai X. S., "Multidimensional chemistry coordinate mapping approach for combustion modelling with finite-rate chemistry", Combustion Theory Modelling 16(6), 1109-1132, 2012.

30. Perini F., Galligani E. and Reitz R. D., "An analytical jacobian approach to sparse reaction kinetics for computationally efficient combustion modeling with large reaction mechanisms", Energy and Fuels 26, 4804-4822, 2012.

31. Cheng X., Ng H. K., Gan S. and Ho J. H., "Advances in computational fluid dynamics (CFD) modeling of in-cylinder biodiesel combustion:, Energy and Fuels 27, 4489-4506, 2013.

32. Ra Y., Reitz R., McFarlane J. and Daw C., "Effects of fuel physical properties on diesel engine combustion using diesel and bio-diesel fuels", SAE International Journal of Fuels and Lubricant 1(1), 703-718, 2008.

33. Cheng X, Ng HK, Gan S, Ho JH. "Development of biodiesel skeletal mechanisms for kinetic combustion modelling", SAE Techical Paper 2013-01-2633, 2013.

34. Chakravarthy K., McFarlane J., Daw S. and Ra Y., "Physical properties of bio-diesel and its implications for use of bio-diesel in diesel engines", SAE Technical Paper 2007-01-4030, 2007.

35. Genzale C. L. and Pickett L. M., "Liquid Penetration of Diesel and Biodiesel Sprays at Late-Cycle Post-Injection Conditions", SAE International Journal of Engines 3(1), 479-495, 2010.

36. Nerva J-G, Genzale C. L., Kook S., Garcia-Oliver J. M. and Pickett L. M., "Fundamental spray and combustion measurements of soy methyl-ester biodiesel", International Journal of Energy Research 14(4), 373-390, 2012.

37. Ochoterena R., Larsson M., Andersson S. and Denbratt I., "Optical studies of spray development and combustion characterization of oxygenated and Fischer-Tropsch fuels", SAE Technical Paper 2008-01-1393, 2008.

38. He C., Ge Y., Tan J. and Han X., "Spray properties of alternative fuels: A comparative analysis of biodiesel and diesel", International Journal of Energy Research 32, 1329-1338, 2008.

39. Kuti O. A., Zhu J., Nishida K., Wang X. and Huang Z., "Characterization of spray and combustion processes of biodiesel fuel injected by diesel engine common rail system", Fuel 104, 838-846, 2013.

40.   Lee Y. and Huh K. Y., "Numerical study on spray and combustion characteristics of diesel and soy-based biodiesel in a CI engine", Fuel 113, 537-545, 2013.

41.   Mohamed Ismail H., Ng H. K., Cheng X., Gan S., Lucchini T. and D'Errico G., "Development of thermophysical and transport properties for the CFD simulations of in-cylinder biodiesel spray combustion", Energy and Fuels 26(8), 4857-4870, 2012.

42.   Demirbas A., "Progress and recent trends in biodiesel fuels", Energy Conversion and Management 50, 14-34, 2009.

43.   Wu Y., Huang R., Leick M. and Lee C. F., "Effect of ambient temperature on flame lift-off and soot formation of biodiesel spray", SAE Techical Paper 2010-01-0606, 2010.

44.   Feng Q., Jalali A., Fincham A. M., Wang Y. L., Tsotsis T. T. and Egolfopoulos F. N., "Soot formation in flames of model biodiesel fuels", Combustion and Flame 159, 1876-1893, 2012.

45.   Schönborn A., Ladommatos N., Williams J., Allan R. and Rogerson J., "The influence of molecular structure of fatty acid monoalkyl esters on diesel combustion", Combustion and Flame 156, 1396-1412, 2009.

46.   Lapuerta M., Herreros J. M., Lyons L.L., García-Contreras R. and Briceño Y., "Effect of the alcohol type used in the production of waste cooking oil biodiesel on diesel performance and emissions", Fuel 87, 3161-3169, 2008.

47.   Fontaras G., Kousoulidou M., Karavalakis G., Tzamkiozis T., Pistikopoulos P., Bakeas E., Stournas S. and Samaras Z., "Effects of low concentration biodiesel blend application on modern passenger cars. Part 1: Feedstock impact on regulated pollutants, fuel consumption and particle emissions", Environmental Pollution 158, 1451-1460, 2010.

48.   Bergthorson J. M. and Thomson M. J., "A review of the combustion and emissions properties of advanced biofuels and their impact on existing and future engines", Renewable and Sustainable Energy Review 42, 1-46, 2014.

49.   Ban-Weiss G. A., Chen J.Y., Buchholz B. A. and Dibble R. W., "A numerical investigation into the anomalous slight NO_x increase when burning biodiesel; A new (old) theory", Fuel Processing Technology 88, 659-667, 2007.

50. Brakora J., Ra Y. and Reitz R. D., "Combustion model for biodiesel-fueled engine simulations using realistic chemistry and physical properties", SAE Technical Paper 2011-01-0831, 2011.

51. Brakora J., Ra Y., Reitz R., McFarlane J. and Daw C., "Development and validation of a reduced reaction mechanism for biodiesel-diesel fueled engine simulations," SAE International Journal of Fuels and Lubrricant 1(1), 675-702, 2008.

52. Luo Z., Plomer M., Lu T., Som S., Longman D. E., Sarathy S. M. and Pitz W. J., "A reduced mechanism for biodiesel surrogates for compression ignition engine applications", Fuel 99, 143-153, 2012.

53. Mohamed Ismail H., Ng H. K., Gan S., Lucchini T. and Onorati A., "Development of a reduced biodiesel combustion kinetics mechanism for CFD modelling of a light-duty diesel engine", Fuel 106, 388-400, 2013.

54. An H., Yang W. M., Maghbouli A., Chou S. K. and Chua K. J., "Detailed physical properties prediction of pure methyl esters for biodiesel combustion modelling", Applied Energy 102, 647-656, 2013.

55. An H., Yang W. M., Maghbouli A., Li J. and Chua K. J., "A skeletal mechanism for biodiesel blend surrogates combustion", Energy Conversion and Management 81, 51-59, 2014.

56. Luo Z., Lu T., Maciaszek M. J., Som S. and Longman D. E., "A reduced mechanism for high-temperature oxidation of biodiesel surrogates", Energy and Fuels 24(12), 6283-6293, 2010.

57. Westbrook C. K., Naik C. V., Herbinet O., Pitz W. J., Mehl M., Sarathy S. M. and Curran H. J., "Detailed chemical kinetic reaction mechanisms for soy and rapeseed biodiesel fuels", Combustion and Flame 158, 742-755, 2011.

58. Golovitchev V. I. and Yang J., "Construction of combustion models for rapeseed methyl ester bio-diesel fuel for internal combustion engine applications", Biotechnol Advances 27(5), 641-655, 2009.

59. Dayma G., Gaïl S. and Dagaut P., "Experimental and kinetic modeling study of the oxidation of methyl hexanoate", Energy and Fuels 22, 1469-1479, 2008.

60. Glaude P. A., Herbinet O., Bax S., Biet J., Warth V. and Battin-Leclerc F., "Modeling of the oxidation of methyl esters-Validation for methyl hexanoate, methyl heptanoate, and methyl decanoate in a jet-stirred reactor", Combustion and Flame 157, 2035-2050, 2010.

61. Dayma G., Togbé C. and Dagaut P., "Detailed kinetic mechanism for the oxidation of vegetable oil methyl esters: New evidence from methyl heptanoate", Energy and Fuels 23, 4264-4268, 2009.

62. Dayma G., Sarathy S. M., Togbé C., Yeung C., Thomson M. J. and Dagaut P., "Experimental and kinetic modeling of methyl octanoate oxidation in an opposed-flow diffusion flame and a jet-stirred reactor", Proceedings of the Combustion Institute 33, 1037-1043, 2011.

63. Sarathy S. M., Thomson M. J., Pitz W. J. and Lu T., "An experimental and kinetic modeling study of methyl decanoate combustion", Proceedings of the Combust Institute 33, 399-405, 2011.

64. Shi Y., Ge H. W., Brakora J. L. and Reitz R. D., "Automatic chemistry mechanism reduction of hydrocarbon fuels for HCCI engines based on DRGEP and PCA methods with error control", Energy and Fuels 24, 1646-1654, 2010.

65. Diévart P., Won S. H., Dooley S., Dryer F. L. and Ju Y., "A kinetic model for methyl decanoate combustion", Combustion and Flame 159, 1793-1805, 2012.

66. Herbinet O., Pitz W. J. and Westbrook C. K., "Detailed chemical kinetic oxidation mechanism for a biodiesel surrogate", Combustion and Flame 154, 507-528, 2008.

67. Herbinet O., Biet J., Hakka M. H., Warth V., Glaude P.A., Nicolle A. and Battin-Leclerc F., "Modeling study of the low-temperature oxidation of large methyl esters from C11 to C19", Proceedings of the Combustion Institute 33, 391-398, 2011.

68. Herbinet O., Pitz W. J. and Westbrook C. K., "Detailed chemical kinetic mechanism for the oxidation of biodiesel fuels blend surrogate", Combustion and Flame 157, 893-908, 2010.

69. Lawrence Livermore National Laboratory Physical and Life Sciences Directorate, Available at <https://www-

pls.llnl.gov/?url=science_and_technology-chemistry-combustion-biodiesel>
[Accessed July 26, 2012].

70.   Luo Z., Plomer M., Lu T., Som S. and Longman D.E., "A reduced mechanism for biodiesel surrogates with low-temperature chemistry", 7th US National Combustion Meeting, Eastern States Section of the Combustion Institute, Atlanta, U.S., March 20- 23, 2011.

71.   Ng H. K., Gan S., Ng J. H. and Pang K. M., "Development and validation of a reduced combined biodiesel-diesel reaction mechanism", Fuel 104, 620-634, 2013.

72.   Tran L. S., Sirjean B., Glaude P. A., Fournet R. and Battin-Leclerc F., "Progress in detailed kinetic modeling of the combustion of oxygenated components of biofuels", Energy 43, 4-18, 2012.

73.   Anand K., Sharma R. P. and Mehta P. S., "A comprehensive approach for estimating thermo-physical properties of biodiesel fuels", Applied Thermal Engineering 31(2-3), 235-242, 2011.

74.   Wang W. and Oehlschlaeger M. A., "A shock tube study of methyl decanoate autoignition at elevated pressures", Combustion and Flame 159(2), 476-481, 2012.

75.   Allen C. M., Toulson E., Hung D. L. S., Schock H., Miller D. and Lee T., "Ignition characteristics of diesel and canola biodiesel sprays in the low-temperature combustion regime", Energy and Fuels 25, 2896-2908, 2011.

76.   Graboski M. S. and McCormick R. L., "Combustion of fat and vegetable oil derived fuels in diesel engines", Progress in Energy and Combustion Science 24, 125-164, 1998.

77.   Patel A., Kong S. and Reitz R. D., "Development and validation of a reduced reaction mechanism for HCCI engine simulations", SAE Technical Paper 2004-01-0558, 2004.

78.   Gustavsson J. and Golovitchev V. I., "Spray combustion simulation based on detailed chemistry approach for diesel fuel surrogate model", SAE Technical Paper 2003-01-1848, 2003.

79.   Tao F., Golovitchev V. I. and Chomiak J., "Self-ignition and early combustion process of n-heptane sprays under diluted air conditions:

numerical studies based on detailed chemistry", SAE Technical Paper 2000-01-2931, 2000.

80. Brakora J. and Reitz R. D., "A comprehensive combustion model for biodiesel-fueled engine simulations", SAE Technical Paper 2013-01-1099, 2013.

81. Westbrook C. K., Pitz W. J., Sarathy S. M. and Mehl M., "Detailed chemical kinetic modeling of the effects of CC double bonds on the ignition of biodiesel fuels", Proceedings of the Combustion Institute 34(2), 3049-3056, 2013.

82. Naik C. V., Westbrook C. K., Herbinet O., Pitz W. J. and Mehl M., "Detailed chemical kinetic reaction mechanism for biodiesel components methyl stearate and methyl oleate", Proceedings of the Combustion Institute 33, 383-389, 2011.

83. Salamanca M., Mondragón F., Agudelo J. R., Benjumea P. and Santamaría A., "Variations in the chemical composition and morphology of soot induced by the unsaturation degree of biodiesel and a biodiesel blend", Combustion and Flame 159, 1100-1108, 2012.

84. Bennadji H, Biet J, Coniglio-Jaubert L, Billaud F, Glaude PA, Battin-Leclerc F. "Experimental autoignition of C4-C6 saturated and unsaturated methyl and ethyl esters", In: Proceedings of the European Combustion Meeting, 2009: 14-17.

85. Hadjali K., Crochet M., Vanhove G., Ribaucour M. and Minetti R., "A study of the low temperature autoignition of methyl esters", Proceedings of the Combustion Institute 32 I, 239-246, 2009.

86. Parsons B. I. and Hinshelwood C., "352. The oxidation of hydrocarbons and their derivatives. Part II. Structural effects in the ester series", Journal of Chemical Society 1799-1803, 1956.

87. Niemeyer K. E., Sung C. J. and Raju M. P., "Skeletal mechanism generation for surrogate fuels using directed relation graph with error propagation and sensitivity analysis", Combustion and Flame 157, 1760-1770, 2010.

88.   Zheng X. L., Lu T. F. and Law C. K., "Experimental counterflow ignition temperatures and reaction mechanisms of 1,3-butadiene", Proceedings of the Combustion Institute. 31 I, 367-375, 2007.

89.   Pepiot-Desjardins P. and Pitsch H., "An efficient error-propagation-based reduction method for large chemical kinetic mechanisms", Combustion and Flame 154, 67-81, 2008.

90.   Metcalfe W. K., Dooley S., Curran H. J., Simmie J. M., El-Nahas A. M. and Navarro M. V., "Experimental and modeling study of $C_5H_{10}O_2$ ethyl and methyl esters", Journal of Physical Chemistry A 111, 4001-4014, 2007.

91.   Sarathy S. M., Gaïl S., Syed S. A., Thomson M. J. and Dagaut P., "A comparison of saturated and unsaturated C4 fatty acid methyl esters in an opposed flow diffusion flame and a jet stirred reactor", Proceedings of the Combustion Institute 31 I, 1015-1022, 2007.

92.   Walton S. M., Wooldridge M. S. and Westbrook C. K., "An experimental investigation of structural effects on the auto-ignition properties of two C5 esters", Proceedings of the Combustion Institute 32 I, 255-262, 2009.

93.   Errico G. D., Ettorre D., Lucchini T. and Milano M., "Simplified and detailed chemistry modeling of constant-volume diesel combustion experiments", SAE Technical Paper 2008-01-0954, 2008.

94.   Liang L., Stevens J. G. and Farrell J. T., "A dynamic adaptive chemistry scheme for reactive flow computations", Proceedings of the Combustion Institute 32 I, 527-534, 2009.

95.   Curran H. J., Gaffuri P., Pitz W. J. and Westbrook C. K., "A comprehensive modeling study of n-heptane oxidation", Combustion and Flame 114, 149-177, 1998.

96.   Hakka M. H., Glaude P. A., Herbinet O. and Battin-Leclerc F., "Experimental study of the oxidation of large surrogates for diesel and biodiesel fuels", Combustion and Flame 156, 2129-2144, 2009.

97.   Ciezki H. K. and Adomeit G., "Shock-tube investigation of self-ignition of n-heptane-air mixtures under engine relevant conditions", Combustion and Flame 93, 421-433, 1993.

98.   Brakora J. L. and Reitz R. D., "A comprehensive combustion model for biodiesel-fueled engine simulations", SAE Technical Paper 2013-01-1099, 2013.

99.   Lu T. and Law C. K., "Linear time reduction of large kinetic mechanisms with directed relation graph: n-heptane and iso-octane", Combustion and Flame 144, 24-36, 2006.

100.   Lu T. and Law C. K., "A directed relation graph method for mechanism reduction", Proceedings of the Combustion Institute 30, 1333-1341, 2005.

101.   Nagy T. and Turanyi T., "Reduction of very large reaction mechanisms using methods based on simulation error minimization", Combustion and Flame 156, 417-428, 2009.

102.   Lu T. and Law C. K., "On the applicability of directed relation graphs to the reduction of reaction mechanisms", Combustion and Flame 146, 472-483, 2006.

103.   Sun W., Chen Z., Gou X. and Ju Y., "A path flux analysis method for the reduction of detailed chemical kinetic mechanisms", Combustion and Flame 157, 1298-1307, 2010.

104.   Kee R., Lutz A. and Rupley F., "OPPDIF: A FORTRAN Program for Computing Opposed-Flow Diffusion Flames", Technical Report for Sandia Laboratories, Sandia National Laboratories, Livermore, 1997.

105.   Goodwin D., "Cantera: Object-Oriented Software for Reacting Flows", A Technical Report: California Institute of Technology, 2005.

106.   Reid R. C., Prausnitz J. M. and Sherwood T. K., "The properties of gases and liquids", 3rd edition, McGraw-Hill, New York, 1977.

107.   Reid R. C., Prausnitz J. M. and Sherwood T. K., "The properties of gases and liquids", 4th edition, McGraw-Hill, New York, 1987.

108.   Poling B., Prausnitz J. M. and O'Connell J., "The properties of gases and liquids", 5th edition, McGraw-Hill, New York, 2001.

109.   Knovel Critical Tables 2nd edition, Available at <http://knovel.com/web/portal/browse/display?_EXT_KNOVEL_DISPLAY_bookid=1187&VerticalID=0> [Accessed July 26, 2012].

110. Design Institute for Physical Property Data, Available at <http://knovel.com/web/portal/browse/display?_EXT_KNOVEL_DISPLAY_bookid=1187&VerticalID=0> [Accessed July 26, 2012].

111. Stringer V., McCrady J., Hansen A. and Lee C. F., "Modeling biodiesel spray breakup with well-defined fuel properties", In: ILASS-Americas. Chicago, U.S., May 15-17, 2007.

112. Yuan W., Hansen A. C. and Zhang Q., "Predicting the physical properties of biodiesel for combustion modelling", ASAE 46(6), 1487-1493, 2003.

113. Lee B. I. and Kesler M. G., "A generalized thermodynamic correlation based on three-parameter corresponding states", American Institute Chemical Engineers Journal 21, 510-527, 1975.

114. Kay W., "Density of hydrocarbon gases and vapors", Industrial and Engineering Chemistry 28, 1014-1019, 1936.

115. Yaws C., "The yaws handbook of thermodynamic properties for hydrocarbon and chemicals", Gulf Publishing, Houston, 2007.

116. Joback K. G., "A unified approach to physical property estimation using multivariate statistical techniques", Masters Thesis, Massachusetts Institute of Technology, 1984.

117. Joback K. G. and Reid R. C., "Estimation of pure-component properties from group-contributions", Chemical Engineering Communications 57, 233-243, 1987.

118. Constantinou L. and Gani R., "New group contribution method for estimating properties of pure compounds", American Institute Chemical Engineers Journal 40, 1697-1710, 1994.

119. Wilson G. and Jasperson L., "Critical constants Tc, Pc, estimation based on zero, first and second order methods", In: AIChE Spring Meeting, New Orleans, U.S., February 25-29, 1996.

120. Marrero-Morejón J. and Pardillo-Fontdevila E., "Estimation of pure compound properties using group-interaction contributions", American Institute Chemical Engineers Journal 45, 615-621, 1999.

121.   Huber M. L., Lemmon E. W., Kazakov A., Ott L. S. and Bruno T. J., "Model for the thermodynamic properties of a biodiesel fuel", Energy and Fuels 23, 3790-3997, 2009.

122.   Rackett H., "Equation state for saturated liquids", Journal of Chemical Engineering Data 15, 514-517, 1970.

123.   Spencer C. F. and Danner R. P., "Improved equation for prediction of saturated liquid density", Journal of Chemical Engineering Data 17, 236-241, 1972.

124.   Elbro H., Fredenslund A. and Rasmussen P., "Group contribution method for the prediction of liquid densities as a function of temperature for solvents, oligomers and polymers", Industrial and Engineering Chemistry Research 30(12), 2576-2582, 1991.

125.   Yamane K., Ueta A. and Shimamoto Y., "Influence of physical and chemical properties of biodiesel fuels on injection, combustion and exhaust emission characteristics in a DI-CI engine", In: 5th International Symposium on Diagnostics and Modelling of Combustion in Internal Combustion Engines, Nagoya, Japan, July 1-4, 2001.

126.   Allen C. A. W., Watts K. C., Ackman R.G. and Pegg M. J., "Predicting the viscosity of biodiesel fuels from their fatty acid ester composition", Fuel 78, 1319-1326, 1999.

127.   Schumacher L., Chellappa A., Wetherell W. and Russell M., "The physical and chemical characterization of biodiesel low sulphur diesel fuels blends", Final Report to the National Biodiesel Board, University of Missouri,1995.

128.   Riddick J. and Bunger W., "Organic solvents: physical properties and methods of purification", Wiley Interscience, New York, 1970.

129.   Letsou A. and Stiel L., "Viscosity of saturated nonpolar liquids at elevated pressures", American Institute of Chemical Engineers Journal 19, 409-411, 1973.

130.   Allen C. A. W., Watts K. C. and Ackman R. G., "Predicting the surface tension of biodiesel fuels from their fatty acid composition", Journal of the American Oil Chemists' Society 76(3), 317-323, 1999.

131.   Durán A., Carmona M. and Monteagudo JM. "Modelling soot and SOF emissions from a diesel engine", Chemosphere 56, 209-225, 2005.

132.   Van Bommel M. J., Oonk H. A. J. and Van Miltenburg J. C., "Heat capacity measurements of 13 methyl esters of n-carboxylic acids from methyl octanoate to methyl eicosanoate between 5 K and 350 K", Journal of Chemical Engineering Data 49, 1036-1042, 2004.

133.   Herb S., Magidman P. and Reimansc R., "Observations on response factors for thermal conductivity detectors in GLC analysis of fatty acid methyl esters", Journal of the American Oil Chemists' Society 44(1), 32-36, 1967.

134.   Tseng C. C. and Viskanta R., "Effect of radiation absorption on fuel droplet evaporation", Combustion Science and Technology 177, 1511-1542, 2005.

135.   Huber M. and Perkins M., "Thermal conductivity correlations for minor constituent fluids in natural gas: n-octane, n-nonane and n-decane", Fluid Phase Equilibria 227, 47-55, 2005.

136.   Baroncini C., Filippo P., Latini G. and Pacetti M., "Organic liquid thermal conductivity: a prediction method in the reduced temperature range of 0.3 to 0.8", International Journal of Thermophysics 2(1), 21-38, 1984.

137.   Araújo M. E. and Meireles M. A. A., "Improving phase equilibrium calculation with the Peng-Robinson EOS for fats and oils related compounds/supercritical CO_2 systems", Fluid Phase Equilibria 169, 49-64, 2000.

138.   Ceriani R. and Meirelles A. J. A., "Predicting vapor-liquid equilibria of fatty systems", Fluid Phase Equilibria 215, 227-236, 2004.

139.   Pitzer K. S., Lippmann D. Z., Curl R., Huggins C. M. and Petersen D. E., "The volumetric and thermodynamic properties of fluids. II. Compressibility factor, vapor pressure and entropy of vaporization", Journal of the American Chemical Society 77, 3433-3440, 1955.

140.   Chung T. H., Ajlan M., Lee L. L. and Starling K. E., "Generalized multiparameter correlation for nonpolar and polar fluid transport properties", Industrial and Engineering Chemistry Research 27(4), 671-679, 1988.

141.   Chung T-H., Lee L. L. and Starling K. E., "Applications of kinetic gas theories and multiparameter correlation for prediction of dilute gas viscosity

and thermal conductivity", Industrial and Engineering Chemistry Fundamentals 23, 8-13, 1984.

142.   Rihani D. and Doraiswamy L. "Estimation of heat capacity of organic compounds from group contribution", Industrial and Engineering Chemistry Fundamentals, 4, 17, 1965.

143.   Skelland A. "Diffusional Mass Transfer", Krieger Publishing Company, Florida, 1985.

144.   Wilke C. and Lee C., "Estimation of diffusion coefficients for gases and vapours", Industrial and Engineering Chemistry 47, 1253, 1955.

145.   Tsonopoulos C., "An empirical correlation of second virial coefficients", American Institute of Chemical Engineers Journal 20, 263-272, 1974.

146.   Tamim J. and Hallett W. L. H., "A continuous thermodynamics model for multicomponent droplet vaporization", Chemical Engineering Science 50, 2933-2942, 1995.

147.   Grunberg L. and Nissan A. H., "Mixture law for viscosity", Nature 164, 799, 1949.

148.   Sastri S. and Rao K., "A new group contribution method for predicting viscosity of organic liquids", The Chemical Engineering Journal 50, 9, 1992.

149.   Przezdziecki J. and Sridhar T., "Prediction of liquid viscosities", American Institute Chemical Engineers Journal 31(2), 333-335, 1985.

150.   Chevalier J., Petrino P. and Gaston-Bonhomme Y., "Estimation method for the kinematic viscosity of a liquid-phase mixture", Chemical Engineering Science 43(6), 1303-1309, 1988.

151.   Gaston-Bonhomme Y., Petrino P. and Chevalier J. L., "UNIFAC—VISCO group contribution method for predicting kinematic viscosity: extension and temperature dependence", Chemical Engineering Science 49, 1799-1806, 1994.

152.   Teja A. S. and Rice P., "Generalized corresponding states method for the viscosities of liquid mixtures", Industrial and Engineering Chemistry Fundamentals 20, 77-81, 1981.

153. Teja A. S. and Rice P., "The measurement and prediction of the viscosities of some binary liquid mixtures containing n-hexane", Chemical Engineering Science 36, 7-10, 1981.

154. Macleod D., "On a relation between surface tension and density", Transactions of the Faraday Society 19, 38-41, 1923.

155. Sugden S., "A relation between surface tension, density, and chemical composition", Journal of Chemical Society 125, 1177-1189, 1924.

156. Ruzicka V. and Domalski E. S. "Estimation of the heat-capacities of organic liquids as a function of temperature using group additive. II. Compounds of carbon, hydrogen, halogens, nitrogen, oxygen, and sulphur", Journal of Physical and Chemical Reference Data 22, 619-657, 1993.

157. Antoine C., "Tensions of the vapors; new relationship between the voltages and temperatures", Records of Meeting of the Academy of Science 107, 681-684, 778-780, 836-837, 1888.

158. Riedel L., "A new universal vapor pressure formula. Studies on an extension of the theorem of corresponding states", Chemie Ingenieur Technik 26, 679, 1954.

159. Lydersen A., Greenkorn R. and Hougen O., "Generalized thermodynamic properties of pure fluids", Engineering Report Station 4: University of Wisconsin College Engineering, Wisconsin, 1955.

160. Chapman S. and Cowling T., "The mathematical theory of non-uniform gases", Cambridge Press, New York, 1939.

161. Reichenberg D., "New methods for the estimation of the viscosity coefficients of pure gases at moderate pressures (with particular reference to organic vapours)", American Institute of Chemical Engineers Journal 21, 181-183, 1975.

162. Reichenberg D., "The estimation of the viscosities of gases and gas mixtures", In: Symposium Transport Properties of Fluids and Fluid Mixtures, Glasgow, April 10-11, 1979.

163. Reichenberg D., "The indeterminacy of the values of potential parameters as derived from transport and virial coefficients", American Institute of Chemical Engineers Journal 19, 854-856, 1973.

164. Reichenberg D., "DSC Report 11", National Physical Laboratory, Teddington, England, 1971.

165. Reichenberg D., "The viscosities of gas mixtures at moderate pressures", National Physical Laboratory, Division of Chemical Standards, Teddington, England, 1974.

166. Reichenberg D., "The viscosities of pure gases at high pressures", National Physical Laboratory, Division of Chemical Standards, Glasgow, Scotland, 1975.

167. Wilke C. R., "A viscosity equation for gas mixture", The Journal of Chemical Physics 18, 517, 1950.

168. Fuller E. and Giddings J., "A comparison of methods for predicting gaseous diffusion coefficients", Journal of Gas Chromatography 3, 222-227, 1965.

169. Fuller E., Schettler P. and Giddings J., "New method for prediction of binary gas-phase diffusion coefficients", Industrial and Engineering Chemistry 58(5), 18-27, 1966.

170. Fuller E. N., Ensley K. and Giddings J. C., "Diffusion of halogenated hydrocarbons in helium. The effect of structure on collision cross sections", Journal of Physical Chemistry 73, 3679-3685, 1969.

171. Lee M-J. and Chen J-T., "An improved model of second virial coefficients for polar fluids and fluid mixtures", Journal of Chemical Engineering Japan 31(4), 518-526, 1998.

172. Hayden J. G. and O'Connell J. P., "A generalized method for predicting second virial coefficients", Industrial and Engineering Chemical Process Design and Development 14, 209-216, 1975.

173. Stein F. and Miller E., "Extension of the Hayden-O'Connell correlation to the second virial coefficients of some hydrogen-bonding mixtures", Industrial and Engineering Chemical Process Design and Development 19, 123-138, 1980.

174. Prausnitz J. M., Anderson T., Grens E., Eckert C., Hsieh R. and O'Connell J., "Computer calculations for multicomponent vapour-liquid and liquid-liquid Equilibria", Prentice-Hall, Englewood Cliffs, 1980.

175. Som S., D'Errico G., Longman D. E. and Lucchini T., "Comparison and standardization of numerical approaches for the prediction of non-reacting and reacting diesel sprays", SAE Technical Paper 2012-01-1263, 2012.

176. Pang K. M., Jangi M., Bai X-S. and Schramm J., "Evaluation and optimisation of phenomenological multi-step soot model for spray combustion under diesel engine-like operating conditions", Combustion Theory Modelling 19(3), 1-30, 2015.

177. Mohamed Ismail H., Ng H. K., Gan S. and Lucchini T., "Computational study of biodiesel-diesel fuel blends on emission characteristics for a light-duty diesel engine using OpenFOAM", Applied Energy 111, 827-841, 2013.

178. Cheng W. L. and Lee C. F., "Comparisons of combustion characteristics of biodiesels in a high speed direct injection diesel engine", SAE Technical Paper 2008-01-1638, 2008.

179. Lee Y., Jang K., Han K., Huh K. Y. and Oh S., "Simulation of a heavy duty diesel engine fueled with soybean biodiesel blends in low temperature combustion", SAE Technical Paper 2013-01-1100, 2013.

180. Ng H. K., Gan S., Ng J. H. and Pang K. M., "Simulation of biodiesel combustion in a light-duty diesel engine using integrated compact biodiesel-diesel reaction mechanism", Applied Energy 102, 1275-1287, 2013.

181. Cui X., Kim T., Fujii Y., Kusaka J. and Daisho Y., "The effects of jatropha-derived biodiesel on diesel engine combustion and emission characteristics", SAE Technical Paper 2012-01-1637, 2012.

182. Yang J., Johansson M., Naik C. K., Puduppakkam K., Golovitchev V. and Meeks E., "3D CFD modeling of a biodiesel-fueled diesel engine based on a detailed chemical mechanism", SAE Technical Paper 2012-01-0151, 2012.

183. Ren Y. and Li X., "Numerical simulation of the soot and NO_x formations in a biodiesel-fuelled engine", SAE Technical Paper 2011-01-1385, 2011.

184. Tonini S., Gavaises M. and Arcoumanis C., "Prediction of liquid and vapor penetration of high pressure diesel sprays", SAE Technical Paper 2006-01-0242, 2006.

185.   Kuti O., Sarathy M., Nishida K. and Roberts W., "Studies of spray combustion processes of palm oil biodiesel and diesel fuels using reduced chemical kinetic mechanisms", SAE Technical Paper 2014-01-1143, 2014.

186.   Cui X., Zhou B., Matsunaga M., Fujii Y., Kusaka J. and Daisho Y., "A numerical study of the effects of FAME blends on diesel combustion and emissions characteristics using a 3-D CFD code combined with detailed kinetics and phenomenological soot formation models", SAE International Journal of Fuels and Lubricant 6(3), 839-851, 2013.

187.   Som S., Longman D. E., Ramírez A. I. and Aggarwal S. K., "A comparison of injector flow and spray characteristics of biodiesel with petrodiesel", Fuel 89(12), 4014-4024, 2010.

188.   Som S. and Longman D. E., "Numerical study comparing the combustion and emission characteristics of biodiesel to petrodiesel", Energy and Fuels 25(4), 1373-1386, 2011.

189.   Leung K. M. and Lindstedt R. P., "A simplified reaction mechanism for soot formation in nonpremixed flame", Combustion and Flame 87, 289-305, 1997.

190.   Bella G., "Atomization of high-pressure diesel spray: Experimental validation of a new breakup model", SAE Technical Paper 2001-01-1070, 2001.

191.   Hsiang L-P. and Faeth G. M., "Near-limit drop deformation and secondary breakup", International Journal of Multiphase Flow18, 635-652, 1992.

192.   Birouk M. and Gokalp I., "Current status of droplet evaporation in turbulent flows", Progress in Energy and Combustion Science 32, 408-423, 2006.

193.   Reitz R. D. and Diwakar R., "Effect of drop breakup on fuel sprays", SAE Technical Paper 860469, 1986.

194.   Mondal H. N. and Roy S., "Numerical analysis of droplet combustion in a cylindrical furnace", Journal of Chemical Engineering 24(1), 14-18, 2006.

195.   Nicholls J.A., "Stream and droplet breakup by shock waves", NASA-SP-194, 126-128, 1972.

196. Margot X., Payri R., Gil A., Chavez M. and Pinzello A., "Combined CFD-phenomenological approach to the analysis of diesel sprays under non-evaporative conditions", SAE Technical Paper 2008-01-0962, 2008.

197. Faeth G. M., "Mixing, transport and combustion in sprays", Progress in Energy and Combustion Science 13(4), 293-345, 1987.

198. Stoer J. and Bulirsch R., "Introduction to numerical analysis", New York, Springer-Verlag, 1993.

199. Fenimore C. P. and Jones G. W., "Oxidation of soot by hydroxyl radicals", Journal of Physical Chemistry 71, 593-597, 1967.

200. Lee K. B., Thring M. W. and Beér J. M., "On the rate of combustion of soot in a laminar soot flame", Combustion and Flame 6, 137-145, 1962.

201. European Stationary Cycle (ESC), Available at <https://www.dieselnet.com/standards/cycles/esc.php> [Accessed September 1, 2014].

202. Lin R. and Tavlarides L. L., "Thermophysical properties needed for the development of the supercritical diesel combustion technology: Evaluation of diesel fuel surrogate models", The Journal of Supercritical Fluids 71, 136-146, 2012.

203. Yuan W., Hansen A. C. and Zhang Q., "Vapor pressure and normal boiling point predictions for pure methyl esters and biodiesel fuels", Fuel 84, 943-950, 2005.

204. Tat M. and Van Gerpen J., "The specific gravity of biodiesel and its blends with diesel fuel", Journal of the American Oil Chemists' Society 77, 115-119, 2000.

205. Higgins B. and Sieber D., "Measurement of the flame lift-off location on DI diesel sprays using OH chemiluminescence", SAE Technical Paper 2001-0918, 2001.

206. Siebers D. and Higgins B., "Flame lift-off on direct-injection diesel prays under quiescent conditions", SAE Technical Paper 2001-01-0530, 2001.

207. Goodrum J. W., "Volatility and boiling points of biodiesel from vegetable oils and tallow", Biomass and Bioenergy 22, 205-211, 2002.

208. Guo Y., Wei H., Yang F., Li D., Fang W. and Lin R., "Study on volatility and flash point of the pseudo-binary mixtures of sunflowerseed-

based biodiesel+ethanol", Journal of Hazardous Material 167(1-3), 625-629, 2009.

209.   Okamoto K., Watanabe N., Hagimoto Y., Miwa K. and Ohtani H., "Changes in evaporation rate and vapor pressure of gasoline with progress of evaporation", Fire Safety Journal 44(5), 756-763, 2009.

210.   Lefebvre A., "Gas Turbine Combustion", Taylor and Francis, 1998.

211.   Lu T. and Law C. K., "Strategies for mechanism reduction for large hydrocarbons: n-heptane", Combustion and Flame 154, 153-163, 2008.

212.   Pepiot-Desjardins P. and Pitsch H., "An automatic chemical lumping method for the reduction of large chemical kinetic mechanisms", Combustion Theory Modelling 12(6), 1089-1108, 2008.

213.   Tan P., Hu Z., Lou D. and Li Z., "Exhaust emissions from a light-duty diesel engine with jatropha biodiesel fuel", Energy 39, 356-362, 2012.

214.   Shan R. and Lu T., "Ignition and extinction in perfectly stirred reactors with detailed chemistry", Combustion and Flame, 159, 2069-2076, 2012.

215.   Oh C. B., Lee E. J. and Jung G. J., "Unsteady auto-ignition of hydrogen in a perfectly stirred reactor with oscillating residence times", Chemical Engineering Science 66, 4605-4614, 2011.

216.   Dec J. E., "A conceptual model of DI diesel combustion based on laser-sheet imaging", SAE Technical Paper 970873, 1997.

217.   United States Environmental Protection Agency, Available at <http://www.epa.gov/region1/eco/diesel/retrofits.html> [Accessed April 10, 2015].

218.   Smith G.P., Golden D.M., Frencklach M., Moriarty N.W., Eiteneer B., Goldenberg M., Bowman T.C., Hanson R.K., Song S., Gardiner Jr. W.C., Lissianski V.V. and Qin Z., Gri-Mech 3.0, Available at <http://www.me.berkeley.edu/gri_mech/> [Accessed September 1, 2014].

219.   Jangi M., Lucchini T., D'Errico G. and Bai X. S., "Effects of EGR on the structure and emissions of diesel combustion", Proceedings of the Combustion Institute 34(2), 3091-3098, 2013.

220.   Pickett L. M., Siebers D. L. and Idicheria C. A., "Relationship between ignition processes and the lift-off length of diesel fuel jets", SAE Technical Paper 2005-01-3843, 2005.

221.   Sanghoon K. and Pickett L. M., "Effect of fuel volatility and ignition quality on combustion and soot formation at fixed premixing conditions", SAE International Journal of Engines 2(2), 11-23, 2009.

222.   Lakshminarayanan P.A. and Aghav Y.V., "Modelling diesel combustion", 13th edition, Springer, 2010.

223.   Puhan S., Saravanan N., Nagarajan G. and Vedaraman N., "Effect of biodiesel unsaturated fatty acid on combustion characteristics of a DI compression ignition engine", Biomass and Bioenergy 34, 1079-108, 2010.

224.   Flynn P. F., Hunter G., Farrell L., Durrett R. P., Akinyemi O., Zur Loye A. O., Westbrook C. K. and Pitz W. J., "The inevitability of engine-out NOx emissions from spark-ignited and diesel engines", Proceedings of the Combustion Institute 28, 1211-1218, 2000.

225.   Flynn P. F., Hunter G. L., Durrett R. P., Farrell L. A. and Akinyemi W. C., "Minimum engine flame temperature impacts on diesel and spark-ignition engine NO$_x$ production", SAE Technical Paper 2000-01-1177, 2000.

Appendices

A. Methods of Evaluation for the Thermo-Physical Properties of Biodiesel

Vapour Properties

Second Virial Coefficient

The equation of state for mixtures is described by second virial coefficient due to the complexity exists among the mixture components. The correlation developed by Tsonopoulos [107] displayed in Equations A-1 to A-4 is employed to calculate the second virial coefficients for biodiesel, as shown in Figure A.1(a).

$$\frac{B_i P_c}{R T_c} = f^{(0)} + \omega f^{(1)} \tag{A-1}$$

$$f^{(0)} = 0.1445 - \frac{0.33}{T_r} - \frac{0.1385}{T_r^2} - \frac{0.0121}{T_r^3} - \frac{0.000607}{T_r^8} \tag{A-2}$$

$$f^{(1)} = 0.0637 + \frac{0.331}{T_r^2} - \frac{0.423}{T_r^3} - \frac{0.008}{T_r^4} \tag{A-3}$$

$$B_m = \sum_i y_i B_i \tag{A-4}$$

Where subscript i refers to pure component, m refers to mixture, B_i is the second virial coefficient of pure component i (m^3 kg^{-1}), B_m is the second virial coefficient of mixture m (m^3 kg^{-1}) and y_i is the mole fraction of pure component i.

Vapour Diffusivity

Vapour diffusivity is important to relate the net transport of material within the vapour phase in the absence of mixing [107]. Here, the vapour diffusivities for CME and SME illustrated in Figure A.1(b) are estimated using the Wilke and Lee method [108] given in Equations A-5 to A-9.

$$D_{ij} = \frac{[3.03 - (0.98/M_{ij}^{1/2})(10^{-3})T^{3/2}]}{PW_{ij}^{1/2}\sigma_{ij}^2\Omega^*} \tag{A-5}$$

$$W_{ij} = 2[(1/W_i) + (1/W_j)]^{-1} \tag{A-6}$$

$$\sigma_{ij} = \frac{\sigma_i + \sigma_j}{2} \tag{A-7}$$

$$\Omega^* = \left(\frac{A}{T^{*B}}\right) + \frac{C}{\exp(DT^*)} + \frac{E}{\exp(FT^*)} + \frac{G}{\exp(HT^*)} \tag{A-8}$$

$$T^* = kT/\varepsilon \tag{A-9}$$

Where subscripts i and j refer to the pure components, D_{ij} denotes the binary vapour diffusivity of pure components i and j (cm^2 s^{-1}), T is the temperature (K), W_i, W_j are the molecular weights of pure components i and j (g mol^{-1}) and P is the pressure (bar). σ_i and σ_j are the potential distance parameter of i and j (Å). Ω^* is the reduced collision integral which depends upon the intermolecular potential chosen and T^* is a dimensionless temperature related to potential energy parameter, ε (m^2 kg s^{-1}) and Boltzmann's constant, k (m^2 kg s^{-2} K^{-1}). A = 1.06036, B = 0.1561, C = 0.193, D = 0.47635, E = 1.03587, F = 1.52996, G = 1.76474, H = 3.89411 and ϵ/k is temperature (K).

Vapour Heat Capacity

In order to calculate the vapour heat capacity, the method of Rihani and Doraiswamy [107] which is an additive group method for hydrocarbons is adopted. The evaluated vapour heat capacities for CME and SME are shown in Figure A.3(c).

$$C_{p,i}{}^{vp} = \sum_i a_i n_i + \sum_i b_i n_i\, T + \sum_i c_i n_i\, T^2 + + \sum_i d_i n_i\, T^3 \tag{A-10}$$

$$C_{p,m,i}{}^{vp} = \sum_i y_i C_{p,i}{}^{o} \tag{A-11}$$

Where subscript i refers to pure component, subscript m refers to mixture, $C_{p,i}{}^{vp}$ and $C_{p,m}{}^{vp}$ (cal g^{-1} mol^{-1} K^{-1}) are the vapour heat capacity for pure component i and mixture m, respectively. n_i is number of groups of type pure component i, a_i, b_i, c_i and d_i are group contributions parameters.
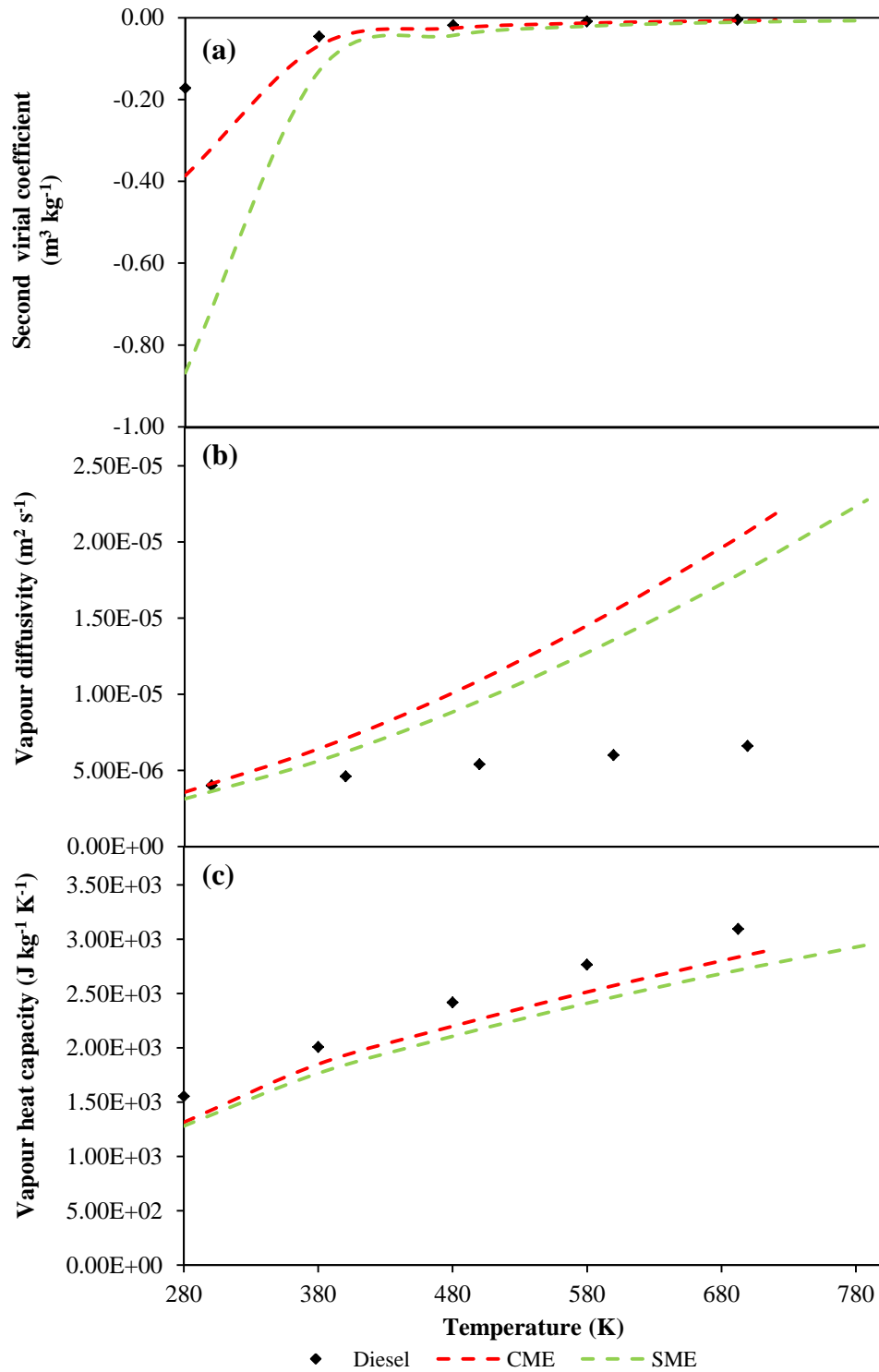
Figure A.1 Evaluated thermo-physical properties of CME, SME and diesel over temperatures of 280 K to critical temperatures of each fuel: (a) second viral coefficients, (b) vapour diffusivities and (c) vapour heat capacities.

Vapour Pressure

Vapour pressure is estimated using the modified Antoine Equation by Ceriani et al. [203]. The vapour pressure correlations as shown in Equations A-12 to A-16 are evaluated for the FAME components. The Kay's mixing rule as displayed in Equation A-17 is then employed to calculate the vapour pressure for CME and SME, seen in Figure A.2(a).

$$\ln P_i^{vp} = \sum_k N_k \left(A_{1,k} + \frac{B_{1,k}}{T^{1.5}} - C_{1,k} \ln T - D_{1,k}T\right) + \left[M_i \sum_k N_k \left(A_{2,k} + \frac{D_{2,k}}{T^{1.5}} - C_{2,k} \ln T - D_{2,k}T\right)\right] Q \tag{A-12}$$

$$Q = \xi_1 q + \xi_2 \tag{A-13}$$

$$q = \alpha + \frac{\beta}{T^{1.5}} - \gamma \ln T - \delta T \tag{A-14}$$

$$\xi_1 = f_0 + N_c f_1 \tag{A-15}$$

$$\xi_2 = s_0 + N_{cs} s_1 \tag{A-16}$$

$$P_m^{vp} = \sum_i P_i^{vp} x_i \tag{A-17}$$

Where subscript i refers to pure component, subscript m refers to mixture, P_i^{vp} is the vapour pressure of pure component i (Pa), P_m^{vp} is the vapour pressure of mixture m (Pa), N_k is the number of groups k in the molecule, M_i is the component molecular weight of pure component i (g mol^{-1}), N_c is the number of carbons, N_{cs} is the number of carbons from alcohol. $A_{1k}, B_{1k}, C_{1k}, D_{1k}, A_{2k}, B_{2k}, C_{2k}, D_{2k}$ are the parameters obtained from the regression of the experimental data and f_0, f_1, s_0 and s_1 are optimised constants.

Vapour Viscosity

In order to relate the viscosities for gases, the vapour viscosity is estimated. The correlations found by Chung et al. [140,141] as shown in Equations A-18 to A-22 are employed. Figure A.2(b) displays the evaluated vapour viscosities for CME and SME.

$$\eta^{vp} = (26.69x10^{-6}) \frac{(WT)^{1/2}}{\sigma^2 \Omega^*} \tag{A-18}$$

$$\sigma = 0.809 V_c^{\frac{1}{3}} \tag{A-19}$$

$$\Omega^* = \left(\frac{A}{T^{*B}}\right) + \frac{C}{\exp(DT^*)} + \frac{E}{\exp(FT^*)} + GT^{*B}\sin(ST^{*Z} - H) \tag{A-20}$$

$$T^* = kT/\varepsilon \tag{A-21}$$

$$\varepsilon/k = T_c/1.2593 \tag{A-22}$$

Where η^{vp} is the vapour viscosity (Pa s), W is the molecular weight (g mol^{-1}), T is the fuel temperature (K), σ is the potential distance parameter (Å), V_c is the critical volume (ml mol^{-1}), and Ω^* is the reduced collision integral which depends upon the intermolecular potential chosen and T^* is a dimensionless temperature related to potential energy parameter, ε (m^2 kg s^{-1}) and Boltzmann's constant, k (m^2 kg s^{-2} K^{-1}). $A = 1.16145$, $B = 0.14874$, $C = 0.52487$, $D = 0.77320$, $E = 2.16178$, $F = 2.43787$, $G = $ -6.435 x10^{-4}, $H = 7.27371$, $S = 18.0323$, $Z = $ -0.76830 and ε/k is temperature (K).

Vapour Thermal Conductivity

The vapour thermal conductivities for FAME components are first calculated using the correlations shown in Equations A-23 to A-27 [140,141]. Then, the vapour thermal conductivity for biodiesel as shown in Figure A.2(c) is calculated using the Kay's mixing rule as expressed in Equation A-28.

$$\lambda_i^{vp} = 7.452(\eta_o/M)\psi$$
(A-23)

$$\psi = 1 + \alpha\left\{\frac{[0.215 + 0.28288\alpha - 1.061\beta + 0.26665Z]}{[0.6366 + \beta Z + 1.061\alpha\beta]}\right\} \tag{A-24}$$

$$\alpha = (C_v/R) - (3/2) \tag{A-25}$$

$$\beta = 0.7862 - 0.7109\omega + 1.3168\omega^2 \tag{A-26}$$

$$Z = 2.0 + 10.5T_r^2 \tag{A-27}$$

$$\lambda_m^{vp} = \sum_i \lambda_i^{vp} y_i$$
(A-28)

Where subscript i refers to pure component and subscript m refers to mixture. λ^{vp} is the vapour thermal conductivity (cal cm^{-1} s^{-1} K^{-1}), C_v is the ideal gas

heat capacity at constant volume (cal mol^{-1} K^{-1}) and R is the gas constant with value of 1.987 cal mol^{-1} K^{-1}.
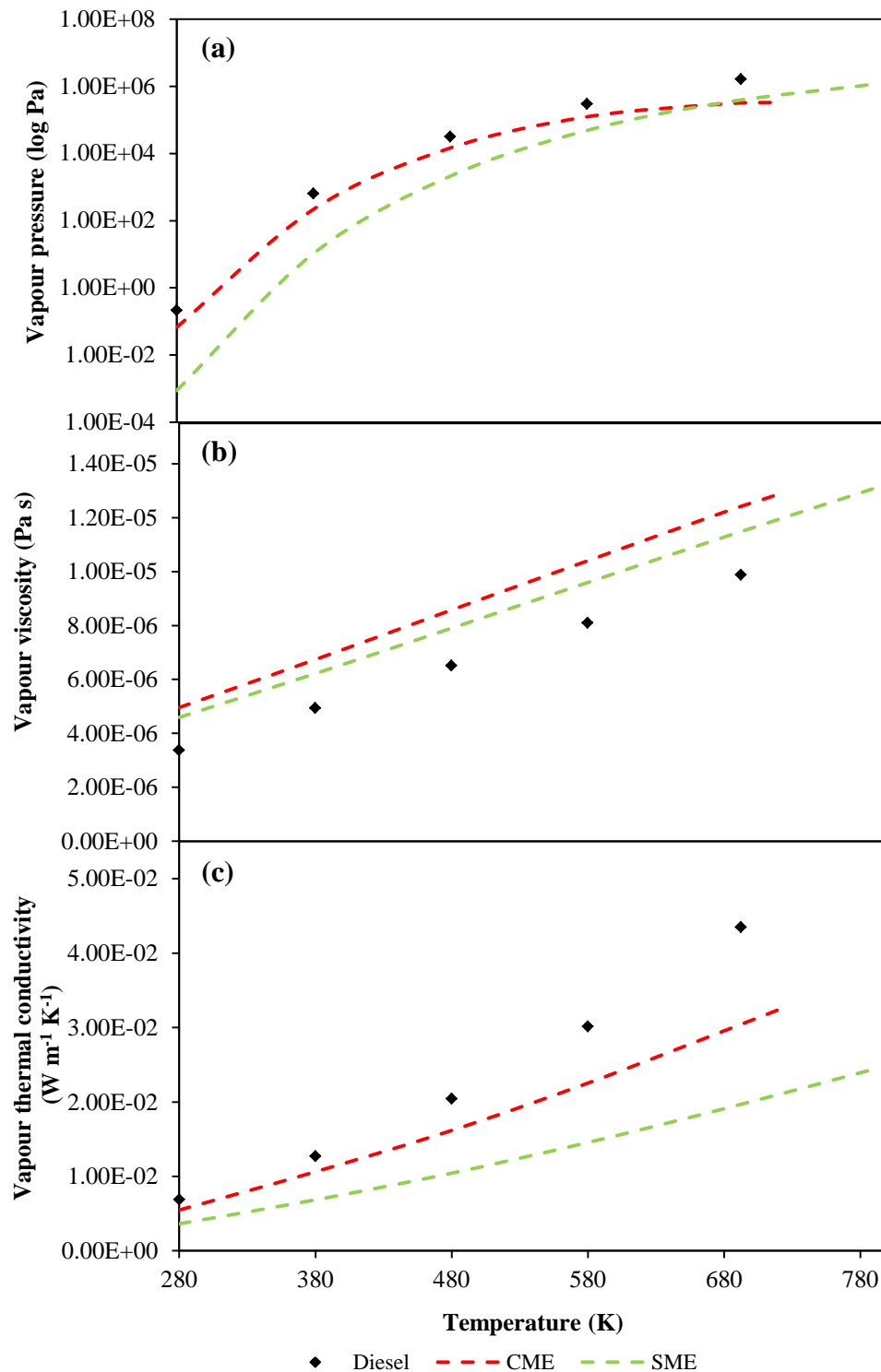
**Figure A.2 Evaluated thermo-physical properties of CME, SME and diesel over temperatures of 280 K to critical temperatures of each fuel: (a) vapour pressures, (b) vapour viscosities and (c) vapour thermal conductivities.**

B. C++ Code for the Integration of Thermo-Physical Properties into OpenFOAM

"NSRDSfunctions" Header File

```
#ifndef NSRDSfuncgRho_H
#define NSRDSfuncgRho_H
#include "thermophysicalFunction.H"
// * * * * * * * * * * * * * * * * * * * * * * * * * * * * * * * * * * * * //
namespace Foam
{
/*---------------------------------------------------------------------------*\
                      Class NSRDSfuncgRho Declaration
\*---------------------------------------------------------------------------*/

class NSRDSfuncgRho
:
    public thermophysicalFunction
{
    // Private data
    // NSRDS function 105 coefficients
        scalar a_, b_, c_, d_;
            scalar rhoY[157];


public:

    //- Runtime type information
    TypeName("NSRDSfuncgRho");


    // Constructors
        //- Construct from components
```

```
NSRDSfuncgRho

(

    const scalar a,

    const scalar b,

    const scalar c,

    const scalar d

);


//- Construct from Istream

NSRDSfuncgRho(Istream& is);


//- Construct from dictionary

NSRDSfuncgRho(const dictionary& dict);

    NSRDSfuncgRho()

    {

    rhoY[56]=888.04;

    rhoY[76]=751.79;

    rhoY[96]=621.01;

    rhoY[116]=493.75;

    rhoY[136]=363.79;

    rhoY[156]=134.90;

    }


// Member Functions

    //- Evaluate the function and return the result

    scalar f(scalar, scalar T) const

    {

        scalar rhoY_=0.0;

            for (int i=56; i<=136; i=i+20)

            {

                    if(T>=5*i && T<5*(i+20))

                    {

                            rhoY_=rhoY[i];
```

216

```
                                break;
                        }
                }
                if (T==773.46)
                {
                        rhoY_=rhoY[156];
                }
        return rhoY_;
    }


    //- Write the function coefficients
    void writeData(Ostream& os) const
    {
      os  << a_ << token::SPACE
        << b_ << token::SPACE
        << c_ << token::SPACE
        << d_;
    }


  // Ostream Operator
    friend Ostream& operator<<(Ostream& os, const NSRDSfuncgRho& f)
    {
      f.writeData(os);
      return os;
    }
};
// * * * * * * * * * * * * * * * * * * * * * * * * * * * * * * * * * * * //
} // End namespace Foam
// * * * * * * * * * * * * * * * * * * * * * * * * * * * * * * * * * * * //
#endif
```

217

"liquidProperties" Header File

#ifndef MD_H
#define MD_H

#include "liquidProperties.H"
#include "myNSRDSfunc0.H"
#include "myNSRDSfuncgRho.H"
#include "myNSRDSfuncgPv.H"
#include "myNSRDSfuncgHl.H"
#include "myNSRDSfuncgCp.H"
#include "myNSRDSfuncgCpg.H"
#include "myNSRDSfuncgB.H"
#include "myNSRDSfuncgMu.H"
#include "myNSRDSfuncgMug.H"
#include "myNSRDSfuncgK.H"
#include "myNSRDSfuncgKg.H"
#include "myNSRDSfuncgSigma.H"
#include "myAPIdiffCoefFuncgD.H"

// * //
namespace Foam
{
/*---*\
                    Class MD Declaration
---/

class MD
:
    public liquidProperties
{
    // Private data
        myNSRDSfuncgRho rho_;

218

```
        myNSRDSfuncgPv pv_;

        myNSRDSfuncgHl hl_;

        myNSRDSfuncgCp Cp_;

        myNSRDSfunc0 h_;

        myNSRDSfuncgCpg Cpg_;

        myNSRDSfuncgB B_;

        myNSRDSfuncgMu mu_;

        myNSRDSfuncgMug mug_;

        myNSRDSfuncgK K_;

        myNSRDSfuncgKg Kg_;

        myNSRDSfuncgSigma sigma_;

        myAPIdiffCoefFuncgD D_;


public:

    //- Runtime type information
    TypeName("MD");
    // Constructors

        //- Construct null
        MD();


        //- Construct from components
        MD
        (
                    const liquidProperties& l,
                    const myNSRDSfuncgRho& density,
                    const myNSRDSfuncgPv& vapourPressure,
                    const myNSRDSfuncgHl& heatOfVapourisation,
                    const myNSRDSfuncgCp& heatCapacity,
                    const myNSRDSfunc0& enthalpy,
                    const myNSRDSfuncgCpg& idealGasHeatCapacity,
                    const myNSRDSfuncgB& secondVirialCoeff,
```
219

```
                    const myNSRDSfuncgMu& dynamicViscosity,
                    const myNSRDSfuncgMug& vapourDynamicViscosity,
                    const myNSRDSfuncgK& thermalConductivity,
                    const myNSRDSfuncgKg& vapourThermalConductivity,
                    const myNSRDSfuncgSigma& surfaceTension,
                    const myAPIdiffCoefFuncgD& vapourDiffussivity
            );


        //- Construct from Istream
        MD(Istream& is);


        //- Construct from dictionary
        MD(const dictionary& dict);


        //- Construct copy
        MD(const MD& liq);


        //- Construct and return clone
        virtual autoPtr<liquidProperties> clone() const
        {
            return autoPtr<liquidProperties>(new MD(*this));
        }


    // Member Functions
        //- Liquid density [kg/m^3]
        inline scalar rho(scalar p, scalar T) const;


        //- Vapour pressure [Pa]
        inline scalar pv(scalar p, scalar T) const;


        //- Heat of vapourisation [J/kg]
        inline scalar hl(scalar p, scalar T) const;
```

```
//- Liquid heat capacity [J/(kg K)]
inline scalar Cp(scalar p, scalar T) const;


//- Liquid Enthalpy [J/kg]
inline scalar h(scalar p, scalar T) const;


//- Ideal gas heat capacity [J/(kg K)]
inline scalar Cpg(scalar p, scalar T) const;


//- Second Virial Coefficient [m^3/kg]
inline scalar B(scalar p, scalar T) const;


//- Liquid viscosity [Pa s]
inline scalar mu(scalar p, scalar T) const;


//- Vapour viscosity [Pa s]
inline scalar mug(scalar p, scalar T) const;


//- Liquid thermal conductivity  [W/(m K)]
inline scalar K(scalar p, scalar T) const;


//- Vapour thermal conductivity  [W/(m K)]
inline scalar Kg(scalar p, scalar T) const;


//- Surface tension [N/m]
inline scalar sigma(scalar p, scalar T) const;


//- Vapour diffussivity [m2/s]
inline scalar D(scalar p, scalar T) const;


//- Vapour diffussivity [m2/s] with specified binary pair
inline scalar D(scalar p, scalar T, scalar Wb) const;
```

```
// I-O
    //- Write the function coefficients
    void writeData(Ostream& os) const
    {
        liquidProperties::writeData(os); os << nl;
        rho_.writeData(os); os << nl;
        pv_.writeData(os); os << nl;
        hl_.writeData(os); os << nl;
        Cp_.writeData(os); os << nl;
        Cpg_.writeData(os); os << nl;
        B_.writeData(os); os << nl;
        mu_.writeData(os); os << nl;
        mug_.writeData(os); os << nl;
        K_.writeData(os); os << nl;
        Kg_.writeData(os); os << nl;
        sigma_.writeData(os); os << nl;
        D_.writeData(os); os << endl;
    }


    //- Ostream Operator
    friend Ostream& operator<<(Ostream& os, const MD& l)
    {
        l.writeData(os);
        return os;
    }
};
// * * * * * * * * * * * * * * * * * * * * * * * * * * * * * * * * * * * //

} // End namespace Foam
// * * * * * * * * * * * * * * * * * * * * * * * * * * * * * * * * * * * //

#include "MDI.H"
// * * * * * * * * * * * * * * * * * * * * * * * * * * * * * * * * * * * //

#endif
```

C. MATLAB Code for DRG Calculation

DRG Calculation

```
fid1=fopen('net_reaction_40bar_ER1_650K_1.txt');
wi = fscanf(fid1, '%e', [1 10806]);
fclose(fid1);

load delta.mat;
load v_ji.mat;
load species_matrix.mat;

fixed_value=10806;
important_species = zeros(3299,1);
wi_prime=wi';
[S T] = size(wi_prime);

wi_var_prime = wi;
numerator1 = 0;
denominator1 = 0;
r_coupling1 = 0;
species_matrix1 = zeros(3299);
[P Q] = size(species_matrix1);

for p=1:P
    for q=1:Q
        if species_matrix(p,q)==1
            % i row in matrix delta and abs_vw
            numerator1=0;
            denominator1=0;
            for i=1:fixed_value
```

```
numerator1=numerator1+abs(delta(q,i)*v_ji(p,i)*wi_var_prime(1,i));
        denominator1=denominator1+abs(v_ji(p,i)*wi_var_prime(1,i));
    end
    if (denominator1 ~= 0)
        r_coupling1=numerator1/denominator1;
        species_matrix1(p,q)=r_coupling1;
    end
    end
    end
end

sparse_matrix1 = sparse(species_matrix1);
[i,j,k]=find(sparse_matrix1);
sparsed1=[i j k];
sparsed1_sort=sortrows(sparsed1,-3);
[row1 col] = size(sparsed1_sort);

loop = zeros(row1,1);
mark = zeros(3299,1);

[s3 s4] = size(mark);

mark(212,1) = 1;
mark(2030,1) =1;

for i=1:row1
    if (mark(sparsed1_sort(i,1)) == 0 && mark(sparsed1_sort(i,2)) == 0)
        loop(i) = 1;
    elseif (mark(sparsed1_sort(i,1)) == 0 && mark(sparsed1_sort(i,2)) ~= 0)
        continue;
    elseif (mark(sparsed1_sort(i,1)) ~= 0 && mark(sparsed1_sort(i,2)) == 0)
        mark(sparsed1_sort(i,2)) = sparsed1_sort(i,3);
```

```
        loop(i) = 2;
        value = sparsed1_sort(i,3);
        target = [sparsed1_sort(i,2)];
        count = 1;
        end_condition = 0;
        while (end_condition ~= 1)
          for k = 1:i
            if (loop(k)  ==1  &&  sparsed1_sort(k,1)  ==  target(count)  &&
mark(sparsed1_sort(k,2)) == 0)
                loop(k) = 2;
                mark(sparsed1_sort(k,2)) = value;
                target = [target sparsed1_sort(k,2)];
            end;
          end
          [srow scol] = size(target);
          if (count < scol)
            count = count + 1;
          else
            end_condition = 1;
          end
        end
    end
end


rdfs_40bar_ER1_650K_1 = mark;


save('C:\Users\Administrator\Desktop\DRG\detailed\40bar_ER1_650K_1\rdfs
_40bar_ER1_650K_1.mat','rdfs_40bar_ER1_650K_1');
disp('working');
```

Revised Depth First Search

load rdfs_40bar_ER1_650K_1.mat;

load rdfs_40bar_ER1_650K_2.mat;

load rdfs_40bar_ER1_950K_1.mat;

load rdfs_40bar_ER1_950K_2.mat;

load rdfs_40bar_ER1_1350K_1.mat;

load rdfs_40bar_ER1_1350K_2.mat;

load rdfs_40bar_ER05_650K_1.mat;

load rdfs_40bar_ER05_650K_2.mat;

load rdfs_40bar_ER05_950K_1.mat;

load rdfs_40bar_ER05_950K_2.mat;

load rdfs_40bar_ER05_1350K_1.mat;

load rdfs_40bar_ER05_1350K_2.mat;

load rdfs_40bar_ER15_650K_1.mat;

load rdfs_40bar_ER15_650K_2.mat;

load rdfs_40bar_ER15_950K_1.mat;

load rdfs_40bar_ER15_950K_2.mat;

load rdfs_40bar_ER15_1350K_1.mat;

load rdfs_40bar_ER15_1350K_2.mat;

load rdfs_60bar_ER1_650K_1.mat;

load rdfs_60bar_ER1_650K_2.mat;

load rdfs_60bar_ER1_950K_1.mat;

load rdfs_60bar_ER1_950K_2.mat;

load rdfs_60bar_ER1_1350K_1.mat;

load rdfs_60bar_ER1_1350K_2.mat;

load rdfs_60bar_ER05_650K_1.mat;

load rdfs_60bar_ER05_650K_2.mat;

load rdfs_60bar_ER05_950K_1.mat;

load rdfs_60bar_ER05_950K_2.mat;

load rdfs_60bar_ER05_1350K_1.mat;

load rdfs_60bar_ER05_1350K_2.mat;

load rdfs_60bar_ER15_650K_1.mat;

```
load rdfs_60bar_ER15_650K_2.mat;
load rdfs_60bar_ER15_950K_1.mat;
load rdfs_60bar_ER15_950K_2.mat;
load rdfs_60bar_ER15_1350K_1.mat;
load rdfs_60bar_ER15_1350K_2.mat;

limit=1.0;

[row2 col2] = size(rdfs_40bar_ER1_650K_1);
important_species=zeros(3299,1);

[row4 col4] = size(important_species);

for rw2=1:row2
    if rdfs_40bar_ER05_650K_1(rw2)<limit
        rdfs_40bar_ER05_650K_1(rw2)=0;
    end
    if rdfs_40bar_ER05_650K_1(rw2)~=0
        important_species(rw2)=1;
    end
end

for rw2=1:row2
    if rdfs_40bar_ER05_650K_2(rw2)<limit
        rdfs_40bar_ER05_650K_2(rw2)=0;
    end
    if rdfs_40bar_ER05_650K_2(rw2)~=0
        important_species(rw2)=1;
    end
end

for rw2=1:row2
    if rdfs_40bar_ER05_950K_1(rw2)<limit
```

```
      rdfs_40bar_ER05_950K_1(rw2)=0;
   end
   if rdfs_40bar_ER05_950K_1(rw2)~=0
      important_species(rw2)=1;
   end
end


for rw2=1:row2
   if rdfs_40bar_ER05_950K_2(rw2)<limit
      rdfs_40bar_ER05_950K_2(rw2)=0;
   end
   if rdfs_40bar_ER05_950K_2(rw2)~=0
      important_species(rw2)=1;
   end
end


for rw2=1:row2
   if rdfs_40bar_ER05_1350K_1(rw2)<limit
      rdfs_40bar_ER05_1350K_1(rw2)=0;
   end
   if rdfs_40bar_ER05_1350K_1(rw2)~=0
      important_species(rw2)=1;
   end
end


for rw2=1:row2
   if rdfs_40bar_ER05_1350K_2(rw2)<limit
      rdfs_40bar_ER05_1350K_2(rw2)=0;
   end
   if rdfs_40bar_ER05_1350K_2(rw2)~=0
      important_species(rw2)=1;
   end
end
```

```
for rw2=1:row2
    if rdfs_40bar_ER1_650K_1(rw2)<limit
        rdfs_40bar_ER1_650K_1(rw2)=0;
    end
    if rdfs_40bar_ER1_650K_1(rw2)~=0
        important_species(rw2)=1;
    end
end

for rw2=1:row2
    if rdfs_40bar_ER1_650K_2(rw2)<limit
        rdfs_40bar_ER1_650K_2(rw2)=0;
    end
    if rdfs_40bar_ER1_650K_2(rw2)~=0
        important_species(rw2)=1;
    end
end

for rw2=1:row2
    if rdfs_40bar_ER1_950K_1(rw2)<limit
        rdfs_40bar_ER1_950K_1(rw2)=0;
    end
    if rdfs_40bar_ER1_950K_1(rw2)~=0
        important_species(rw2)=1;
    end
end

for rw2=1:row2
    if rdfs_40bar_ER1_950K_2(rw2)<limit
        rdfs_40bar_ER1_950K_2(rw2)=0;
    end
    if rdfs_40bar_ER1_950K_2(rw2)~=0
```

```
        important_species(rw2)=1;
    end
end


for rw2=1:row2
    if rdfs_40bar_ER1_1350K_1(rw2)<limit
        rdfs_40bar_ER1_1350K_1(rw2)=0;
    end
    if rdfs_40bar_ER1_1350K_1(rw2)~=0
        important_species(rw2)=1;
    end
end


for rw2=1:row2
    if rdfs_40bar_ER1_1350K_2(rw2)<limit
        rdfs_40bar_ER1_1350K_2(rw2)=0;
    end
    if rdfs_40bar_ER1_1350K_2(rw2)~=0
        important_species(rw2)=1;
    end
end


for rw2=1:row2
    if rdfs_40bar_ER15_650K_1(rw2)<limit
        rdfs_40bar_ER15_650K_1(rw2)=0;
    end
    if rdfs_40bar_ER15_650K_1(rw2)~=0
        important_species(rw2)=1;
    end
end


for rw2=1:row2
    if rdfs_40bar_ER15_650K_2(rw2)<limit
```

```
        rdfs_40bar_ER15_650K_2(rw2)=0;
    end
    if rdfs_40bar_ER15_650K_2(rw2)~=0
        important_species(rw2)=1;
    end
end


for rw2=1:row2
    if rdfs_40bar_ER15_950K_1(rw2)<limit
        rdfs_40bar_ER15_950K_1(rw2)=0;
    end
    if rdfs_40bar_ER15_950K_1(rw2)~=0
        important_species(rw2)=1;
    end
end


for rw2=1:row2
    if rdfs_40bar_ER15_950K_2(rw2)<limit
        rdfs_40bar_ER15_950K_2(rw2)=0;
    end
    if rdfs_40bar_ER15_950K_2(rw2)~=0
        important_species(rw2)=1;
    end
end


for rw2=1:row2
    if rdfs_40bar_ER15_1350K_1(rw2)<limit
        rdfs_40bar_ER15_1350K_1(rw2)=0;
    end
    if rdfs_40bar_ER15_1350K_1(rw2)~=0
        important_species(rw2)=1;
    end
end
```

231

```
for rw2=1:row2
    if rdfs_40bar_ER15_1350K_2(rw2)<limit
        rdfs_40bar_ER15_1350K_2(rw2)=0;
    end
    if rdfs_40bar_ER15_1350K_2(rw2)~=0
        important_species(rw2)=1;
    end
end


for rw2=1:row2
    if rdfs_60bar_ER05_650K_1(rw2)<limit
        rdfs_60bar_ER05_650K_1(rw2)=0;
    end
    if rdfs_60bar_ER05_650K_1(rw2)~=0
        important_species(rw2)=1;
    end
end


for rw2=1:row2
    if rdfs_60bar_ER05_650K_2(rw2)<limit
        rdfs_60bar_ER05_650K_2(rw2)=0;
    end
    if rdfs_60bar_ER05_650K_2(rw2)~=0
        important_species(rw2)=1;
    end
end


for rw2=1:row2
    if rdfs_60bar_ER05_950K_1(rw2)<limit
        rdfs_60bar_ER05_950K_1(rw2)=0;
    end
    if rdfs_60bar_ER05_950K_1(rw2)~=0
```

```
      important_species(rw2)=1;
   end
end


for rw2=1:row2
   if rdfs_60bar_ER05_950K_2(rw2)<limit
      rdfs_60bar_ER05_950K_2(rw2)=0;
   end
   if rdfs_60bar_ER05_950K_2(rw2)~=0
      important_species(rw2)=1;
   end
end


for rw2=1:row2
   if rdfs_60bar_ER05_1350K_1(rw2)<limit
      rdfs_60bar_ER05_1350K_1(rw2)=0;
   end
   if rdfs_60bar_ER05_1350K_1(rw2)~=0
      important_species(rw2)=1;
   end
end


for rw2=1:row2
   if rdfs_60bar_ER05_1350K_2(rw2)<limit
      rdfs_60bar_ER05_1350K_2(rw2)=0;
   end
   if rdfs_60bar_ER05_1350K_2(rw2)~=0
      important_species(rw2)=1;
   end
end


for rw2=1:row2
   if rdfs_60bar_ER1_650K_1(rw2)<limit
```

```
        rdfs_60bar_ER1_650K_1(rw2)=0;
    end
    if rdfs_60bar_ER1_650K_1(rw2)~=0
        important_species(rw2)=1;
    end
end


for rw2=1:row2
    if rdfs_60bar_ER1_650K_2(rw2)<limit
        rdfs_60bar_ER1_650K_2(rw2)=0;
    end
    if rdfs_60bar_ER1_650K_2(rw2)~=0
        important_species(rw2)=1;
    end
end


for rw2=1:row2
    if rdfs_60bar_ER1_950K_1(rw2)<limit
        rdfs_60bar_ER1_950K_1(rw2)=0;
    end
    if rdfs_60bar_ER1_950K_1(rw2)~=0
        important_species(rw2)=1;
    end
end


for rw2=1:row2
    if rdfs_60bar_ER1_950K_2(rw2)<limit
        rdfs_60bar_ER1_950K_2(rw2)=0;
    end
    if rdfs_60bar_ER1_950K_2(rw2)~=0
        important_species(rw2)=1;
    end
end
```

```
for rw2=1:row2
    if rdfs_60bar_ER1_1350K_1(rw2)<limit
        rdfs_60bar_ER1_1350K_1(rw2)=0;
    end
    if rdfs_60bar_ER1_1350K_1(rw2)~=0
        important_species(rw2)=1;
    end
end

for rw2=1:row2
    if rdfs_60bar_ER1_1350K_2(rw2)<limit
        rdfs_60bar_ER1_1350K_2(rw2)=0;
    end
    if rdfs_60bar_ER1_1350K_2(rw2)~=0
        important_species(rw2)=1;
    end
end

for rw2=1:row2
    if rdfs_60bar_ER15_650K_1(rw2)<limit
        rdfs_60bar_ER15_650K_1(rw2)=0;
    end
    if rdfs_60bar_ER15_650K_1(rw2)~=0
        important_species(rw2)=1;
    end
end

for rw2=1:row2
    if rdfs_60bar_ER15_650K_2(rw2)<limit
        rdfs_60bar_ER15_650K_2(rw2)=0;
    end
    if rdfs_60bar_ER15_650K_2(rw2)~=0
```

```
          important_species(rw2)=1;
      end
  end


  for rw2=1:row2
      if rdfs_60bar_ER15_950K_1(rw2)<limit
          rdfs_60bar_ER15_950K_1(rw2)=0;
      end
      if rdfs_60bar_ER15_950K_1(rw2)~=0
          important_species(rw2)=1;
      end
  end


  for rw2=1:row2
      if rdfs_60bar_ER15_950K_2(rw2)<limit
          rdfs_60bar_ER15_950K_2(rw2)=0;
      end
      if rdfs_60bar_ER15_950K_2(rw2)~=0
          important_species(rw2)=1;
      end
  end


  for rw2=1:row2
      if rdfs_60bar_ER15_1350K_1(rw2)<limit
          rdfs_60bar_ER15_1350K_1(rw2)=0;
      end
      if rdfs_60bar_ER15_1350K_1(rw2)~=0
          important_species(rw2)=1;
      end
  end


  for rw2=1:row2
      if rdfs_60bar_ER15_1350K_2(rw2)<limit
```

```
        rdfs_60bar_ER15_1350K_2(rw2)=0;
    end
    if rdfs_60bar_ER15_1350K_2(rw2)~=0
        important_species(rw2)=1;
    end
end

disp('working');
```

D. Grouped Isomers

Table D.1 Isomer groups in the 404-species reduced mechanism.

Group	Lumped species
mf4dmj	mf4d2j, mf4d3j
md6o2	mdmo2, md2o2, md3o2, md4o2, md5o2, md7o2, md8o2, md9o2
md6j	mdmj, md2j, md3j, md4j, md5j, md7j, md8j, md9j, md10j
md9d6j	md9d2j, md9d3j, md9d5j, md9d7j, md9d8j, md9dxj
mp2d2j	mp2dmj, mp2d3j
me2o2	memo2
mpmo2	mp3o2
mpmooh2j	mp3ooh2j
md6ooh8j	md2ooh4j, md3ooh5j, md4ooh2j, md4ooh6j, md5ooh3j, md5ooh7j, md5ooh8j, md7ooh5j, md7ooh9j, md8ooh6j, md9ooh6j, md9ooh7j, md10ooh8j
md6o	mdmo, md2o, md3o, md4o, md5o, md7o, md8o, md9o
md6ooh8o2	md2ooh4o2, md3ooh5o2, md4ooh2o2, md4ooh6o2, md5ooh3o2, md5ooh3o2, md5ooh8o2, md7ooh5o2, md8ooh6o2, md9ooh6o2, md9ooh7o2, md10ooh8o2
mdket68o	mdket24o, mdket35o, mdket42o, mdket46o, mdket53o, mdket57o, mdket58o, mdket75o, mdket86o, mdket96o, mdket97o, mdket108o
mdket68	mdket24, mdket35, mdket42, mdket46, mdket53, mdket57, mdket58, mdket75, mdket86, mdket96, mdket97, mdket108
mf4oxo5j	mf5oxo5j
mp2oxo3j	mp3oxo3j
ms6oxo7j	ms5oxo7j
md2oxomj	mdmoxo2j
mp2oxomj	mpmoxo2j, mpmoxo3j, mp3oxomj

mpom-2	mpom-3
mdom-2	mdo8-10
mn8doh8	mn8doh9
md9doh9	md9doh10
md9d6o2	md9d2o2, md9d3o2, md9d5o2, md9d7o2, md9d8o2, md8dxo2
md9d2ooh	md9d3ooh, md9d5ooh, md9d7ooh, md9d8ooh
md9d6ooh8j	md9d5ooh8j, md8dxooh7j
md9d2o	md9d3o, md9d5o, md9d7o, md9d8o
md9d6ooh8o2	md9d5ooh8o2, md8dxooh7o2
me2oohmj	memooh2j
mpmj	mp3j
me2j	memj
me2oxomj	memoxo2j
mh6j	mh2j
me2o	memo
me2ooh	memooh

E. Validation of Reduced Biodiesel Chemical Kinetic Mechanism
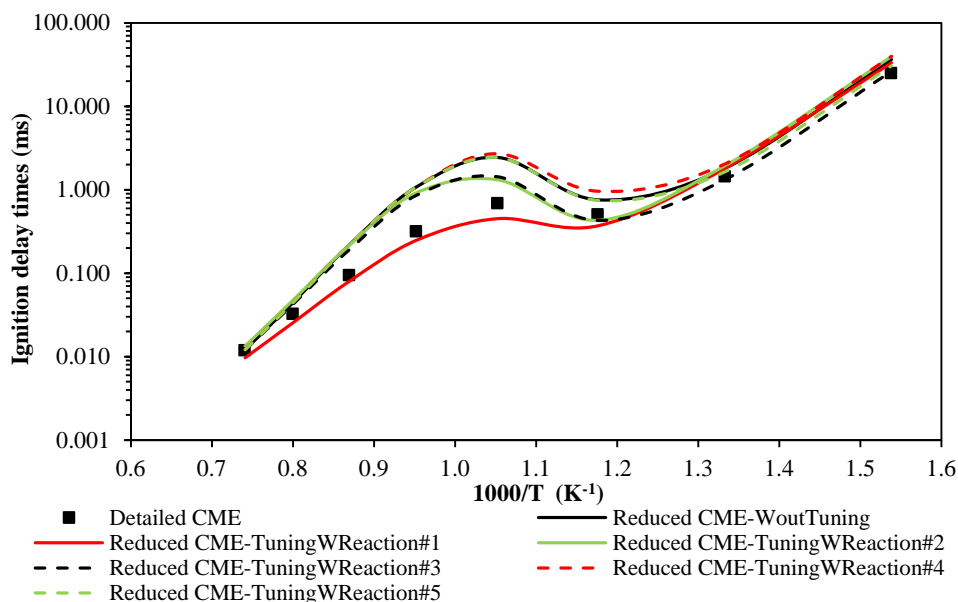
Figure E.1 Predicted ID periods for the detailed and reduced mechanisms of CME at an initial pressure of 40.0 bar and equivalence ratio of 1.0, with adjustment to individual Arrhenius rate constants.
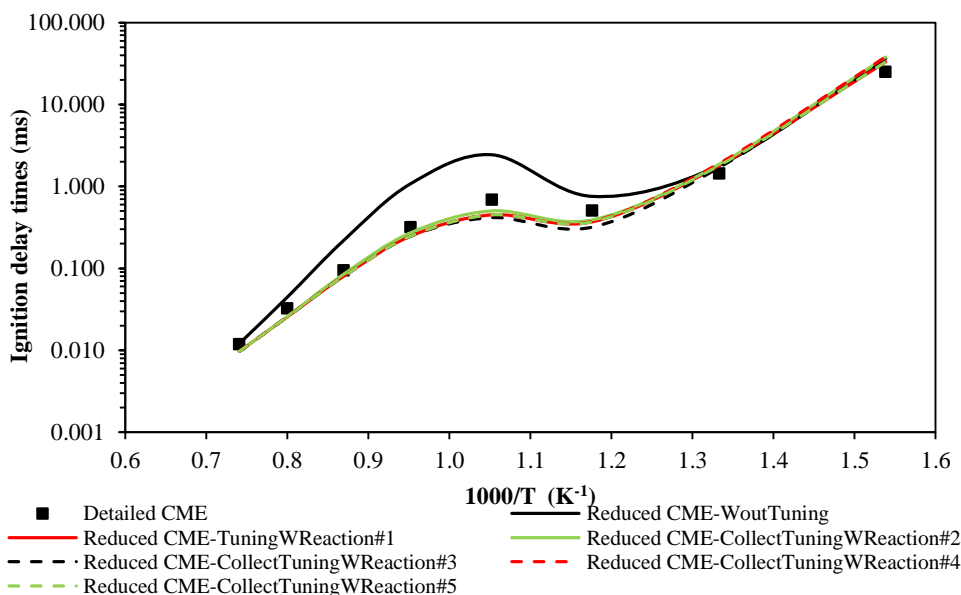
Figure E.2 Predicted ID periods for the detailed and reduced mechanisms of CME at an initial pressure of 40.0 bar and equivalence ratio of 1.0, with adjustment to collective Arrhenius rate constants.
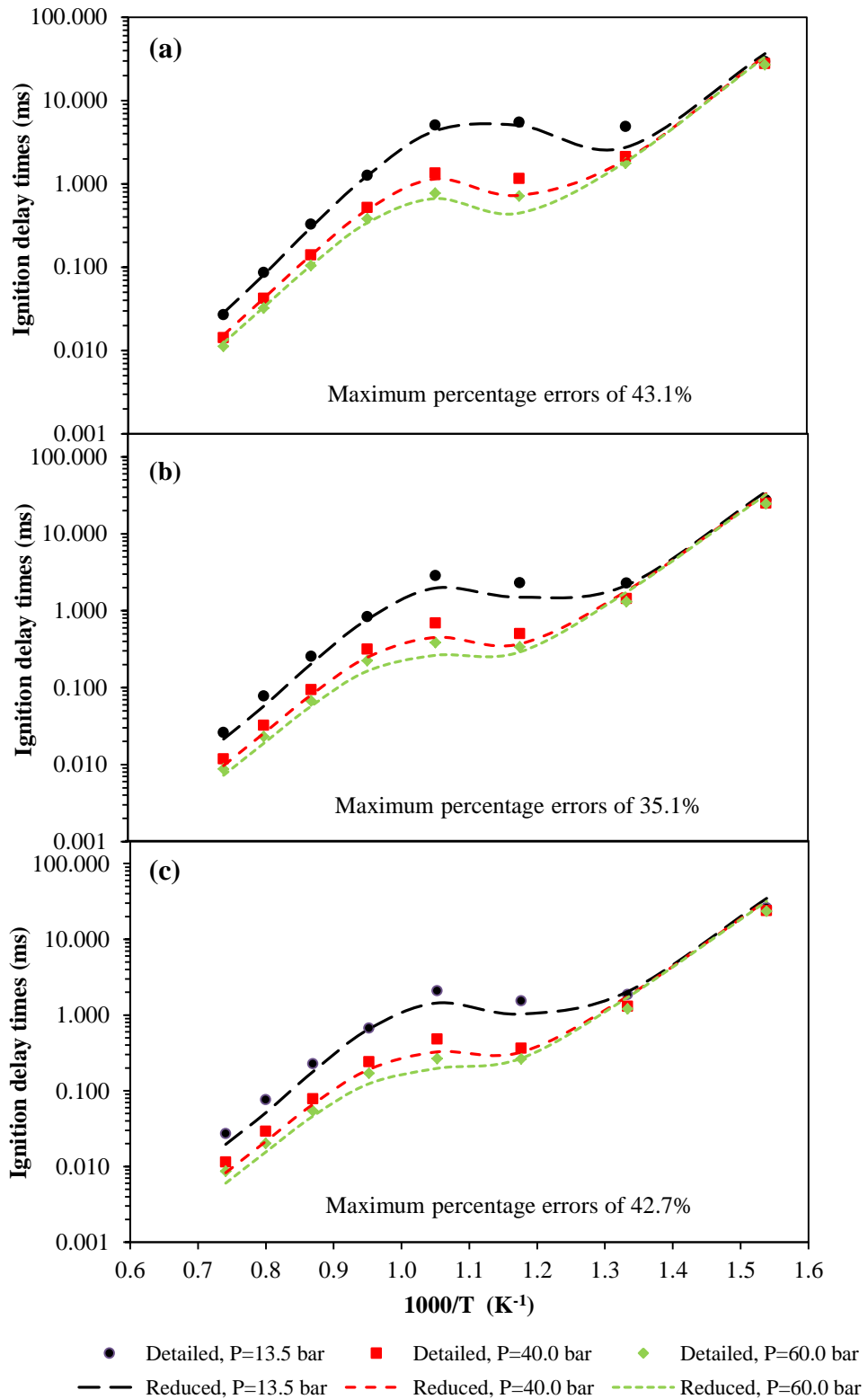
Figure E.3 Predicted ID periods for the detailed and reduced mechanisms of CME at initial pressures of 13.5 bar, 40.0 bar and 60.0 bar, with equivalence ratios of (a) 0.5, (b) 1.0 and (c) 1.5.
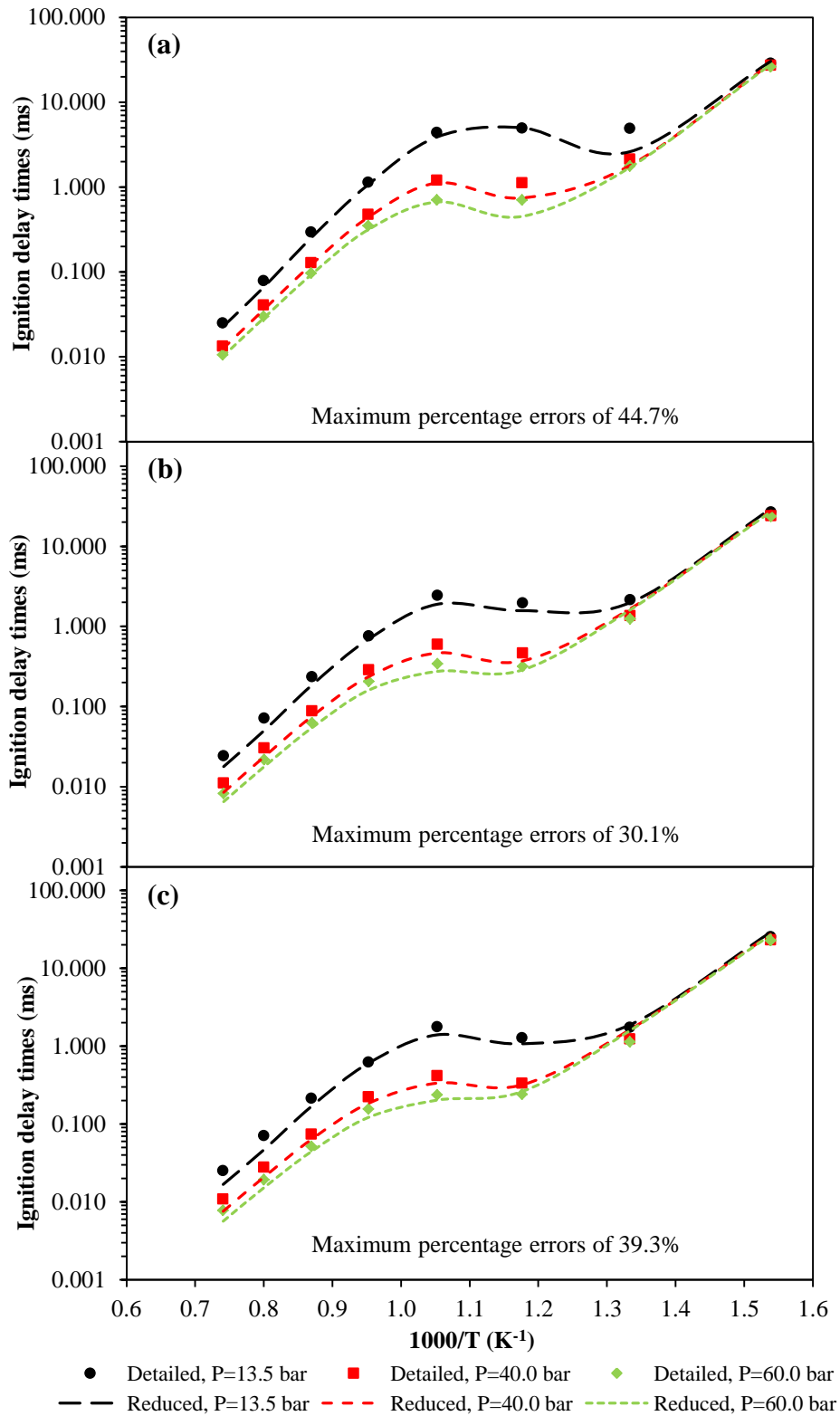
Figure E.4 Predicted ID periods for the detailed and reduced mechanisms of PME at initial pressures of 13.5 bar, 40.0 bar and 60.0 bar, with equivalence ratios of (a) 0.5, (b) 1.0 and (c) 1.5.
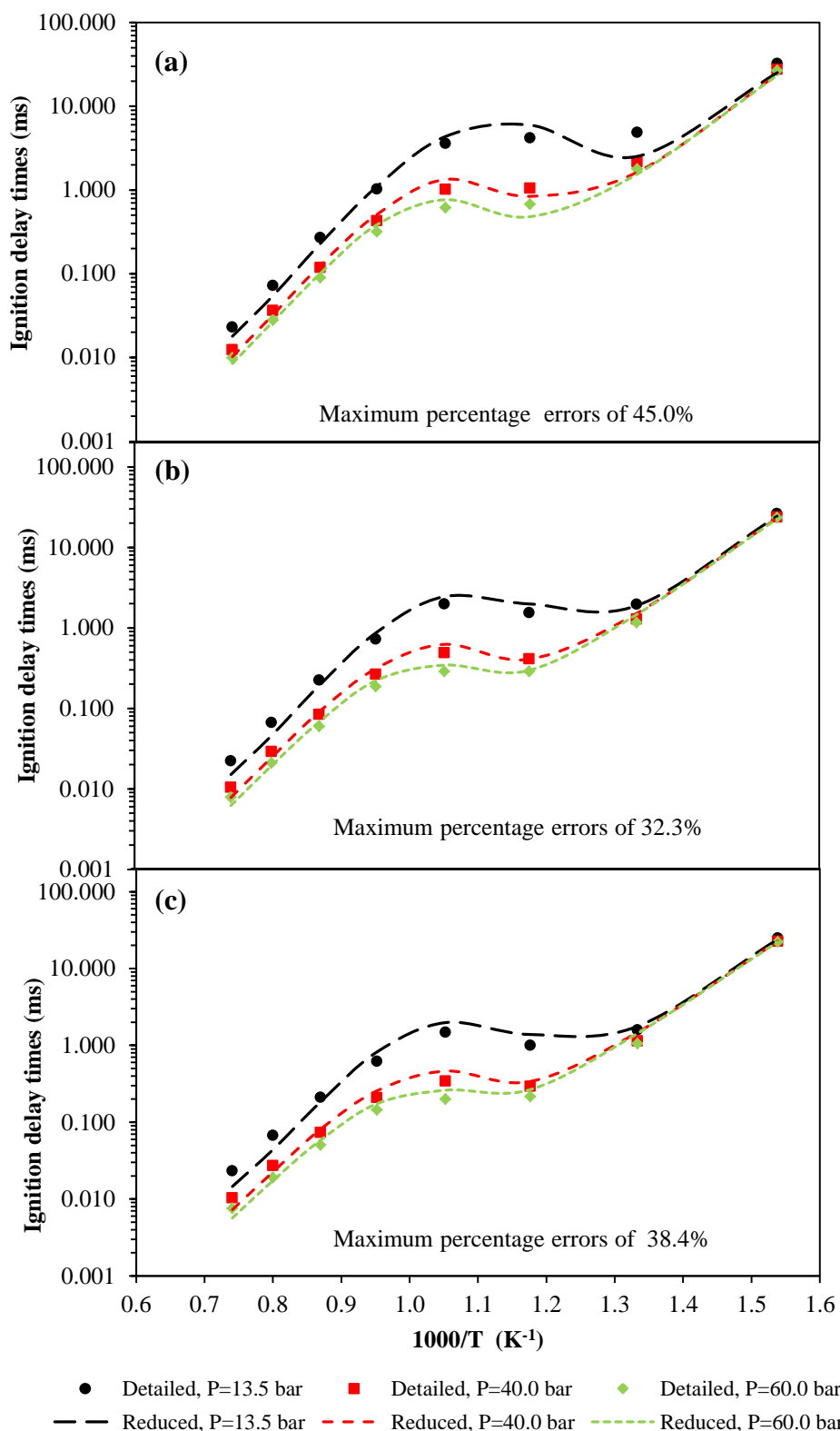
Figure E.5 Predicted ID periods for the detailed and reduced mechanisms of RME at initial pressures of 13.5 bar, 40.0 bar and 60.0 bar, with equivalence ratios of (a) 0.5, (b) 1.0 and (c) 1.5.
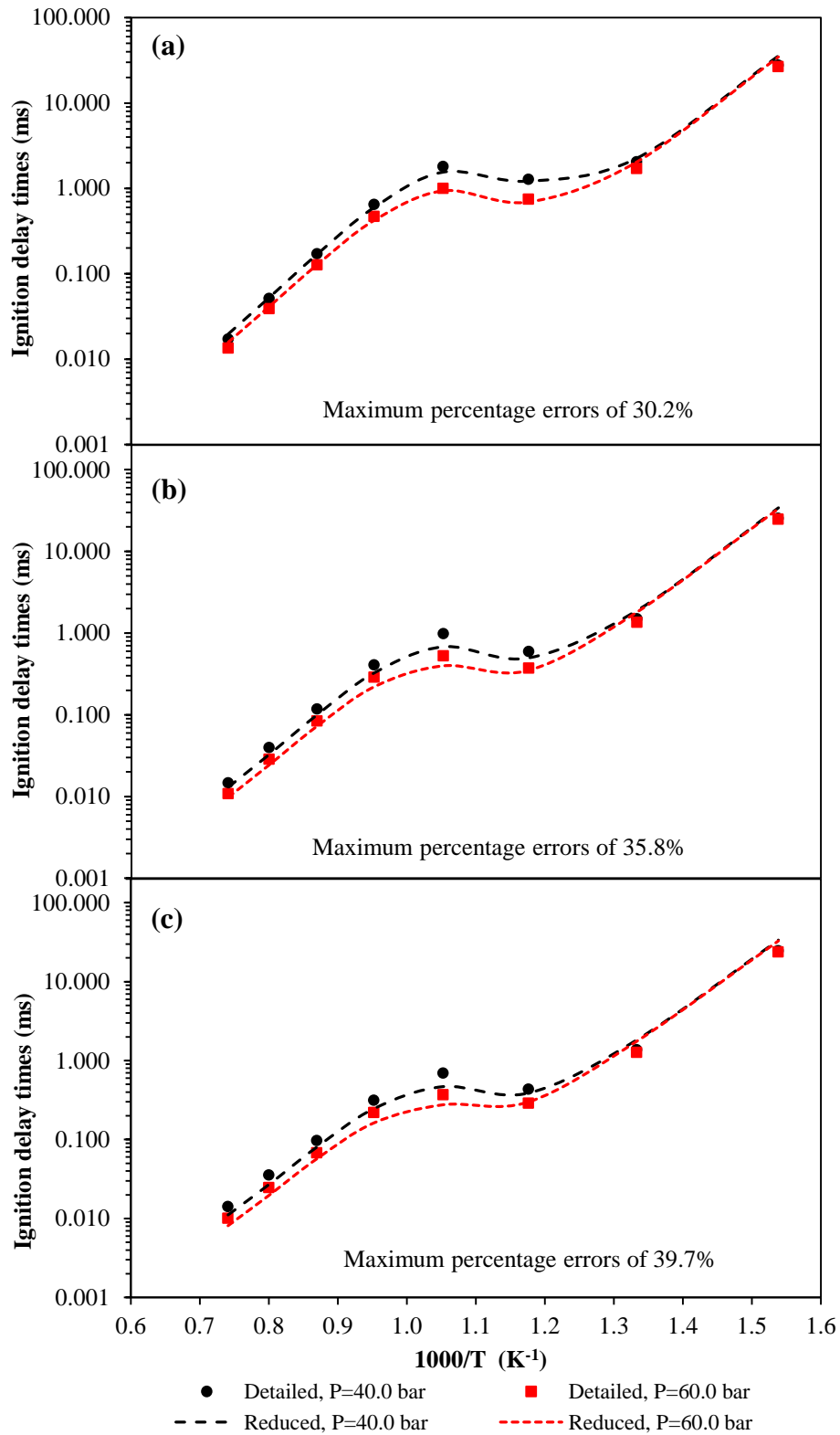
Figure E.6 Predicted ID periods for the detailed and reduced mechanisms of B50 CME at initial pressures of 40.0 bar and 60.0 bar, with equivalence ratios of (a) 0.5, (b) 1.0 and (c) 1.5.
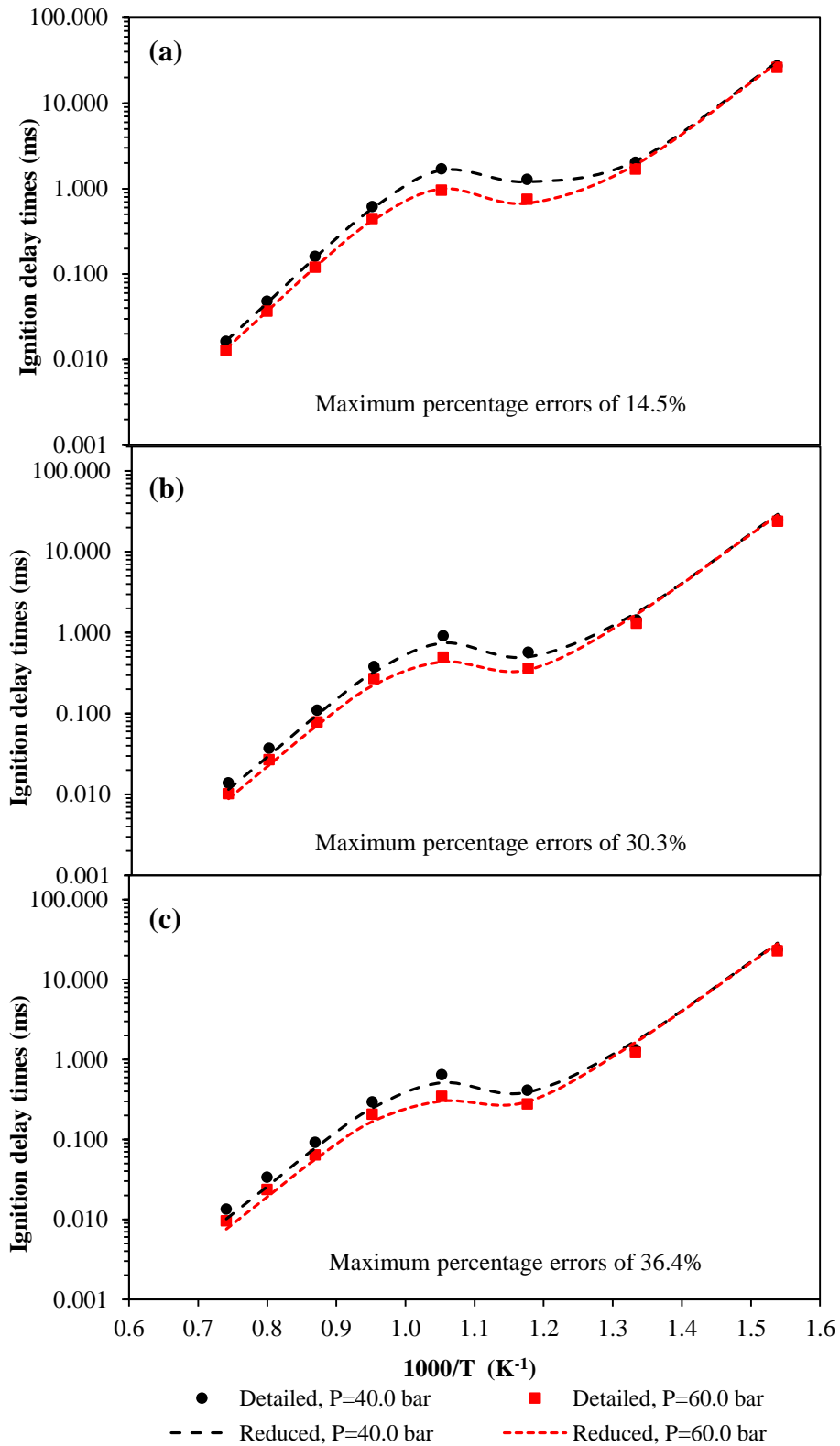
**Figure E.7 Predicted ID periods for the detailed and reduced mechanisms of B50 PME at initial pressures of 40.0 bar and 60.0 bar, with equivalence ratios of (a) 0.5, (b) 1.0 and (c) 1.5.**
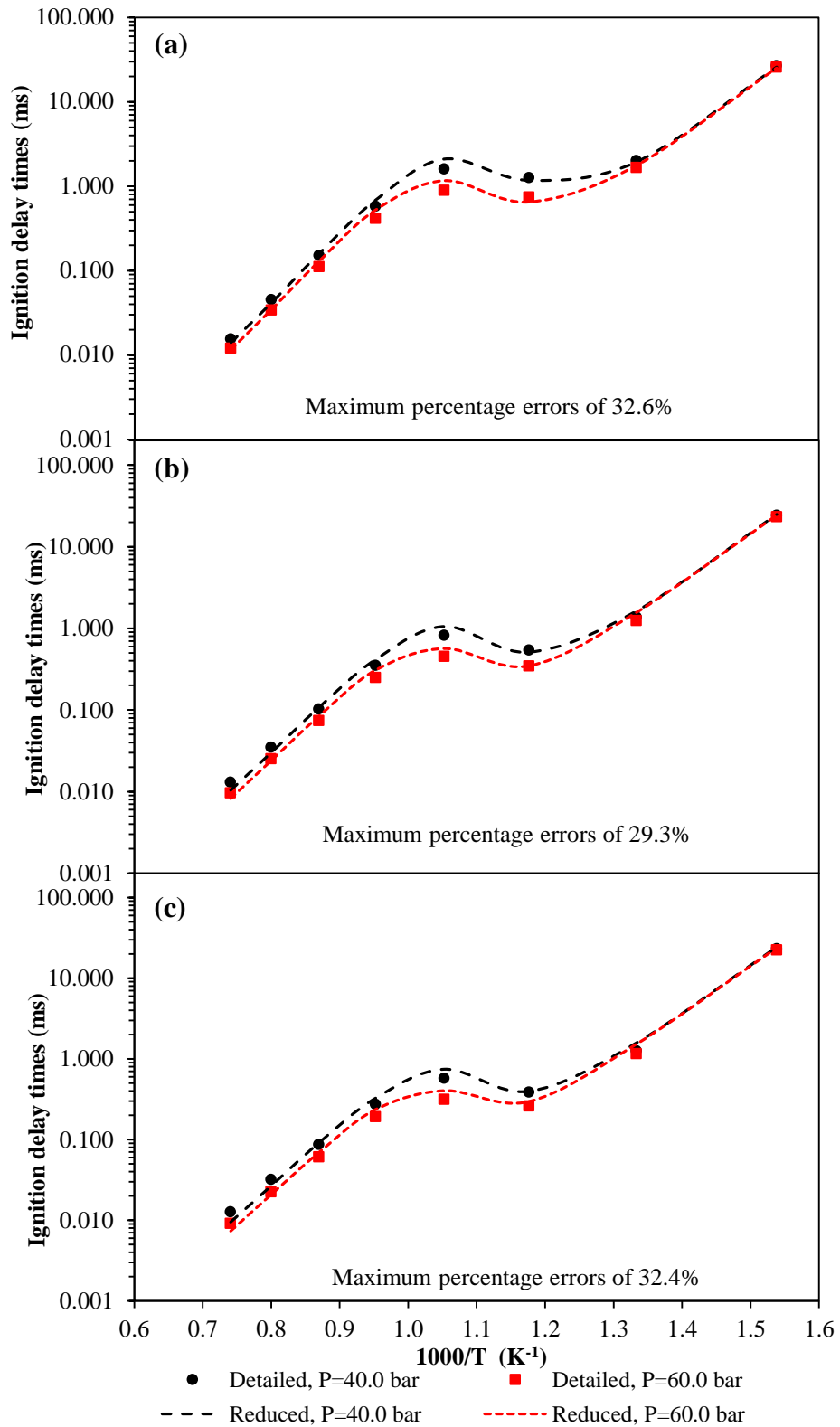
**Figure E.8 Predicted ID periods for the detailed and reduced mechanisms of B50 RME at initial pressures of 40.0 bar and 60.0 bar, with equivalence ratios of (a) 0.5, (b) 1.0 and (c) 1.5.**
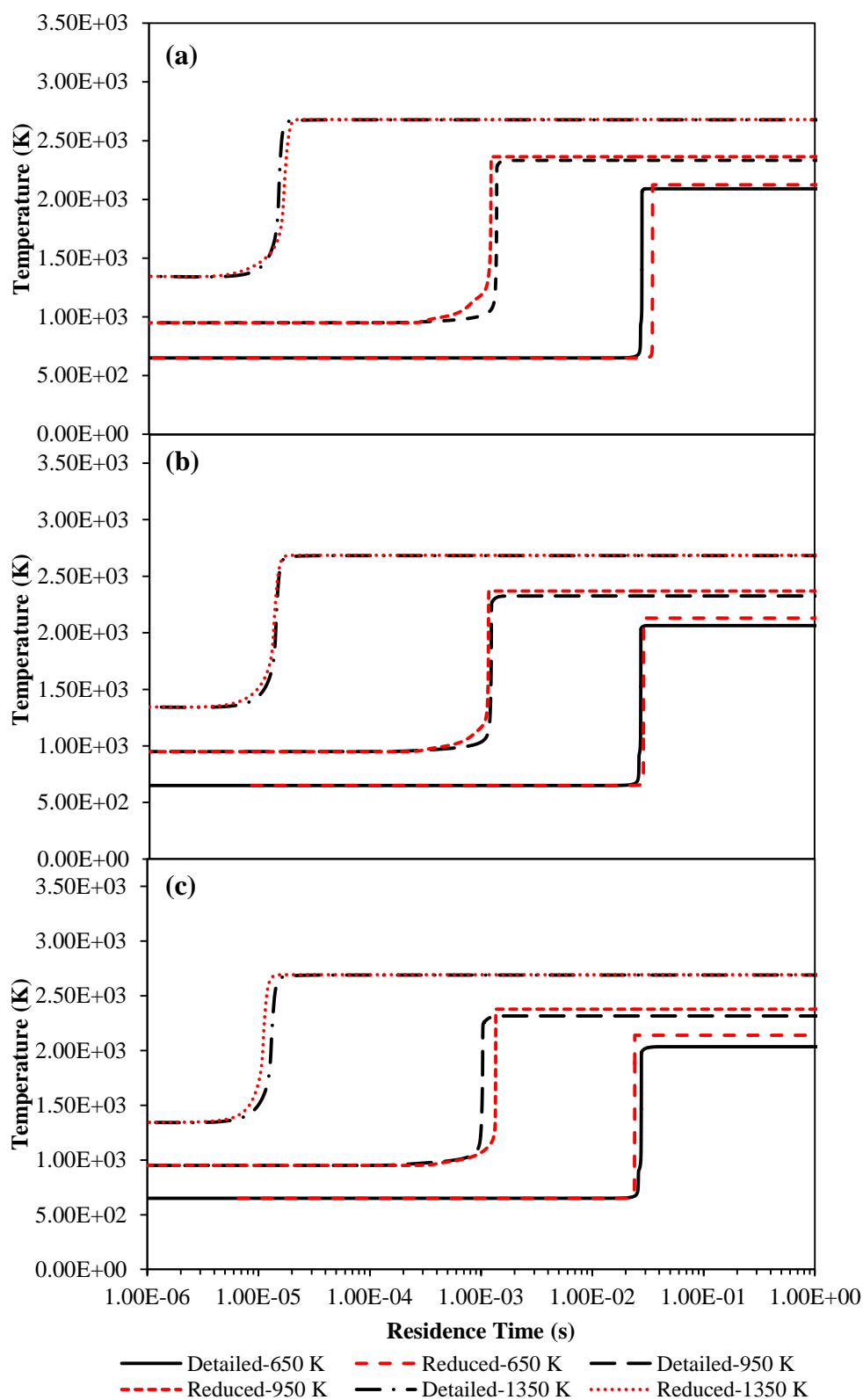
Figure E.9 Predicted temperatures against residence times for the detailed and reduced mechanisms of (a) CME, (b) PME and (c) RME, with an initial pressure of 40.0 bar, equivalence ratio of 0.5 and initial temperatures of 650 K, 950 K and 1350 K.
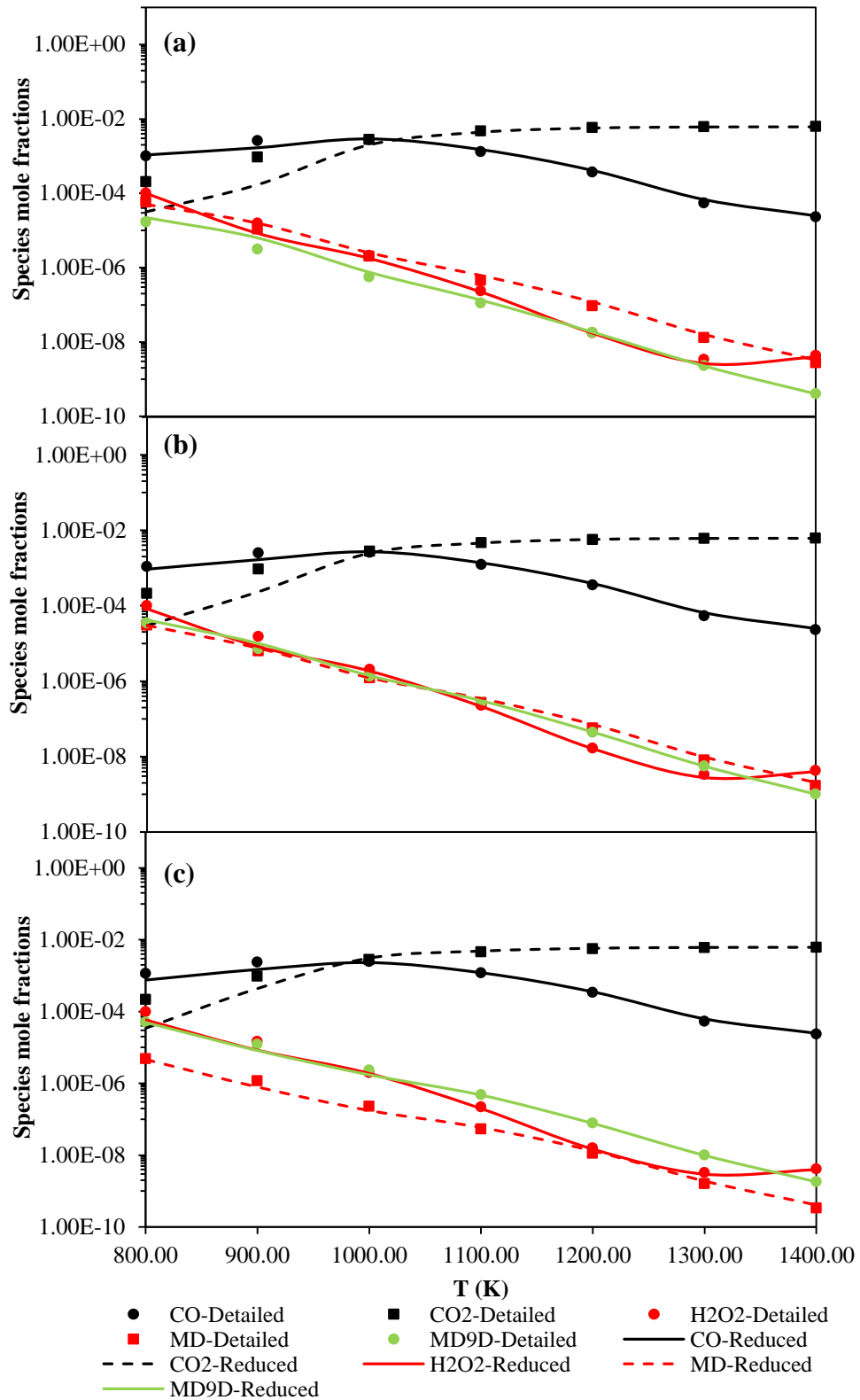
Figure E.10 Predicted mole fractions of CO, CO₂, H₂O₂, MD and MD9D under JSR conditions for the detailed and reduced mechanisms of (a) CME, (b) PME and (c) RME, with an initial pressure of 10.1 bar, equivalence ratio of 1.0 and nitrogen dilution of 99.95% [18].
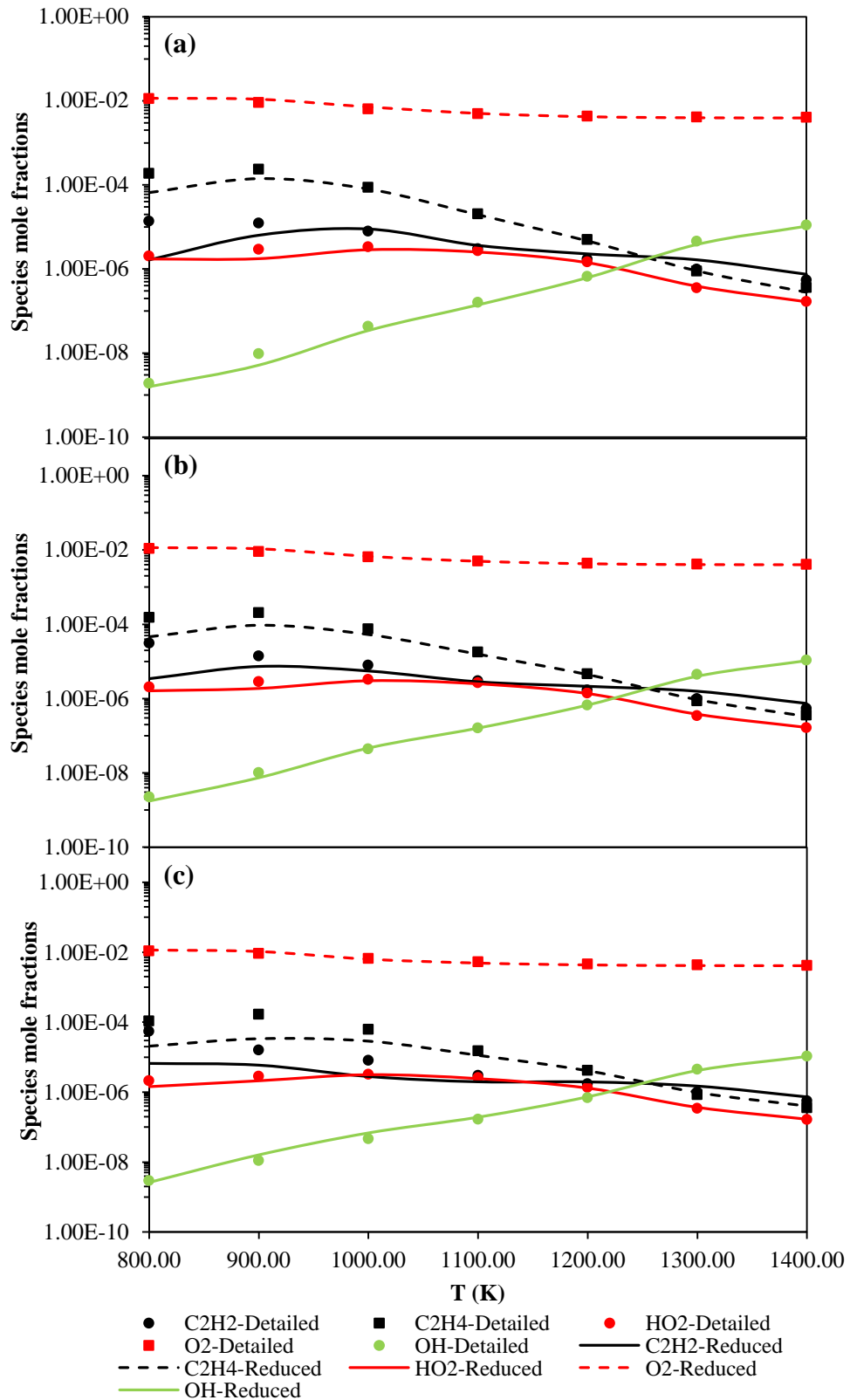
Figure E.11 Predicted mole fractions of C_2H_2, C_2H_4, HO_2, O_2 and OH under JSR conditions for the detailed and reduced mechanisms of CME, PME and RME, with an initial pressure of 10.1 bar, equivalence ratio of 1.0 and nitrogen dilution of 99.95% [18].

F. Chemical Kinetic Mechanisms

Table F.1 The reduced chemical kinetic mechanism for biodiesel.

No.	Reactions Considered	A (mol cm s K)	b	E (cal mol^{-1})
1	H+O2<=>O+OH	3.55E+15	-0.4	16600
	Reverse Arrhenius coefficients:	1.02E+13	0	-133
2	O+H2<=>H+OH	5.08E+04	2.7	6292
	Reverse Arrhenius coefficients:	2.67E+04	2.6	4880
3	OH+H2<=>H+H2O	2.16E+08	1.5	3430
	Reverse Arrhenius coefficients:	2.30E+09	1.4	18320
4	O+H2O<=>OH+OH	2.97E+06	2	13400
	Reverse Arrhenius coefficients:	1.46E+05	2.1	-2904
5	H2+M<=>H+H+M	4.58E+19	-1.4	104400
	Reverse Arrhenius coefficients:	1.15E+20	-1.7	820
	H2	Enhanced	by	2.50E+00
	H2O	Enhanced	by	1.20E+01
	CO	Enhanced	by	1.90E+00
	CO2	Enhanced	by	3.80E+00
6	O2+M<=>O+O+M	4.52E+17	-0.6	118900
	Reverse Arrhenius coefficients:	6.16E+15	-0.5	0
	H2	Enhanced	by	2.50E+00
	H2O	Enhanced	by	1.20E+01
	CO	Enhanced	by	1.90E+00
	CO2	Enhanced	by	3.80E+00
	CH4	Enhanced	by	2.00E+00
	C2H6	Enhanced	by	3.00E+00
7	OH+M<=>O+H+M	9.88E+17	-0.7	102100
	Reverse Arrhenius coefficients:	4.71E+18	-1	0
	H2	Enhanced	by	2.50E+00
	H2O	Enhanced	by	1.20E+01
	CO	Enhanced	by	1.50E+00
	CO2	Enhanced	by	2.00E+00
	CH4	Enhanced	by	2.00E+00
	C2H6	Enhanced	by	3.00E+00
8	H2O+M<=>H+OH+M	1.91E+23	-1.8	118500
	Reverse Arrhenius coefficients:	4.50E+22	-2	0
	H2	Enhanced	by	7.30E-01
	H2O	Enhanced	by	1.20E+01
	CH4	Enhanced	by	2.00E+00
	C2H6	Enhanced	by	3.00E+00
9	H+O2(+M)<=>HO2(+M)	1.48E+12	0.6	0
	Low pressure limit:	3.48E+16	-4.11E-01	-1.12E+03

	TROE centering:	5.00E-01	1.00E-30	1.00E+30
	H2	Enhanced	by	1.30E+00
	H2O	Enhanced	by	1.40E+01
	CO	Enhanced	by	1.90E+00
	CO2	Enhanced	by	3.80E+00
	CH4	Enhanced	by	2.00E+00
	C2H6	Enhanced	by	3.00E+00
10	HO2+H<=>H2+O2	1.66E+13	0	823
	Reverse Arrhenius coefficients:	3.16E+12	0.3	5510
11	HO2+H<=>OH+OH	7.08E+13	0	295
	Reverse Arrhenius coefficients:	2.03E+10	0.7	36840
12	HO2+O<=>OH+O2	3.25E+13	0	0
	Reverse Arrhenius coefficients:	3.25E+12	0.3	53280
13	HO2+OH<=>H2O+O2	2.89E+13	0	-497
	Reverse Arrhenius coefficients:	5.86E+13	0.2	69080
14	H2O2+O2<=>HO2+HO2	4.63E+16	-0.3	50670
	Reverse Arrhenius coefficients:	4.20E+14	0	11980
	Declared duplicate reaction...			
15	H2O2+O2<=>HO2+HO2	1.43E+13	-0.3	37060
	Reverse Arrhenius coefficients:	1.30E+11	0	-1629
	Declared duplicate reaction...			
16	H2O2(+M)<=>OH+OH(+M)	2.95E+14	0	48430
	Low pressure limit:	1.20E+17	0.00E+00	4.55E+04
	TROE centering:	5.00E-01	1.00E-30	1.00E+30
	H2	Enhanced	by	2.50E+00
	H2O	Enhanced	by	1.20E+01
	CO	Enhanced	by	1.90E+00
	CO2	Enhanced	by	3.80E+00
	CH4	Enhanced	by	2.00E+00
	C2H6	Enhanced	by	3.00E+00
17	H2O2+H<=>H2O+OH	2.41E+13	0	3970
	Reverse Arrhenius coefficients:	1.27E+08	1.3	71410
18	H2O2+H<=>H2+HO2	6.02E+13	0	7950
	Reverse Arrhenius coefficients:	1.04E+11	0.7	23950
19	H2O2+O<=>OH+HO2	9.55E+06	2	3970
	Reverse Arrhenius coefficients:	8.66E+03	2.7	18560
20	H2O2+OH<=>H2O+HO2	1.00E+12	0	0
	Reverse Arrhenius coefficients:	1.84E+10	0.6	30890
	Declared duplicate reaction...			
21	H2O2+OH<=>H2O+HO2	5.80E+14	0	9557
	Reverse Arrhenius coefficients:	1.07E+13	0.6	40450
	Declared duplicate reaction...			
22	CO+O(+M)<=>CO2(+M)	1.80E+10	0	2384
	Low pressure limit:	1.35E+24	-2.79E+00	4.19E+03
	H2	Enhanced	by	2.00E+00
	O2	Enhanced	by	6.00E+00

	H2O	Enhanced	by	6.00E+00	
	CO	Enhanced	by	1.50E+00	
	CO2	Enhanced	by	3.50E+00	
	CH4	Enhanced	by	2.00E+00	
	C2H6	Enhanced	by	3.00E+00	
23	CO+O2<=>CO2+O	1.05E+12	0	42540	
	Reverse Arrhenius coefficients:	7.95E+15	-0.8	51230	
24	CO+OH<=>CO2+H	1.75E+05	1.9	-434.8	
	Reverse Arrhenius coefficients:	4.63E+11	0.8	24990	
25	CO+HO2<=>CO2+OH	1.57E+05	2.2	17940	
	Reverse Arrhenius coefficients:	1.19E+08	1.7	79910	
26	HCO+M<=>H+CO+M	1.86E+17	-1	17000	
	Reverse Arrhenius coefficients:	1.40E+16	-0.6	1670	
	H2	Enhanced	by	2.00E+00	
	H2O	Enhanced	by	1.20E+01	
	CO	Enhanced	by	1.50E+00	
	CO2	Enhanced	by	2.00E+00	
	CH4	Enhanced	by	2.00E+00	
	C2H6	Enhanced	by	3.00E+00	
27	HCO+O2<=>CO+HO2	2.71E+10	0.7	-469	
	Reverse Arrhenius coefficients:	4.28E+09	1	33070	
28	HCO+H<=>CO+H2	7.34E+13	0	0	
	Reverse Arrhenius coefficients:	2.21E+12	0.7	88230	
29	HCO+OH<=>CO+H2O	1.02E+14	0	0	
	Reverse Arrhenius coefficients:	3.27E+13	0.6	103100	
30	HCO+CH3<=>CH4+CO	2.65E+13	0	0	
	Reverse Arrhenius coefficients:	7.29E+14	0.2	89770	
31	HCO+HO2<=>CH2O+O2	2.50E+14	-0.1	13920	
	Reverse Arrhenius coefficients:	8.07E+15	0	53420	
32	HCO+HO2<=>CO2+H+OH	3.00E+13	0	0	
	Warning...all REV parameters are zero… this reaction will be treated as irreversible	0.00E+00	0	0.00E+00	
33	CH2O+CO<=>HCO+HCO	9.19E+13	0.4	73040	
	Reverse Arrhenius coefficients:	1.80E+13	0	0	
34	HCO+HCO<=>H2+CO+CO	3.00E+12	0	0	
	Warning...all REV parameters are zero… this reaction will be treated as irreversible	0.00E+00	0	0.00E+00	
35	HCO+H(+M)<=>CH2O(+M)	1.09E+12	0.5	-260	
	Low pressure limit:	1.35E+24	-2.57E+00	1.43E+03	
	TROE centering:	7.82E-01 6.57E+03	2.71E+02	2.76E+03	
	H2	Enhanced	by	2.00E+00	
	H2O	Enhanced	by	6.00E+00	
	CO	Enhanced	by	1.50E+00	
	CO2	Enhanced	by	2.00E+00	
	CH4	Enhanced	by	2.00E+00	

	C2H6	Enhanced	by	3.00E+00
36	CH2O+OH<=>HCO+H2O	7.82E+07	1.6	-1055
	Reverse Arrhenius coefficients:	4.91E+06	1.8	29030
37	CH2O+H<=>HCO+H2	5.74E+07	1.9	2740
	Reverse Arrhenius coefficients:	3.39E+05	2.2	27930
38	CH2O+O<=>HCO+OH	6.26E+09	1.1	2260
	Reverse Arrhenius coefficients:	1.94E+07	1.4	16040
39	CH2O+CH3<=>HCO+CH4	3.83E+01	3.4	4312
	Reverse Arrhenius coefficients:	2.06E+02	3.2	21040
40	CH2O+HO2<=>HCO+H2O2	7.10E-03	4.5	6580
	Reverse Arrhenius coefficients:	2.43E-02	4.1	5769
41	HOCHO<=>CO+H2O	2.30E+13	0	50000
	Reverse Arrhenius coefficients:	2.12E+04	2.1	42420
42	HOCHO<=>CO2+H2	1.50E+16	0	57000
	Reverse Arrhenius coefficients:	2.40E+14	0.5	61020
43	HOCHO<=>HCO+OH	3.47E+22	-1.5	110700
	Reverse Arrhenius coefficients:	1.00E+14	0	0
44	HOCHO+OH<=>H2O+CO2+H	2.62E+06	2.1	916
	Warning...all REV parameters are zero…	0.00E+00	0	0.00E+00
	this reaction will be treated as irreversible			
45	HOCHO+OH<=>H2O+CO+OH	1.85E+07	1.5	-962
	Warning...all REV parameters are zero…	0.00E+00	0	0.00E+00
	this reaction will be treated as irreversible			
46	HOCHO+H<=>H2+CO+OH	6.03E+13	-0.3	2988
	Warning...all REV parameters are zero…	0.00E+00	0	0.00E+00
	this reaction will be treated as irreversible			
47	HOCHO+CH3<=>CH4+CO+OH	3.90E-07	5.8	2200
	Warning...all REV parameters are zero…	0.00E+00	0	0.00E+00
	this reaction will be treated as irreversible			
48	HOCHO+HO2<=>H2O2+CO+OH	1.00E+12	0	11920
	Warning...all REV parameters are zero…	0.00E+00	0	0.00E+00
	this reaction will be treated as irreversible			
49	CH3O(+M)<=>CH2O+H(+M)	6.80E+13	0	26170
	Low pressure limit:	1.87E+25	-3.00E+00	2.4307E+04
	TROE centering:	9.00E-01	2.50E+03 1.30E+03 0.100+100	
	H2	Enhanced	by	2.00E+00
	H2O	Enhanced	by	6.00E+00
	CO	Enhanced	by	1.50E+00
	CO2	Enhanced	by	2.00E+00
	CH4	Enhanced	by	2.00E+00
	C2H6	Enhanced	by	3.00E+00
50	CH3O+O2<=>CH2O+HO2	4.38E-19	9.5	-5501
	Reverse Arrhenius coefficients:	1.42E-20	9.8	21080
51	CH3O+CH3<=>CH2O+CH4	1.20E+13	0	0
	Reverse Arrhenius coefficients:	6.75E+13	0.2	82810
52	CH3O+H<=>CH2O+H2	2.00E+13	0	0

253

	Reverse Arrhenius coefficients:	1.23E+11	0.7	81270
53	CH3O+HO2<=>CH2O+H2O2	3.01E+11	0	0
	Reverse Arrhenius coefficients:	1.07E+12	0	65270
54	CH3+H(+M)<=>CH4(+M)	2.11E+14	0	0
	Low pressure limit:	3.17E+23	-1.80E+00	0.00E+00
	TROE centering:	3.70E-01 3.32E+03 6.10E+01	0.100+100	
	H2	Enhanced	by	2.00E+00
	H2O	Enhanced	by	6.00E+00
	CO	Enhanced	by	1.50E+00
	CO2	Enhanced	by	2.00E+00
	CH4	Enhanced	by	2.00E+00
	C2H6	Enhanced	by	3.00E+00
55	CH4+OH<=>CH3+H2O	5.83E+04	2.6	2190
	Reverse Arrhenius coefficients:	6.80E+02	2.9	15540
56	CH4+O<=>CH3+OH	4.40E+05	2.5	6577
	Reverse Arrhenius coefficients:	2.53E+02	2.9	3625
57	CH4+HO2<=>CH3+H2O2	7.05E+04	2.5	21000
	Reverse Arrhenius coefficients:	4.47E+04	2.2	3462
58	CH4+CH2<=>CH3+CH3	2.46E+06	2	8270
	Reverse Arrhenius coefficients:	1.09E+03	2.8	10570
59	CH3+OH<=>CH3O+H	7.23E+11	0	5484
	Reverse Arrhenius coefficients:	1.56E+16	-0.8	-5821
60	CH3+OH<=>CH2+H2O	5.60E+07	1.6	5420
	Reverse Arrhenius coefficients:	1.48E+09	1.2	16470
61	CH3+HO2<=>CH3O+OH	1.00E+12	0.3	-687.5
	Reverse Arrhenius coefficients:	6.19E+12	0.1	24550
62	CH3+HO2<=>CH4+O2	1.16E+05	2.2	-3022
	Reverse Arrhenius coefficients:	2.02E+07	2.1	53210
63	CH3+O<=>CH2O+H	5.54E+13	0.1	-136
	Reverse Arrhenius coefficients:	3.87E+15	-0.1	68410
64	CH3+O2<=>CH3O+O	7.55E+12	0	28320
	Reverse Arrhenius coefficients:	4.67E+14	-0.5	288
65	CH3+O2<=>CH2O+OH	5.87E+11	0	13840
	Reverse Arrhenius coefficients:	1.18E+11	0.2	65660
66	CH3+O2(+M)<=>CH3O2(+M)	1.01E+08	1.6	0
	Low pressure limit:	3.82E+31	-4.89E+00	3.43E+03
	TROE centering:	4.50E-02 8.80E+02 2.50E+09	1.79E+09	
67	CH3O2+CH2O<=>CH3O2H+HCO	1.99E+12	0	11660
	Reverse Arrhenius coefficients:	1.32E+14	-0.8	9259
68	CH4+CH3O2<=>CH3+CH3O2H	1.81E+11	0	18480
	Reverse Arrhenius coefficients:	2.23E+12	-0.7	-655
69	CH3O2+CH3<=>CH3O+CH3O	9.00E+12	0	-1200
	Reverse Arrhenius coefficients:	3.48E+12	0.2	28280
70	CH3O2+HO2<=>CH3O2H+O2	2.47E+11	0	-1570
	Reverse Arrhenius coefficients:	5.30E+14	-0.8	35520
71	CH3O2+CH3O2<=>O2+CH3O+CH3O	1.40E+16	-1.6	1860

254

	Warning...all REV parameters are zero... this reaction will be treated as irreversible	0.00E+00	0	0.00E+00
72	CH3O2+H<=>CH3O+OH	9.60E+13	0	0
	Reverse Arrhenius coefficients:	1.72E+09	1	40780
73	CH3O2+O<=>CH3O+O2	3.60E+13	0	0
	Reverse Arrhenius coefficients:	2.25E+11	0.6	57520
74	CH3O2H<=>CH3O+OH	6.31E+14	0	42300
	Reverse Arrhenius coefficients:	2.51E+06	1.9	-2875
75	CH2+H(+M)<=>CH3(+M)	2.50E+16	-0.8	0
	Low pressure limit:	3.20E+27	-3.14E+00	1.23E+03
	TROE centering:	6.80E-01 7.80E+01 2.00E+03 5.59E+03		
	H2	Enhanced	by	2.00E+00
	H2O	Enhanced	by	6.00E+00
	CO	Enhanced	by	1.50E+00
	CO2	Enhanced	by	2.00E+00
	CH4	Enhanced	by	2.00E+00
	C2H6	Enhanced	by	3.00E+00
76	CH2+O2<=>CO2+H+H	2.27E+12	0	1000
	Warning...all REV parameters are zero... this reaction will be treated as irreversible	0.00E+00	0	0.00E+00
77	C2H6(+M)<=>CH3+CH3(+M)	1.88E+50	-9.7	107300
	Low pressure limit:	3.72E+65	-1.31E+01	1.02E+05
	TROE centering:	3.90E-01 1.00E+02 1.90E+03 6.00E+03		
	H2	Enhanced	by	2.00E+00
	H2O	Enhanced	by	6.00E+00
	CO	Enhanced	by	1.50E+00
	CO2	Enhanced	by	2.00E+00
	CH4	Enhanced	by	2.00E+00
	C2H6	Enhanced	by	3.00E+00
78	C2H5+H(+M)<=>C2H6(+M)	5.21E+17	-1	1580
	Low pressure limit:	1.99E+41	-7.08E+00	6.69E+03
	TROE centering:	8.42E-01 1.25E+02 2.22E+03 6.88E+03		
	H2	Enhanced	by	2.00E+00
	H2O	Enhanced	by	6.00E+00
	CO	Enhanced	by	1.50E+00
	CO2	Enhanced	by	2.00E+00
	CH4	Enhanced	by	2.00E+00
	C2H6	Enhanced	by	3.00E+00
79	C2H6+H<=>C2H5+H2	1.15E+08	1.9	7530
	Reverse Arrhenius coefficients:	1.06E+04	2.6	9760
80	C2H6+O<=>C2H5+OH	3.55E+06	2.4	5830
	Reverse Arrhenius coefficients:	1.72E+02	3.1	6648
81	C2H6+OH<=>C2H5+H2O	1.48E+07	1.9	950
	Reverse Arrhenius coefficients:	1.45E+04	2.5	18070
82	C2H6+O2<=>C2H5+HO2	6.03E+13	0	51870
	Reverse Arrhenius coefficients:	2.92E+10	0.3	-593

83	C2H6+CH3<=>C2H5+CH4	1.51E-07	6	6047
	Reverse Arrhenius coefficients:	1.27E-08	6.2	9817
84	C2H6+HO2<=>C2H5+H2O2	3.46E+01	3.6	16920
	Reverse Arrhenius coefficients:	1.85E+00	3.6	3151
85	C2H6+CH3O2<=>C2H5+CH3O2H	1.94E+01	3.6	17100
	Reverse Arrhenius coefficients:	2.02E+01	3.2	1734
86	C2H4+H(+M)<=>C2H5(+M)	5.40E+11	0.5	1820
	Low pressure limit:	6.00E+41	-7.62E+00	6.97E+03
	TROE centering:	9.75E-01	2.10E+02 9.84E+02	4.37E+03
	H2	Enhanced	by	2.00E+00
	H2O	Enhanced	by	6.00E+00
	CO	Enhanced	by	1.50E+00
	CO2	Enhanced	by	2.00E+00
	CH4	Enhanced	by	2.00E+00
	C2H6	Enhanced	by	3.00E+00
87	H2+CH3O2<=>H+CH3O2H	1.50E+14	0	26030
	Reverse Arrhenius coefficients:	1.69E+18	-1.1	8434
88	C2H5+C2H3<=>C2H4+C2H4	6.86E+11	0.1	-4300
	Reverse Arrhenius coefficients:	4.82E+14	0	71530
89	CH3+C2H5<=>CH4+C2H4	1.18E+04	2.5	-2921
	Reverse Arrhenius coefficients:	2.39E+06	2.4	66690
90	C2H5+H<=>CH3+CH3	3.27E+17	-0.9	310
	Reverse Arrhenius coefficients:	6.84E+12	0.1	10600
91	C2H5+H<=>C2H4+H2	2.00E+12	0	0
	Reverse Arrhenius coefficients:	4.44E+11	0.4	68070
92	C2H5+O<=>CH3CHO+H	1.10E+14	0	0
	Reverse Arrhenius coefficients:	1.04E+17	-0.5	77420
93	C2H5+HO2<=>C2H5O+OH	1.10E+13	0	0
	Reverse Arrhenius coefficients:	9.68E+15	-0.7	27650
94	CH3O2+C2H5<=>CH3O+C2H5O	8.00E+12	0	-1000
	Reverse Arrhenius coefficients:	4.40E+14	-0.4	30890
95	C2H5O+O2<=>CH3CHO+HO2	4.28E+10	0	1097
	Reverse Arrhenius coefficients:	1.32E+08	0.6	34140
96	C2H5O<=>CH3+CH2O	1.32E+20	-2	20750
	Reverse Arrhenius coefficients:	3.00E+11	0	6336
97	C2H5O<=>CH3CHO+H	5.42E+15	-0.7	22230
	Reverse Arrhenius coefficients:	8.00E+12	0	6400
98	C2H4O2H<=>C2H5+O2	1.81E+45	-11.5	14600
	Reverse Arrhenius coefficients:	7.52E+42	-10.9	-1816
99	C2H5+O2<=>C2H4+HO2	7.56E+14	-1	4749
	Reverse Arrhenius coefficients:	8.80E+14	-1	18130
	Declared duplicate reaction...			
100	C2H5+O2<=>C2H4+HO2	4.00E-01	3.9	13620
	Reverse Arrhenius coefficients:	4.66E-01	3.9	27000
	Declared duplicate reaction...			
101	C2H5+O2<=>C2H4O1-2+OH	1.63E+11	-0.3	6150

	Reverse Arrhenius coefficients:	3.63E+13	-0.6	39840
102	C2H5+O2<=>CH3CHO+OH	8.26E+02	2.4	5285
	Reverse Arrhenius coefficients:	2.25E+03	2.3	65970
103	C2H5O2<=>C2H4O2H	2.28E+39	-8.5	45170
	Reverse Arrhenius coefficients:	1.20E+36	-8.1	27020
104	C2H5O2<=>CH3CHO+OH	2.52E+41	-10.2	43710
	Reverse Arrhenius coefficients:	1.50E+36	-9.3	69840
105	C2H5O2<=>C2H4+HO2	1.82E+38	-8.4	37890
	Reverse Arrhenius coefficients:	4.63E+32	-7.4	16700
106	C2H4O2H<=>C2H4O1-2+OH	8.85E+30	-6.1	20660
	Reverse Arrhenius coefficients:	8.20E+30	-5.8	37930
107	C2H4O2H<=>C2H4+HO2	3.98E+34	-7.2	23250
	Reverse Arrhenius coefficients:	1.92E+32	-6.6	20210
108	C2H4O1-2<=>CH3+HCO	3.63E+13	0	57200
	Reverse Arrhenius coefficients:	1.01E+04	1.6	-2750
109	C2H4O1-2<=>CH3CHO	7.41E+12	0	53800
	Reverse Arrhenius coefficients:	9.01E+10	0.2	80800
110	CH3CHO<=>CH3+HCO	7.69E+20	-1.3	86950
	Reverse Arrhenius coefficients:	1.75E+13	0	0
111	CH3CHO+H<=>CH3CO+H2	1.11E+13	0	3110
	Reverse Arrhenius coefficients:	7.67E+09	0.6	17060
112	CH3CHO+O<=>CH3CO+OH	5.94E+12	0	1868
	Reverse Arrhenius coefficients:	2.16E+09	0.6	14410
113	CH3CHO+OH<=>CH3CO+H2O	2.00E+06	1.8	1300
	Reverse Arrhenius coefficients:	1.47E+04	2.3	30140
114	CH3CHO+O2<=>CH3CO+HO2	3.01E+13	0	39150
	Reverse Arrhenius coefficients:	1.09E+11	0.3	-1588
115	CH3CHO+CH3<=>CH3CO+CH4	1.76E+03	2.8	4950
	Reverse Arrhenius coefficients:	1.11E+03	3	20440
116	CH3CHO+HO2<=>CH3CO+H2O2	3.01E+12	0	11920
	Reverse Arrhenius coefficients:	1.20E+12	-0.1	9877
117	CH3O2+CH3CHO<=>CH3O2H+CH3CO	3.01E+12	0	11920
	Reverse Arrhenius coefficients:	2.34E+13	-0.5	8282
118	CH3CHO+OH<=>CH3+HOCHO	3.00E+15	-1.1	0
	Reverse Arrhenius coefficients:	2.37E+16	-1.3	23750
119	CH3CHO+OH<=>CH2CHO+H2O	1.72E+05	2.4	815
	Reverse Arrhenius coefficients:	1.34E+05	2.5	24950
120	CH3CO(+M)<=>CH3+CO(+M)	3.00E+12	0	16720
	Low pressure limit:	1.20E+15	0.00E+00	1.25E+04
121	CH3CO+CH3<=>CH2CO+CH4	5.00E+13	0	0
	Reverse Arrhenius coefficients:	8.77E+18	-1	62270
122	CH2CHO<=>CH2CO+H	1.10E+13	0.4	50430
	Reverse Arrhenius coefficients:	5.00E+13	0	12300
123	CH2CHO+O2<=>CH2O+CO+OH	2.00E+13	0	4200
	Warning...all REV parameters are zero…	0.00E+00	0	0.00E+00
	this reaction will be treated as irreversible			

124	CH2+CO(+M)<=>CH2CO(+M)	8.10E+11	0	0
	Low pressure limit:	2.69E+33	-5.11E+00	7.10E+03
	TROE centering:	5.91E-01 2.75E+02	1.23E+03	5.19E+03
	H2	Enhanced	by	2.00E+00
	H2O	Enhanced	by	6.00E+00
	CO	Enhanced	by	1.50E+00
	CO2	Enhanced	by	2.00E+00
	CH4	Enhanced	by	2.00E+00
	C2H6	Enhanced	by	3.00E+00
125	CH2CO+H<=>CH3+CO	1.10E+13	0	3400
	Reverse Arrhenius coefficients:	2.40E+12	0	40200
126	CH2CO+H<=>HCCO+H2	2.00E+14	0	8000
	Reverse Arrhenius coefficients:	3.00E+09	0.6	-1100
127	CH2CO+O<=>CH2+CO2	1.75E+12	0	1350
	Reverse Arrhenius coefficients:	1.24E+10	0.7	51680
128	CH2CO+O<=>HCCO+OH	1.00E+13	0	8000
	Reverse Arrhenius coefficients:	7.88E+07	0.6	-2512
129	CH2CO+OH<=>HCCO+H2O	1.00E+13	0	2000
	Reverse Arrhenius coefficients:	1.60E+09	0.5	7792
130	HCCO+OH<=>H2+CO+CO	1.00E+14	0	0
	Warning...all REV parameters are zero…	0.00E+00	0	0.00E+00
	this reaction will be treated as irreversible			
131	HCCO+O<=>H+CO+CO	8.00E+13	0	0
	Warning...all REV parameters are zero…	0.00E+00	0	0.00E+00
	this reaction will be treated as irreversible			
132	HCCO+O2<=>OH+CO+CO	4.20E+10	0	850
	Warning...all REV parameters are zero…	0.00E+00	0	0.00E+00
	this reaction will be treated as irreversible			
133	C2H3+H(+M)<=>C2H4(+M)	1.36E+14	0.2	660
	Low pressure limit:	1.40E+30	-3.86E+00	3.23E+03
	TROE centering:	7.82E-01 2.08E+02	2.66E+03	6.10E+03
	H2	Enhanced	by	2.00E+00
	H2O	Enhanced	by	6.00E+00
	CO	Enhanced	by	1.50E+00
	CO2	Enhanced	by	2.00E+00
	CH4	Enhanced	by	2.00E+00
	C2H6	Enhanced	by	3.00E+00
134	C2H4(+M)<=>C2H2+H2(+M)	8.00E+12	0.4	88770
	Low pressure limit:	1.58E+51	-9.30E+00	9.78E+04
	TROE centering:	7.35E-01 1.80E+02	1.04E+03	5.42E+03
	H2	Enhanced	by	2.00E+00
	H2O	Enhanced	by	6.00E+00
	CO	Enhanced	by	1.50E+00
	CO2	Enhanced	by	2.00E+00
	CH4	Enhanced	by	2.00E+00
	C2H6	Enhanced	by	3.00E+00

135	C2H4+H<=>C2H3+H2	5.07E+07	1.9	12950
	Reverse Arrhenius coefficients:	1.60E+04	2.4	5190
136	C2H4+O<=>CH3+HCO	8.56E+06	1.9	183
	Reverse Arrhenius coefficients:	3.33E+02	2.6	26140
137	C2H4+O<=>CH2CHO+H	4.99E+06	1.9	183
	Reverse Arrhenius coefficients:	1.56E+09	1.2	18780
138	C2H4+OH<=>C2H3+H2O	2.09E+06	2	1160
	Reverse Arrhenius coefficients:	7.02E+03	2.4	8292
139	C2H4+CH3<=>C2H3+CH4	6.62E+00	3.7	9500
	Reverse Arrhenius coefficients:	1.44E+00	4	5472
140	C2H4+O2<=>C2H3+HO2	4.00E+13	0	58200
	Reverse Arrhenius coefficients:	6.63E+10	0.2	-4249
141	C2H4+CH3O2<=>C2H3+CH3O2H	2.23E+12	0	17190
	Reverse Arrhenius coefficients:	7.93E+12	-0.6	-8167
142	C2H4+CH3O2<=>C2H4O1-2+CH3O	2.82E+12	0	17110
	Reverse Arrhenius coefficients:	3.38E+13	-0.1	41660
143	C2H4+C2H5O2<=>C2H4O1-2+C2H5O	2.82E+12	0	17110
	Reverse Arrhenius coefficients:	7.64E+15	-0.9	42830
144	C2H4+HO2<=>C2H4O1-2+OH	2.23E+12	0	17190
	Reverse Arrhenius coefficients:	4.28E+14	-0.4	37500
145	C2H2+H(+M)<=>C2H3(+M)	5.60E+12	0	2400
	Low pressure limit	3.80E+40	-7.27E+00	7.22E+03
	TROE centering:	7.51E-01	9.85E+01 1.30E+03	4.17E+03
	H2	Enhanced	by	2.00E+00
	H2O	Enhanced	by	6.00E+00
	CO	Enhanced	by	1.50E+00
	CO2	Enhanced	by	2.00E+00
	CH4	Enhanced	by	2.00E+00
	C2H6	Enhanced	by	3.00E+00
146	C2H3+O2<=>C2H2+HO2	2.12E-06	6	9484
	Reverse Arrhenius coefficients:	1.09E-05	5.9	24040
147	C2H3+O2<=>CH2O+HCO	1.70E+29	-5.3	6500
	Reverse Arrhenius coefficients:	7.99E+27	-4.9	93450
148	C2H3+O2<=>CH2CHO+O	5.50E+14	-0.6	5260
	Reverse Arrhenius coefficients:	2.97E+18	-1.4	16300
149	CH3+C2H3<=>CH4+C2H2	3.92E+11	0	0
	Reverse Arrhenius coefficients:	3.50E+14	-0.2	70780
150	C2H3+H<=>C2H2+H2	3.00E+13	0	0
	Reverse Arrhenius coefficients:	2.93E+13	0.2	69240
151	C2H3+OH<=>C2H2+H2O	5.00E+12	0	0
	Reverse Arrhenius coefficients:	5.20E+13	0.1	84130
152	C2H2+O2<=>HCCO+OH	2.00E+08	1.5	30100
	Reverse Arrhenius coefficients:	1.58E+07	1	26820
153	C2H2+O<=>CH2+CO	6.94E+06	2	1900
	Reverse Arrhenius coefficients:	6.53E+04	2.3	50770
154	C2H2+O<=>HCCO+H	1.35E+07	2	1900

	Reverse Arrhenius coefficients:	3.73E+08	1.1	15350
155	C2H2+OH<=>CH2CO+H	3.24E+13	0	12000
	Reverse Arrhenius coefficients:	1.14E+20	-1.6	35960
156	C2H2+OH<=>CH3+CO	4.83E-04	4	-2000
	Reverse Arrhenius coefficients:	3.49E-06	4.6	52120
157	C2H5OH(+M)<=>C2H5+OH(+M)	2.40E+23	-1.6	99540
	Low pressure limit:	5.11E+85	-1.88E+01	1.19E+05
	TROE centering:	5.00E-01 6.50E+02 8.00E+02		1.00E+15
	H2	Enhanced	by	2.00E+00
	H2O	Enhanced	by	5.00E+00
	CO	Enhanced	by	2.00E+00
	CO2	Enhanced	by	3.00E+00
158	C2H5OH+OH<=>C2H5O+H2O	7.46E+11	0.3	1634
	Reverse Arrhenius coefficients:	3.65E+11	0.4	16310
159	C2H5OH+H<=>C2H5O+H2	1.50E+07	1.6	3038
	Reverse Arrhenius coefficients:	6.90E+05	1.8	2821
160	C2H5OH+HO2<=>C2H5O+H2O2	2.50E+12	0	24000
	Reverse Arrhenius coefficients:	6.66E+13	-0.5	7782
161	C2H5OH+O<=>C2H5O+OH	1.58E+07	2	4448
	Reverse Arrhenius coefficients:	3.82E+05	2.2	2819
162	C2H3CHO<=>C2H3+HCO	2.00E+24	-2.1	103400
	Reverse Arrhenius coefficients:	1.81E+13	0	0
163	C2H3CHO+H<=>C2H3CO+H2	1.34E+13	0	3300
	Reverse Arrhenius coefficients:	3.31E+10	0.6	22680
164	C2H3CHO+O<=>C2H3CO+OH	5.94E+12	0	1868
	Reverse Arrhenius coefficients:	7.70E+09	0.6	19840
165	C2H3CHO+OH<=>C2H3CO+H2O	9.24E+06	1.5	-962
	Reverse Arrhenius coefficients:	2.43E+05	2	33310
166	C2H3CHO+O2<=>C2H3CO+HO2	1.00E+13	0	40700
	Reverse Arrhenius coefficients:	1.30E+11	0.3	5391
167	C2H3CHO+HO2<=>C2H3CO+H2O2	3.01E+12	0	11920
	Reverse Arrhenius coefficients:	4.30E+12	-0.1	15300
168	C2H3CHO+CH3<=>C2H3CO+CH4	2.61E+06	1.8	5911
	Reverse Arrhenius coefficients:	5.88E+06	1.9	26830
169	C2H3CHO+CH3O2<=>C2H3CO+CH3O2H	3.01E+12	0	11920
	Reverse Arrhenius coefficients:	8.37E+13	-0.5	13710
170	C2H3CO<=>C2H3+CO	1.37E+21	-2.2	39410
	Reverse Arrhenius coefficients:	1.51E+11	0	4810
171	C2H5CHO<=>C2H5+HCO	1.50E+27	-3.2	87040
	Reverse Arrhenius coefficients:	1.81E+13	0	0
172	C2H5CHO+O<=>C2H5CO+OH	5.00E+12	0	1790
	Reverse Arrhenius coefficients:	1.56E+09	0.6	14310
173	C2H5CHO+OH<=>C2H5CO+H2O	2.69E+10	0.8	-340
	Reverse Arrhenius coefficients:	1.70E+08	1.3	28480
174	C2H5CHO+CH3<=>C2H5CO+CH4	2.61E+06	1.8	5911
	Reverse Arrhenius coefficients:	1.41E+06	2	21380

175	C2H5CHO+HO2<=>C2H5CO+H2O2	2.80E+12	0	13600
	Reverse Arrhenius coefficients:	9.61E+11	0	11530
176	C2H5CHO+CH3O2<=>C2H5CO+CH3O2H	3.01E+12	0	11920
	Reverse Arrhenius coefficients:	2.01E+13	-0.5	8260
177	C2H5CHO+C2H5<=>C2H5CO+C2H6	1.00E+12	0	8000
	Reverse Arrhenius coefficients:	6.42E+12	0	19700
178	C2H5CHO+C2H5O<=>C2H5CO+C2H5OH	6.03E+11	0	3300
	Reverse Arrhenius coefficients:	3.02E+11	0	18160
179	C2H5CHO+O2<=>C2H5CO+HO2	1.00E+13	0	40700
	Reverse Arrhenius coefficients:	3.12E+10	0.3	-58
180	C2H5CHO+C2H3<=>C2H5CO+C2H4	1.70E+12	0	8440
	Reverse Arrhenius coefficients:	3.19E+12	0.1	30130
181	C2H5CO<=>C2H5+CO	2.46E+23	-3.2	17550
	Reverse Arrhenius coefficients:	1.51E+11	0	4810
182	CH3OCO<=>CH3+CO2	7.98E+12	0.3	15640
	Reverse Arrhenius coefficients:	4.76E+07	1.5	34700
183	CH3OCO<=>CH3O+CO	3.18E+13	0.5	23400
	Reverse Arrhenius coefficients:	1.55E+06	2	5730
184	C2H5CHO+C3H5-A<=>C2H5CO+C3H6	1.70E+12	0	8440
	Reverse Arrhenius coefficients:	1.00E+13	0	28000
185	C3H6<=>C2H3+CH3	2.73E+62	-13.3	123200
	Reverse Arrhenius coefficients:	6.81E+53	-11.8	20560
186	C3H6<=>C3H5-A+H	2.01E+61	-13.3	118500
	Reverse Arrhenius coefficients:	1.02E+61	-13.5	30840
187	C3H6+O<=>C2H5+HCO	1.58E+07	1.8	-1216
	Reverse Arrhenius coefficients:	9.27E+01	2.7	23120
188	C3H6+O<=>CH2CO+CH3+H	2.50E+07	1.8	76
	Warning...all REV parameters are zero…	0.00E+00	0	0.00E+00
	this reaction will be treated as irreversible			
189	C3H6+O<=>C3H5-A+OH	5.24E+11	0.7	5884
	Reverse Arrhenius coefficients:	5.59E+10	0.7	20380
190	C3H6+OH<=>C3H5-A+H2O	3.12E+06	2	-298
	Reverse Arrhenius coefficients:	6.75E+06	1.9	30500
191	C3H6+HO2<=>C3H5-A+H2O2	9.64E+03	2.6	13910
	Reverse Arrhenius coefficients:	1.14E+06	1.9	13820
192	C3H6+H<=>C3H5-A+H2	1.73E+05	2.5	2492
	Reverse Arrhenius coefficients:	3.52E+04	2.5	18400
193	C3H6+H<=>C2H4+CH3	1.45E+34	-5.8	18500
	Reverse Arrhenius coefficients:	4.57E+28	-4.5	27160
194	C3H6+O2<=>C3H5-A+HO2	4.00E+12	0	39900
	Reverse Arrhenius coefficients:	4.27E+12	-0.3	1117
195	C3H6+CH3<=>C3H5-A+CH4	2.21E+00	3.5	5675
	Reverse Arrhenius coefficients:	4.10E+02	3.1	23120
196	C3H6+C2H5<=>C3H5-A+C2H6	1.00E+11	0	9800
	Reverse Arrhenius coefficients:	5.37E+05	1.3	16440
197	C3H6+CH3O2<=>C3H5-A+CH3O2H	3.24E+11	0	14900

	Reverse Arrhenius coefficients:	2.00E+10	0	15000
198	C3H5-A<=>C2H2+CH3	2.40E+48	-9.9	82080
	Reverse Arrhenius coefficients:	2.61E+46	-9.8	36950
199	C3H5-A+HO2<=>C3H5O+OH	7.00E+12	0	-1000
	Reverse Arrhenius coefficients:	3.20E+12	0.1	11440
200	C3H5-A+CH3O2<=>C3H5O+CH3O	7.00E+12	0	-1000
	Reverse Arrhenius coefficients:	1.99E+15	-0.7	17020
201	C3H5-A+C2H5<=>C2H4+C3H6	4.00E+11	0	0
	Reverse Arrhenius coefficients:	6.94E+16	-1.3	52800
202	C3H5-A+O2<=>CH2CHO+CH2O	7.14E+15	-1.2	21050
	Reverse Arrhenius coefficients:	4.94E+16	-1.4	88620
203	C3H5-A+O2<=>C2H3CHO+OH	2.47E+13	-0.4	23020
	Reverse Arrhenius coefficients:	3.96E+13	-0.6	74920
204	C3H5-A+O2<=>C2H2+CH2O+OH	9.72E+29	-5.7	21450
	Warning...all REV parameters are zero… this reaction will be treated as irreversible	0.00E+00	0	0.00E+00
205	C3H5O<=>C2H3CHO+H	1.00E+14	0	29100
	Reverse Arrhenius coefficients:	1.68E+14	-0.2	19690
206	C3H5O<=>C2H3+CH2O	1.46E+20	-2	35090
	Reverse Arrhenius coefficients:	1.50E+11	0	10600
207	C3H5O+O2<=>C2H3CHO+HO2	1.00E+12	0	6000
	Reverse Arrhenius coefficients:	1.29E+11	0	32000
208	C4H8-1<=>C3H5-A+CH3	1.50E+19	-1	73400
	Reverse Arrhenius coefficients:	1.35E+13	0	0
209	C4H8-1<=>C2H3+C2H5	1.00E+19	-1	96770
	Reverse Arrhenius coefficients:	9.00E+12	0	0
210	C4H8-1<=>H+C4H7-13	4.11E+18	-1	97350
	Reverse Arrhenius coefficients:	5.00E+13	0	0
211	C4H8-1+O2<=>C4H7-13+HO2	2.00E+13	0	37190
	Reverse Arrhenius coefficients:	4.65E+12	0.1	-168
212	C4H8-1+H<=>C4H7-13+H2	3.38E+05	2.4	207
	Reverse Arrhenius coefficients:	4.32E+06	2.1	20330
213	C4H8-1+OH<=>C4H7-13+H2O	2.76E+04	2.6	-1919
	Reverse Arrhenius coefficients:	1.53E+06	2.4	33360
214	C4H8-1+CH3<=>C4H7-13+CH4	3.69E+00	3.3	4002
	Reverse Arrhenius coefficients:	1.23E+03	3	24610
215	C4H8-1+HO2<=>C4H7-13+H2O2	4.82E+03	2.5	10530
	Reverse Arrhenius coefficients:	1.59E+06	2	14350
216	C4H8-1+CH3O2<=>C4H7-13+CH3O2H	4.82E+03	2.5	10530
	Reverse Arrhenius coefficients:	3.30E+06	1.8	11330
217	C4H8-1+C3H5-A<=>C4H7-13+C3H6	7.90E+10	0	12400
	Reverse Arrhenius coefficients:	1.00E+11	0	17500
218	C4H8-1+C4H6<=>C4H7-13+C4H7-13	2.35E+12	0	46720
	Reverse Arrhenius coefficients:	1.60E+12	0	0
219	C4H7-13<=>C4H6+H	1.20E+14	0	49300
	Reverse Arrhenius coefficients:	4.00E+13	0	1300

220	C4H7-13+C2H5<=>C4H8-1+C2H4	2.59E+12	0	-131
	Reverse Arrhenius coefficients:	1.15E+13	0.1	49440
221	C4H7-13+CH3O<=>C4H8-1+CH2O	2.41E+13	0	0
	Reverse Arrhenius coefficients:	2.48E+12	0.3	66330
222	C4H7-13+O<=>C2H3CHO+CH3	6.03E+13	0	0
	Reverse Arrhenius coefficients:	3.38E+15	-0.8	81630
223	C4H7-13+HO2<=>C4H7O+OH	9.64E+12	0	0
	Reverse Arrhenius coefficients:	7.29E+15	-1.1	15530
224	C4H7-13+CH3O2<=>C4H7O+CH3O	9.64E+12	0	0
	Reverse Arrhenius coefficients:	7.12E+17	-1.7	20290
225	C3H5-A+C4H7-13<=>C3H6+C4H6	6.31E+12	0	0
	Reverse Arrhenius coefficients:	1.00E+10	0	50000
226	C4H7-13+O2<=>C4H6+HO2	1.00E+09	0	0
	Reverse Arrhenius coefficients:	1.00E+11	0	17000
227	H+C4H7-13<=>C4H6+H2	3.16E+13	0	0
	Reverse Arrhenius coefficients:	1.07E+13	0	56810
228	C2H5+C4H7-13<=>C4H6+C2H6	3.98E+12	0	0
	Reverse Arrhenius coefficients:	3.21E+12	0	49840
229	C2H3+C4H7-13<=>C2H4+C4H6	3.98E+12	0	0
	Reverse Arrhenius coefficients:	1.16E+13	0	57710
230	C4H7-13+C2H5O2<=>C4H7O+C2H5O	3.80E+12	0	-1200
	Reverse Arrhenius coefficients:	2.00E+10	0	0
231	C4H7O<=>CH3CHO+C2H3	7.94E+14	0	19000
	Reverse Arrhenius coefficients:	1.00E+10	0	20000
232	C4H7O<=>C2H3CHO+CH3	7.94E+14	0	19000
	Reverse Arrhenius coefficients:	1.00E+10	0	20000
233	C4H6<=>C2H3+C2H3	4.03E+19	-1	98150
	Reverse Arrhenius coefficients:	1.26E+13	0	0
234	C4H6+OH<=>C2H5+CH2CO	1.00E+12	0	0
	Reverse Arrhenius coefficients:	3.73E+12	0	30020
235	C4H6+OH<=>CH2O+C3H5-A	1.00E+12	0	0
	Reverse Arrhenius coefficients:	3.50E+06	0	71060
236	C4H6+OH<=>C2H3+CH3CHO	1.00E+12	0	0
	Reverse Arrhenius coefficients:	5.44E+11	0	18550
237	C4H6+O<=>C2H4+CH2CO	1.00E+12	0	0
	Reverse Arrhenius coefficients:	6.38E+11	0	94340
238	C2H3+C2H4<=>C4H6+H	5.00E+11	0	7300
	Reverse Arrhenius coefficients:	1.00E+13	0	4700
239	C2H4CHO<=>C2H4+HCO	3.13E+13	-0.5	24590
	Reverse Arrhenius coefficients:	1.50E+11	0	8300
240	MD6J+H=MD	1.00E+14	0	0
241	MB4J+C6H13-1=MD	8.00E+12	0	0
242	ME2J+C8H17-1=MD	8.00E+12	0	0
243	MD+H=MD6J+H2	1.30E+06	2.4	4471
244	MD+HO2=MD6J+H2O2	5.88E+06	2.5	14860
245	MD+OH=MD6J+H2O	4.67E+08	1.6	-35

246	MD+O2=MD6J+HO2	4.00E+13	0	50160
247	MD+O=MD6J+OH	5.95E+05	2.4	2846
248	MD+CH3=MD6J+CH4	8.40E+04	2.1	7574
249	MD+CH3O2=MD6J+CH3O2H	5.88E+04	2.5	14860
250	MD+C2H3=MD6J+C2H4	4.00E+11	0	16800
251	MD+C2H5=MD6J+C2H6	5.00E+10	0	10400
252	MD9D+H=MD6J	2.50E+11	0.5	2620
253	C5H10-1+MF5J=MD6J	8.80E+03	2.5	6130
254	C6H12-1+MB4J=MD6J	8.80E+03	2.5	6130
255	C8H16-1+ME2J=MD6J	2.00E+11	0	7600
256	C2H4+MP3J=MF5J	8.80E+03	2.5	6130
257	CH2O+C2H5CO=MP3J	2.00E+11	0	20090
258	C2H4+ME2J=MB4J	2.00E+11	0	7600
259	CH2CO+CH3O=ME2J	5.00E+11	0	-1000
260	C2H4+C6H13-1=C8H17-1	8.80E+03	2.5	6130
261	C8H16-1+H=C8H17-1	2.50E+11	0.5	2620
262	C6H12-1+H=C6H13-1	2.50E+11	0.5	2620
263	CH2O+CH3CO=ME2J	2.00E+11	0	20090
264	CH3+C6H12-1=C7H15-2	8.80E+03	2.5	6130
265	C2H5+C5H10-1=C7H15-2	1.76E+04	2.5	6130
266	CH2CO+CH3=C2H5CO	1.00E+11	0	7600
267	C6H13-1+O2=C6H12-1+HO2	1.60E+12	0	5000
268	C8H17-1+O2=C8H16-1+HO2	1.60E+12	0	5000
269	MD6J+O2=MD9D+HO2	1.60E+12	0	5000
270	C8H16-1+H=C8H15-18+H2	9.40E+04	2.8	6280
271	C8H16-1+HO2=C8H15-18+H2O2	4.05E+04	2.5	16690
272	C8H16-1+OH=C8H15-18+H2O	5.27E+09	1	1590
273	C8H16-1+O2=C8H15-18+HO2	6.00E+13	0	52800
274	C8H16-1+O=C8H15-18+OH	1.05E+06	2.4	4766
275	C8H16-1+CH3=C8H15-18+CH4	4.52E-01	3.6	7154
276	C8H16-1+CH3O2=C8H15-18+CH3O2H	4.05E+04	2.5	16690
277	C6H12-1+H=C6H11-14+H2	1.30E+06	2.4	4471
278	C6H12-1+HO2=C6H11-14+H2O2	5.88E+04	2.5	14860
279	C6H12-1+OH=C6H11-14+H2O	4.67E+07	1.6	-35
280	C6H12-1+O2=C6H11-14+HO2	4.00E+13	0	50160
281	C6H12-1+O=C6H11-14+OH	5.95E+05	2.4	2846
282	C6H12-1+CH3=C6H11-14+CH4	8.40E+04	2.1	7574
283	C6H12-1+CH3O2=C6H11-14+CH3O2H	5.88E+04	2.5	14860
284	C6H12-1+C2H3=C6H11-14+C2H4	4.00E+11	0	16800
285	C6H12-1+C2H5=C6H11-14+C2H6	5.00E+10	0	10400
286	C5H10-1+H=C5H9-15+H2	9.40E+04	2.8	6280
287	C5H10-1+HO2=C5H9-15+H2O2	4.05E+04	2.5	16690
288	C5H10-1+OH=C5H9-15+H2O	5.27E+09	1	1590
289	C5H10-1+O=C5H9-15+OH	1.05E+06	2.4	4766
290	C5H10-1+CH3=C5H9-15+CH4	4.52E-01	3.6	7154
291	C5H10-1+CH3O2=C5H9-15+CH3O2H	4.05E+04	2.5	16690

292	C5H10-1+C2H5=C5H9-15+C2H6	5.00E+10	0	13400
293	C4H8-1+O=C4H7-13+OH	6.60E+05	2.4	1210
294	C4H8-1+C2H3=C4H7-13+C2H4	2.21E+00	3.5	4690
295	C4H8-1+C2H5=C4H7-13+C2H6	1.00E+11	0	9800
296	C2H3+C4H8-1=C6H11-14	2.00E+11	0	2007
297	CH3+C5H8-14=C6H11-14	8.80E+03	2.5	6130
298	H+C5H8-14=C5H9-15	5.00E+11	0.5	2620
299	C5H9-15=C2H4+C3H5-A	3.31E+13	0	21460
300	MS6D=C3H5-A+MB4J	2.50E+16	0	71000
301	C8H16-1=C3H6+C5H10-1	3.98E+12	0	57630
302	C6H12-1=C3H6+C3H6	3.98E+12	0	57630
303	C5H10-1=C3H6+C2H4	3.98E+12	0	57630
304	MD9D=C3H6+MS6D	3.98E+12	0	57630
305	MD6J+O2=MD6O2	7.54E+12	0	0
306	MF5J+O2=MF5O2	4.52E+12	0	0
307	MF5O2=MF5OOH3J	2.50E+10	0	20850
308	MD6O2=MD6OOH8J	2.50E+10	0	20850
309	MD6OOH8J+O2=MD6OOH8O2	7.54E+12	0	0
310	MF5OOH3J+O2=MF5OOH3O2	7.54E+12	0	0
311	MD6OOH8O2=MDKET68+OH	1.25E+10	0	17850
312	MF5OOH3O2=MFKET53+OH	2.50E+10	0	21400
313	MDKET68=C2H5CHO+MS6OXO7J+OH	1.05E+16	0	41600
314	MFKET53=OH+CH2CHO+MP3OXO	1.05E+16	0	41600
315	CH2CO+MF5J=MS6OXO7J	1.51E+11	0	4810
316	MP3OXO+H=MP2OXO3J+H2	4.00E+13	0	4200
317	MP3OXO+OH=MP2OXO3J+H2O	2.69E+10	0.8	-340
318	CO+ME2J=MP2OXO3J	1.51E+11	0	4810
319	MD9D=MS7J+C3H5-A	2.50E+16	0	71000
320	C2H4+MF5J=MS7J	8.80E+03	2.5	6130
321	C5H9-15+MF5J=MD9D	8.00E+12	0	0
322	C8H15-18+ME2J=MD9D	8.00E+12	0	0
323	MD9D6J+H=MD9D	1.00E+14	0	0
324	MD9D+H=MD9D6J+H2	1.30E+06	2.4	4471
325	MD9D+HO2=MD9D6J+H2O2	5.88E+04	2.5	14860
326	MD9D+OH=MD9D6J+H2O	4.67E+08	1.6	-35
327	MD9D+O2=MD9D6J+HO2	4.00E+13	0	50160
328	MD9D+O=MD9D6J+OH	5.95E+05	2.4	2846
329	MD9D+CH3=MD9D6J+CH4	8.40E+04	2.1	7574
330	MD9D+CH3O2=MD9D6J+CH3O2H	5.88E+04	2.5	14860
331	MD9D+C2H3=MD9D6J+C2H4	4.00E+11	0	16800
332	MD9D+C2H5=MD9D6J+C2H6	5.00E+10	0	10400
333	C6H10-15+MB4J=MD9D6J	8.80E+03	2.5	6130
334	MD9D6J=C3H5-A+MS6D	3.31E+13	0	21460
335	C5H8-14+MF5J=MD9D6J	8.80E+03	2.5	6130
336	C5H9-15+O2=C5H8-14+HO2	1.60E+12	0	5000
337	C2H3+C3H5-A=C5H8-14	8.00E+12	0	0

338	C6H10-15=C3H5-A+C3H5-A	2.50E+16	0	71000
339	C5H8-14=C2H2+C3H6	2.52E+13	0	59020
340	MD9D6J+O2=MD9D6O2	7.54E+12	0	0
341	MD9D6O2=MD9D6OOH8J	1.25E+10	0	16350
342	MD9D6OOH8J+O2=MD9D6OOH8O2	7.54E+12	0	0
343	MD9D6OOH8O2=MD9DKET68+OH	2.25E+09	0	17850
344	MD9DKET68=OH+C2H3CHO+MS6OXO7J	5.05E+16	0	41600
345	C7H16=H+C7H15-2	6.50E+87	-21	139500
	Reverse Arrhenius coefficients:	5.21E+80	-19.7	38890
346	C7H15-2+O2=C7H15O2-2	7.54E+12	0	0
347	C7H15O2-2=C7H14OOH2-4	2.50E+10	0	20850
348	C7H14OOH2-4+O2=C7H14OOH2-4O2	7.54E+12	0	0
349	C7H14OOH2-4O2=NC7KET24+OH	1.25E+10	0	17850
350	NC7KET24=OH+NC7KET24O	1.05E+16	0	41600
351	CH3COCH2+C3H7CHO=NC7KET24O	3.33E+10	0	6397
352	C7H16=C6H13-1+CH3	2.93E+73	-16.6	118900
	Reverse Arrhenius coefficients:	8.35E+66	-15.8	31830
353	C7H16+H=C7H15-2+H2	2.60E+06	2.4	4471
	Reverse Arrhenius coefficients:	3.93E+03	2.7	11260
354	C7H16+O=C7H15-2+OH	9.54E+04	2.7	2106
	Reverse Arrhenius coefficients:	6.33E+01	3	6798
355	C7H16+OH=C7H15-2+H2O	9.40E+12	1.6	35
	Reverse Arrhenius coefficients:	6.15E+05	1.9	21910
356	C7H16+HO2=C7H15-2+H2O2	1.12E+13	0	17690
	Reverse Arrhenius coefficients:	4.35E+11	0	8165
357	C7H16+O2=C7H15-2+HO2	4.00E+13	0	50150
	Reverse Arrhenius coefficients:	1.10E+09	0.7	-541
358	C7H16+C2H5=C7H15-2+C2H6	1.00E+11	0	10400
	Reverse Arrhenius coefficients:	1.00E+11	0	12900
359	C7H16+C2H3=C7H15-2+C2H4	8.00E+11	0	16800
	Reverse Arrhenius coefficients:	2.00E+12	0	24200
360	C7H16+CH3O2=C7H15-2+CH3O2H	8.06E+12	0	17700
	Reverse Arrhenius coefficients:	2.38E+11	0	3700

Table F.2 The thermal NO mechanism.

No.	Reactions Considered	A (mol cm s K)	b	E (cal mol^{-1})
1	N+NO<=>N2+O	2.70E+13	0	355
2	N+O2<=>NO+O	9.00E+09	1	6500
3	N+OH<=>NO+H	3.36E+13	0	385

G. Numerical Results for CME at Ambient O_2 Levels of 15.0% and 21.0%
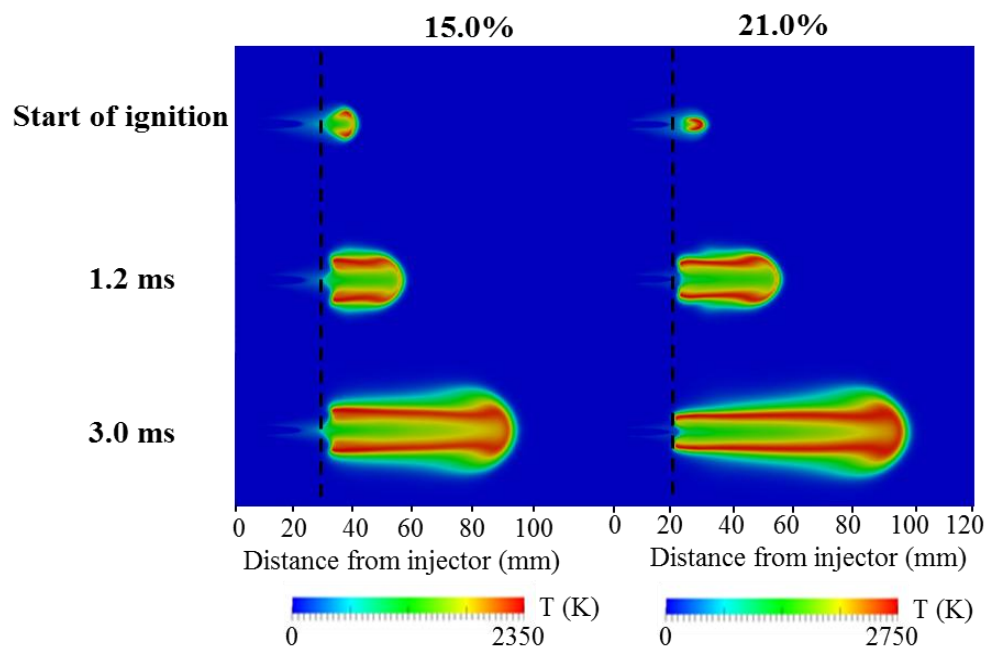
Figure G.1 Predicted flame distributions for CME, at 15.0% and 21.0% ambient O_2 levels, constant volume bomb condition. LOL is denoted by vertical dashed line.
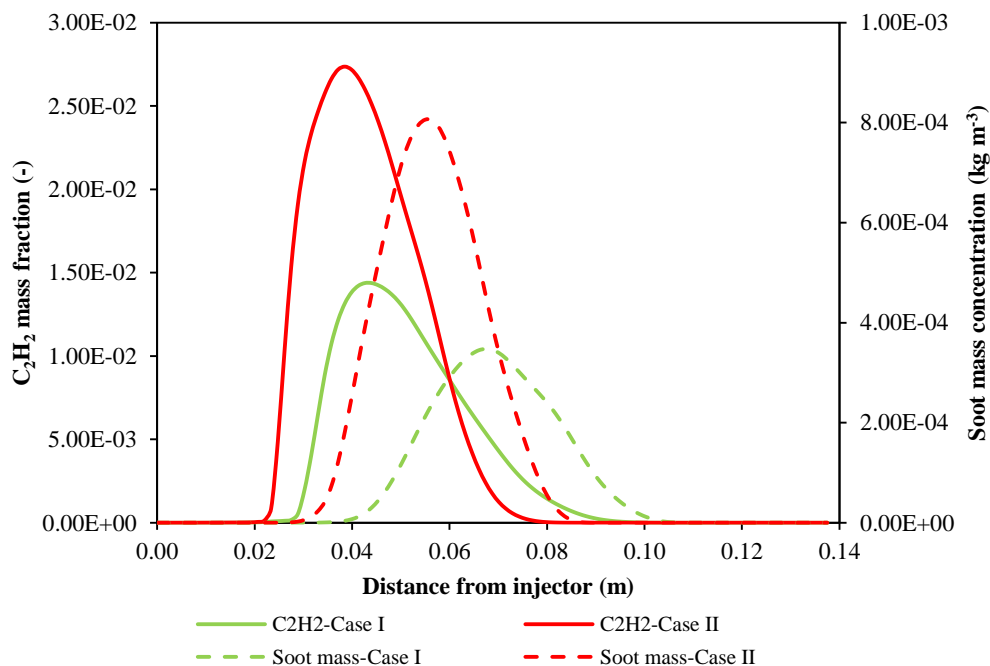
Figure G.2 Predicted spatial C$_2$H$_2$ mass fractions and soot mass concentrations for CME, at 15.0% and 21.0% ambient O$_2$ levels, constant volume bomb condition.
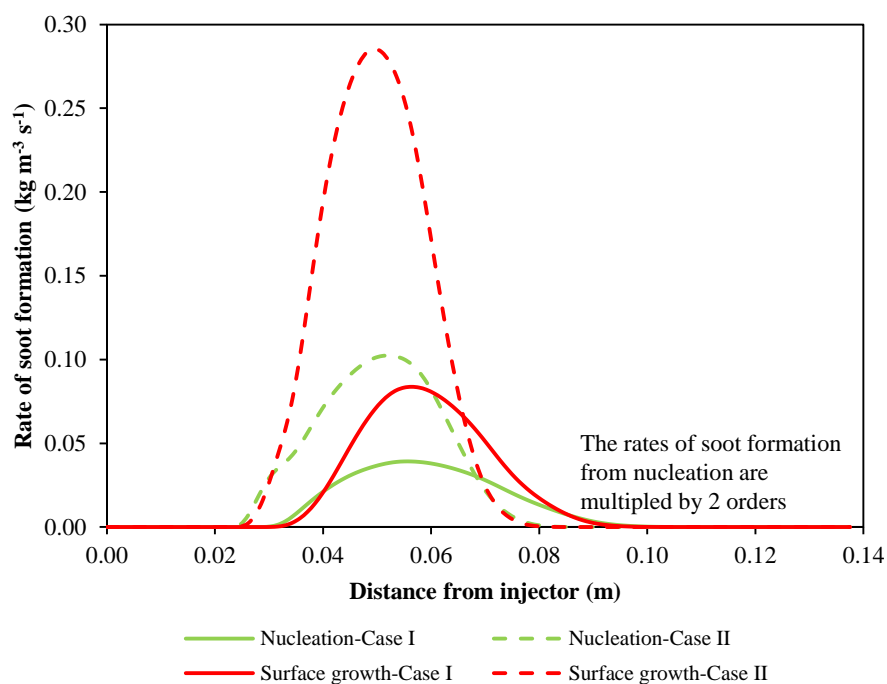

Figure G.3 Predicted spatial rates of soot formation from nucleation and surface growth for CME, at 15.0% and 21.0% ambient O$_2$ levels, constant volume bomb condition.
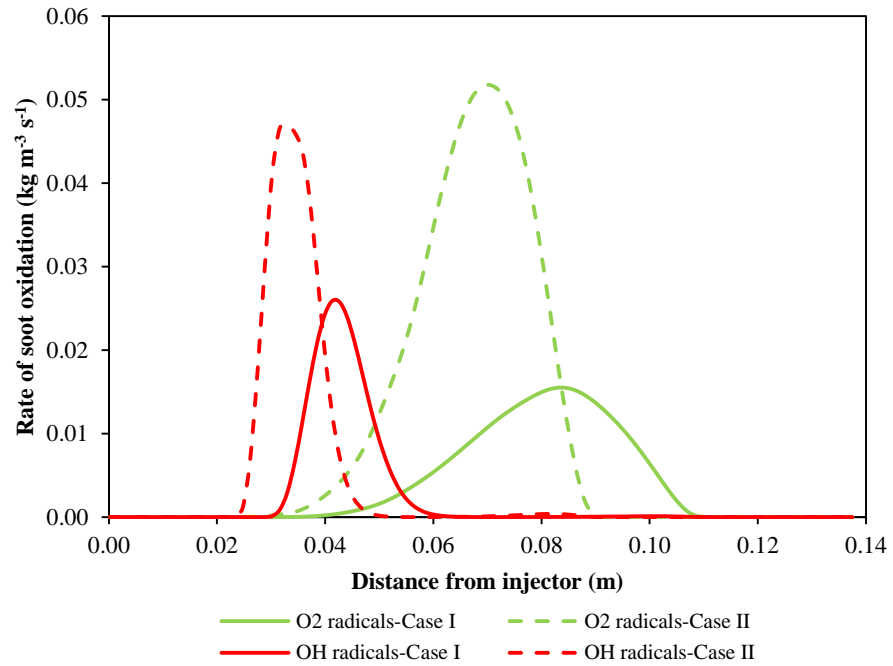
Figure G.4 Predicted spatial rates of soot oxidation by O_2 and OH radicals for CME, at 15.0% and 21.0% ambient O_2 levels, constant volume bomb condition.
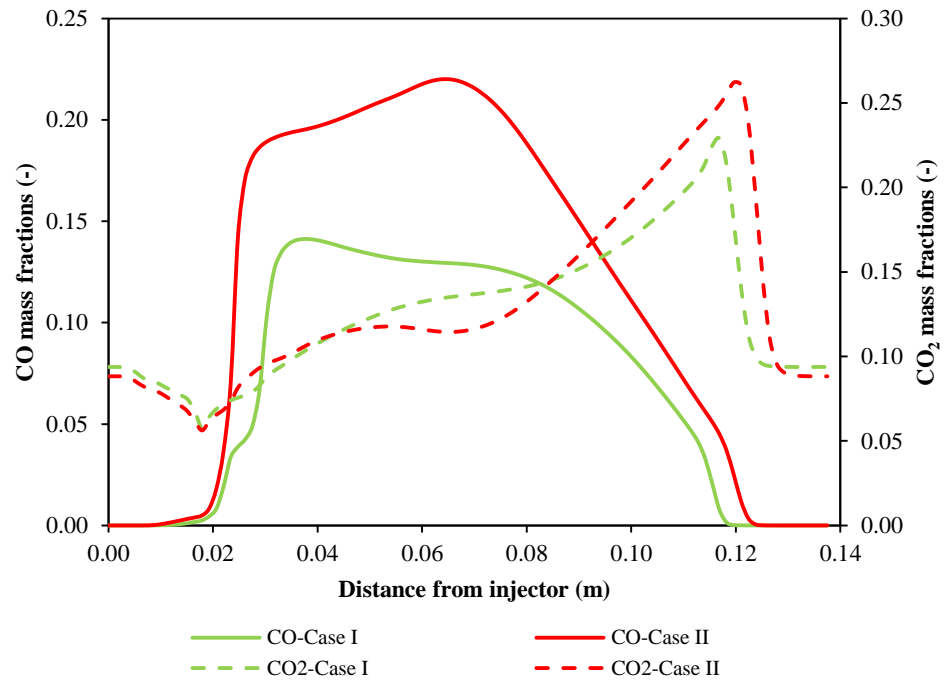

Figure G.5 Predicted spatial CO and CO_2 mass fractions for CME, at 15.0% and 21.0% ambient O_2 levels, constant volume bomb condition.